

**DOCTORAL THESIS**

# Advancements in Sensor Fusion Enabled Indirect Positioning Methods

Aleksei Fjodorov

TALLINN UNIVERSITY OF TECHNOLOGY  
DOCTORAL THESIS  
73/2025

# **Advancements in Sensor Fusion Enabled Indirect Positioning Methods**

ALEKSEI FJODOROV





TALLINN UNIVERSITY OF TECHNOLOGY  
SCHOOL OF INFORMATION TECHNOLOGIES  
THOMAS JOHANN SEEBECK DEPARTMENT OF ELECTRONICS

**The dissertation was accepted for the defence of the degree of Doctor of Philosophy (Information and Communication Technology) on 17 September 2025**

**Supervisor:** Professor Muhammad Mahtab Alam,  
Thomas Johann Seebeck Department of Electronics,  
School of Information Technologies,  
Tallinn University of Technology  
Tallinn, Estonia

**Co-supervisor:** Dr. Taavi Laadung, PhD,  
Eliko Tehnoloogia Arenduskeskus OÜ  
Tallinn, Estonia

**Co-supervisor:** Dr. Alar Kuusik, PhD,  
Thomas Johann Seebeck Department of Electronics,  
School of Information Technologies,  
Tallinn University of Technology  
Tallinn, Estonia

**Opponents:** Professor Sotiris Makis,  
University of Patras,  
Patras, Greece

Dr. Aamir Mahmood,  
Mid-Sweden University,  
Östersund, Sweden

**Defence of the thesis:** 24th October 2025

**Declaration:**

*Hereby I declare that this doctoral thesis, my original investigation and achievement, submitted for the doctoral degree at Tallinn University of Technology, has not been submitted for any academic degree elsewhere.*

Aleksei Fjodorov

---

signature

Copyright: Aleksei Fjodorov, 2025  
ISSN 2585-6898 (publication)  
ISBN 978-9916-80-389-9 (publication)  
ISSN 2585-6901 (PDF)  
ISBN 978-9916-80-390-5 (PDF)  
DOI <https://doi.org/10.23658/taltech.73/2025>

Fjodorov, A. (2025). *Advancements in Sensor Fusion Enabled Indirect Positioning Methods* [TalTech Press]. <https://doi.org/10.23658/taltech.73/2025>

TALLINNA TEHNIKAÜLIKOOL  
DOKTORITÖÖ  
73/2025

# **Andurisulandusel põhinevate kaudsete positsioneerimismeetodite edasiarendused**

ALEKSEI FJODOROV



# Contents

List of Publications .....	7
List of Side Contributions.....	8
Author's Contributions to the Publications .....	9
Abbreviations.....	11
Terms .....	13
1 Introduction .....	14
1.1 Background .....	14
1.2 Introduction to Product Tracking Techniques .....	14
1.3 Problem Formulation & Research Questions .....	15
1.4 Thesis Contributions .....	16
1.5 Thesis Organization .....	18
2 State-of-the-art .....	19
2.1 Indirect Tracking.....	19
2.1.1 Quasi-indirect Techniques .....	19
2.1.2 Indirect Tracking Methods .....	20
2.1.3 Gap in State-of-the-art Methods .....	22
2.2 Heading Estimation .....	23
2.2.1 Drift Effect in Inertial Sensors.....	24
2.2.2 Drift Mitigation Techniques for Inertial Sensors .....	24
2.2.3 Gap in State-of-the-art Methods .....	32
3 Indirect Tracking Methodology .....	37
3.1 Methodology .....	37
3.2 Technology & Sensors' Selection .....	40
3.2.1 Underlying Positioning Unit.....	41
3.2.2 Heading Tracking Unit .....	44
3.2.3 Tynes' Elevation Tracking Unit .....	48
3.2.4 Fork Occupancy Detection Unit.....	51
4 Heading Estimation .....	54
4.1 Positioning Data-based Approach for Vehicle Heading Estimation .....	54
4.1.1 Positioning Data-based IMU Heading Drift Correction Algorithm....	54
4.1.2 Experimental Testing of the Drift Correction Algorithm .....	56
4.2 Kalman Filter Background.....	58
4.2.1 Linear Kalman Filter .....	58
4.2.2 Nonlinear Kalman Filters .....	59
4.2.3 Adaptive Kalman Filter .....	60
4.3 Kalman Filter for Position Estimation .....	60
4.4 Adaptive Tandem Kalman Filter Algorithm for Vehicle Heading Estimation ..	62
4.4.1 Adaptivity Model of the ATKF Algorithm .....	62
4.4.2 Structure of the ATKF Algorithm .....	64
4.4.3 Simulations .....	67
4.4.4 Experimental Testing .....	73

4.5	Discussion .....	79
5	Indirect Tracking .....	81
5.1	Resulting Structure & Description of the Developed Method .....	81
5.2	Automatic Pick-up & Drop-Down Detection Algorithm .....	83
5.3	Preliminary Testing .....	85
5.4	Full-Scale Experimental Testing .....	88
5.4.1	Full-scale Test Campaign Description .....	88
5.4.2	Absolute and Repeatability Performance Results .....	89
5.4.3	Example of Positioning Information Flow in Indirect Tracking Method .....	92
5.4.4	Comparison With the Direct Tracking Approach .....	94
5.4.5	Positioning Quality of Direct and Indirect Tracking Methods .....	95
5.5	Discussion .....	98
6	Conclusions & Future Work .....	99
6.1	Research Questions .....	100
6.2	Future Perspectives .....	102
	List of Figures .....	104
	List of Tables .....	105
	References .....	106
	Acknowledgements .....	123
	Abstract .....	124
	Kokkuvöte .....	126
	Appendix 1 .....	129
	Appendix 2 .....	139
	Appendix 3 .....	155
	Appendix 4 .....	169
	Appendix 5 .....	185
	Appendix 6 .....	187
	Appendix 7 .....	189
	Appendix 8 .....	191
	Appendix 9 .....	197
	Curriculum Vitae .....	199
	Elulookirjeldus .....	202

## List of Publications

The present Ph.D. thesis is based on the following publications that are referred to in the text by Roman numerals.

### Publications

- I A. Fjodorov, S. Ulp, M. M. Alam, and A. Kuusik, "Inertial and Positioning Sensors Fusion for Indirect Location Tracking in Warehouse Inventory Management," *2023 International Conference on Control, Automation and Diagnosis (ICCAD)*, pp. 1–7, 2023
- II T. Laadung, S. Ulp, A. Fjodorov, M. M. Alam, and Y. Le Moullec, "Adaptive Extended Kalman Filter Position Estimation Based on Ultra-Wideband Active-Passive Ranging Protocol," *IEEE Access*, 2023

### Under review

- III A. Fjodorov, S. Ulp, T. Laadung, M. M. Alam, and A. Kuusik, "Vehicle Heading Estimation Using Positioning and Inertial Data-Based Adaptive Tandem Kalman Filter," *IEEE Transactions on Intelligent Vehicles*, 2025

### Accepted

- IV A. Fjodorov, S. Ulp, T. Laadung, M. M. Alam, and A. Kuusik, "Accurate Indirect 3D Localization of Markerless Industrial Products," *IEEE Sensors Journal*, *Accepted: 18.09, 2025*

## List of Side Contributions

Following publications represent parallel contributions outside the primary research focus.

- A. Fjodorov, A. Masood, M. M. Alam, and S. Päränd, "5G Testbed Implementation and Measurement Campaign for Ground and Aerial Coverage," *2022 18th Biennial Baltic Electronics Conference (BEC)*, pp. 1–6, 2022
- I. Mürsepp, A. Fjodorov, and M. M. Alam, "Non-Line of Sight Detection Based on 5G Signal Strength-and Quality Measurements and its Impact on Mobile Positioning Accuracy," in *2024 International Wireless Communications and Mobile Computing (IWCMC)*, pp. 256–261, IEEE, 2024

## Author's Contributions to the Publications

- I Publication I: I was the lead author, contributing with the overview of the available state-of-the-art heading estimation methods, their advantages and limitations in the context of vehicle applications; Proposal of the positioning data-based IMU heading drift mitigation approach; Complete designing and development of the IMU heading drift correction prototype algorithm for the positioning data-based approach verification, as well as the implementation of the corresponding algorithm software for the experimental testing; Implementation of the data collecting setup and software, preparation of the experimental testing, as well as data collection, results acquisition and analysis; Preparation of the corresponding manuscript and its components (figures & tables), as well as its eventual feedback-based revision.
- II Publication II, I was a co-author, contributing by cooperating in the design and implementation of the A-EKF (Adaptive Extended Kalman Filter) algorithm for AP-TWR (Active-Passive Two-Way Ranging) UWB ranging data filtering and processing in the resulting tracked location estimation.
- III Publication III, I was the lead author, contributing with a further overview of the available heading estimation methods, state-of-the-art sensor fusion algorithms, their advantages, limitations, and possible applications in the context of reliable vehicle heading estimation; Complete designing and development of the Kalman filter-based algorithm for heading estimation, as well as its software implementation for testing; Implementation of the simulated testing environment for this algorithm, its simulated testing and comparison with another developed algorithm, the corresponding results acquisition and analysis; Preparation of the data collecting setup and software for the experimental testing; Experimental data collection, results acquisition and analysis; Preparation of the corresponding manuscript components (figures & tables), manuscript writing, and its eventual feedback-based review.
- IV Publication IV, I was the lead author, contributing with the investigation and overview of the available state-of-the-art indirect tracking methods, their advantages and limitations, as well as capability to answer the markerless indirect tracking problem, addressed with this research; Proposition of the fully markerless indirect tracking method, its conceptual description and selection of the suitable hardware, methods and algorithms for its implementation; Designing and development of the Automatic Pick-up and Drop-down Detection algorithm (A-PDD) for complete indirect tracking method automation, as well as its software implementation on the embedded platform for the live experimental testing; Implementation of the prototype test setup for the indirect tracking method experimental testing, necessary data collection in the industrial environment, as well as further results acquisition and analysis; Preparation of the corresponding manuscript components (figures & tables), manuscript writing, and its eventual feedback-based revision.





## Abbreviations

2D	Two-Dimensional
3D	Three-Dimensional
5G	5 <sup>th</sup> Generation of Cellular Technology
A-EKF/AEKF	Adaptive Extended Kalman Filter
A-PDD	Automatic Pick-up & Drop-down Detection
ABAS	Adaptive Beetle Antennae Search
AGV	Automated Guided Vehicles
AHRS	Attitude and Heading Reference System
AI	Artificial Intelligence
AMR	Anisotropic Magnetoresistance
AoA	Angle of Arrival
AoD	Angle of Departure
AP-TWR	Active-Passive Two-Way Ranging
AR	Auto-Regressive
ARW	Angular Random Walk
ATKF	Adaptive Tandem Kalman Filter
AUKF	Adaptive Unscented Kalman Filter
AUV	Autonomous Underwater Vehicles
BT	Bluetooth
BLE	Bluetooth Low Energy
CatBoost	Categorical Boosting
CDF	Cumulative Distribution Function
CKF	Cascaded Kalman filter
CNN	Convolutional Neural Network
DoF	Degrees of Freedom
DR	dead reckoning
DVL	Doppler Velocity Log
ECF	Explicit Complementary Filter
EKF	Extended Kalman Filter
EMD	Empirical Modal Decomposition
ENN	Elman Neural Network
ESKF	Error-State Kalman filter
FIFO	First In, First Out
FOG	Fiber-Optic Gyroscope
FTM	Fine Timing Measurement
GLONASS	Global Navigation Satellite System
GMR	Giant Magnetoresistance
GNSS	Global Navigation Satellite System
GPS	Global Positioning System
IoT	Internet of Things
IMU	Inertial Measurement Unit
InEKF	Invariant Extended Kalman Filter
INS	Inertial Navigation System
IR	Infrared
KF	Kalman Filter
LiDAR	Light Detection and Ranging
LightGBM	Light Gradient Boosting Machine
LPV	Linear Parameter Varying
LSTM	Long Short-Term Memory
LVC	Lateral Velocity Constraint

MARG	Magnetic, Angular Rate, and Gravity
MarLO	Marker-based Local positioning system
MCU	Microcontroller Unit
MdAD	Median Absolute Deviation
MdAE	Median Absolute Error
MEMS	Micro-electro-mechanical systems
MHE	Material Handling Equipment
ML	Machine Learning
mmWave	Millimeter Wave
MnAD	Mean Absolute Deviation
MnAE	Mean Absolute Error
NMNI	No Motion, No Integration
NN	Neural Network
OACP	Orientation Axes Crossover Processing
OFS	Optical Flow Sensor
PAKF	Parallel Adaptive Kalman Filter
PF	Particle Filter
PIR	Passive Infrared
PNDR	Positioning-Noise-to-traveled-Distance Ratio
QR	Quick-Response
QUEST	Quaternion Estimation
RBF	Radial Basis Function
RFID	Radio-Frequency Identification
RLG	Ring Laser Gyroscopes
RMSE	Root Mean Squared Error
RQ	Research Question
RSSI	Received Signal Strength Indicator
RTK	Real Time Kinematic
RTLS	Real-Time Location System
SAR	Synthetic Aperture Radars
SFDI	Sensor Fault Detection and Isolation
SPKF	Sigma Point Kalman Filter
SCKF/SRCKF	Square-Root Cubature Kalman Filter
SS-TWR	Single-Sided Two-Way Ranging
SD	Standard Deviation
SVR	Support Vector Regression
TMR	Tunnel Magnetoresistance
ToF	Time of Flight
UAV	Unmanned Aerial Vehicle
UKF	Unscented Kalman Filter
UWB	Ultra-Wideband
Wi-Fi	Wireless Fidelity
XGBoost	Extreme Gradient Boosting
ZUPT	Zero Velocity Potential Update

## Terms

Tynes	Fork of the forklift
Asset/Product	Any payload, which is transported by material handling equipment and requires localization

# 1 Introduction

## 1.1 Background

Today, the industry is rapidly developing by integrating numerous intelligent technologies and innovative systems for its process automation and optimization, thus reshaping industrial production and warehousing. The integration of different smart solutions in these fields aims to improve overall process efficiency, transparency, and scalability, while bolstering workplace safety and reducing the risk of human error [7, 8, 9]. Real-time localization and identification of stored products or processed materials remains one of the essential aspects of warehousing and production management. In this realm, accurate tracking ensures seamless inventory control, minimizes delays, misplacements, and operational bottlenecks. The increasing adoption of IoT (Internet of Things) devices and AI (Artificial Intelligence) further revolutionizes warehousing operations, allowing predictive maintenance, intelligent resource allocation, and real-time data analytics, enhancing the decision-making processes. Moreover, integration of automated guided vehicles (AGVs), collaborative robots, and intelligent machinery redefines traditional workflows, enhancing production scale, speed, and precision [10]. These technological advancements also lead to an increase in production sustainability by optimizing resource usage, reducing waste, and minimizing energy consumption.

## 1.2 Introduction to Product Tracking Techniques

A variety of different positioning methods are actively advancing and being integrated for industrial needs. Direct tracking of industrial equipment, personnel, machinery, products, or other objects can be considered the most straightforward and widely utilized localization approach. It unites a variety of different tracking methods and solutions, in which the tracked object is physically marked with a piece of positioning equipment, localized by its corresponding specialized infrastructure. Physically attached positioning units - tags, can be classified into active and passive units, which determine their participation in the positioning process and overall intelligence [11, 12]. Active tags can be mainly determined by their capability to actively communicate with the positioning infrastructure. Passive tags, on the other hand, do not support the active data exchange with the positioning infrastructure and only perform a passive data reception or provide a one-time predefined response.

Active positioning systems are used in the industry and warehousing for real-time tracking of specialized equipment, machinery, or products. Being one of the most advanced industry-level localization systems, the Ultra-Wideband (UWB) indoor positioning system is widely used. It is designed to provide accurate and real-time tracking in the indoor environment and can be successfully used to track industrial assets or specialized equipment, as stated by Shyam *et al.* [13] and Volpi *et al.* [14] in their works. Direct equipment and product localization may also be based on various alternative and widely available technologies, including active RFID (Radio-Frequency Identification) tags [15] to Wi-Fi (Wireless Fidelity) [16], Bluetooth [17], or cellular technologies such as 5G (5<sup>th</sup> Generation of cellular technology) [18]. The use of active tag positioning systems, however, leads to different essential limitations and drawbacks for industrial management and warehousing. One of the major limitations is the limited scalability of those methods, as the number of required positioning units increases proportionally to the number of tracked products. Finally, direct tagging of a larger number of products and equipment with active tracking units will naturally decrease the cost- and energy efficiency of this approach, as well as increase the data processing complexity and hardware maintenance requirements.

Passive tag-based methods are widely used in modern warehousing and industry primarily for product or equipment identification purposes. The broad use of product identification technologies, such as passive RFID tags [19], QR (Quick-Response) codes [20], or barcodes [21], is explained by their widest availability and cost efficiency. Even though these technologies also provide significant scalability in product identification, they are not initially designed for their localization purposes. Nevertheless, according to numerous available/developed methods, real-time product localization based on passive tags will require the deployment of additional, expensive, and complex supporting infrastructure. This infrastructure can be deployed on the asset storage shelves and racks, as in methods described by Poon *et al.* [22] and Motroni *et al.* [23], within the selected production area [24], or across the ceiling of the entire industrial area, as proposed by Jeon *et al.* [25] and Nepa *et al.* [26] in their works. Non-real-time localization of RFID-tagged products can also be performed by using mobile platforms, such as drones or robots. Equipped with the necessary sensor setup, a mobile platform performs a continuous mapping of the available RFID-marked products in the area, thus localizing them. This approach may rely on different techniques from base RFID scanning, as proposed by Kapoor *et al.* [27] and Li *et al.* [28], to Synthetic Aperture Radars (SAR), as developed by Motroni *et al.* [29] and Buffi *et al.* [30].

Although traditional direct localization methods are actively and widely adopted in the industry, in certain cases and scenarios, they remain inapplicable. Throughout their active production process, different industrial materials, such as wood, metal, or stone, often face frequent physical processing, high temperatures, critical accelerations, or other extreme conditions. These conditions are likely to lead to damaging or altogether destroying any attached tracking or identification unit, thus restricting the possible use of traditional direct tracking methods. Accurate real-time identification and localization of those products requires an alternative, indirect, and fully markerless method [31, 32].

### 1.3 Problem Formulation & Research Questions

This research addresses the problem of accurate real-time localization of industrial products and equipment in cases where their direct physical marking with neither active positioning tags nor passive identification tags is possible. Thus, the main topic of this research attempts to formulate and develop an ***Indirect Tracking Method for Accurate, Automatic, and Three-dimensional Localization of Fully Markerless Industrial Products***. As it is further described in Section 3, the indirect tracking methodology formulation process has also revealed the importance of ***Accurate Vehicle Heading Estimation Method, Suitable For Industrial Environments***, which eventually became the separate and primary subtopic for this research. This research aims to meet the following criteria, initially formulated for this work from the perspective of the Industry 4.0 [33], and applicable to both topics of this research:

1. Tracked products and equipment must remain fully markerless. In particular cases, when the direct product marking with identification tags is acceptable, it may be integrated as an entirely auxiliary technology.
2. A three-dimensional product tracking must be supported to cover most of the possible product storage scenarios, including their stacking and shelving.
3. The proposed method must provide a possible cost efficiency and computational incomplexity of the resulting solution. Overall criteria for the sensors & hardware setup include:

- Essential set of hardware and sensors with minimized use of extra supporting and auxiliary units (the necessary minimum of sensors & hardware).
  - Cost-efficiency of the chosen setup of sensors.
  - Possible computational incompleteness and minimized data processing requirements
4. The proposed method must be automated to increase the time efficiency and minimize the impact of human error.
  5. Seamless deployment of the necessary infrastructure, requiring minimal adjustments and changes in both the covered industrial environment and the natural workflow.
  6. Minimal integration of the designed method components into the mechanisms of the used industrial machinery, such as Material Handling Equipment (MHE) (e.g., forklifts, lifters, cranes).

### Research Questions

This research is based on the following research questions, which cover both the main topic and primary subtopic of this research:

- **RQ1:** *What method should be developed in order to provide accurate automatic real-time 3D **positioning of markerless industrial products/assets**?*
- **RQ2:** *Can the positioning data be reliably used in combination with inertial data for accurate **vehicle heading estimation** in an industrial environment? Will this approach be sufficient for accurate heading tracking of highly maneuverable industrial vehicles?*
- **RQ3:** *What sensor fusion method should be developed to utilize the benefits and overcome the limitations of positioning and inertial data in **vehicle heading estimation**? Are the extra/additional supporting sensors required in this method? What is a suitable sensor fusion algorithm for inertial and positioning data-based real-time vehicle heading estimation?*

### 1.4 Thesis Contributions

The following contributions were presented in this research to respond to the research questions defined in the previous section:

- **Publication I** contributes by addressing the primary subtopic of this research, focused on the accurate heading estimation methods for industrial vehicles. This publication investigates the possibility of effectively using the positioning and inertial data combination for reliable heading estimation in cases when the available state-of-the-art methods are inapplicable. This publication addresses the fundamental problem of the over time error accumulation in an inertial (gyroscope) sensor estimated orientation and proposes an algorithmic method for the drift correction in gyroscope estimated heading. Publication I covers the experimental testing of the proposed algorithmic method and provides the corresponding promising results. Thus, Publication I fully answers **RQ2**, as well as initially addresses the research question **RQ3**. Additionally, this publication addresses the targeted real-life application for the proposed method and partially provides the brief background context

of the main research topic of this work - indirect localization of markerless industrial products, thus partially addressing the research question **RQ1**.

- **Publication II** reflects the further research on the vehicle heading estimation subtopic and practically investigates advanced features and possible use of one of the potentially suitable state-of-the-art fusion algorithms - the Kalman filter. This publication contributes by practically investigating the use of various Kalman filter algorithm versions, including their nonlinear and adaptive versions, thus partially answering the research question **RQ3**. The contribution of this publication results in the implementation of the Adaptive Extended Kalman Filter (A-EKF) algorithm for UWB positioning, which practically validates the performance of the Kalman filter algorithm and its adaptivity features.
- **Publication III** concludes the research on the vehicle heading estimation subtopic and contributes by designing and implementing the Adaptive Tandem Kalman Filter (ATKF) algorithm for accurate vehicle heading estimation, based on the alternative approach in inertial and positioning sensor fusion. This publication covers the simulated and experimental testing of the designed ATKF algorithm and provides the achieved promising results, thus answering the research questions **RQ2** and **RQ3**. Additionally, this publication experimentally demonstrates the performance of one of the state-of-the-art algorithms and provides its comparison with the designed ATKF algorithm. Section 4.4.4 of this thesis extends the comparison of the designed methods with multiple state-of-the-art algorithms.
- **Publication IV** contributes by addressing the main research topic of markerless indirect tracking method, investigates the available methods and their limitations, as well as eventually proposes a suitable method for the indirect localization of fully markerless industrial products. This publication defines the necessary requirements, components, and algorithms for the designed method. This publication also contributes by designing and implementing a sensor fusion algorithm for an Automatic payload Pick-up and Drop-down Detection (A-PDD). Publication IV covers the conducted experimental testing of the prototype indirect tracking setup and provides promising results on the markerless product positioning. This publication also provides a direct comparison of the developed indirect tracking method with a more traditional direct localization approach. Thus, Publication IV answers the research question **RQ1** and concludes the main topic of this research.

Table 1: Formulated research questions answered in published works

Research Questions	Publication I	Publication II	Publication III	Publication IV
<b>RQ1</b>	x			x
<b>RQ2</b>	x		x	
<b>RQ3</b>	x	x	x	

Table 1 reflects research questions, addressed and answered in particular publications. Gray markers indicate the partial (**RQ1** & **RQ3**) or extensive (**RQ2**) coverage of the corresponding research question. The research question **RQ1** is initially addressed in Publication I and fully answered in Publication IV. Research question **RQ2**, on the other hand, is



fully answered in Publication I, while Publication III provides an extensive answer. Particular aspects of the research question **RQ3** are preliminarily covered in Publications I and II, while Publication III provides a comprehensive answer to this research question.

## 1.5 Thesis Organization

The thesis includes two key topics in different fields, requiring separate state-of-the-art analysis: the main research topic, which covers the indirect tracking of markerless products, and the primary subtopic, focused on the industrial vehicle heading estimation. While the presented research is performed from the perspective of the main indirect products tracking topic, it starts by fully addressing the primary subtopic of vehicle heading estimation. Therefore, the thesis is organized as follows: The thesis starts with the introduction to the performed research in Section 1, covering the background of the main research topics, the definition of the main research problem, and the corresponding research questions. Section 2 is separated into two subsections, independently investigating the available state-of-the-art methods and solutions for both main topics of this research, as well as applying the defined research questions to determine the existing gaps in both fields. Section 3 introduces the methodology behind the main topic of this research and selects its necessary components. This provides the background and justifies/motivates the primary subtopic of this research. Section 4 describes the performed work on the main subtopic, based on the defined methodology. It includes the explanation of the proposed methodology, a description of multiple developed algorithmic methods, their preliminary simulated and experimental testing, as well as the analysis of the results. Based on methods and techniques defined in the aforementioned chapters, Section 5 proceeds with the main research topic, covering the resulting execution of the proposed method, description of developed algorithmic methods, as well as both preliminary and full-scale experimental test campaigns with a discussion of the corresponding results. Section 6 provides the resulting discussion of this research, further development possibilities, and concludes the thesis.

## 2 State-of-the-art

The state-of-the-art section covers the literature analysis for the Indirect Tracking research topic, from separate contactless identification methods to indirect tracking methods, available in the literature and the industry. As the key subtopic of this research is related to accurate Vehicle Heading Estimation, the second section in the state-of-the-art analysis covers the literature overview for the corresponding field.

### 2.1 Indirect Tracking

According to the literature in the field of industrial positioning, the broad term "indirect tracking" refers to object positioning methods, which exclusively prohibit the direct attachment of any active positioning units, such as UWB or active RFID tags [34, 35, 36, 37]. These methods, however, may still involve the direct marking of tracked objects using passive identification tags (e.g., passive RFID, QR codes, or barcodes), which in the literature is considered consistent with the principles of indirect tracking. This research, on the other hand, is focused on shifting the paradigm and removing the direct tagging altogether, leading to the strict definition of (markerless) indirect tracking.

#### 2.1.1 Quasi-indirect Techniques

Certain product positioning methods may be categorized as quasi-indirect, as in these approaches, the tracked product may not require direct tagging and is bound to specific reference objects instead. In this case, the necessary tracking and identification information is bound to the reference objects, such as industrial pallets, shelves, or moving platforms. For instance, as proposed by Volpi *et al.*, the industrial equipment and assets may be localized together with mobile shelves and platforms, actively tracked in real-time by using the UWB indoor positioning system [14]. In this case, industrial assets may be associated with the corresponding transportation platforms and tracked in real time.

Alternatively, industrial pallets can be equipped with more cost-effective passive markers, such as RFID tags, increasing both availability and scalability of these methods. The different approaches can then be used to monitor the movement of the pallet within the area over time. For instance, as proposed by Rosli *et al.* and Motroni *et al.* in their respective works, the pallet movement between specific zones can be tracked using RFID scanning gates, deployed between zones of interest [38, 39]. Li *et al.*, on the other hand, have proposed a method for a more comprehensive pallet tracking between specific storage areas [40]. In their method, the tracked pallets and specific storage spots and shelves are tagged with passive RFID tags, where the RFID scanning equipment is deployed on the material handling equipment (i.e., forklift), used for their transportation. In this approach, the pallet and its storage spot identification information are scanned simultaneously by the forklift at the moment of pallet interaction. Implementation variants of the analogous tracking approach are also available in the industry [41, 42].

Integration of different smart technologies also supports the active development in the field of vision-based recognition of industrial pallets. This field covers different intelligent methods allowing the detection of industrial pallets, from fiducial markers-supported detection [43] to the pallet shape recognition, based on technologies such as LiDARs (Light Detection and Ranging) [44], ML (Machine Learning) assisted rangefinders [45, 46], and intelligent vision [47, 48]. In the context of this research, however, these methods can be considered quasi-indirect, as the presence of reference objects remains essential for tracked asset identification and localization.

Visual recognition of the tracked object can also be performed without the use of ref-

erence objects and, in the context of this research, can be considered as indirect identification. However, this approach becomes significantly limited by the variety and shapes of detectable objects [49]. Positioning methods, based on signal reflection sensing (e.g., by using common positioning technologies, such as UWB [50], RFID [51], or ultrasonic sensing [52]), can also be considered as indirect tracking methods. These methods, however, are sensitive to all objects in the line of sight without the possibility of differentiating them. In order to support active positioning of specific objects, these methods would require comprehensive control over the surrounding environment. This may be achieved by a preliminary mapping of the stationary environmental background and specifying restricted and permitted zones for movement, such as corridors between shelving units. Methods such as capacitive sensing-based positioning may provide the differentiation of the tracked object at a higher level [53]. This technology is capable of detecting non-ferrous materials within a range, limited to a few decimeters, which reduces the effectiveness of this method, especially in three-dimensional positioning.

### 2.1.2 Indirect Tracking Methods

Several methods for the indirect tracking of industrial objects, in accordance with the broad definition, are available in the literature and are reflected in this section. These methods propose different approaches and sensor setups to perform the localization of industrial assets, where the main part of the tracking setup is deployed on the material handling equipment, such as an industrial forklift. However, the available methods follow the broad definition of the "indirect tracking" term, provided in Section 3, and remain fully or partially reliant on the direct marking of tracked assets with passive tags.

One of the available methods for indirect tracking of industrial pallets was proposed by Kovavisaruch *et al.* [54]. This method is primarily based on the real-time location of the used forklift, tracked by the deployed UWB positioning system. In their approach, the transported industrial pallets are tracked by associating their location with the real-time coordinates of the forklift. However, the direct association of the transported pallet's position with the forklift's coordinates introduces a substantial localization error, typically exceeding 1 meter in the estimated pallet location. This error is explained by the physical offset between the deployed positioning unit and the transported object, which is located in the fork (tynes) area of the forklift. The tracked forklift location is also used to identify one of the possible predefined forklift movement routes to further improve its positioning. In the presented method, the tracked pallets remain directly marked with barcodes for their identification. Along with pick-up & drop-down detection, the barcode scanning routine is performed manually by the forklift operator. This significantly limits the automation of the described method. Nevertheless, this approach allows positioning of the barcode-marked pallets with a declared average precision of 47 cm.

A similar method for automated indirect asset tracking was proposed by Zhao *et al.* and Frankó *et al.* in their respective works [34, 35]. The localization method proposed in their works, however, follows the broad definition of indirect tracking and entirely relies on the direct marking of industrial assets with passive RFID tags to identify the particular asset and detect its pick-up for transportation. The continuous presence of a particular asset within the fork area is detected by the onboard RFID reader unit, thus confirming its transportation status. This approach provides full automation of the tracking process of the transported assets for the proposed methods. Coordinates of the transported product are then directly associated with the real-time location of the forklift, actively tracked by the UWB indoor positioning system. However, since in the forklift body frame, the positioning unit is physically deployed with a certain offset from the transported product, this

offset becomes a constant, beyond-meter error in the resulting asset coordinates. The indirect tracking method, proposed by Frankó *et al.*, additionally utilizes the geofencing technique, in which the asset transportation is only performed between predetermined storage areas. This approach may partially compensate for the aforementioned offset error in the tracked asset location. Also, in their method, the RFID tags scanning routine, similarly used for the payload loading detection, is triggered by the onboard accelerometer unit and performed only during the forklift movement periods.

Barral *et al.* in their work discuss the theoretical approach for industrial product localization by precise tracking of MHE, such as forklifts [55]. In their work, authors have proposed a method for forklift orientation and positioning data tracking, based on the fusion of the UWB positioning system, IMU (Inertial Measurement Unit), and PX4 optical flow camera. In simulation tests, their method has shown below 20 cm Mean Absolute Error (MnAE) in forklift positioning, while its performance in the forklift heading estimation is not evaluated. Even though their work is primarily focused on the performance enhancement of the UWB positioning system in challenging line-of-sight conditions, authors also briefly discuss the possibility of the product positioning. However, possible approaches for the transported payload positioning, further method automation, or the expected performance of their method in the actual product localization are not covered in their work.

A different pallet monitoring system, based on the passive planar Markers-based Local Positioning System (MarLO) was proposed by Borstell *et al.* [36]. This method was designed for vehicle and asset localization in industrial areas and is assisted by specialized gates with additional integrated sensors, installed between sections of the industrial area. Integrated sensors include RFID scanners and depth sensors, used for identification and dimension measurement of the transported assets. Even though this method provides extra information on the transported assets, it remains significantly dependent on the deployment of additional complex infrastructure in the industrial area. Additionally, the automatic detection of the asset pick-up or drop-down events is not covered in their method, and is performed manually by the working personnel.

Motroni *et al.* in [56] proposed an indirect asset tracking method based on a multi-sensor setup, primarily deployed on an industrial forklift. This method attempts to provide an automatic indirect 2D localization of industrial assets, normally transported by forklifts. The real-time location of the transported asset is determined by the multi-sensor setup of the UWB positioning system, IMU, and Optical Flow Sensor (OFS), aided with laser distance sensors. These sensors are fused to determine the position and orientation of the forklift, and therefore estimate the exact location of the transported asset. Sensor fusion is performed by a computationally heavy and reliable version of the Kalman filter algorithm for non-linear models - the Unscented Kalman Filter (UKF) [57, 58]. Even though their work is mainly focused on the forklift position & orientation tracking, the authors also theoretically discuss a possible approach for asset identification, tracking, and loading/unloading detection. Their discourse leads to the automatic detection of the asset loading by the ultrasonic distance sensor deployed in front of the forklift. Their method, however, requires the direct marking of assets with passive RFID tags for further identification purposes. The RFID tag of the asset is scanned by the forklift-deployed RFID reader unit during the loading process, thus identifying the interacted asset. Unfortunately, the experimental validation and evaluation of the presented indirect tracking method were not covered in their research.

Recently, Zealabs and Sewio have developed a solution for indirect (by their definition, tag-less) localization of industrial coils for the Prokab cabling factory [59, 60]. In this

method, the industrial materials are transported by the UWB-tracked forklift, equipped with the necessary sensors for process automation and product identification. Similar to methods proposed by Frankó *et al.*, Zhao *et al.*, and Kovavisaruch *et al.*, the location of the transported material is directly associated with the forklift coordinates, causing the aforementioned fork-to-positioning unit offset error. Unlike previously described methods, this approach provides a complete three-dimensional tracking of the transported materials by measuring the fork elevation level using an air pressure sensor. The load sensor, deployed within the fork area, allows real-time detection of the material loading and unloading, thus automating the tracking process. However, for material identification purposes, this method relies on the direct product marking with QR codes, eventually scanned by the onboard camera, which makes this method not entirely tagless.

### 2.1.3 Gap in State-of-the-art Methods

Table 2 reflects the key features and limitations of the state-of-the-art indirect tracking methods, described in Section 2.1.2. Available state-of-the-art indirect tracking methods are evaluated from the perspective of this research, based on the key requirements defined in Section 1.3.

Table 2: Key aspects, features and gaps in available state-of-the-art indirect tracking methods. Highlighted cells indicate significant deviations from the requirements defined in this work and represent gaps in corresponding methods.

	Kovavisaruch <i>et al.</i> [54]	Zhao <i>et al.</i> [34]	Frankó <i>et al.</i> [35]	Barral <i>et al.</i> [55]	Borstell <i>et al.</i> [36]	Mottroni <i>et al.</i> [56]	Zealabs [59, 60]
Direct product marking is required	Yes	Yes	Yes	- <sup>1</sup>	Yes	Yes	Yes
Product identification technology	Barcode	RFID	RFID	- <sup>2</sup>	RFID	RFID	QR
Supported product tracking dimensions	2D	2D	2D	- <sup>1</sup> (2D)	2D	2D	3D
Product loading detection technology	Manual	RFID	RFID	- <sup>1</sup>	Manual	Ultrasonic sensor	Pressure sensor
Total number of sensors used	2	2	3	3	4	6	4
Number of sensors for product positioning	1	1	1	- <sup>1</sup> (3)	1-2	4	2
Expected product positioning accuracy	Low	Low	Medium	High <sup>2</sup>	Low	High	Low
Extra product information collected <sup>3</sup>	None	None	None	None	Dimensions	None	Weight
Approximate data processing complexity	Low	Low	Low	High	Medium	Medium to High	Medium
Adjustments in application environment	Dedicated storage <sup>4</sup>	Dedicated storage <sup>4</sup>	Dedicated storage <sup>4</sup>	- <sup>1</sup>	RFID gates	No	No
Embedded sensors' deployment on MHE	No	No	No	No	No	Moderate	Yes

<sup>1</sup>Not covered in the referred work.

<sup>2</sup>Product positioning is outside the scope of the referred work, and is only briefly mentioned with no details & clarification information provided.

<sup>3</sup>Extra information collected by the proposed method regarding the tracked products beside the base location and identification data.

<sup>4</sup>Products are strictly stored in predefined locations.

According to the research on state-of-the-art methods for indirect localization of industrial objects, the available methods are initially determined by the broad term of "indirect tracking", presented in the literature and defined in Section 2.1. Thus, the available methods remain fully or partially dependent on the direct marking of tracked products with passive identification tags, including RFID [34, 35, 56, 36], QR codes [59, 60], and barcodes [54], which represents the primary gap in the field of indirect tracking. Additionally, the vast majority of the available methods are unable to support three-dimensional positioning, essential in warehousing and industry [54, 34, 35, 36, 56]. Among the available indirect tracking methods, the 3D positioning of the tracked product is only supported in the industrial solution proposed by Zealabs [59, 60].

The majority of the available indirect tracking methods also require the integration of necessary regulations or adjustments in the operating environment (e.g., warehouse). Thus, methods proposed by Kovavisaruch *et al.* [54], Zhao *et al.* [34], Frankó *et al.* [35], and Borstell *et al.* [36], for instance, strictly rely on the products' storage only in dedicated areas. Additionally, the proposed approach of Borstell *et al.* requires the installation of specialized scanning gates within the tracked environment, equipped with RFID and depth sensors. These approaches lead to a more discrete and less flexible product storage model, which may affect the natural industrial and warehousing workflow and be unsuitable in certain cases. Methods, proposed by Zealabs [59, 60] and Motroni *et al.* [56], on the other hand, utilize sensors, which potentially require an invasive installation into the mechanisms of the used MHE, significantly limiting the setup deployment in various cases, such as rented industrial equipment and MHE.

Even though the available state-of-the-art indirect tracking methods remain primarily incomplex, the majority of them tend to rely on insufficient data for highly accurate asset positioning. For instance, in approaches proposed by Kovavisaruch *et al.* [54], Zhao *et al.* [34], Frankó *et al.* [35], and Zealabs [59, 60], the product location is directly associated with the coordinates of the forklift, which is expected to introduce a significant, above-meter offset error in the resulting product positioning.

This work addresses the selected key limitations of the available methods and aims to propose a fully markerless method for accurate, automatic, real-time, and indirect 3D localization of industrial products. It focuses on the use of a minimal number of sensors, reduced computational complexity, and data processing requirements, while ensuring seamless method integration into the natural industrial process by minimizing possible adjustments to the used machinery, equipment, or the operating environment. This work also aims to mitigate the aforementioned offset error in the tracked product position by using accurate heading estimations of the utilized MHE. Section 2.2 investigates the available methods and techniques for vehicle heading estimation, along with their existing limitations.

## 2.2 Heading Estimation

As it was addressed in the previous section and is closely described in Section 3, this work focuses on the use of accurate vehicle heading information in order to mitigate the offset error in the indirectly tracked product position, addressed in the previous section. In order to provide the accurate heading tracking of industrial material handling equipment, this work focuses on the use of inertial sensors - MEMS (Micro-Electro-Mechanical Systems) gyroscope, which is closely discussed and justified further in Section 3.2.2. It was chosen as widely available and the most suitable option for the aforementioned role in the context of this research and the proposed markerless indirect tracking method. This section introduces the main drawback of the inertial gyroscope sensors, and covers the

main available state-of-the-art methods for its mitigation from the perspective of the main topic and criteria, defined in Section 1.3, as well as mentions alternative state-of-the-art heading estimation methods.

### **2.2.1 Drift Effect in Inertial Sensors**

Sensor systems and measurement units are naturally prone to different internal noises and minor errors, caused by a variety of possible factors, from expected design and build imperfections to sensitivity to particular environmental aspects. These internal errors may differently affect a sensor's performance, depending on the used frame of reference. Using this criterion, sensors can be classified as either absolute, which perform the measurements with respect to a fixed reference or known standard, or relative, which operate based on a local, changing reference or previous measurements. In the case of absolute sensors and measurements, these internal errors may often be negligible and have a minor impact on the resulting sensor performance. Relative sensors, on the other hand, may require the integration of measurements, thus accumulating minor internal errors and noise over time. This effect is also known as drift [61].

Similarly, this effect may also be encountered in the case of the absolute sensors, which are utilized for relative measurements, such as inertial gyroscopes or accelerometers, when used respectively for orientation or linear motion tracking. MEMS gyroscopes, for instance, are widely known for their availability, compactness, and cost-efficiency, as well as for relatively poor reliability in long-term orientation tracking. As the gyroscopes initially measure the momentary and absolute triaxial angular velocity, the actual orientation estimation requires further integration of this data. Thus, the orientation is calculated in relation to the previous state. However, the bias instabilities and internal noise of MEMS gyroscopes cause the occurrence of minor errors in the measured angular velocity data, which are eventually integrated and accumulated in the orientation estimations, causing the over time drift effect, also referred to as Angular Random Walk (ARW) [62, 63, 64].

Due to their portability and cost-efficiency, MEMS gyroscopes are often available along with accelerometer sensors as part of 6DoF (Degrees of Freedom) inertial measurement units [65]. Extended 9DoF IMU units, sometimes referred to as MARG (Magnetic, Angular Rate, and Gravity) or AHRS (Attitude and Heading Reference System) units, additionally include magnetometer sensors [66, 67]. These additional sensors are capable of providing the supporting information, reflecting the approximate absolute orientation, thus assisting the gyroscope unit. Triaxial accelerometer units are capable of sensing the gravitational acceleration of the Earth, thus reflecting the absolute Euler's roll and pitch rotations. For this reason, the combination of gyroscope and accelerometer sensors is often used as a balancing unit (e.g., on drones). Absolute heading (Euler's yaw rotation) can be measured by the included magnetometer unit in relation to the magnetic north of the Earth. Fusion of the aforementioned IMU sensors is extensively investigated in the literature and is widely used in a variety of applications [64].

### **2.2.2 Drift Mitigation Techniques for Inertial Sensors**

This section covers the state-of-the-art methods and techniques used to mitigate the drift errors in inertial sensors, described in the previous section. In this section, the relevant works are separated into three main groups: gyroscope initial filtering methods, the orientation bias compensation approach, and sensor fusion methods. These main groups are further discussed in their respective subsections. Due to the diversity of available sensor fusion methods, they were also organized into subgroups within the corresponding "sensor fusion methods" group, based on the most widely used sensor combinations. These

subgroups include methods of gyroscope fusion with accelerometers only, accelerometers & magnetometers, as well as approaches for gyroscope fusion with other sensors.

### Gyroscope Filtering Techniques

One of the most fundamental methods for drift error mitigation in inertial sensors (e.g., gyroscopes or accelerometers) is the use of different data filtering techniques and algorithms. For instance, the low-pass filter can be used for relatively rudimentary processing of the gyroscope readings in the low-intensity rotations as proposed by Wang *et al.* in their work [68]. They proposed using the low-pass filtering model with the first-order inertia link to mitigate the high-frequency noise in the gyroscope. This approach has been successfully used to eliminate the gyroscope angular drift, caused by internal static noise, even though, by introducing a certain time delay in the filter response. A similar approach can be used for noise filtering in another inertial sensor - the accelerometer. For instance, Suwandi *et al.* have used the combination of low-pass and Least Mean Squares filters to eliminate the accelerometer noise, caused by vehicle vibrations [69].

Filtering of raw sensor data is also sometimes used for preliminary processing as part of more complex drift mitigation methods like sensor fusion, which is more closely discussed later in Section 2.2.2. For instance, Ariffin *et al.* and Min *et al.* have used high-pass and low-pass filtering techniques for the respective preliminary processing of the gyroscope and accelerometer sensors' data [70, 71]. Ariffin *et al.* have then used the complementary filter to fuse the aforementioned sensors to estimate Euler's roll and pitch rotations. Min *et al.* have used the least squares-based complementary filter to fuse the accelerometer and gyroscope sensors for the angle estimation, and compared its performance with the regular complementary filter-based fusion method. Similarly, Hoang *et al.* have used the low-pass filter to initially mitigate the accelerometer noise before its use in their proposed Orientation Axes Crossover Processing (OACP) algorithm [72]. This algorithm is used to calculate the approximate Euler's roll & pitch rotations directly from the accelerometer information without the need for additional sensor fusion.

Certain case-specific techniques, such as NMNI (No Motion, No Integration), thoroughly described by Hoang in his PhD thesis, can also be classified as a filtering approach [73]. This method disables the integration of gyroscope readings, which are below the defined threshold amplitude, thus preventing the angular drift error accumulation in stationary cases. In case of sufficient motion, on the other hand, the gyroscope data integration, along with the inherently present internal noise, is performed regularly. For this reason, this technique can be labeled as a "threshold filter" or "no motion filter". Gradual and slow motion, however, may be entirely disregarded by this technique, which is an essential disadvantage in different applications, such as vehicle or vessel motion tracking. Nevertheless, this technique may be successfully used for the initial data processing in applications, such as drones or robots, where only sufficiently rapid motions are encountered. For instance, Hoang *et al.* have used the NMNI technique for the gyroscope data filtering in the drone orientation tracking application [74] and investigated its use in combination with other state-of-the-art fusion algorithms in this field, such as Mahony and Madgwick filters [75].

Kalman filter (KF), more closely described in Section 4.2, in its numerous variations, is one of the most versatile and widely used algorithmic methods for data filtering and fusion in a variety of different fields, including drift error mitigation in inertial sensors. Its capability of state estimation and filtering allows the KF to be solely used as an effective filtering algorithm for the gyroscope data. A linear Kalman filter algorithm was used by Alfian *et al.* for the gyroscope and accelerometer output data filtering on an embedded



system to investigate the algorithm performance at different configurations and with each sensor separately [76]. Abbasi *et al.* have used a modified Kalman filter for the MEMS gyroscope denoising to mitigate long-term drift errors [77]. They have proposed to integrate the auto-regressive model (AR) into the Kalman filter to estimate and compensate for the long-term gyroscope errors. They have validated the performance of their method by using it for the tracked object Dead Reckoning (DR) in periods of GNSS (Global Navigation Satellite System) outage.

A more advanced and frequently used adaptive variation of the Kalman filter was used by Bai *et al.* in their work for the gyroscope noise filtering [78]. They have used the dynamic sensor noise model to estimate the approximate sensor noise and allow the KF algorithm to apply adaptive filtering to the gyroscope data. A similar approach was also used by Wang *et al.* for the drift error mitigation in Ring Laser Gyroscopes (RLG) [79]. They have also used features of the adaptive Kalman filter, assisted by the drift noise model and  $H_\infty$  techniques. For a similar task, Wang *et al.* have used the Sage-Husa Kalman filtering in [80]. They have assessed the performance of the Sage-Husa algorithm, compared its performance with the regular Kalman filter algorithm, and proposed their improved version of the Sage-Husa Kalman filter algorithm for gyroscope noise mitigation. Abdelzaher *et al.* have utilized the Wavelet denoising technique together with the Kalman filtering algorithm for the noise reduction in optical gyroscopes [81]. They have also investigated and determined the better-performing combination of these techniques for the given task. Chen *et al.* have used a similar approach of combining the Kalman filter, Wavelet denoising technique, and least squares method for the gyroscope data filtering [82]. In their research, they have successfully used this approach to experimentally track the sway of the subway train.

Recent advances in the inertial sensor noise filtering methods also utilize different machine learning and Neural Network (NN) techniques, aimed at improving and optimizing the filtering quality. Zhu *et al.*, for instance, have used the Kalman filter-based gyroscope noise filtering method, combined with the Long Short-Term Memory (LSTM) neural network [83]. This approach allows for iterative updating and optimization of the Kalman filtering parameters for increased performance. A similar approach was used by Mi *et al.* in [84], where they also utilized the combination of the LSTM neural network and Kalman filter to mitigate the noise in the gyroscope data. For their model training, they have used an array of multiple MEMS gyroscopes. Wand *et al.* have used the unscented Kalman filter algorithm, combined with the Support Vector Regression (SVR) for the random noise minimization in Fiber Optic Gyroscopes (FOG) [85]. Their method is also assisted by the Adaptive Beetle Antennae Search (ABAS) algorithm, which is used for SVR optimization.

A different approach of temperature-based drift error compensation in MEMS gyroscopes was used by Li *et al.* in [86]. They have used the Empirical Modal Decomposition (EMD) to select the high-, medium-, and low-frequency components in the initial gyroscope data. Radial Basis Function Neural Network (RBF NN) and the Kalman filter combination were then applied to filter the selected medium-frequency component, while the temperature-based compensation was applied to the low-frequency component. The gyroscope readings were then reconstructed from the medium- and low-frequency components, while the high-frequency component was disregarded as noise.

Damagatla *et al.* in their works have proposed a machine learning-assisted MEMS gyroscope drift mitigation method for the GNSS-supported Inertial Navigation System (INS). Within the same base method they have proposed the use of different machine learning techniques, such as Light Gradient Boosting Machine (LightGBM) [87, 88, 89], Categorical Boosting (CatBoost) [88, 89], Convolutional Neural Network (CNN) [89], and Extreme

Gradient Boosting (XGBoost) [90], for the gyroscope error filtering. In their method, the chosen ML algorithm is trained by the developed Extended Kalman Filter (EKF) algorithm and inverse kinematics model by using the available GNSS and IMU data during the GNSS data availability periods. During the GNSS outage period, the gyroscope data is directly filtered by the trained machine learning algorithm and used for the inertial navigation until the GNSS data becomes available.

Due to the chaotic nature of the inertial sensor noise, in the context of vehicle orientation tracking, the filtering methods may only be effective in the short-term perspective, reducing the drift error accumulation rate, without its proper elimination. Long-term and reliable mitigation of the drift error, on the other hand, requires a different approach, such as multi-sensor fusion or proper bias compensation [91].

### Drift Correction Methods

While the filtering methods focus on the initial sensor noise reduction, the bias compensation methods attempt to estimate and correct the drift errors present in the resulting data.

One of the most widely known methods in this category is the ZUPT (Zero Velocity Potential Update) algorithm, which is frequently used for inertial drift error elimination in fields of human gait analysis and pedestrian tracking. This algorithm relies on the eventual detection of the motion absence, indicating the stationary condition of the tracked object, which allows the algorithm to perform the necessary recalibration of inertial units and eliminate the occurred drift errors. This makes the ZUPT algorithm highly effective in scenarios with repeating static stages, such as human gait monitoring, as it was done by Shi *et al.* in [92]. Cho *et al.* and Zhao *et al.* have successfully used the zero velocity update technique and inertial sensors for pedestrian tracking [93, 94]. Zhang *et al.* and Pla *et al.* in their works have additionally assessed and tested the applicability of this method at the sprinting speeds [95, 96].

Nevertheless, the zero velocity update method may also be used for different applications outside of the field of pedestrian tracking. For instance, Zhang *et al.* have utilized this technique in the industrial pipe jacking guidance system [97]. Similar to the NMNI method discussed earlier in this section, the ZUPT technique can also be used as a supportive part of the more complex fusion methods. Wang *et al.* have used this technique as part of the pedestrian positioning method, based on the particle filter fusion of IMU and UWB positioning system [98]. Li *et al.*, on the other hand, have used the zero velocity update technique as part of the EKF (Extended Kalman Filter) based GNSS and IMU fusion method for vehicle stationary condition detection [99].

Some of the recent advances in the inertial drift compensation also adopt different machine learning and neural network techniques to further improve the performance of the existing methods. For instance, An *et al.* have utilized the LSTM neural network technique to recognize the human gait patterns and improve the performance of the previously mentioned zero-velocity update method with the adaptive threshold input [100]. The NN-enhanced adaptive ZUPT technique was then successfully used as part of the pedestrian tracking method. Similarly, Li *et al.* have utilized the LSTM neural network to enhance the performance of the ZUPT technique for inertial data processing [101]. This approach was then used as part of the inertial navigation system, utilized for inertial vehicle navigation.

## Sensor Fusion Methods

**Gyroscope and Accelerometer-based:** One of the most widely used and effective approaches for gyroscope drift mitigation, especially in the field of vehicle navigation, relies on its fusion with different supportive sensors. Available state-of-the-art methods are based on various sensor combinations and utilize different fusion algorithms from complementary filters to Kalman filter variations and particle filters. MEMS gyroscopes are often fused with accelerometer sensors, providing available and cost-efficient estimation of Euler's roll and pitch rotations, for instance, used in different applications, such as drone balancing. Accelerometer units are used to measure linear accelerations, including the free-fall acceleration, caused by the Earth's gravity, which makes them naturally capable of real-time monitoring the absolute Earth's gravity vector. Thus, from the orientation tracking perspective, the accelerometer unit becomes an absolute reference for gyroscope sensors in Euler's roll and pitch rotations estimation.

As, for instance, was mentioned earlier in this section, Min *et al.* and Ariffin *et al.* in their works have used variants of complementary filters to fuse the filtered accelerometer and gyroscope units to mitigate the gyroscope drift error and reliably estimate Euler's roll and pitch tilt angles [71, 70]. Wang *et al.* have also used the complementary filter-based fusion accelerometer and gyroscope sensors to estimate the Euler's roll, pitch, and yaw rotations in stationary conditions [102]. They have tested the complementary filter algorithm with a double PID (Proportion Integration Differentiation) loop and investigated its performance in triaxial rotation estimation quality.

A group of sensor fusion approaches was tested by Hoang *et al.* in their research, where they assessed the performance of the earlier described NMNI algorithm in combination with the Madgwick filter, widely known in the field of orientation estimation [75, 103]. The Madgwick filter is a kinematic observer that represents the enhanced version of the complementary filter, utilizing the proportional controller for the gyroscope error mitigation. In these works, Hoang *et al.* have used this filter for gyroscope and accelerometer sensor fusion, and compared its performance with the Mahony filter. Similar to the Madgwick filter, the Mahony filter represents an enhanced version of the complementary filter for gyroscope error mitigation, based on proportional and integral controllers. Hoang *et al.* have used this algorithm for accelerometer and gyroscope fusion and investigated its performance in combination with the earlier described NMNI algorithm [75]. Zhu *et al.* have also used the Mahony filter in [104] for inertial sensors fusion. For their Mahony filter implementation, Zhu *et al.* have adopted the Allan variance method to analyze and compensate for the gyroscope bias. Eventually, they have used the UAV (Unmanned Aerial Vehicle) to experimentally validate the performance of the proposed Mahony filter-based algorithmic method.

Inertial sensor fusion is also frequently performed by using different Kalman filter algorithm variations. For instance, Akbari *et al.* have implemented and used the extended Kalman filter along with the Explicit Complementary Filter (ECF) as benchmark techniques to evaluate their proposed Linear Parameter Varying (LPV)  $H^\infty$  filter [105]. Performance capabilities of these algorithms in Euler's roll and pitch rotation estimation, based on the accelerometer and gyroscope data, were assessed in their work, along with the required computational time. According to the outcomes, the aforementioned algorithms have demonstrated similar performance. The slightly higher overall performance of the EKF algorithm was accompanied by a higher computation time. In the field of pedestrian tracking and gait monitoring, Luo *et al.* have used another Kalman filter-based algorithm for the inertial sensor fusion [106]. To perform the pedestrian tracking, they have proposed a Square Root Cubature Kalman Filter (SRCKF) algorithm, aided by the zero-velocity update

technique.

The main limitation of these methods, however, is their inability to reliably estimate Euler's yaw rotation, also referred to as heading. Since the accelerometer unit is only capable of detecting the tilt rotations (Euler's roll and pitch), based on the Earth's gravity vector monitoring, the reliable heading estimation requires the integration of additional supporting sensors. This is especially valid in cases, such as vehicle or robot navigation, where its movement nature prevents the effective use of certain zero velocity-based filtering (NMNI) or bias compensation (ZUPT) techniques. One of the most widely used supporting sensor options for the fusion-based heading estimation is the magnetometer unit [75, 103, 102, 104, 107]. Magnetometer sensor provides the absolute orientation information in relation to the Earth's magnetic north and is often available as part of 9DoF IMU units. The ability to provide absolute heading measurements naturally allows the magnetometer to become an absolute reference for gyroscope sensors in Euler's yaw rotation estimation.

**Gyroscope and Magnetometer-based:** Different algorithms and techniques are used to perform the gyroscope, accelerometer, and magnetometer fusion. Wittmann *et al.* have used the Madgwick algorithm to perform the drift error correction in triaxial orientation tracking [108]. Their method was used to track the orientation of the human arm, which was further used as a controlling input for the side software. Hoang *et al.* in their works, earlier mentioned in this section, have proposed the gyroscope and accelerometer sensor fusion by using the NMNI technique integrated Madgwick filter [75, 103]. The performance of this method was also evaluated in comparison with a group of other fusion algorithms, including Kalman and Madgwick filters for a fusion of gyroscope, accelerometer, and magnetometer sensors. Due to the specificity of the performed tests, their proposed method has demonstrated superior performance over the magnetometer-based fusion method.

The performance of inertial and magnetic sensors-based Madgwick and Mahony filters in the heading estimation was also assessed by Diaz *et al.* in [109]. These methods were also compared to multiple other commercial methods and in the context of human-carried IMU scenarios. Similarly, the orientation estimation performance of the Madgwick and Mahony filter algorithms in the case of the foot-mounted 9DoF IMU was evaluated by Ludwig *et al.* in [110]. They have investigated both the precision and execution time of these algorithms in triaxial orientation calculation. In their more comprehensive work, Ludwig *et al.* have evaluated the orientation estimation accuracy and precision of the aforementioned Madgwick and Mahony filters in the context of the drone-deployed 9DoF IMU [111]. A significantly modified Madgwick filter algorithm was used by Justa *et al.* for the AHRS sensors fusion [112]. They have proposed a Separated Correction Filter (SCF) algorithm, designed to perform the preliminary filtering for the used IMU sensors before their complementary fusion.

Due to its main advantages of state estimation and flexibility, the Kalman filter remains the most widely utilized fusion algorithm in a variety of methods. For instance, the Kalman filter algorithm variations for magnetometer and inertial sensors fusion and orientation estimation were also evaluated along with Madgwick and Mahony filters by Ludwig *et al.* and Hoang *et al.* in the earlier mentioned works [111, 75]. Ludwig *et al.* have used the extended Kalman filter for a complete fusion of the gyroscope, accelerometer, and magnetometer sensors. Hoang *et al.*, on the other hand, have excluded the accelerometer unit and used a Kalman filter for a more simplified fusion of the gyroscope and magnetometer. A fusion of three aforementioned sensors was also performed by Zhou *et al.* in their work

[113]. They have used the extended Kalman filter and specifically designed a coordinate switch algorithm for the sensor fusion-based estimation of three Euler rotations. A similar approach was used by Farahan *et al.* in [114]. They have also utilized the Extended Kalman Filter for 9DoF IMU sensor fusion-based orientation estimation for camera stabilization applications. Among other parameters, their Kalman filter implementation also attempts to perform the bias estimation and compensation for each of the three fused sensors.

Badawy *et al.* have performed the gyroscope, accelerometer, and magnetometer sensor fusion for the orientation estimation [115]. They used the Adaptive Extended Kalman Filter (AEKF) to fuse the available inertial sensors, where the magnetometer data-based correction was applied externally. The resulting orientation information was then used to enhance the accuracy of the GNSS positioning information for the resulting INS system by using the EKF algorithm. The resulting algorithmic structure, combining AEKF and EKF for the resulting navigation, Badawy *et al.* have named as Cascaded Kalman filter (CKF). To control the selective use of the supporting accelerometer and magnetometer sensors in orientation tracking, Vaitali *et al.* have proposed an Error-State Kalman filter (ESKF) [116]. Depending on the IMU state and reading, this algorithm is capable of selecting sensors to be used in the orientation estimation.

A method for satellite orientation tracking was described by Hajiyeve *et al.* in their work [117]. They have used the Singular Value Decomposition (SVD) based extended Kalman filter algorithm to fuse the gyroscope, magnetometer, and Sun detection unit for reliable satellite orientation monitoring. Another method for satellite orientation tracking was proposed by Chen *et al.* [118]. They have used a neural network-integrated method for the gyroscope, accelerometer, and magnetometer sensor fusion, as well as for their fault detection and isolation. An Adaptive Unscented Kalman Filter (AUKF) and Quaternion Estimation (QUEST) algorithms were used in parallel to fuse the aforementioned sensors and provide their orientation estimations. Based on this data, the fault detection neural networks were trained to detect the faulty sensors and isolate them from the orientation estimation process. The resulting orientation was then calculated by the Adaptive Complementary Filter, combining outputs of AUKF, QUEST, and fault detection neural networks. Another fault detection and isolation approach for IMU sensors in UAV applications was proposed by D'Amato *et al.* in their research [119]. They have used two parallel Particle Filter (PF) algorithms for the simultaneous sensor fusion in two deployed 9DoF Inertial measurement units. Results were then analyzed and utilized by the SFDI (Sensor Fault Detection and Isolation) algorithm.

According to the conducted research, magnetometers are widely used as auxiliary sensors for gyroscope drift mitigation, specifically in heading estimation. However, as it is confirmed in [75, 102, 103, 104, 107, 108, 109, 111, 114, 116, 119, 112], magnetometers are sensitive to surrounding magnetic interferences, which significantly limit their reliability and performance in a variety of applications, especially in industrial areas.

**Other Gyroscope Fusion Approaches:** Despite the wide use of magnetometers as supporting sensors in state-of-the-art fusion techniques for gyroscope heading error mitigation, their sensitivity to environmental magnetic distortions may significantly corrupt their performance in certain scenarios, such as industrial applications. In these cases, magnetometer units may require their complete replacement with alternative sensors, such as LiDARs or vision-based options.

For instance, Kaltenthaler *et al.* in their work on pose estimation and environment mapping have used the LiDAR unit to possibly mitigate the orientation errors of inertial sensors [120]. For the pose estimation, they used the complementary filter, fusing the

LiDAR ranging data with the accelerometer and gyroscope units. Nazemipour *et al.* have used the extended Kalman filter to fuse the gyroscope sensor with the camera-based visual gyroscope method for accurate vehicle orientation estimation [121]. This visual gyroscope method represents the camera-based orientation estimation, performed by visual motion monitoring of observed reference objects. Tao *et al.* in [122] have used the camera-based method for gyroscope live calibration. In their method, the camera is used for the live motion estimation, based on the visual landmark points tracking. This information is then used to calibrate the corresponding readings of the IMU sensors.

Heading estimation is also one of the aspects in the field of vehicle state estimation, which covers comprehensive analysis and tracking of various vehicle dynamic parameters, such as vehicle kinematic parameters, side slip, or tilt for stability control applications. Aside from the inertial sensors, the field of vehicle state estimation often relies on a variety of supporting sensors, such as steering or wheel odometry sensors. For instance, Xia *et al.* in their work on the vehicle heading estimation have proposed the fusion of inertial gyroscope and accelerometer sensors with the vehicle preinstalled wheel and steering odometry sensors [123]. Fusion was performed by using the Kalman filter algorithm with the integrated sensors' bias estimation functionality.

Park *et al.* and Bersani *et al.* have proposed vehicle state monitoring approaches, based on the inertial gyroscope and accelerometer units, aided by the GNSS positioning system, steering, and wheel odometry sensors [124, 125]. Park *et al.* have used a pair of extended Kalman filters to respectively process the kinematic and bicycle models of the tracked vehicle. Bersani *et al.* have compared the performance of the extended (EKF) and unscented (UKF) variations of the Kalman Filter, separately used to combine the aforementioned sensors. Song *et al.* in their work have used the Square-root Cubature Kalman Filter (SCKF) to combine the GNSS positioning system, gyroscope, accelerometer, and steering sensors [126]. For the error compensation in the kinematics model, they have additionally used the modified Elman Neural Network (ENN). To mitigate the gyroscope noise for Autonomous Underwater Vehicles (AUV), Ramezanifard *et al.* have also utilized the set of application-specific supporting sensors [127]. They proposed the gyroscope and accelerometer fusion with the Doppler Velocity Log (DVL) and depth sensor. In their method, the initial gyroscope filtering was performed by its fusion with the DVL unit, using the Kalman filter. The second Kalman filter algorithm was then used to fuse the aforementioned sensors' setup to estimate the resulting pose information.

An alternative approach for the heading estimation may be exclusively based on the positioning data. For instance, Xiong *et al.* have used the Parallel Adaptive Kalman Filter (PAKF) algorithm, combining the readings from the gyroscope, accelerometer, and GNSS units [128] for the vehicle side slip estimation. In their method, however, the reliable heading data was primarily provided by the dual antenna GNSS unit. A method for boat navigation, based on inertial sensors and GNSS, was proposed by Cahyadi *et al.* in [129]. To perform a fusion of the aforementioned sensors for boat tracking, they have used the UKF algorithm, designed to additionally monitor the variables of kinematic, dynamic, and external forces. The used approach for the gyroscope heading error mitigation, however, is not specified in their work.

To reduce the drift error presence in the gyroscope-tracked orientation, Xu *et al.* have used the GNSS positioning data. They have proposed a Kalman filter algorithm to fuse the aforementioned sensors for reliable heading estimation [130]. In their research, Xu *et al.*, however, conclude the unreliability of this method in the stationary scenarios, as well as the necessity of additional supporting sensors for reliable heading estimation. Zhang *et al.* have proposed a discrete Kalman filter algorithm to directly combine the heading

information, provided by the IMU and GPS (Global Positioning System) units [131]. Their algorithmic method, however, is based on the simplified linear Kalman filter and does not provide the adaptivity functionality. For these reasons, this method becomes only operational at higher movement speeds and fully relies on the GPS unit-provided movement direction. An Extended Kalman filter algorithm was proposed by Li *et al.* for the vehicle heading tracking [132]. Their method combines the inertial information with movement velocities, provided by the GNSS unit. Similar to the method proposed by Zhang *et al.*, this approach significantly relies on the quality of GNSS-provided velocity information, thus requiring higher vehicle movement speed for an accurate heading estimation. Wu *et al.* have proposed a Kalman filter-based fusion method to combine the GNSS, IMU, and LVC (Lateral Velocity Constraint) to estimate the road vehicle orientation, including the heading [133]. In multiple tests, conducted in urban conditions, their method has achieved a sub-2 degrees level of tracked heading RMSE (Root Mean Squared Error). With the excluded LVC, their method has demonstrated RMSE at the 5-degree level in the road vehicle heading tracking. As one of the most recent advances in this field, the IMU and UWB positioning data-based heading estimation topic was also addressed in parallel with this research by Oursland *et al.* in one of their recent works [134]. They have used the inertial and UWB positioning information, fused by an Invariant Extended Kalman filter for the drone orientation estimation, and have achieved the drone heading RMSE of 4.6 degrees. This method and the achieved results are also briefly compared with the proposed ATKF algorithm further in Section 4.5.

### 2.2.3 Gap in State-of-the-art Methods

Table 3 reflects the key features of the state-of-the-art methods for the inertial sensors-based heading estimation, described in Section 2.2.2. Chosen features were selected to reflect the key limitations of the available approaches from the perspective of this research in accordance with its key requirements, defined in Section 1.3.

The conducted research on the state-of-the-art methods for inertial sensor drift mitigation indicates the frequent use of inertial sensor preliminary filtering. As this approach does not require the use of additional supporting sensors, it provides the advantage of cost-efficiency and relatively low computational complexity, depending on the used algorithmic method. For this reason, the initial data filtering approach demonstrates high feasibility for real-time applications. However, due to the absence of absolute reference information and unpredictable sensor noise behavior, filtering methods are only able to demonstrate reliable short-term drift mitigation. In long-term mitigation schemes, inertial data filtering typically serves as a supporting technique.

Drift compensation methods, on the other hand, perform the correction of the resulting integrated drift error, thus demonstrating higher reliability and stability in long-term applications. Similarly, reliable drift correction requires absolute reference information, such as predictable and periodically occurring stationary cases (zero velocity), widely used in the ZUPT technique. This makes the main drift correction techniques highly application-specific and widely used only in suitable fields, such as human gait analysis and pedestrian tracking. In the case of the vehicle heading estimation, this approach may only be occasionally used as an auxiliary technique.

Table 3: Key aspects, features and gaps of available state-of-the-art inertial sensor-based heading estimation methods; Highlighted cells indicate deviations of the available methods from the requirements defined in this work, preventing their direct use within this research.

	Gyroscope filtering methods	Gyroscope drift correction methods	Gyroscope + Accelerometer fusion methods	Gyroscope + Magnetometer fusion methods	Gyroscope + Camera/LiDAR fusion methods	Gyroscope + Positioning data fusion methods	Gyroscope + Odometry & other sensors fusion <sup>5</sup>
Possible heading improvement	Yes	Yes	No	Yes	Yes	Yes	Yes
Long-term performance	Low to Moderate <sup>6</sup>	High	High	High	High	High	Moderate to High
Environmental sensitivity	Low	Low	Low	High	Moderate	Moderate	Low to Moderate
Application limitations	Moderate	High	Low	Moderate	Low	Moderate	Moderate to High
Processing complexity	Low to Moderate <sup>6</sup>	Low	Moderate	Moderate	High	Moderate	Moderate
Integration into MHE mechanisms	None	None	Low	Low	Low to Moderate	Low	High
Suitable for the research context <sup>7</sup>	Supporting role	Supporting role	No	No	No	Partially <sup>8</sup>	No
References	[68, 69, 70, 71, 72, 73, 74, 75, 76, 77, 78, 79, 80, 81, 82, 83, 84, 85, 86, 87, 88, 89, 90]	[92, 93, 94, 95, 96, 97, 98, 99, 100, 101]	[70, 71, 75, 102, 103, 104, 105, 106]	[75, 103, 108, 109, 110, 111, 112, 113, 114, 115, 116, 117, 118, 119]	[120, 121, 122]	[128, 129, 130, 134, 132, 131, 133]	[123, 124, 125, 126, 127]

The research on the state-of-the-art methods for inertial sensor-based heading estimation indicates the wide use of sensor fusion methods and techniques. The vast majority of the available sensor fusion methods are based on sensors, often available in different IMU units, which include gyroscopes, accelerometers, and sometimes magnetometers. Due to their operating nature, the accelerometer units are unable to provide suitable reference information, particularly on the sensor's heading orientation. Therefore, the accelerometer and gyroscope fusion methods are unable to perform the gyroscope drift mitigation for reliable heading estimation and are only used for tilt (roll & pitch) rotations tracking. Sensor fusion methods, used for the gyroscope heading drift mitigation, primarily rely on the use of magnetometers as the supporting units, providing the absolute heading measurements. In the context of this research, however, the use of magnetometers in the industrial environment is expected to have significant performance limitations due to their high sensitivity to surrounding magnetic interferences and distortions, as it is previously concluded in Section 2.2.2. This limitation prevents the use of the primary state-of-the-art method for inertial heading estimation for this research.

Certain sensor fusion methods and approaches are frequently used in the field of ve-

<sup>5</sup>Results depend on the specific use case.

<sup>6</sup>Machine learning and neural network aided methods may provide increased performance at the cost of increased computational complexity.

<sup>7</sup>Suitable for an industrial vehicle heading tracking as part of the indirect tracking method in the context of this research

<sup>8</sup>Available methods focus on regular road vehicles (e.g., cars) and do not cover the intense maneuvering & backward movement, typical for targeted industrial machinery



hicle state estimation and are often based on a variety of different supporting sensors, such as steering and wheel encoders. These odometry sensors provide the vehicle movement speed and steering, thus allowing to track its relative heading by using the proper motion model. However, as the resulting heading estimation in this approach remains relative, it may be unable to fully mitigate the over time accumulating drift error, thus compromising its long-term stability. This may explain the frequent use of extra supporting sensors aside from the mentioned odometry units [124, 125, 126]. Additionally, the use of the aforementioned odometry sensors also requires their invasive integration into the vehicle mechanisms, which is avoided in the context of this research, in accordance with key criteria defined in Section 1.3. Similarly, the use of vision- or LiDAR-based methods for the gyroscope error compensation is also avoided in the context of this research, due to the high processing complexity and high volumes of the sensors' provided data. This ensures a reliable real-time data transmission and processing with minimal delays.

According to the conducted research, the fusion of inertial and positioning information represents the most suitable approach for the gyroscope heading drift error mitigation in the context of this work. Unlike the other state-of-the-art sensor fusion techniques for heading drift mitigation, this method provides relatively low computational complexity, minor integration into the vehicle mechanisms (e.g., as wheel or steering sensors), and is fully applicable in industrial areas. The primary prerequisite of this approach is the availability of the positioning infrastructure deployed in the targeted area (e.g., in the case of the UWB indoor positioning systems). According to research on the available methods for positioning and inertial sensor fusion, the vast majority of available works are entirely focused on the performance improvement of the used positioning system itself [135, 136, 137, 138, 139, 140]. Numerous publications describe the use of inertial sensors as auxiliary units to improve the positioning quality of the primary system or perform short-term inertial positioning during periods of the primary system outage. A relatively minor availability of publications describing the use of positioning data for inertial sensor heading drift mitigation indicates the gap in this field, as well as the wide use of other state-of-the-art techniques.

The available positioning data-based methods in this field, such as those proposed by Zhang *et al.* [131], Li *et al.* [132], and Wu *et al.* [133], rely on the quality of the movement direction and velocity information provided by the positioning unit. These methods are primarily designed and tested for the use of regular road vehicles at high movement speed and low maneuvering intensity. Available methods, however, may not be effectively applicable in the case of industrial machinery, which operates at low movement speed and high maneuvering intensity, where the positioning data becomes significantly less reliable for the vehicle heading tracking. For instance, Xu *et al.* in [130] address the significant complexity of the positioning data used for the reliable heading estimation. Its high unreliability as a reference for the IMU heading drift mitigation is reported, especially in cases of poor positioning data and the absence of movement. Their paper concludes the need for additional sensors for reliable heading estimation. ***Thus, the currently available positioning and inertial data-based methods for the vehicle heading estimation focus on the regular road vehicles and do not consider possible cases of accurate heading tracking at low movement speeds and intense maneuvering, including the essential aspect of possible reverse movement.***

The use of positioning and inertial sensors for accurate vehicle heading estimation requires the implementation of a reliable algorithmic fusion method, which takes into account the main advantages and limitations of both fused sensors. The implemented method is expected to provide a reliable vehicle heading estimation even in cases of in-

tense maneuvering, low movement speed, and potentially poor quality of the available data. This represents the research gap in the field of inertial and positioning sensors-based heading estimation, addressed and filled in Section 4 of this research.

### Algorithms Used in Drift Mitigation Techniques

The research also reflects the available state-of-the-art sensor fusion algorithms, widely used in the corresponding related literature. Table 4 reflects the prevalence of particular algorithms and techniques in different gyroscope error handling approaches, selected in Section 2.2.2. This analysis draws on related publications cited in the state-of-the-art section of this work and reflects the overall state of this field. Obtaining more precise results would require a comprehensive, detailed, and systematic review of the available literature across other relevant fields.

*Table 4: Algorithms used in different available inertial sensor (gyroscope) drift mitigation approaches. The color intensity represents the percentage of algorithm usage within a given drift mitigation approach.*

Algorithm	Gyroscope drift mitigation approach			
	Initial filtering	Drift error (bias) correction	Sensor fusion	Machine learning enabled methods
ZUPT	-	[92, 93, 94, 95, 96, 97, 98, 99, 100, 101]	-	[100, 101]
NMNI	[73, 74, 75]	-	-	-
Band pass filters	[68, 69, 70, 71, 72]	-	-	-
Complementary filter	-	-	[71, 70, 102, 120]	-
Madgwick filter	-	-	[75, 103, 108, 109, 110, 111, 112]	-
Mahony filter	-	-	[75, 104, 109, 110, 111]	-
Kalman filter variations	[76, 77, 78, 79, 80, 81, 82, 83, 84, 85, 86, 87, 88, 89, 90]	-	[75, 105, 106, 111, 113, 114, 115, 116, 117, 118, 121, 123, 124, 125, 126, 127, 128, 129, 130, 132, 131, 133]	[83, 84, 85, 86, 87, 88, 89, 90, 118, 126]
Particle filter	-	-	[119]	-

Overall, the breakdown of research presented in Table 4 on available inertial sensor drift mitigation methods illustrates the relative popularity of specific algorithms across different drift mitigation approaches. For example, due to its nature, the zero velocity potential update technique for periodic drift error elimination is almost exclusively utilized in the field of human gait analysis and pedestrian navigation. Algorithms such as NMNI, high- and low-pass filters, on the other hand, are naturally only used for inertial sensor data filtering and are frequently used for preliminary sensor filtering in different fusion methods. Complementary filter and its advanced and application-specific versions - Mahony and Madgwick filters are primarily used for the fundamental fusion of IMU sensors, including gyroscopes, accelerometers, and magnetometers.

Nevertheless, the literature analysis on available inertial sensor drift mitigation methods clearly indicates the high popularity of the Kalman filter algorithm variations. It is justified by multiple factors and advantages of this algorithm, including the high versatility and flexibility of this algorithm, its capability for model state estimation, as well as its wide functionality and applicability. The capability for state estimation allows the Kalman filter algorithm to provide both filtering and sensor fusion functionality, which explains

its wide use in a variety of applications, including both inertial sensor filtering and fusion approaches. While the Kalman filter is initially designed for linear model estimation, its advanced variations, such as extended (EKF) and unscented (UKF) Kalman filters, are also able to effectively process the non-linear models. Kalman filter algorithm and its variations also enable features of adaptive fusion, which makes this algorithm highly suitable and effective for different real-life fusion methods. For its versatility, the Kalman filter was chosen as the primary fusion algorithm to be used in the context of this work. Additionally, according to the conducted research, the Kalman filter algorithm and its variations are also frequently combined with different machine learning and neural network techniques, and primarily used for sensor filtering purposes.

### 3 Indirect Tracking Methodology

This section introduces the methodology behind the proposed markerless indirect tracking method, defines its key components, as well as selects the necessary technologies and sensors required for its implementation. This method is designed to fill the existing gap in available state-of-the-art approaches, previously defined in Section 2.1.3. The developed method directly answers the research question **RQ1**, as well as represents one of the main contributions of this research and Publication IV. Background and the main concept of the developed indirect tracking method are also briefly introduced in publication I [1]. The resulting structure of the developed indirect tracking method, developed algorithms, as well as the experimental implementation and testing of the proposed method are provided later in Section 5.

#### 3.1 Methodology

The proposed markerless indirect tracking method is closely described in Section 5 and in Publication IV, as well as briefly mentioned as background in Publication I. This method is based on the hypothesis that completely untagged industrial products or equipment can be accurately localized in real-time during their transportation by industrial material handling equipment, such as forklifts, lifters, or cranes. The transported object is physically loaded on the specialized material handling unit of MHE, such as forklift tynes or crane hook/magnet unit, and remains in the corresponding three-dimensional location in the MHE body frame throughout the transportation process. Therefore, the real-time 3D location of the material handling unit directly reflects the corresponding real-time 3D coordinates of the transported object with sufficient accuracy. Therefore, this method only requires an initial product coordinates assignment upon its arrival at the warehouse or production area. This, for instance, may be automatically performed during the initial product registration routine in a specialized area, such as an arrival dock, after its unloading from the transportation vehicle (e.g., logistics truck) into dedicated geofenced zones with pre-measured coordinates. Based on the industrial preferences, a variety of different product registration approaches may be used to assign the necessary product information to the corresponding geofenced unloading zone (i.e., initial product coordinates), from manual logistics information input up to the AI-enhanced vision-based methods.

With reliable and time-synchronized detection of the object loading and unloading events, this approach may also automatically provide the exact storage location of the object, thus fully automating the tracking process. Access to an accurate 3D positioning information of the tracked object during its transportation and storage additionally allows to bind the identification information to its physical location. This mitigates the need for direct object marking with identification tags, thus resulting in a fully markerless indirect tracking method. This approach is based on the following key assumptions:

- Objects tracked with this method are only transported by the material handling equipment (e.g., forklift), equipped with the necessary setup of sensors for markerless indirect tracing.
- Objects tracked with this method must remain stationary when stored and must not be significantly displaced during this period.
- Uncontrolled displacement of the tracked object may require a manual position update.

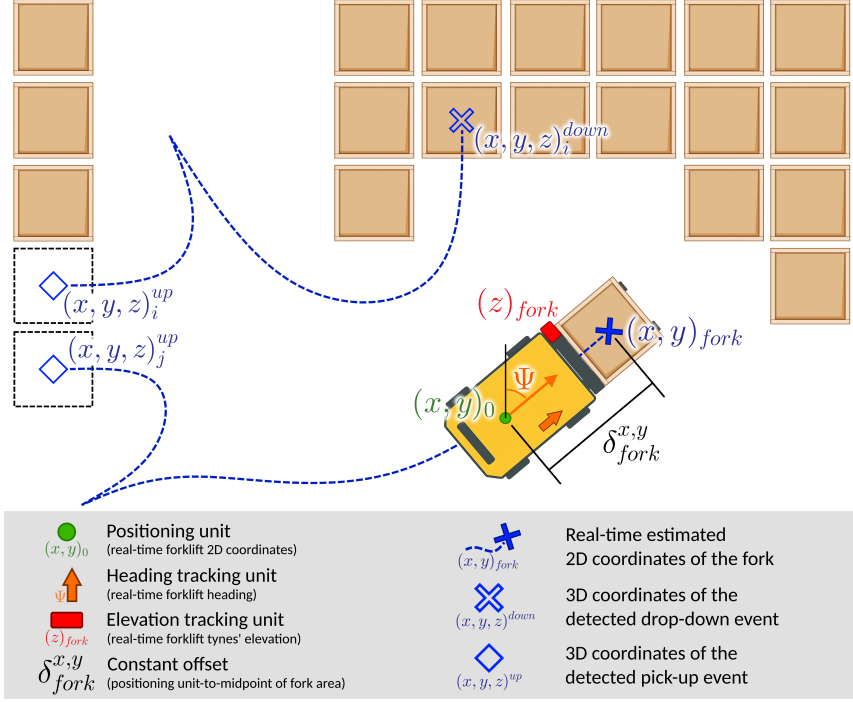


Figure 1: Conceptual illustration of the designed markerless indirect tracking method.

Although this work is focused exclusively on the forklift-based application scenario, with certain adjustments, the developed method may be applicable to different industrial machinery, such as lifters or cranes. The conceptual representation of the proposed indirect tracking method is illustrated in Fig. 1, reflecting the key aspects of the tracking process and deployment. In the case of the forklift, the application of the proposed method requires the real-time and accurate localization of the center spot of the fork area  $(x, y)_{fork}$ , which reflects the approximate location of the transported product. The center spot of the fork area is marked as a blue "X" in Fig. 1. Direct deployment of the **positioning unit** within the tynes area, however, often may not be possible as this area physically interacts with heavy objects, which can eventually damage or destroy the deployed tracking unit. For this reason, the positioning unit is intended to be deployed in a reliable location within the forklift body frame, resulting in the constant, above-meter offset  $\delta_{fork}^{x,y}$  between the positioning unit and the midpoint of the fork area. In Fig. 1, this (underlying) positioning unit is marked as a green dot.

Compensating for this offset is essential for the accurate product position estimation, which is often overlooked in the available state-of-the-art methods, provided in Section 2.1.2. The offset can be reliably compensated by using accurate real-time information of the forklift heading  $\Psi$ , thus requiring a corresponding **heading tracking unit**. In Fig. 1, the heading tracking unit is marked with an orange arrow. By leveraging the heading information, the exact fork location  $(x, y)_{fork}$  can be geometrically calculated from the initially measured forklift coordinates  $(x, y)_o$  as follows:

$$\begin{cases} x_{fork} = x_o + \sin(\Psi) \cdot \delta_{fork}^{x,y} \\ y_{fork} = y_o + \cos(\Psi) \cdot \delta_{fork}^{x,y} \end{cases} \quad (1)$$

The detailed explanation for the resulting fork location calculation is provided in Publica-

tion 1, additionally covering the case of random placement of the positioning unit within the forklift body frame.

Accurate tracking of the real-time forklift heading is essential, since it directly impacts the estimation of the resulting location of the transported payload. For evaluation purposes, the resulting error in the indirectly tracked product location, caused exclusively by the error in the tracked forklift heading, can be geometrically derived as shown in Fig. 2 and expressed as follows:

$$\varepsilon_{fork} = 2 \cdot \sin\left(\frac{\varepsilon^\Psi}{2}\right) \cdot \delta_{fork}^{x,y}, \quad (2)$$

where  $\varepsilon_{fork}$  represents the error in the forklift tynes' position, and hence, in the position of the tracked payload. It is calculated from the constant offset  $\delta_{fork}^{x,y}$  between the deployed positioning unit and the fork area, and error in the forklift heading  $\varepsilon^\Psi$ .

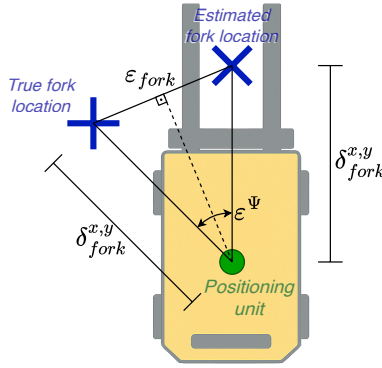


Figure 2: Geometric interpretation of the fork positioning error, exclusively caused by inaccuracy in forklift heading estimation.

In order to extend the positioning capabilities of the proposed indirect tracking method and allow three-dimensional product localization, fork elevation tracking is also needed. **In the context of this work, elevation reflects the object lifting height above the ground level.** This requires the integration of the **elevation tracking unit**, capable of reliable and accurate measurement of the forklift tynes elevation  $z_{fork}$ , which corresponds to the vertical coordinate of the transported product. In Fig. 1, the elevation tracking unit is marked with a red box. Combined with the earlier determined 2D fork location, it results in 3D coordinates of the transported product. Integration of the fork **occupancy detection unit** allows the automatic detection and distinguishes the product loading and unloading events, thus fully automating the proposed indirect tracking method. Timely detection of these events allows to accurately define the corresponding pick-up  $(x, y, z)^{up}$  and drop-down  $(x, y, z)^{down}$  locations, respectively marked as an empty blue rhombus and "X" in Fig. 1. Accurately detected pick-up location allows to indirectly identify the picked-up product from its earlier known storage location, while the confirmed drop-down location corresponds to the exact coordinates of the stored product.

As defined in this section, the designed method for markerless indirect tracking of industrial products requires the following set of components, providing the corresponding real-time information:

- **Underlying positioning unit:** The primary task of this unit is to provide the current location of the industrial transportation machinery, which will be further used for the exact location estimation of the tracked product. The secondary role of this unit

is closely described in Section 4 and Publications I & III, and focuses on supporting the heading tracking unit in the accurate forklift heading estimation.

- *Heading tracking unit*: This unit is used to track the real-time heading of the industrial transportation machinery for its further use in the resulting location estimation of the transported product.
- *Elevation tracking unit*: The main purpose of this unit is an accurate measurement of the forklift tynes' elevation to enable the accurate 3D localization of the tracked product, thus covering the possible scenarios of the tracked product shelving and stacking. The secondary role of this unit is focused on the support for the occupancy detection unit in the precise and reliable recognition of the payload pick-up and drop-down events. Its role in the proposed algorithm for automatic pick-up & drop-down detection (A-PDD) is described in Section 5.2 and in Publication IV.
- *Occupancy detection unit*: This unit is aimed at tracking the real-time occupancy status of the forklift tynes area and detecting possible payload pick-up or drop-down events, thus fully automating the proposed indirect tracking method.

### 3.2 Technology & Sensors' Selection

This section justifies the selection of suitable technologies and sensors for the key information providing units, needed in the designed indirect tracking method, and previously defined in Section 3.1. It gives a brief overview of the available options for each required unit and justifies the resulting choice. In accordance with the key requirements for the proposed method, defined in Section 1.3, the sensors' selection must meet the following criteria:

- *Minimal viable/feasible number of sensors*: The resulting setup must include a minimal number of sensors, sufficient to provide the necessary functionality of the proposed indirect tracking method. Each sensor must have a specifically defined primary purpose for the designed method, while the use of entirely supporting sensors is avoided. This is done to increase the cost- and energy efficiency of the designed method, as well as to reduce its complexity and maintenance requirements.
- *Minimal data volumes and processing complexity*: Chosen sensors must provide lower data volumes, requiring minimal pre-processing before use in the indirect tracking process. Minimizing the size of the initially provided data reduces the requirements for the wireless data transmission channel between sensors and the main processing server, thus preventing possible delays and/or retransmissions in the sensors' data stream. Minimized data pre-processing complexity reduces the possible delay between input data reception and its further use, thus increasing the sensor data relevance in the time domain. For instance, the data stream of vision-based methods requires higher transmission bandwidth and complex processing for its conversion into the relevant information, such as heading data.
- *Applicability in industrial environment*: Chosen sensors must provide a reliable performance in the application environment (e.g., industrial environment) and robustness against surrounding interference. The selection process must consider existing limitations of chosen sensors, related to the application environment.
- *Minimal integration into the machinery mechanisms*: In many cases, the direct modification of industrial machinery is not possible (e.g., due to the machinery rental

regulations). For this reason, the chosen sensors must be minimally intrusive to the used industrial equipment and machinery (e.g., wheels or steering sensors).

- *Minimal adjustments to the operating environment:* The use of chosen sensors must require minimal adjustments to be made in the application environment, allowing a seamless deployment of the necessary sensors and infrastructure. This criterion is aimed at minimizing any interference of the proposed indirect tracking system on the natural workflow of the covered warehouse or production site.

As the key requirements for the resulting setup include its possible minimization and avoidance of supportive-only sensors, this section also briefly covers the possible multi-role use of the selected sensors and technologies. Possibly maximized and combined use of the selected sensors and technologies is favored as it leads to a possible performance increase and potential extra features for the indirect tracking method.

### 3.2.1 Underlying Positioning Unit

A positioning system is the central unit of the designed indirect tracking method, essential to initially obtain the real-time location of the used MHE. The chosen positioning system directly determines the initial expected product positioning accuracy, precision, and quality of the developed method. As certain positioning systems are designed specifically for either indoor (e.g., UWB Real-Time Location System (UWB RTLS)) or outdoor (e.g., GNSS), the selected positioning system also determines the covered operating environment for the designed indirect tracking method. The designed method, however, is not bound to any specific positioning system and allows the use of any source of positioning data or their combinations as a positioning unit in the proposed method. Thus, a positioning unit in the proposed method may be replaced/represented with a seamless fusion of indoor and outdoor positioning systems, operating in a unified coordinate system for multi-environmental indirect product tracking.

**GNSS & Cellular positioning:** A variety of different positioning technologies can be used as a positioning unit for the designed indirect tracking method. Global Navigation Satellite System (GNSS) is one of the most widely known and used positioning technologies, which includes systems, such as GPS, Galileo, GLONASS (Global Navigation Satellite System), and BeiDou Navigation Satellite System [141, 142, 143]. This technology provides a global positioning at a relatively moderate cost to the end user. This technology provides a meter-level accuracy positioning in outdoor environments. However, since the GNSS technology is based on satellites, it naturally requires the open sky for effective positioning and remains sensitive to various high environmental obstacles, such as buildings. Open and plain areas, on the other hand, are the most optimal environmental conditions for this technology. Introduction of the field-deployed supportive infrastructure - RTK (Real Time Kinematic) allows the GNSS technology to achieve up to centimeter-level accuracy [144]. Since this requires additional direct communication of the GNSS unit with the field-deployed base station, it leads to the area of coverage limitation of the GNSS RTK system down to multiple kilometers, scalable with the deployment of additional base stations. Although the GNSS RTK significantly improves positioning accuracy, the deployment of auxiliary field infrastructure also leads to a significant cost increase.

Alternatively, the outdoor and partially indoor positioning can be performed by using cellular technology [142, 145]. The 5G technology is designed to support the Millimeter Wave-based (mmWave-based) positioning with declared sub-meter accuracy in dense urban areas and partially indoors. Recent advances in this field also indicate that a sig-



nificant positioning performance increase can be achieved by integrating various intelligent technologies, such as machine learning for cellular LOS/NLOS detection [6]. With the pre-deployed infrastructure, this technology is also expected to be relatively cost-efficient for the end user. However, the required mmWave infrastructure is not widely deployed, which makes this approach currently impractical.

**Ultra-Wideband:** Among the indoor positioning systems, the UWB RTLS provides low-latency and high-accuracy positioning of 10 cm to 30 cm, along with a capability to cover large indoor areas of industrial size [141, 142, 145, 146, 147]. This technology relies on a field-deployed infrastructure, consisting of interconnected anchor units, performing the localization of the mobile tag unit by using the multilateration method. Similar to other localization technologies, UWB positioning systems are sensitive to various line-of-sight-blocking obstacles in the environment, which may noticeably impact the resulting positioning quality. Nevertheless, UWB positioning technology also provides significant performance reliability, allowing it to remain operational even in NLOS conditions. It is achieved by the superior obstacle penetration capabilities of UWB signals due to the wide frequency spectrum, as well as high resistance against multipath signal interference. A reliable deployment of the UWB positioning infrastructure remains essential in various complex environments, such as industrial areas, to ensure precise positioning, minimize the impact of numerous environmental obstacles, as well as maximize the resulting coverage.

**Wi-Fi & Bluetooth positioning:** Alternatively, the indoor positioning can be based on widely available technologies such as BLE (Bluetooth Low Energy) and Wi-Fi (Wireless Fidelity). Similar to UWB positioning, these technologies are sensitive to environmental obstructions, affecting the resulting localization accuracy, thus requiring proper deployment of the positioning infrastructure, such as BLE beacons and Wi-Fi access points. In comparison with the above-described UWB indoor positioning systems, these technologies provide wider hardware availability and accessibility, noticeably increasing the potential cost efficiency.

Similar to the UWB technology, the Wi-Fi-based positioning also allows for coverage of large indoor areas, while providing a significantly reduced accuracy of approximately 5-10 m [141, 142, 143, 145, 146, 147, 148]. This positioning accuracy, however, is expected in the case of RSSI-based (Received Signal Strength Indicator) Wi-Fi positioning. The use of more advanced techniques in Wi-Fi-based position estimation, such as FTM (Fine Timing Measurement), increases positioning accuracy to 1-3 m at the cost of higher computational complexity.

On the other hand, positioning systems based on BLE technology and its received signal strength indicator initially provide a positioning accuracy of 1-5 m [141, 142, 145, 146, 147, 148]. The use of more advanced and computationally complex techniques, such as Angle of Arrival (AoA) and Angle of Departure (AoD), improves the positioning accuracy to sub-meter level. However, while providing the coverage within the approximate range of 100 m, Bluetooth low-energy positioning systems are significantly prone to the RF (Radio Frequency) interference, which noticeably limits their potential application range and environments.

**Magnetic field-based positioning:** Short-range indoor positioning can also be based on magnetic field sensing [142, 149]. Even though in certain cases this approach may provide up to a centimeter-level positioning accuracy, it is significantly limited by the small coverage area and multiple environmental limitations. These limitations include the

requirement for a controlled application environment, free of different strong or time-varying magnetic noise sources and distortions, as well as preliminary mapping of the existing magnetic fields in the area of positioning.

**Vision-based positioning:** Multi-environment localization can also be performed by using Vision-based positioning or INS systems, as these methods do not directly rely on the deployed positioning infrastructure [141, 145, 147, 148]. Vision-based methods primarily utilize different high-cost vision sensors, such as stereo cameras or LiDARs, combined with intelligent vision and ML techniques and algorithms, thus leading to higher processing complexity, and therefore creating a requirement for specialized vision processing hardware. This significantly decreases the possible cost and energy efficiency of the vision-based methods. Even though the vision-based methods are capable of performing the relative positioning with up to centimeter-level accuracy, the estimation of the absolute location additionally requires the preliminary mapping of the covered area to determine the set of reference spots. To perform properly, the camera-based methods additionally require the presence of sufficient lighting and a variety of visual features within the operating area.

**Inertial Navigation System:** Initially, the widely available inertial sensors can be used as inertial navigation systems, providing a relative positioning by using a dead reckoning technique [141, 143, 146]. In this technique, a position is estimated based on the previously known location of the tracked object and its kinematics, measured by inertial sensors, such as accelerometers and gyroscopes. Inertial sensors, however, are naturally prone to over time error accumulation (drift), which consequently impacts the resulting positioning by gradually decreasing its accuracy. Drift error reduction requires the inclusion of additional auxiliary sensors, such as magnetometers or other odometry sensors, such as steering sensors and wheel encoders. Additionally, for the absolute location estimation, inertial sensors can be combined with an absolute positioning system and used as a supporting unit. Therefore, the expected cost efficiency and positioning accuracy of INS systems are dependent on the additional use of supplemental sensors and the presence of over time error accumulation by inertial sensors.

## Discussion

The summarized results of the above analyzed positioning methods and technologies for use as the underlying positioning system in the proposed indirect tracking method are provided in Table 5, along with their main features, acceptable trade-offs, and critical limitations. The significance of the particular aspect is reflected by the color intensity. As stated earlier in this section, the proposed indirect tracking method is not strictly bound to any type of positioning system, and any of the available methods or their combinations can be used in this role. However, from the perspective of industrial use and in accordance with sensors' selection requirements defined in Section 3.2, this research focuses on the use of the UWB positioning system in indoor environments and GNSS/ GNSS RTK in outdoor environments. In cases of mixed environments, the interchanging combination of these positioning systems is used. These positioning systems were chosen as they meet the defined sensor selection requirements and provide sufficient positioning accuracy at a suitable combination of cost efficiency and computational complexity in their coverage area.

In comparison with the UWB indoor positioning system, alternative methods, such

as Wi-Fi or BLE (RSSI) positioning, are unable to provide sufficient positioning accuracy, while methods such as BLE or magnetic field-based positioning provide insufficient coverage for industrial applications. Additionally, the magnetic field-based positioning methods are expected to be naturally inapplicable in the industrial environment due to major and inconsistent magnetic distortions. Even though vision-based methods may provide a multi-environment and highly accurate positioning, they will also introduce a significant cost inefficiency and high computational and maintenance complexity to the resulting indirect tracking method. During this research, the validation of the proposed method was performed by using Eliko UWB RTLS [150] while the FieldBee GNSS RTK [151] system was used for the conducted outdoor experiments.

Table 5: Summarized results of underlying positioning system selection with highlighted features, trade-offs, and major limitations.

Underlying Positioning System			
	Features	Trade-offs	Critical limitations
GNSS & GNSS RTK	Decimeter accuracy	Outdoor only	-
	World-wide deployed infrastructure	Susceptibility to obstructions	
	*Centimeter accuracy (RTK)	*Higher cost (RTK)	
Cellular	Cost-efficiency	Primarily outdoors	Sub-meter accuracy
			Underdeveloped infrastructure
Ultra-Wideband	Decimeter accuracy	Primarily indoors	-
		Moderate to high infrastructure cost	
Wi-Fi	Wide availability	Primarily indoors	5-10 meters accuracy (RSSI)
	Cost efficiency	*Increased computational complexity (FTM)	*Meter-level accuracy (FTM)
Bluetooth	Wide availability	Primarily indoors	Sensitive to RF interference
	Cost efficiency	*Increased computational complexity (AoA, AoD)	Meter-level accuracy (default)
Magnetic field-based	Centimeter accuracy	Short-range	*Sub-meter accuracy (AoA,AoD)
	Infrastructure-free		High environmental sensitivity
Vision-based	Centimeter accuracy	High-cost	Operational only in supervised environments
	Infrastructure-free	High computational complexity	Environmental mapping needed
	Multi-environment	High data transmission requirements	High-end processing hardware required
Inertial (gyro, accl)	Wide availability	Supporting technology required	Over time error accumulation (gradual accuracy drop)
	Cost efficiency		
	Infrastructure-free		

### 3.2.2 Heading Tracking Unit

Heading information is one of the main aspects of vehicle navigation, along with its position and speed [152]. The accurate information on the real-time heading of the used MHE plays an essential role in the proposed indirect tracking method, allowing a significant mitigation of the earlier defined offset between the positioning unit and fork area, and therefore, achieving high accuracy of the resulting indirect product localization. This section gives an overview of available sensor options for heading estimation and covers the selection of a suitable sensor for the accurate, robust, and real-time heading tracking of industrial machinery in the corresponding environment. The selection of the heading tracking unit also takes into account the presence of the previously chosen positioning system and its potential use for heading estimation, either independently or in combination with another unit.

**Gyroscopes:** Gyroscopes are one of the most prevalent and widely adopted sensor types, allowing the real-time tracking of the relative three-dimensional orientation by frequently measuring the instantaneous angular velocity [153, 154]. Gyroscope sensors include different types, from consumer-grade and widely available MEMS gyroscopes to more advanced optical solutions and experimental prototypes. Due to their compactness and cost-efficiency, MEMS gyroscopes are widely used in various applications from smartphones to robotics, as well as are often available as part of multi-sensor units, such as IMU (Inertial Measurement Unit). Despite their moderate sensitivity to temperature changes and mechanical vibrations, caused by their mechanical nature, MEMS gyroscopes are capable of detecting minor rotations with an approximate resolution of  $0.01^\circ$  with minor data processing requirements. As it was previously discussed in Section 2.2.1, one of the key disadvantages of MEMS gyroscopes is represented by the over time accumulated error in the measured angular data, caused by temperature-varying internal white noise and bias instability.

The available types of optical gyroscopes include ring laser gyroscopes and fiber optic gyroscopes, based on the principle of the Sagnac effect, discovered in 1913 by George Marc Sagnac [155, 156, 63, 157]. It describes the interferometry phenomenon, when in the rotating interferometer, two laser beams, propagating in opposite directions, will have a phase shift proportional to the angular velocity of the rotating interferometer. In contrast to mechanical gyroscopes, optical units offer significantly higher stability and robustness against mechanical vibrations and varying temperatures. Optical gyroscopes are less susceptible, although not fully immune, to the drift effect, which still may eventually cause an accumulation of a significant error over longer periods of time. The performance advantages of the optical gyroscopes are also counteracted by significantly lower compactness, cost- and energy efficiency in comparison with MEMS units.

**Steering & Wheel Encoders:** Vehicle heading estimation can also be based on odometry sensors, such as steering and wheel encoders, supported by a lateral velocity constraint model [158, 159]. These sensors measure the vehicle's state parameters as movement speed and steering angle, used to estimate its relative heading. Despite the wide availability, significant cost efficiency, and minor data processing requirements, these sensors are prone to different physical aspects of vehicle motion, such as the sideslip effect, and are often used in combination with inertial sensors (gyroscopes & accelerometers). Additionally, these sensors require direct integration into the vehicle mechanisms and implementation of the vehicle-specific lateral velocity constraint model.

**Magnetometers:** Another widely used method for heading tracking is based on the principle of magnetic field sensing by using magnetometers [160, 161, 162]. These units measure the strength of surrounding magnetic fields, which can be used to calculate the absolute heading in relation to the magnetic north of the Earth, also referred to as bearing or azimuth. Widely accessible and cost-efficient types of magnetometers based on the Anisotropic Magnetoresistance (AMR), Giant Magnetoresistance (GMR), or Tunnel Magnetoresistance (TMR) effects may provide absolute heading estimation with approximately  $1^\circ$  resolution and precision. Improved performance can be expected from more specialized and less accessible magnetometer types, such as Fluxgate magnetometers. However, due to the natural sensitivity of magnetometers to different magnetic distortions, the high-performance results may only be achieved in controlled environments with minimized presence of magnetic noise. Since for the absolute heading measurement the

magnetometers naturally rely on the relatively weak magnetic field of the Earth, the presence of significantly stronger magnetic distortions may entirely deny the use of magnetometers in industrial areas, such as warehouses or production sites.

**Positioning Data-based:** Absolute heading information within the used coordinate system can also be estimated by using the positioning data. With varying accuracy, the momentary vehicle heading can be estimated by using the consecutive positioning data samples from single- [132, 130] or multi-antenna [163, 164, 165, 128] positioning units. This method provides potentially high reliability in different environments, while its stability directly depends on the positioning quality of the underlying positioning system. The heading estimation accuracy of this method is directly determined by the movement speed of the tracked vehicle and the precision of the used positioning system.

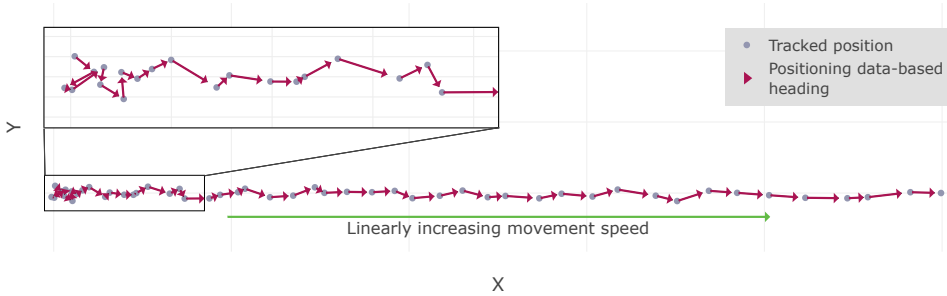


Figure 3: Illustrative example of the heading precision, based on the noisy positioning data, and at linearly increasing movement speed.

Figure 3 illustrates the heading estimation quality, based on the noisy positioning data at varying moment speed. Sample positioning data is shown with gray points, the corresponding positioning data-based heading is represented with dark red arrows, while the green arrow illustrates the true movement direction, accompanied by linearly increasing (left to right) movement speed from a stationary state. As it is illustrated, in stationary cases and at lower movement speeds of a single antenna-based setup, the estimated movement direction (heading) is highly affected by positioning data errors and becomes fully unpredictable. Increasing movement speed compensates for positioning data errors, rapidly improving the heading estimation accuracy and precision. This significantly complicates the sole use of positioning data for proper heading estimation. A certain improvement in heading estimation stability and reliability at lower movement speeds can be expected in the case of a less cost- and energy-efficient multi-antenna positioning system. Unlike the single antenna unit, it provides synchronized information from multiple, physically separated receivers (antennas), which allows to perform the heading estimation within each data sample independently.

**Vision based:** Accurate, potentially stable, and sub-degree heading estimation can also be performed as part of the vision-based positioning option, described in the previous Section 3.2.1 by using different high-cost sensors such as stereo cameras, optical flow sensors, intelligent vision, or LiDARs [166, 167, 168]. In some cases, this approach may provide a 1.5-degree accuracy in the platform heading estimation [169]. Similar to the vision-based positioning, however, this heading estimation approach leads to significant processing complexity, specialized hardware requirements, as well as preliminary mapping of the operating area to determine the environmental reference points, necessary

for the absolute orientation estimation.

## Discussion

Table 6 provides the summarized results of the above analyzed vehicle heading tracking techniques from the perspective of their use as part of the proposed indirect tracking method. It covers the main features of the considered methods, their acceptable trade-offs, and critical limitations. Color intensity corresponds to the relative significance of the corresponding aspect. From the perspective of industrial application and in accordance with the sensors' selection criteria, defined in Section 3.2, the suitable option for the heading estimation of industrial material handling equipment includes the inertial (gyroscope) and positioning data-based methods. Both of these methods, however, contain significant limitations, denying their sole use for accurate and reliable vehicle heading tracking. These limitations include the drift effect of the inertial unit and direct dependence on the movement speed of the positioning data-based method.

Since the positioning system was selected earlier for use as part of the indirect tracking method, this research focuses on the combined use of inertial and positioning data for accurate heading tracking. Therefore, the MEMS gyroscope unit is selected for the role of the heading tracking unit in this section due to its wide availability, portability, cost- and energy efficiency in comparison to the optical gyroscopes.

The use of magnetic field-based methods was avoided due to their critical sensitivity to magnetic distortions and thus inapplicability in industrial environments. Odometry and vision-based heading estimation were also not considered due to their respective requirements for integration into the machinery mechanisms, high computational complexity, and cost inefficiency. The combined use of inertial and positioning data for accurate vehicle heading estimation was separately investigated as part of this research, while the developed and used algorithmic method is described in the Section 4. The experimental tests in this research were conducted using the MEMS gyroscope sensor of the Bosch BNO055 inertial measurement unit, which also includes an accelerometer and magnetometer [170].

Table 6: Summarized results of heading tracking unit selection with highlighted features, trade-offs, and major limitations.

Heading Tracking Unit			
	Features	Trade-offs	Critical limitations
Gyroscope	Wide availability Cost efficiency	Supporting technology required <b>(Positioning unit available)</b>	Over time error accumulation (drift → gradual accuracy drop)
	*Higher accuracy & decreased drift effect (RLG, FOG)	*Significantly higher cost (RLG, FOG)	
Steering & Wheel Encoders	Wide availability Cost efficiency	Highly detailed motion model is required	Direct integration into vehicle mechanisms
		Supporting technologies needed	
Magnetometer	Wide availability & Cost efficiency Absolute heading measurement *Possible high accuracy	*Operational only in supervised environments	Extreme sensitivity to magnetic distortions
	Absolute heading information <b>Previously selected &amp; available (may be used as aux. technology)</b>	Sensitivity to positioning data quality at low speeds <b>(may be supported by gyro.)</b>	Accuracy & reliability only at higher speeds
Vision-based	Potentially high accuracy Absolute heading information	High-cost High computational complexity	Environmental mapping needed High-end processing hardware required
		High data transmission requirements	

### 3.2.3 Tynes' Elevation Tracking Unit

Supporting 3D product localization is essential in the majority of industrial applications, particularly those involving extensive product shelving or stacking. To extend the positioning capabilities of the proposed indirect tracking method and enable the complete three-dimensional product positioning, accurate tynes' elevation tracking is required. This section covers the review and selection of a suitable technology for the accurate and reliable real-time measurement of the forklift tynes' elevation. The availability of the previously selected positioning and inertial (gyroscope/IMU) technologies, as well as their possible use for the fork elevation tracking, is also taken into account in this section.

#### ***Barometric Pressure Sensors***

Barometric pressure sensors can be used for the absolute altitude estimation, by measuring the momentary atmospheric pressure [171, 172, 173, 174]. This technology is widely available and, due to its wide altitude measurement range, is used in different applications covering higher altitude tracking, such as in drones or airplanes (barometric altimeters). Widely available pressure sensors provide altitude measurements with meter to centimeter accuracy levels. The performance of the barometric pressure sensors, however, may be significantly affected by environmental factors, including changes in the surrounding temperature, humidity, and airflow, thus leading to performance inconsistency and requiring proper calibration.

***Ultrasonic Distance Sensors:*** Centimeter to sub-centimeter accuracy in the elevation measurement can be achieved by using widely available ultrasonic distance sensors [175, 176]. Although these sensors demonstrate lower susceptibility to environmental effects in comparison with barometric sensors, they also provide a significantly lower operating range of approximately 5 m. In the case of ultrasonic distance sensors, a higher operating range may be achieved by lowering the operating frequency of the emitted sound, which consequently leads to a decrease in measurement accuracy. The use of higher frequencies, on the other hand, provides higher, up to millimeter accuracy at the cost of a significant decrease in the operating range. In the context of this work, the forklift tynes' elevation measurement additionally requires a precise and reliable installation of the ultrasonic distance sensor within the fork area, and pointed towards the ground surface. Being a proximity detection unit, the ultrasonic sensor performs the distance measurement to the nearest object in its line of sight, therefore enabling various foreign objects, including forklift parts, within its coverage area to affect the resulting measurement accuracy.

***Laser Distance Sensors:*** Alternatively, the elevation measurement may be performed by a laser distance sensor, providing millimeter accuracy along with higher measurement range and measurement resolution [177, 178]. Unlike the ultrasonic distance sensors, the laser-based unit performs the distance measurements by forming a narrow laser beam, thus avoiding the false detection of the nearest object in proximity. Laser distance sensors, however, demonstrate decreased cost-efficiency and moderate sensitivity to different environmental factors, including fog or dust, heavily present in industrial areas, as well as the quality of the reflecting surfaces. Similar to ultrasonic distance sensors, in the context of the forklift tynes' elevation tracking, laser distance sensors require reliable and precise installation within the fork area, which may also lead to the eventual damage of the fragile sensor parts due to impacts or vibrations present on MHE.

**IR Distance Sensors:** Distance measurements can also be based on Infrared (IR) light technology. IR distance sensors provide significant cost-efficiency together with centimeter measurement accuracy and millimeter resolution, similar to ultrasonic sensors [179, 180, 181]. IR sensors, however, are significantly limited to a slightly beyond 1 m detection range and high sensitivity to different environmental aspects, such as ambient lighting, reflection properties, and color of the reflecting surface. The requirement for a precise installation of this sensor within the fork area may also lead to the inevitable damage to the fragile sensor parts.

**Wire Displacement Sensors:** A variety of different mechanical approaches are used in the industry for accurate displacement measurements [182, 183, 184]. However, a majority of those sensors, such as strain gauge displacement sensors, only provide a centimeter-level measurement range, which proves their inapplicability in the context of this work. A higher measurement range can be provided by industrial-grade wire displacement sensors. These sensors represent the wire reel, equipped with either a rotary encoder or a potentiometer unit, respectively used to measure relative or absolute linear wire displacement. These sensors allow displacement measurements with millimeter accuracy and sub-millimeter resolution at the operating ranges of up to dozens of meters, depending on the used configuration [185]. The build quality of the industrial-grade sensors provides high reliability in different environmental conditions. While the potentiometer-based sensors offer high measurement stability and robustness, the rotary encoder-based units may experience an over time error accumulation due to their relative nature of measurements. In the context of forklift tynes' elevation measurement, these sensors may require minor to moderate integration into the fork mechanisms, depending on the final deployment.

**Positioning Unit:** The vertical position of the forklift tynes may also be measured by the positioning systems, such as the previously selected UWB indoor positioning system, providing the declared positioning accuracy of 10-30 cm [186, 187]. Positioning performance, however, is significantly dependent on the positioning infrastructure deployment within the operating area. While the horizontal deployment of the UWB infrastructural components (anchor units) may be optimized, improving the horizontal positioning accuracy, the vertical deployment remains significantly limited. Higher positioning performance requires the deployment of the UWB anchor units at varying heights between the ground and the ceiling levels within the operating area. However, in most cases, the positioning infrastructure is mainly deployed near the ceiling level due to the lower presence of line-of-sight blocking obstacles, which significantly affects the vertical positioning accuracy. Thus, in practice, depending on the particular deployment, the expected vertical accuracy of UWB positioning systems may be reduced down to a 0.5 - 1 m level [186, 187]. A similar effect of reduced vertical positioning accuracy may also be expected from other positioning systems, such as GNSS [188, 189].

**Inertial Sensors:** The previously selected MEMS gyroscope unit is often available as part of inertial measurement units, together with an accelerometer sensor used for the linear acceleration measurements [190, 191, 192]. As the integration of the linear acceleration data reflects the linear displacement, accelerometer units can also be used as a cost-effective method for elevation tracking, providing theoretically an unlimited measurement range. Even though this approach potentially allows displacement measurement with a sub-millimeter resolution, it is unable to provide stable and reliable accuracy for longer periods of time. Similar to MEMS gyroscopes, the MEMS accelerometer units



are prone to the drift effect, which causes the over time accumulated errors, thus leading to the over time degrading accuracy of the displacement measurements.

## Discussion

The summarized results of the above provided analyzed approaches for the forklift tynes' elevation monitoring in the proposed indirect tracking method are presented in Table 7, along with their main features, acceptable trade-offs, and critical limitations. The significance of the particular aspect is reflected in the color intensity. The resulting selection of tynes' elevation tracking unit was performed by taking into account the selection requirements, defined earlier in Section 3.2, as well as the expected use of the selected sensor in industrial conditions, where the risk of physical damage is greatly increased. Among the technologies mentioned in this section, the potentiometer-based wire displacement sensor was selected for use as an elevation tracking unit in this research. Even though a robust deployment of this sensor may require minor to moderate integration into the lifting mechanisms of the forklift, it also provides a combination of significant advantages. These include sufficient measurement range for forklift applications, high measurement accuracy and resolution, as well as low sensitivity to environmental effects, high stability, and reliability in industrial applications.

Alternative options for the elevation tracking include barometric sensors, which, compared to wire displacement sensors, require minimal integration into the forklift mechanisms, while providing lower measurement accuracy, resolution, and reliability, as well as higher environmental sensitivity. Positioning and inertial sensor-based methods are unable to provide reliable and stable elevation measurements at sufficient centimeter-level accuracy, which prevents their use in this research. As ultrasonic, IR, or laser technology-based sensors perform distance measurements against the corresponding reflecting sur-

Table 7: Summarized results of tynes' elevation tracking unit selection with highlighted features, trade-offs, and major limitations.

	Tynes' Elevation Tracking Unit		
	Features	Trade-offs	Critical limitations
Barometric Pressure Sensors	Wide availability	Calibration requirements	Meter-to-centimeter accuracy
	Absolute measurement		Significant environmental sensitivity
			Inconsistent performance
Ultrasonic Distance Sensors	Wide availability & Cost efficiency	*Measurement accuracy to max. operating range trade-off	Sensitivity to surrounding objects
	*Sub-centimeter-level accuracy		Deployment difficulty for the given task
	Low environmental sensitivity		*Possible range limitations
Laser Distance Sensors	Millimeter accuracy	Moderate sensitivity to reflecting surfaces & environment	Sensitivity to vibrations & impacts
	Cost efficiency		Deployment difficulty for the given task
	Sufficient operating range		
IR Distance Sensors	Cost efficiency	-	Limited range
	Centimeter accuracy		High environmental sensitivity
			Deployment difficulty for the given task
<b>Displacement (Wire) Sensors</b>	Absolute measurement	Physical wear	-
	Millimeter to centimeter accuracy & resolution	Moderate cost	
		Minor deployment difficulties	
Positioning System	Absolute measurement	Infrastructure required (Expected by default)	Meter-level vertical accuracy
	<b>Previously selected &amp; available</b>		
Inertial sensors (accelerometer)	Wide availability & Cost efficiency	-	Over time error accumulation & degrading accuracy
	<b>Previously selected &amp; available</b>		

faces, they require precise deployment under the fork area, measuring towards the ground surface. Aside from the other performance disadvantages of these sensors, this deployment may lead to their inevitable damage. In the experimental tests, conducted as part of this research, the elevation tracking was performed by using a Miran potentiometer-based draw wire encoder [193].

#### 3.2.4 Fork Occupancy Detection Unit

Reliable and real-time detection of the fork occupancy status is essential information for the proposed indirect tracking method. It allows to minimize the involvement of the working personnel in the product and equipment tracking process, thus minimizing the impact of the human factor. Synchronized use with the tracked product location also allows for the accurate estimation of the product pick-up or drop-down coordinates, eventually used for product identification. This section covers the selection of suitable technology and sensors for the reliable detection of the forklift tynes' occupancy status in the industrial environment. Sensors and technologies selected in previous Sections 3.2.1, 3.2.2, and 3.2.3 are also taken into account as possible supporting units for the selected occupancy tracking unit.

**Load Cells:** One of the most straightforward methods for the physical occupancy detection can be based on load cells. Although industrial-grade load cells are typically costly, they can provide a broad range of physical weight detection from a gram, and sometimes, milligram level up to dozens of tons [194, 195, 196, 197]. This weight detection range, together with high reliability in industrial environments and the capability to provide extra information on the detected object's weight, makes these sensors a viable option for a variety of industrial applications, including the proposed indirect tracking method. However, the forklift deployment of the industrial load sensor for tynes' occupancy detection requires its major integration into the lifting mechanisms. Flat load (strain gauge) sensors (e.g., based on the piezoresistive structure) may be considered as an alternative option to load cells in weight measurement. Unlike the earlier described load cells, these units may be directly deployed within the fork area, potentially requiring minimal integration into the lifting mechanisms. This advantage, together with the slightly increased cost efficiency, however, is compensated by the noticeably lower weight detection range up to a few tons and lower durability.

**Laser Distance Sensors:** Object detection within a certain area may be performed using various cost-efficient distance sensors, such as ultrasonic or laser distance measurement units [198, 199]. As these sensors are able to detect the object's presence remotely, they do not require significant integration into the MHE mechanisms. Laser distance sensors are used for accurate and precise distance measurement at the expense of lower cost efficiency, higher environmental sensitivity, and data processing complexity. From the perspective of general object presence detection, however, laser-based sensors offer a significant operating range of dozens of meters, while the high distance measurement accuracy and precision are not essential. The case-specific disadvantage of these sensors is the potential requirement for precise installation, allowing the narrow laser beam to reliably detect the transported payload of any possible shape and size.

**Ultrasonic Distance Sensors:** Ultrasonic sensors, on the other hand, perform the distance measurements to the nearest object within a relatively wide cone-shaped beam [200, 201, 202]. Although this might be considered a drawback in the field of precise dis-

tance measurements, this feature makes ultrasonic sensors suitable for area occupancy tracking and object detection. In comparison with laser distance sensors, the ultrasonic sensors provide a lower operating range within 5-10 m, together with centimeter-level accuracy in distance measurements. These parameters can be alternated by changing the operating frequency of the sensor as was explained in Section 3.2.3. Unlike laser-based units, ultrasonic distance sensors offer high cost-efficiency and low data processing complexity. Despite their moderate sensitivity to environmental conditions, they are often designed for real-world applications, including outdoor environments.

**IR/PIR sensors:** Sensors, based on IR and Passive IR (PIR) technologies, are primarily designed and used for general object presence detection [203, 204, 205]. Despite their cost efficiency and low computational complexity, these sensors also demonstrate relatively high environmental sensitivity and a variety of additional method-specific limitations. For instance, the IR reflection-based sensors are significantly limited to below half a meter detection range and highly sensitive to the environmental aspects, such as ambient light and reflective properties of the detected object. More advanced and less cost-efficient ToF (Time-of-Flight) IR sensors, on the other hand, provide additional features, such as distance measurements with approximate centimeter accuracy and increased operating range up to dozens of meters. These sensors, however, keep the aforementioned environmental limitations of IR sensors. PIR sensors are only capable of detecting heat-emitting and moving objects within a 10 m range, which primarily narrows their main field of applications to various human and animal detection systems. In the context of industrial object detection, these sensors are expected to be highly ineffective.

**Vision-Based Detection:** Different vision-based methods can be used for reliable and intelligent detection of the tynes' occupancy status, potentially allowing to detect and recognize different reference objects, such as industrial pallets, or environmental surroundings within a significant range [206, 207, 208]. This, however, results in reduced cost- and energy efficiency of the vision-based object detection approach, along with increased environmental sensitivity, data volume, and processing complexity. The integration of advanced, machine learning-based processing methods further increases processing complexity and results in significant cost and energy inefficiency, primarily due to the need for high-performance computing equipment.

**Capacitive/Inductive Sensors:** Capacitive and inductive sensors may also be used to detect the presence of specific objects in close proximity of approximately 10 cm, which, however, is insufficient in the context of forklift tynes' occupancy detection [209, 210, 211]. Additionally, these sensors only allow the detection of specific types of objects. For instance, inductive sensors are only capable of detecting various metal objects, while capacitive units are only sensitive to dielectric materials. Therefore, more versatile occupancy detection might require the combined use of both sensors.

## Discussion

Table 8 reflects the summarized outcomes of the above-provided analysis of different approaches for the fork occupancy status monitoring and a possible further use as part of the proposed indirect tracking method. It covers the key features, limitations, and possible trade-offs of the addressed approaches. The color intensity reflects the significance of a corresponding aspect. The resulting selection of the fork occupancy detection unit was based on the selection criteria defined in Section 3.2 and aims for robust object de-

tection within the forklift tynes area. Due to its wide detection area and supported operating range, which is sufficient to cover the entire tynes area, the ultrasonic distance sensor was chosen for the fork occupancy tracking. Its ability to perform distance measurements to the picked-up object with centimeter accuracy provides additional real-time information regarding the payload pick-up or drop-down process. Even though ultrasonic distance sensors have a moderate environmental sensitivity to different factors, such as high temperature and humidity, they remain significantly reliable in industrial and outdoor environments.

Laser distance sensors, on the other hand, require a precise deployment for the reliable detection of the picked-up payload. Alternatively, with proper integration into the lifting mechanisms of the forklift, industrial load sensors can also be used for the tynes' occupancy detection, providing additional weight information on the lifted payload. Options, such as IR, PIR, inductive, and capacitive sensors, introduce significant limitations from insufficient detection range and major environmental sensitivity to the inability to detect different materials. Vision-based sensors provide a potentially significant informational capacity regarding the environmental surroundings and the occupancy status of the tracked area, which, however, is achieved at the expense of a significant computational complexity, as well as low cost- and energy efficiency. Taking into account the usage of the previously selected tynes' elevation tracking unit, this research focuses on its combination with the fork occupancy detection sensor. This provides extended real-time information on detected payload pick-up and drop-down events, allowing the recognition of the aforementioned events and their stages. Fusion of tynes' elevation and occupancy tracking units is performed by the A-PDD algorithm, proposed as part of this research and further described in Section 5.2, as well as in Publication IV. During the experimental testing, the fork occupancy tracking was performed by using a weatherproof ultrasonic distance sensor SEN0208 [212].

Table 8: Summarized results of fork occupancy detection unit selection with highlighted features, trade-offs, and major limitations.

Fork Occupancy Detection Unit			
	Features	Trade-offs	Critical limitations
Load Cells	Reliable & accurate detection Weight information	Possible deployment difficulties Possible physical wear	Moderate to major integration into machinery mechanisms
Laser Distance Sensors	Cost efficiency Distance information Detection accuracy	Moderate environmental sensitivity	No areal coverage Sensitivity to vibrations & impacts
<b>Ultrasonic Distance Sensors</b>	Cost efficiency & Distance info. Areal coverage Low environmental sensitivity	Sensitivity to surroundings (false detection possibility)	-
IR Sensors	Cost efficiency	Possible distance information at higher cost	Limited range High environmental sensitivity
PIR Sensors	Cost efficiency	-	Detection of heat-emitting moving objects only
Vision-Based Detection	High reliability Contextual information	High-cost High computational complexity High data transmission requirements	High-end processing hardware required
Capacitive Sensors	Object material information	-	Limited range Detection of dielectric materials only
Inductive Sensors	Object material information	-	Limited range Detection of metal objects only

## 4 Heading Estimation

As it was previously defined in Section 3, one of the key aspects of the proposed indirect product tracking method is the accurate heading estimation of the used material handling equipment. According to the sensors selection performed in Section 3.2.2, this research focuses on the use of inertial sensors, particularly the gyroscope, for the real-time heading tracking of industrial machinery. The primary drawback (i.e., drift error accumulation) of inertial sensor-based heading estimation is introduced in Section 2.2.1, followed by the investigation of the current state-of-the-art methods for its mitigation in Section 2.2.2. In research on the available methods for inertial sensor heading error mitigation, the rarely used positioning and inertial data fusion approach was selected as the most suitable method in the context of this work. This section describes the main algorithmic methods for the positioning and inertial data-based vehicle heading estimation, proposed in Publications I & III. This section also covers a description of the algorithmic method for the UWB positioning system enhancement, implemented as part of the publication II [2].

### 4.1 Positioning Data-based Approach for Vehicle Heading Estimation

This section addresses the main limitations of the positioning and inertial data-based heading estimation, as it was also addressed by Xu *et al.* in one of the state-of-the-art works [130]. The key feature of the heading estimation approach, based on the positioning data (coordinates), is its dependence on the movement speed. Even minor positioning data noise and errors could lead to significant heading estimation uncertainty in stationary or slow movement cases. As it was visually illustrated in Fig. 3, the increasing movement speed significantly reduces the impact of positioning data errors and improves the heading estimation accuracy. The dependence of the positioning data-based heading errors on the movement speed is also later discussed in Section 4.4.3.

This research investigates the applicability of the positioning data for the mitigation of inertial sensor heading drift. In order to verify the sufficiency of the positioning information for a reliable gyroscope heading drift correction, a prototype algorithm was proposed and originally presented in Publication I. This section provides a brief description of the originally published algorithm and its experimental testing. This section also covers a minor extension to the originally published algorithm, and not included in Publication I. In this work, the algorithm is hereafter referred to as the Drift Correction Algorithm (DCA).

#### 4.1.1 Positioning Data-based IMU Heading Drift Correction Algorithm

The proposed DCA algorithm represents a novel, positioning information-based approach for the conditional correction of the gyroscope-accumulated heading drift error. A flowchart of the developed DCA algorithm is demonstrated in Fig. 4, while the corresponding detailed pseudo-code is available in Appendix 5. Both flowchart and pseudo-code representations of the DCA algorithm also include a highlighted extension, added after the original algorithm publication in I, and described later in this section.

In this algorithm, the real-time heading of the tracked vehicle is monitored by the inertial (gyroscope) sensor, while the positioning data is used to conditionally estimate the necessary heading correction. The drift correction  $\delta^\psi$  is applied to the inertial heading measurement  $\psi_k$ , thus compensating for the accumulated drift error and resulting in the corrected heading  $\Psi_k$ , representing the output of the algorithm. The arrival of the positioning data sample  $(x, y)_k$  triggers the drift correction value recalculation sequence. The latest positioning data sample (coordinates) is stored in the FIFO (First In, First Out) buffer  $\mathbf{W}$  of size  $\mu$  for further analysis to validate the movement behavior and possibility of a

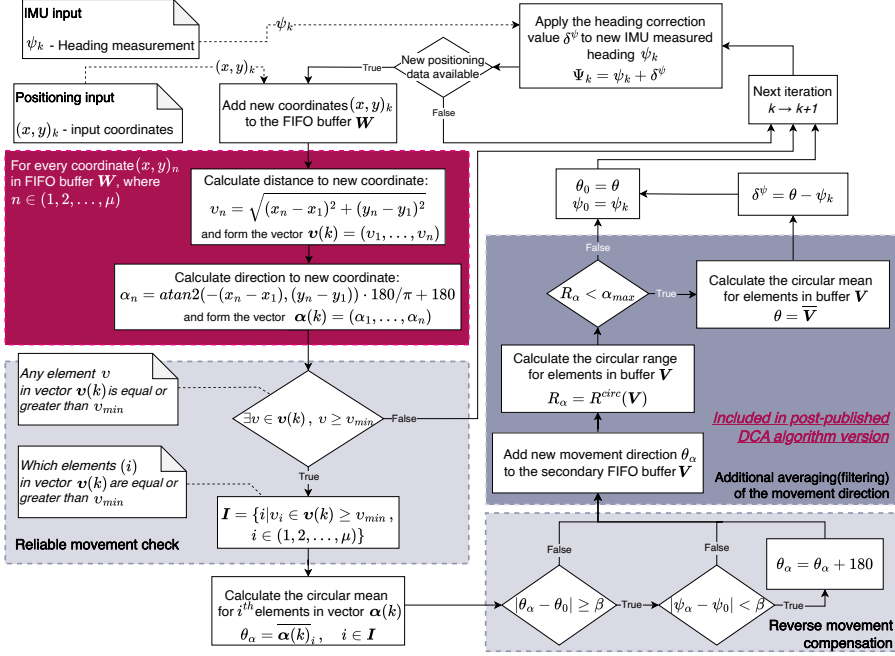


Figure 4: Flowchart of the proposed IMU heading drift correction algorithm. A minor extension for the originally published algorithm is highlighted with dark gray box.

reliable heading correction.

In the proposed algorithm, the received positioning information is required to indicate the movement with sufficient speed and minimal maneuvering intensity to be used for the drift correction update. Thus, the newest positioning data, stored in the FIFO buffer  $\mathbf{W}$  is used to calculate sets of the latest movement directions  $\alpha(k)$  and the coordinates' displacement in the positioning data  $\mathbf{v}(k)$ , which directly reflect the speed of movement. As the next step, the algorithm verifies the sufficient movement speed of the tracked vehicle and defines the indices  $i \in \mathbf{I}$  of elements in coordinates' displacement set  $\mathbf{v}(k)$ , which exceed the displacement threshold  $v_{min}$  (i.e., minimal required movement speed threshold). For  $i^{th}$  elements in the set of movement directions  $\alpha(k)$ , which correspond to the verified sufficient movement speed, the algorithm calculates the averaged movement direction  $\theta_\alpha$  by using the circular mean technique.

Afterward, the proposed drift correction algorithm attempts to recognize the possible case of reverse movement, which is essential in the case of industrial machinery tracking. To detect the reverse movement event, this algorithm separately evaluates changes of both inertial ( $\psi_k$ ) and positioning ( $\theta_\alpha$ ) data-based heading measurements by comparing them to their previous valid states ( $\psi_0$ ) and ( $\theta_0$ ). In the case of reverse movement, the positioning data-based heading is expected to indicate a close to 180-degree movement direction change, while the inertial sensor-provided heading remains mainly unchanged. In this case, the absolute difference between the latest valid positioning data-based headings  $\theta_\alpha$  and  $\theta_0$  is expected to be beyond the user-defined threshold value  $\beta$ , while the absolute difference between the latest inertial data-based headings must be below the  $\beta$  threshold. This allows to distinguish the reverse movement scenario from the case of intense maneuvering and apply the corresponding compensation for 180 degrees rotation

in the resulting movement direction  $\theta_\alpha$ . The threshold value  $\beta$  represents the reverse movement detection insensitivity of the algorithm. In the published version of this algorithm, the resulting movement direction  $\theta_\alpha$  was then directly used to recalculate the drift compensation parameter  $\delta^\psi$ . A detailed explanation of the algorithm for the correction of the IMU heading drift is provided in Publication I.

The original published version of the DCA algorithm was later extended with an additional filtering of the resulting heading information. The included filtering step is selected with a dark grey box in Fig. 4 and is used to further reduce the impact of possible outliers and increase the overall stability of the drift correction algorithm. After the reverse movement correction, the resulting movement direction  $\theta_\alpha$  is added to the secondary FIFO buffer  $\mathbf{V}$  of size  $\eta$ , for an additional averaging. A distribution level of the latest movement directions  $R_\alpha$  in the buffer  $\mathbf{V}$  is then calculated by using the circular range technique, which reflects the stability of the measured movement direction, and thus, the current maneuvering intensity. In case of sufficiently low maneuvering intensity with the variance of the movement directions below the defined maximal threshold  $\alpha_{max}$ , the resulting averaged movement direction  $\theta$  is calculated and used to update the drift compensation parameter  $\delta^\psi$ . This extended version of the DCA algorithm is later used for the comparison with the developed ATKF algorithm in Section 4.4.3 and in Publication III.

#### 4.1.2 Experimental Testing of the Drift Correction Algorithm

The suitability of the positioning and inertial data fusion approach for reliable vehicle heading tracking was experimentally validated by a conducted test campaign. In the context of this research, the proposed DCA algorithm was developed for the accurate heading

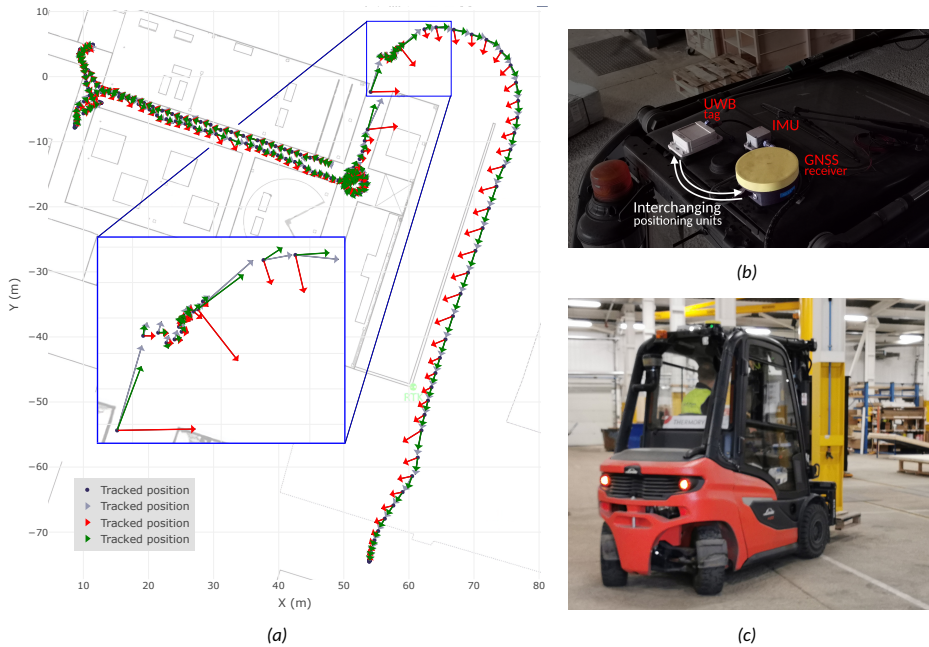


Figure 5: (a) Visualized results of the experimentally tracked forklift position (blue dots) and orientation, estimated by the sole IMU (red arrows), Drift correction algorithm (green arrows) and true heading (gray arrows); (b) Deployment of the used sensors setup on top of the used forklift; (c) The forklift used in the test campaign.

estimation of industrial vehicles in an industrial environment. Therefore, for the experimental performance evaluation of this algorithm it was chosen an operating wood manufacturing site, containing large industrial machinery and potentially significant magnetic distortions, preventing the use of state-of-the-art magnetometer-based methods. The test campaign was conducted for the originally published version of the DCA algorithm, and, along with the corresponding results, is described in Publication I. Tests were performed in operating industrial production site using a highly maneuverable forklift, shown in Fig. 5c, with the deployed positioning and inertial sensors shown in Fig. 5b.

The test campaign was conducted in both indoor and outdoor environments in order to diversify the test scenario and evaluate the performance of the proposed DCA algorithm in different environments and at different levels of positioning quality. To cover both indoor and outdoor environments, the deployed sensors' setup included two positioning units (i.e., GNSS RTK and UWB), alternating based on the current operating environment. Significantly varying movement speed, intense maneuvering events, and occasional reverse movement were used to further diversify the testing scenario for a proper method evaluation.

The visualized movement track of the corresponding test campaign is shown in Fig. 5a along with the corresponding heading tracking results. Positioning data of the tracked forklift is shown with blue dots, while red, green, and gray arrows respectively demonstrate the tracked forklift heading of the sole IMU, after processing by the designed DCA algorithm, and the true forklift heading. The zoomed-in area in Fig. 5a demonstrates the moment of the significant positioning data quality drop, caused by the transition between indoor and outdoor environments, and the corresponding switch from indoor UWB to outdoor GNSS positioning system.

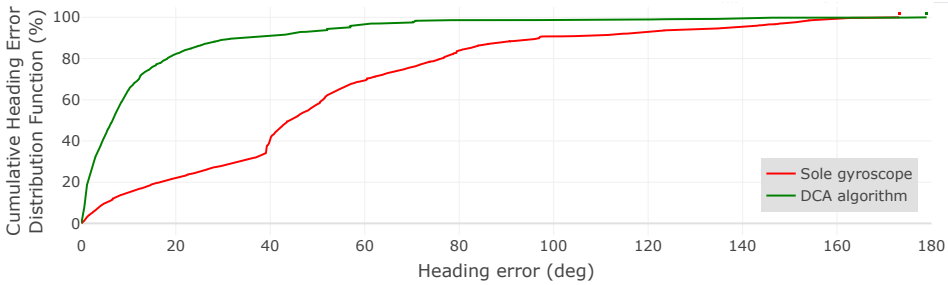


Figure 6: Cumulative error distribution function of the resulting forklift heading, initially measured by IMU (red) and after its correction by the DCA algorithm (green).

The proposed algorithm was able to decrease the Median Absolute Error (MdAE) of the sole IMU provided heading by approximately 86.8%, from 44.1 degrees down to 5.9 degrees. This reflects the overall improvement of IMU heading tracking accuracy, provided by the drift correction algorithm, and does not take into account the momentary outliers. The obtained heading error Standard Deviation (SD) of 23.8 degrees, however, has indicated a noticeable presence of outliers in the corrected forklift heading data. These results are also reflected by the heading error Cumulative Distribution Function (CDF), shown in Fig. 6. Thus, 90% of errors in the DCA algorithm estimated heading do not exceed 30 degrees, while 75% of errors reach a sub-11 degrees level. In contrast, 60% of errors in the IMU estimated forklift heading rapidly exceed 40 degrees, with over 10% of errors beyond 90 degrees. Significant errors in the DCA algorithm estimated heading were primarily experienced during the periods of significant positioning data accuracy drops, as



well as during the event of intense forklift maneuvering. Nevertheless, these results have confirmed the effectiveness of the positioning information for inertial sensor drift mitigation in heading estimation applications.

Evaluation of experimentally obtained results has identified two key prerequisites for a reliable use of positioning data in vehicle heading estimation. These requirements include robustness against inaccurate positioning information and minimal response to the input data. The increased reliability against the potential poor positioning data requires a higher level of real-time adaptivity of the fusion algorithm and possible integration of input data filtering. The criteria of minimal response to the input data, on the other hand, requires the use of a suitable state estimator or integration of different machine learning techniques in parallel to minimize potential response delays, naturally caused by data filtering methods. These identified key requirements were considered in further research on the vehicle heading estimation topic.

Publication 1 [1] also provides a brief introduction to the indirect tracking topic as the targeted application of the designed heading estimation method. Afterward, it provides the theoretical analysis of the obtained heading estimation results in the context of this topic. According to the published results, the aforementioned reduction in median heading absolute error from 44.1 degrees to 5.9 degrees is a theoretical equivalent of the indirect product positioning accuracy improvement from 1.914 meters to 0.262 meters. This additionally conforms to the necessity of accurate forklift heading tracking for indirect product localization methods.

## 4.2 Kalman Filter Background

As it was concluded in Section 4.1.2, a reliable positioning and inertial data-based method for vehicle heading estimation is required to provide sufficient adaptivity, state estimation, and possible data filtering features. According to the analysis of state-of-the-art inertial data processing methods, performed in Section 2.2.3, the aforementioned required features can be provided by the different variations of the Kalman filter algorithm.

### 4.2.1 Linear Kalman Filter

The Kalman Filter represents a type of Bayesian filter, and is a recursive state estimation algorithm, developed by Rudolf Kalman and described in one of his works in 1960 [213]. In its standard linear variation, this algorithm estimates the state of the observed system by using the prediction model, information on previous system states, noisy measurement input data, as well as optionally available control information input. This variation of the Kalman filter presumes the processed system model presumes to be linear with errors, having a Gaussian (normal) distribution.

The general and widely used structure of the standard Kalman filter is described by numerous authors, as, for instance, by Labbe R. or Becker A. in their books [214, 215, 216]. The general structure of the standard Kalman filter is separated into two main steps, including system state prediction and correction. As the first step, the Kalman filter performs the prediction of the upcoming system state and its covariance by using the prediction model, previous system state information, and the possible control information input. The Kalman prediction step can be expressed as follows:

$$\hat{\mathbf{x}}_k = \mathbf{A} \cdot \mathbf{x}_{k-1} + \mathbf{B} \cdot \mathbf{u}_k + \mathbf{w}_k, \quad (3)$$

$$\hat{\mathbf{P}}_k = \mathbf{A} \cdot \mathbf{P}_{k-1} \cdot \mathbf{A}^T + \mathbf{Q}, \quad (4)$$

where  $\hat{\mathbf{x}}_k$ <sup>9</sup> represents the Kalman filter prediction for the system state vector of the iteration  $k$ , which is based on the system state of the previous iteration  $\mathbf{x}_{k-1}$ , state transition model  $\mathbf{A}$ <sup>10</sup>, control input vector  $\mathbf{u}_k$ , control transition matrix  $\mathbf{B}$ <sup>11</sup>, and the process noise vector  $\mathbf{w}_k$ . The corresponding Kalman filter prediction for the state covariance is represented with  $\hat{\mathbf{P}}_k$ <sup>12</sup>, which is calculated by using the covariance matrix of previous iteration  $\mathbf{P}_{k-1}$ , process noise covariance matrix  $\mathbf{Q}$  and the earlier defined state transition matrix.

The correction step of the Kalman filter introduces the measurement input for the system and performs controlled corrections in the earlier predicted state, thus providing the resulting state estimation. This step can be expressed as follows:

$$\mathbf{K}_k = \hat{\mathbf{P}}_k \cdot \mathbf{H}^T \cdot (\mathbf{H} \cdot \hat{\mathbf{P}}_k \cdot \mathbf{H}^T + \mathbf{R})^{-1}, \quad (5)$$

$$\mathbf{x}_k = \hat{\mathbf{x}}_k + \mathbf{K}_k \cdot (\mathbf{z}_k - \mathbf{H} \cdot \hat{\mathbf{x}}_k), \quad (6)$$

$$\mathbf{P}_k = (\mathbf{I} - \mathbf{K}_k \cdot \mathbf{H}) \cdot \hat{\mathbf{P}}_k, \quad (7)$$

where the Kalman gain matrix  $\mathbf{K}_k$  is calculated by using the observation or measurement transition matrix  $\mathbf{H}$ <sup>13</sup>, measurement noise covariance matrix  $\mathbf{R}$  and the earlier predicted state covariance matrix  $\hat{\mathbf{P}}_k$ . The Kalman gain matrix reflects the weights proportion of the predicted state and obtained measurements, thus defining the impact of the correction step. The resulting system state estimate  $\mathbf{x}_k$  and the corresponding covariance matrix  $\mathbf{P}_k$  are then calculated by using the previously defined components and the measurement vector  $\mathbf{z}_k$ <sup>14</sup>, which contains the measurements input of the current iteration  $k$ .

#### 4.2.2 Nonlinear Kalman Filters

Even though all of the real-life problems and systems are inevitably nonlinear, many of them can be relatively effectively described by linear models and processed by algorithms, such as a linear Kalman filter [214, 215]. Others, however, require more advanced nonlinear processing methods and estimator algorithms, for example, the widely used variations of the extended Kalman filter [214, 215, 216], the unscented Kalman filter [214, 215], as well as the particle filter [214, 215]. Linear Kalman filter variations provide a significant advantage over nonlinear methods in cases when the processed model can be successfully linearized with sufficient accuracy. The linear model processing provides noticeably lower computational time and complexity, which makes the linear Kalman filter highly suitable for real-time applications and in cases of limited computational capability (e.g., embedded systems).

The extended Kalman filter is one of the most widely used Kalman filter algorithms, allowing the processing of various nonlinear models [217, 218]. In different EKF algorithm variations, the nonlinear process is locally linearized and filtered by using techniques of the linear Kalman filter. It is often represented with the use of nonlinear estimation models in the default linear Kalman filter algorithm. Depending on the used nonlinear model, the EKF may provide a significantly improved estimation accuracy over the linear Kalman filter at the cost of increased computational complexity and time, sometimes comparable to the UKF [218]. The use of simplified estimation models, on the contrary, allows the EKF to achieve computational time and complexity, as well as estimation accuracy levels of the

<sup>9</sup>In Section 4.4.2 of this work is alternatively notated as  $\mathbf{X}$

<sup>10</sup>In the literature may be alternatively notated as  $\mathbf{F}$  or  $\Phi$

<sup>11</sup>In the literature may be alternatively notated as  $\mathbf{G}$

<sup>12</sup>In the literature may be alternatively notated as  $\Sigma$

<sup>13</sup>In the literature may be alternatively notated as  $\mathbf{F}$  or  $\mathbf{C}$

<sup>14</sup>In the literature may be alternatively notated as  $\mathbf{y}$

linear Kalman filter. Thus, Extended Kalman filters often provide a suitable compromise between estimation accuracy and processing complexity, and are widely used in nonlinear applications [217, 218].

Unscented Kalman filter, also known as a Sigma Point Kalman Filter (SPKF), represents a nonlinear Bayes filter, which attempts to use the combined principles and advantages of lower computational complexity of the Kalman filter and increased performance of the Particle filter [217, 218]. Similar to the Particle filter, the UKF algorithm is based on particles - Sigma points, used to estimate the nonlinearity of the observed model and predict its future states. While the Particle filter is based on an unlimited number of randomly chosen particles (points), the UKF fully relies on a strictly dedicated number of carefully selected sigma points. Even though, in comparison with the Particle filter, this limits the computational complexity of the UKF algorithm, it remains significantly complex in relation to previously mentioned KF algorithms, such as EKF. The computational complexity of UKF algorithms, and especially particle filters, makes them less suitable for real-time applications, and thus, they were not used in the scope of this research.

#### 4.2.3 Adaptive Kalman Filter

Adaptive Kalman filters represent the class of KF algorithms, capable of dynamic adjustment of the algorithmic response to input data depending on the selected factors, thus actively adapting to possible changes [215]. One of the most widely used adaptivity methods in Kalman filters is represented with dynamically changing process or measurement noise covariance matrices, respectively notated as  $\mathbf{Q}$  and  $\mathbf{R}$ . Process and measurement noise covariance values, respectively, represent the reciprocal weights of the Kalman filter prediction and the corresponding measurement. The relation of the corresponding noise covariance values defines the resulting weight, given by the Kalman filter (Kalman gain), to the introduced measurement over the filter's own prediction. It depicts how much the given measurement input will be trusted by the Kalman filter over its own prediction. Thus, a desired Kalman filter behavior in sensor fusion may be achieved with the continuous adjustment of process or measurement noise covariance values, while more detailed tuning can be performed by the simultaneous or independent adjustment of both process and noise covariance values. This feature of the Kalman filter is actively used in the proposed ATKF algorithm for vehicle heading estimation, described further in Section 4.4.

More discrete adaptivity of the Kalman filter algorithm can also be performed by dynamically adjusting other components of the algorithm, such as the process model  $\mathbf{A}$  or the control input vector  $\mathbf{u}_k$ . Depending on the discrete states of the observed system, certain components of the Kalman filter may be replaced with more suitable alternatives, which introduce other parameters or use the same parameters differently. Certain processing steps or inputs can also be temporarily excluded from the Kalman filter process under specific conditions, thus adapting to the specific state of the observed system. For instance, in case of confirmed poor input data quality or other specific conditions, the use of the erroneous input data may be ignored, allowing the Kalman filter to proceed by relying only on its own predictions. This adaptivity approach was also used in the developed ATKF algorithm to exclude gyroscope inputs and prevent accumulation of potential drift errors during longer stationary periods.

### 4.3 Kalman Filter for Position Estimation

The study of the Kalman filter algorithm, conducted as part of this research, has also resulted in the implementation of multiple variations of the KF algorithm for different purposes and tasks. One of the side contributions of this thesis includes the implementation

of the Adaptive Extended Kalman Filter algorithm (further referred to as A-EKF) for the UWB AP-TWR (Active-Passive Two-Way Ranging) protocol-based position calculation & filtering, presented in one of the publications by Laadung *et al.* [2].

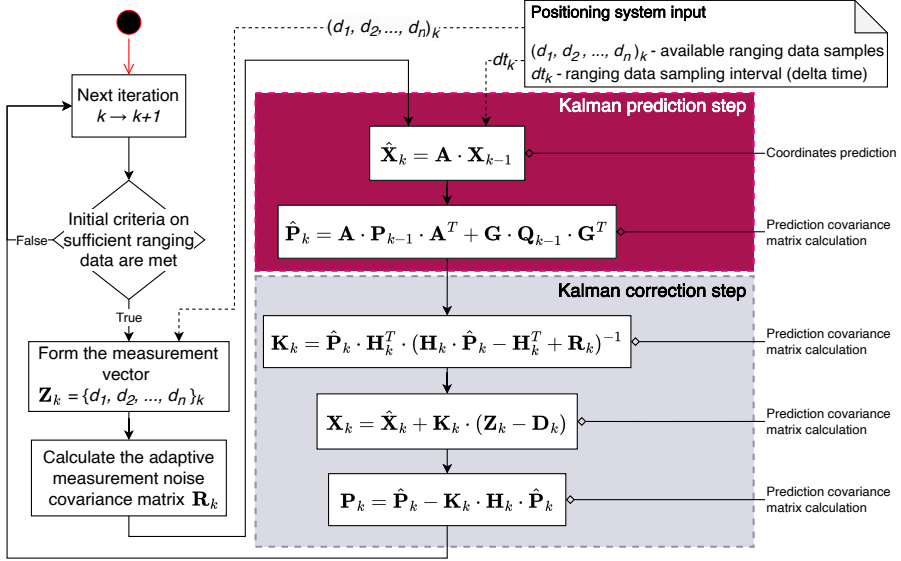


Figure 7: Generalized flowchart of the Adaptive Extended Kalman Filter for the AP-TWR based UWB positioning.

The general flowchart of this algorithm is shown in Fig. 7, where the implemented A-EKF algorithm represents an adaptive filtering approach for UWB ranging data and the automatic calculation of the resulting 3D coordinates using the multilateration technique. The implemented filter adapts to the estimated quality of the input ranging data by iteratively recalculating the measurement noise covariance matrix  $\mathbf{R}_k$  as a Hadamard product of the previously calculated row variance vector  $\mathbf{S}_k$ , distance penalty  $\mathbf{B}_k$  and intermittency penalty  $\mathbf{C}_k$  vectors. As the available ranging information has an over time varying cardinality, one of the key features of this algorithm is the adaptive size of the observation vector  $\mathbf{Z}_k$  and the observation transition Jacobian matrix  $\mathbf{H}_k$ .

Varying cardinality of the observation input vector may also be considered as the additional discrete adaptivity of the A-EKF algorithm with the dynamically changing measurement model over time. In combination with the AP-TWR method, this algorithm has demonstrated a significant, over 3 times improvement in stationary 3D positioning RMSE results in comparison with sole SS-TWR (Single-Sided Two-Way Ranging) and AP-TWR-based positioning. In the tested moment scenario, the A-EKF-enhanced AP-TWR positioning method has demonstrated a ninefold reduction of the peak RMSE errors from 4.5 m to 0.5 m, over both tested sole SS-TWR and AP-TWR methods. These results have confirmed the importance of the Kalman filter adaptivity feature, especially in real-life and dynamic scenarios. The experience gained during the collaborative implementation of the A-EKF algorithm was further used during the development of the Adaptive Tandem Kalman Filter algorithm for vehicle heading estimation, described in the next section.

## 4.4 Adaptive Tandem Kalman Filter Algorithm for Vehicle Heading Estimation

This section covers further advancements in the topic of positioning and inertial data-based vehicle heading estimation, which takes into account the results and conclusions achieved during the research and described in previous sections. These include (advantages and drawbacks) of positioning data use in heading estimation, concluded in Section 4.1, as well as study on the Kalman filter algorithm and its adaptivity features, described in Section 4.2, and their implementation experience, described in Section 4.3.

Further research has resulted in the development of the Adaptive Tandem Kalman Filter (ATKF) algorithm for vehicle heading estimation. This algorithm represents an adaptive version of the Kalman filter algorithm with a custom tandem structure, designed for the vehicle heading estimation through the competitive fusion of the inertial and positioning data. Competitive fusion refers to a sensor fusion configuration, where sensors independently provide the information of the same property, thus allowing to improve overall measurement reliability and accuracy [219]. The competitive fusion configuration was chosen to allow the weighted balancing between the fused positioning and inertial units and to utilize the strengths of both data sources.

This algorithm also contributes with a non-traditional tandem structure of the Kalman filter. A variety of different non-traditional Kalman filter structure options can be encountered in the literature, including augmented [220], dual [221], or sequential [222] versions. These versions consider integration of additional algorithms (augmented) or sections of another Kalman filter (dual) into the Kalman filter structure, while layouts, such as a sequential Kalman filter, consider consecutive data processing by multiple Kalman filters. The proposed tandem structure, on the other hand, separates the Kalman filter correction section into multiple phases, which allows to perform multiple consecutive processing steps of the input data within a single filter iteration.

A thorough description of the proposed ATKF algorithm is provided in Publication III, along with the results of its simulated and experimental tests. This section provides a brief description of this algorithm, the selective results of its experimental testing, as well as the extended results of preliminary simulated tests.

### 4.4.1 Adaptivity Model of the ATKF Algorithm

This subsection provides an extended description of the adaptivity of the designed ATKF algorithm. As the precision of the positioning data-based heading directly depends on the movement speed, this parameter was decided to be used to enable the adaptivity of the designed algorithm. The adaptivity of this Kalman filter algorithm is achieved by dynamically adjusting the corresponding weights in the process and measurement covariance matrices  $\mathbf{Q}$  and  $\mathbf{R}$ , as it was previously described in Section 4.2.3. To calculate the necessary weights for both noise covariance matrices, the ATKF algorithm uses a specifically designed exponential weight function  $f^W$ , defined as follows:

$$f_{exp}^W(v_k, v_{thr}, a, \sigma_{min}, \sigma_{max}) = e^{a \cdot (v_k + b - v_{thr})} + \sigma_{min}, \quad (8)$$

$$b = \frac{\ln(\sigma_{max} - \sigma_{min})}{a}, \quad (9)$$

where  $v_k$  is the ongoing movement speed,  $v_{thr}$  is the corresponding threshold value,  $\sigma_{min}$  &  $\sigma_{max}$  are maximum and minimum noise covariance parameters respectively, while  $a$  and  $b$  represent input and internal function tuning coefficients. The overall increasing or decreasing behavior of the weight function is respectively defined by a negative or positive

value of the tuning input coefficient  $a$ , while the scalar value of this parameter defines the increase/decrease rate. The threshold value  $v_{thr}$  determines the inflection point of the weight function, while noise covariance parameters  $\sigma_{min}$  &  $\sigma_{max}$  define upper and lower limits of the function output  $f_{exp}^W \in (\sigma_{min}, \sigma_{max}]$ . A visualized representation of the proposed exponential weight function for different sample values of the tuning parameter  $a$  is shown in Fig. 8a, which reflects the roles of the main input parameters.

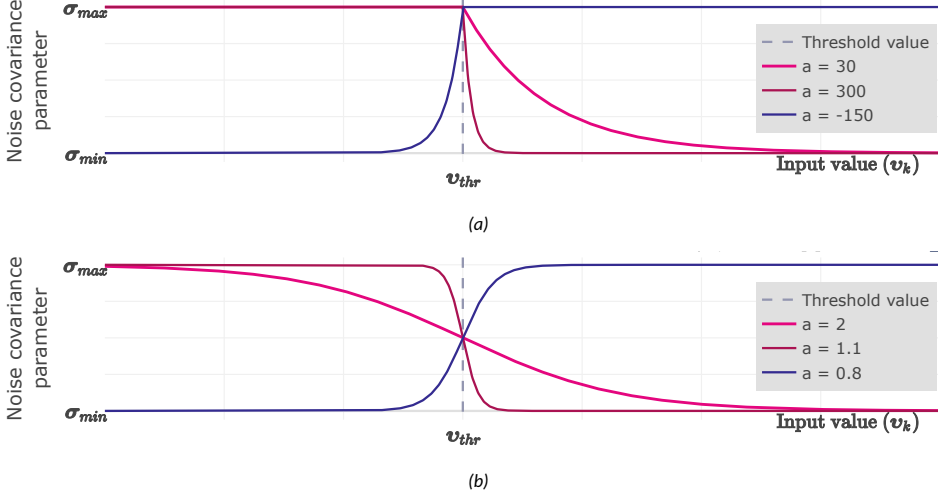


Figure 8: **(a)** Visualized dependence of the proposed exponential weight function on its positive (magenta and dark red) and negative (dark blue) tuning parameter  $a$ , velocity threshold  $v_{thr}$  and noise covariance parameters  $\sigma_{min}$  &  $\sigma_{max}$ ; **(b)** Visualized dependence of the alternative logistic weight function on above 1 (magenta & dark red) and below 1 (dark blue) tuning parameter  $d$ , velocity threshold  $v_{thr}$  and noise covariance parameters  $\sigma_{min}$  &  $\sigma_{max}$  at constant tuning parameter  $c = 0.05$ .

In the proposed algorithm, the exponential weight function is used for a more rapid transition between sensors in their fusion process to minimize the use of the currently unreliable sensor. For a smoother transition between fused sensors' data, the exponential weight function can be replaced with the logistic weight function, expressed as follows:

$$f_{lgs}^W(v_k, v_{thr}, c, d, \sigma_{min}, \sigma_{max}) = \frac{\sigma_{max}}{1 + e^{a_{lgs} \cdot v_k - b_{lgs}}} + \sigma_{min}, \quad (10)$$

$$a_{lgs} = \frac{\log\left(\frac{\sigma_{max}}{c} - 1\right)}{d \cdot v_{thr} - v_{thr}}, \quad (11)$$

$$b_{lgs} = a_{lgs} \cdot v_{thr}, \quad (12)$$

where  $c$  and  $d$  are the input tuning coefficients, while  $a_{lgs}$  and  $b_{lgs}$  are the internal coefficients of the function. The visualized dependence of this logistic weight function for different sample values of the tuning parameter  $d$  and at the constant tuning parameter  $c = 0.05$  is shown in Fig. 8b. This logistics weight function was initially prepared as part of this research for its use in the ATKF algorithm. However, the initial testing of the ATKF algorithm has demonstrated the requirement for a more rapid transition between fused sensors to minimize the use of unreliable sensor data. Thus, the logistics weight function was eventually replaced with the aforementioned exponential weight function.

In the proposed ATKF algorithm, the inverse weights of the used inertial and positioning units are iteratively calculated by using the exponential weight function (8) and,

respectively, used to form the noise covariance matrices  $\mathbf{Q}$  and  $\mathbf{R}$ . The exact structure of these matrices is provided in Appendix 6. The aforementioned noise covariance parameters (inverse weights) are calculated symmetrically for  $\mathbf{Q}$  and  $\mathbf{R}$  matrices by using, respectively, positive and negative tuning coefficient  $a$ . Figure 9 illustrates the fusion weights of positioning data-based (blue line) and inertial data-based (red line) heading information, depending on the movement speed parameter  $v_k$ .

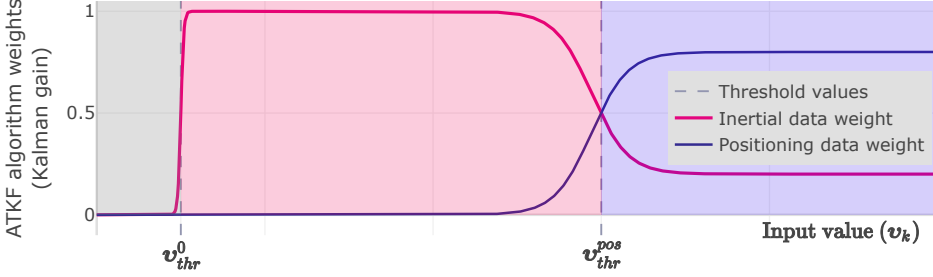


Figure 9: Illustrative dependence of the positioning (blue) and inertial (red) input data weights (Kalman gain) on the movement speed in the Adaptive Tandem Kalman Filter algorithm.

Since at higher movement speed the positioning data-based heading information can be considered more reliable, the corresponding data source is assigned a higher weight, while the inertial unit data source is used in a lower proportion. Below a certain user-defined movement speed threshold  $v_{thr}$ , the positioning data is considered unreliable for accurate heading estimation and is assigned with a minimal weight to avoid its negative impact on the resulting heading estimation. In this case, the ATKF algorithm focuses on the use of inertial gyroscope data. To avoid an unwanted accumulation of the potential drift error in stationary cases, the ATKF algorithm disables the integration of the inertial unit data at movement speeds below the zero movement threshold  $v_{thr}^0$ . This represents an integration of the zero velocity update technique into the Kalman filter as a discrete adaptivity feature, discussed in Section 4.2.3.

#### 4.4.2 Structure of the ATKF Algorithm

This section provides a brief overview of the proposed ATKF algorithm structure, while a more detailed explanation of this algorithm is presented in Publication III. The overall structure of the ATKF algorithm is shown as a flowchart in Fig. 10. The algorithm starts with the Kalman estimation step by evaluating the latest available movement speed  $v_{k-1}$ . In cases when the movement speed of the previous iteration exceeds the defined zero movement threshold  $v_{k-1} > v_{thr}^0$ , the algorithm calculates the predicted model state estimation vector  $\hat{\mathbf{X}}_k$  for the current iteration  $k$ . It is calculated by using the previous state vector  $\mathbf{X}_{k-1}$ , estimation model  $\mathbf{A}$ , state control vector  $\mathbf{u}_k$ , and its conversion matrix  $\mathbf{B}$ :

$$\hat{\mathbf{X}}_k = \mathbf{A} \cdot \mathbf{X}_{k-1} + \mathbf{B} \cdot \mathbf{u}_k, \quad (13)$$

$$\hat{\mathbf{X}}_k = \begin{bmatrix} 1 & 0 & dr_k^{x,y} & 0 & 0 & 0 & 0 \\ 0 & 1 & 0 & dr_k^{x,y} & 0 & 0 & 0 \\ 0 & 0 & 1 & 0 & 0 & 0 & 0 \\ 0 & 0 & 0 & 1 & 0 & 0 & 0 \\ 0 & 0 & 0 & 0 & 1 & 0 & 0 \\ 0 & 0 & 0 & 0 & 0 & 1 & 0 \\ 0 & 0 & 0 & 0 & 0 & 0 & 1 \end{bmatrix} \cdot \begin{bmatrix} x_{k-1} \\ y_{k-1} \\ v_{k-1}^x \\ v_{k-1}^y \\ v_{k-1} \\ \phi_{k-1} \\ \Psi_{k-1} \end{bmatrix} + \begin{bmatrix} 0 \\ 0 \\ 0 \\ 0 \\ 0 \\ 0 \\ dt_k^\omega \end{bmatrix} \cdot [\omega_k], \quad (14)$$

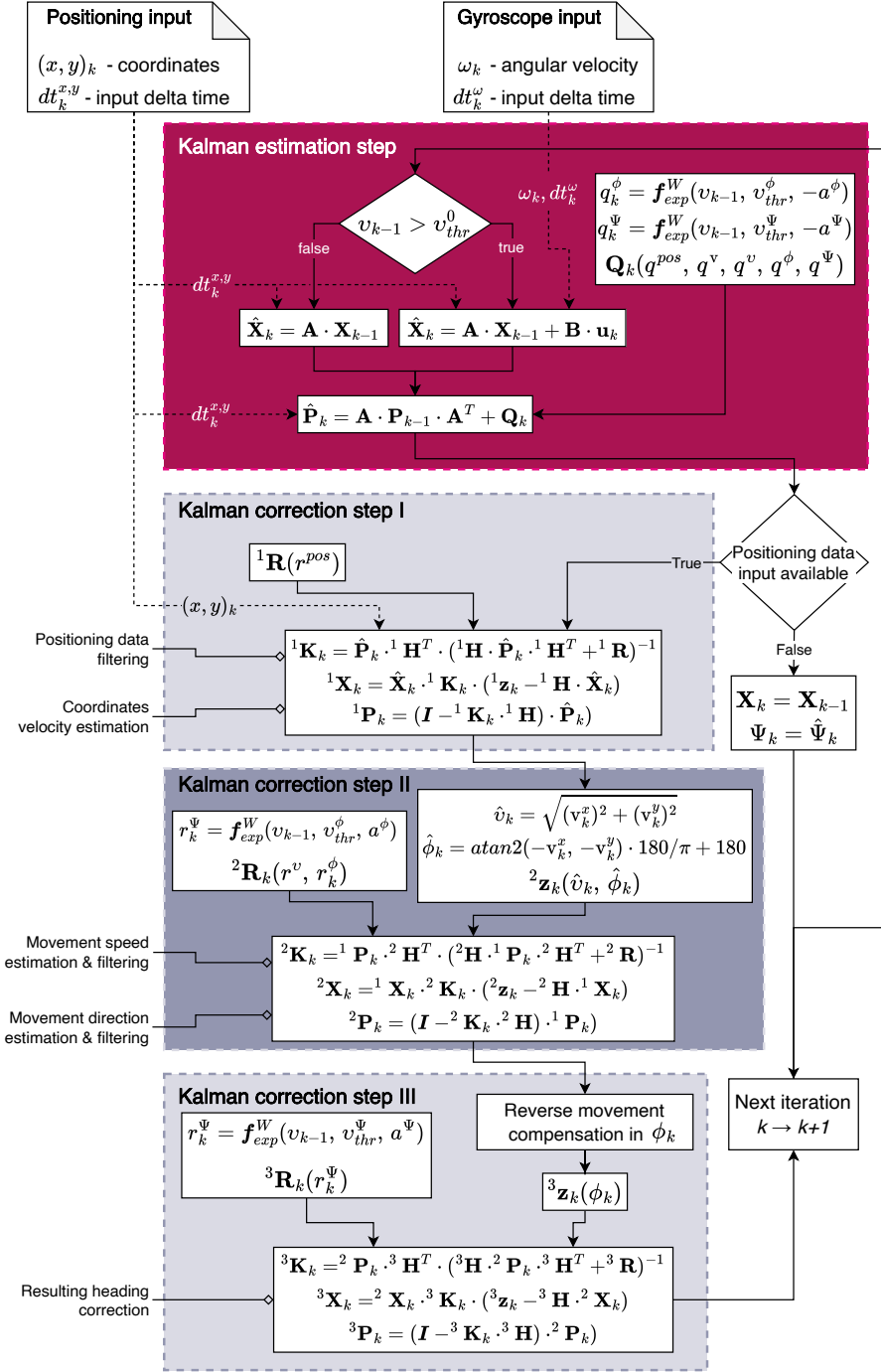


Figure 10: Flowchart of the proposed Adaptive Tandem Kalman Filter algorithm for vehicle heading estimation.



$$\hat{\mathbf{X}}_k = \begin{bmatrix} x_{k-1} + v_{k-1}^x \cdot dt_k^{x,y} \\ y_{k-1} + v_{k-1}^y \cdot dt_k^{x,y} \\ v_{k-1}^x \\ v_{k-1}^y \\ v_{k-1} \\ \phi_{k-1} \\ \Psi_{k-1} + \omega_k \cdot dt_k^\omega \end{bmatrix} = \begin{bmatrix} \hat{x}_k \\ \hat{y}_k \\ v_{k-1}^x \\ v_{k-1}^y \\ v_{k-1} \\ \phi_{k-1} \\ \hat{\Psi}_k \end{bmatrix}, \quad (15)$$

where  $dt_k^{x,y}$  and  $dt_k^\omega$  are respectively the delta-time values of positioning and inertial (gyroscope) data, and  $\omega_k$  is the gyroscope-provided heading angular velocity. In the cases when the positioning data input is not available for the current iteration, a corresponding delta-time value can be replaced with zero. The state vector of the previous iteration  $k-1$  includes the tracked 2D coordinates  $(x_{k-1}, y_{k-1})$ , axial velocities of these coordinates  $(v_{k-1}^x, v_{k-1}^y)$ , the overall movement speed  $v_{k-1}$  and direction  $\phi_{k-1}$  in the local coordinates system, as well as the resulting heading estimation of the previous iteration  $\Psi_{k-1}$ . Algorithm predictions on 2D coordinates and the resulting heading estimation of the current iteration  $k$  are respectively  $\hat{x}_k, \hat{y}_k$  and  $\hat{\Psi}_k$ . The control vector  $\mathbf{u}_k$ , which contains the heading angular velocity  $\omega_k$  data input from the gyroscope unit, is only introduced in case of sufficient movement speed, above the defined threshold  $v_{k-1} > v_{thr}^0$ .

The state estimation covariance matrix  $\hat{\mathbf{P}}_k$  is calculated by using the state covariance matrix of the previous iteration  $\mathbf{P}_{k-1}$ , the estimation model  $\mathbf{A}$  and the process noise covariance matrix  $\mathbf{Q}_k$  as follows:

$$\hat{\mathbf{P}}_k = \mathbf{A} \cdot \mathbf{P}_{k-1} \cdot \mathbf{A}^T + \mathbf{Q}_k. \quad (16)$$

Process noise covariance matrix  $\mathbf{Q}_k$  is assembled by using the predefined constant ( $q^{pos}$ ,  $q^v$ ,  $q^\psi$ ) and dynamically adaptive ( $q_k^\phi$ ,  $q_k^\psi$ ) noise covariance parameters, as it is thoroughly described in Publication III and shown in Appendix 6. By using the exponential weighting function, described in (8), the adaptive process noise covariance parameters are calculated as follows:

$$q_k^\phi = f_{exp}^W(v_{k-1}, v_{thr}^\phi, -a^\phi, q_{min}^\phi, q_{max}), \quad (17)$$

$$q_k^\psi = f_{exp}^W(v_{k-1}, v_{thr}^\psi, -a^\psi, q_{min}^\psi, q_{max}), \quad (18)$$

where  $v_{k-1}$  is the movement speed estimation of the previous iteration,  $a^\phi$ ,  $a^\psi$ ,  $q_{min}^\phi$ ,  $q_{min}^\psi$  and  $q_{max}$  are the predefined tuning parameters of the weighting function. Predefined threshold parameters  $v_{thr}^\phi$  and  $v_{thr}^\psi$  reflect the sufficient movement speed for reliable calculation of the movement direction, based on the positioning data, for its resulting fusion with the inertial data.

In iterations, when positioning data is available, the ATKF algorithm performs three consecutive correction steps, each using the output of the previous step as its input.. This algorithm structure, referred to as Tandem, differs from the traditional Kalman Filter by allowing input measurement data to undergo multiple consecutive processing steps within a single iteration. This ensures the immediate use of the input data, thus reducing delays in algorithmic response. At each correction step, the algorithm recalculates the Kalman gain matrix  ${}^n\mathbf{K}_k$ , state vector  ${}^n\mathbf{X}_k$  and covariance matrix  ${}^n\mathbf{P}_k$  by using measurement model matrix  ${}^n\mathbf{H}$ , the measurement noise covariance matrix  ${}^n\mathbf{R}_k$  and measurement vector  ${}^n\mathbf{z}_k$  of the corresponding correction step  $n$ , as well as state vector and its covariance matrix of the previous step  $n-1$  as follows:

$${}^n\mathbf{K}_k = {}^{n-1}\mathbf{P}_k \cdot {}^n\mathbf{H}^T \cdot ({}^n\mathbf{H} \cdot {}^{n-1}\mathbf{P}_k \cdot {}^n\mathbf{H}^T + {}^n\mathbf{R}_k)^{-1}, \quad (19)$$

$${}^n\mathbf{X}_k = {}^{n-1}\mathbf{X}_k + {}^n\mathbf{K}_k \cdot ({}^n\mathbf{z}_k - {}^n\mathbf{H} \cdot {}^{n-1}\mathbf{X}_k), \quad (20)$$

$${}^n\mathbf{P}_k = (\mathbf{I} - {}^n\mathbf{K}_k \cdot {}^n\mathbf{H}) \cdot {}^{n-1}\mathbf{P}_k. \quad (21)$$

The measurement noise covariance matrix of each correction step  ${}^n\mathbf{R}_k$  is prepared by using the predefined constant and dynamically adaptive noise covariance parameters:  $r^{pos}$  at the first step ( ${}^1\mathbf{R}_k$ ),  $r^v$  and  $r_k^\phi$  at the second step ( ${}^2\mathbf{R}_k$ ), and  $r_k^\Psi$  at the third step ( ${}^3\mathbf{R}_k$ ). The adaptive measurement noise covariance parameters are calculated by using (8) as follows:

$$r_k^\phi = f_{exp}^W(v_{k-1}, v_{thr}^\phi, a^\phi, r_{min}^\phi, r_{max}), \quad (22)$$

$$r_k^\Psi = f_{exp}^W(v_{k-1}, v_{thr}^\Psi, a^\Psi, r_{min}^\Psi, r_{max}), \quad (23)$$

where  $r_{min}^\phi$ ,  $r_{min}^\Psi$ , and  $r_{max}$  are predefined tuning parameters for the measurement noise covariance matrix.

At the first correction step, the ATKF algorithm introduces the positioning data input  $(x_k^{meas}, y_k^{meas})$  in the corresponding measurement vector  ${}^1\mathbf{z}_k$  and performs its filtering by using the previous positioning information. During this process, the ATKF algorithm also updates the hidden variables of the corresponding axial velocities  $v_k^x$  and  $v_k^y$ . Axial velocity parameters are used to calculate the overall positioning data-based movement speed  $\hat{v}_k$  and direction  $\hat{\phi}_k$  as follows:

$$\hat{v}_k = \sqrt{v_k^x{}^2 + v_k^y{}^2} \quad (24)$$

$$\hat{\phi}_k = \text{atan2}(-v_k^x, -v_k^y) \cdot \frac{180}{\pi} + 180 \quad (25)$$

These parameters are then used as input for the second correction step of the ATKF in the corresponding measurement vector  ${}^2\mathbf{z}_k$ . In the second step, the algorithm performs filtering of these parameters, where the estimated movement direction  $\hat{\phi}_k$  is filtered adaptively. The filtered movement direction  $\phi_k$  is then used as an input for the third and the last correction step in the corresponding measurement vector  ${}^3\mathbf{z}_k$ , while the filtered movement speed  $v_k$  will be used in the next algorithm iteration for weights recalculation. As the last correction step, the ATKF algorithm performs the weighted fusion of the calculated movement direction  $\phi_k$  and the gyroscope data-based predicted heading  $\hat{\Psi}_k$ . This fusion results in the ATKF estimated heading  $\Psi_k$ . Key matrices of the designed ATKF algorithm are available in Publication III, as well as in Appendix 6.

#### 4.4.3 Simulations

This section covers the comprehensive simulated testing and comparison of the proposed ATKF heading estimation algorithm and the IMU heading drift correction algorithm (DCA), respectively described in Sections 4.4.2 and 4.1.1. Simulated testing was primarily performed to validate and estimate the expected performance, stability, and robustness of the ATKF algorithm in challenging scenarios, determine its potential limitations, as well as assess its performance in comparison with the developed DCA algorithm. Parameters for both tested algorithms, used in simulations, are provided in Appendix 7. The key take-aways of the achieved simulation results are also presented in Publication III.

As both of the tested algorithms fuse the positioning and inertial information for the heading estimation, conducted simulations evaluate the performance of the aforementioned algorithms at different positioning data error standard deviations and inertial sensor drift rates. Both the DCA and ATKF algorithms were assessed in two simulated movement scenarios shown in Fig. 11a and Fig. 11b, which respectively cover the moderate

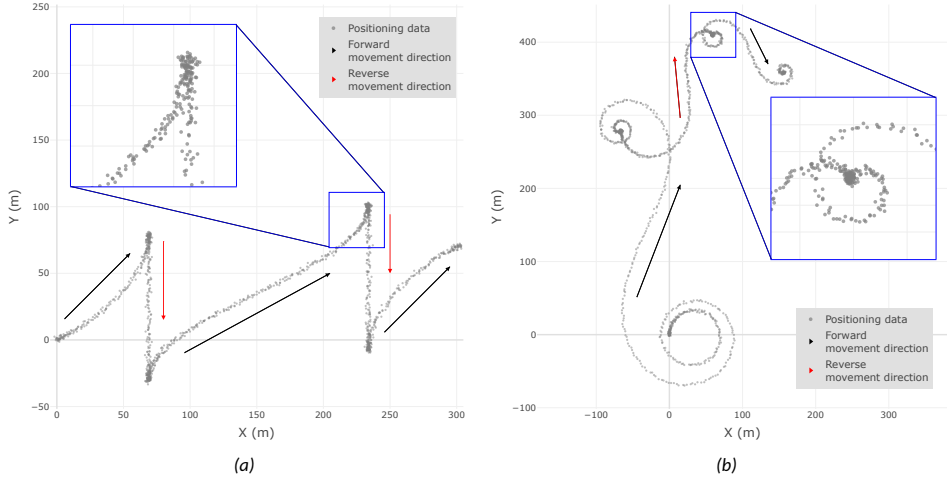


Figure 11: Visualization of simulated movement scenarios I (a) and II (b), respectively describing moderate and high maneuvering intensity; Forward and reverse movement periods of the simulated vehicle are respectively depicted with black and red arrows.

and high maneuvering intensity of the simulated vehicle. Both scenarios cover the varying movement speed in the range of 0.1 - 1 m/s and occasional reverse movement of the simulated vehicle. Simulated positioning and inertial data were respectively provided at 1 Hz and 10 Hz update rates to replicate the different sampling rates of later experimentally used sensors. Simulations were performed separately for 15 different inertial sensor drift rates in the range between 0 deg/s and 1 deg/s, as well as for 22 different positioning data error standard deviations between 0 m and 1.5 m. The selected range of simulated inertial data drift rates was chosen primarily to evaluate the performance of the tested algorithms at very high levels of gyroscope drift. Nevertheless, according to the literature and practical observations during this research, the expected drift rates of MEMS gyroscope units often do not exceed the level of 0.1 deg/s [83, 85, 74, 77, 81, 121].

The selected range of positioning data error standard deviations was chosen in accordance with the aforementioned movement speed of the simulated vehicle. For instance, at the highest simulated movement speed  $v_{max} = 1$  m/s and the update rate of 1 Hz, the distance traveled between two positioning data samples is  $\Delta^{pos} = 1$  m. In this scenario, at the positioning data error of  $\epsilon^{pos} = 1$  m and above, the actual movement becomes frequently indistinguishable from the positioning data noise. This significantly increases the uncertainty of positioning data-based heading estimation, which is expected to critically affect the heading accuracy and precision.

As it was previously illustrated in Fig. 3, the precision of the positioning data-based heading is directly proportional to the movement speed, as well as inversely proportional to the positioning data error and update rate. The dependence of the positioning data-based heading error on the movement speed at the uniformly distributed positioning data error with the constant magnitude of  $\epsilon^{pos} = 1$  m and update rate of 1 Hz is illustrated in Fig. 12a. The corresponding mean absolute heading error (magenta), heading RMSE (dark red), and heading error standard deviation (dark blue) are shown with the respective graphs. The uniformly distributed positioning data error with a constant magnitude was used in this example to clearly outline the maximal expected positioning data-based heading error

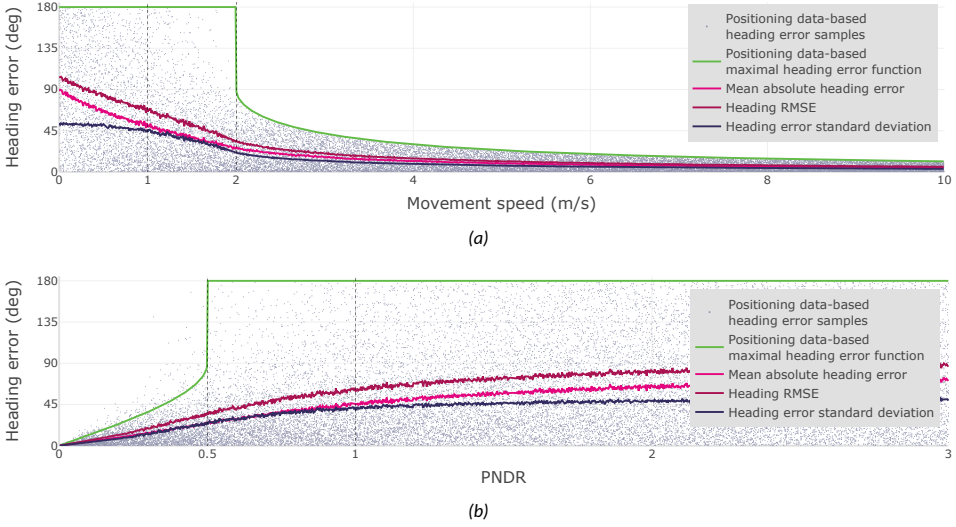


Figure 12: Visualized dependence of the positioning data-based heading error on **(a)** movement speed and **(b)** PNDR ratio. Mean absolute heading error, heading RMSE, heading error standard deviation, and maximal heading error function are respectively shown with magenta, dark red, dark blue and green lines.

depending on the movement speed. In Fig. 12a, this dependence is visualized with the green and can be described with the following function:

$$\varepsilon_{max}^{\phi} = \begin{cases} \arccos\left(\frac{\sqrt{(\Delta^{pos})^2 - 4 \cdot (\varepsilon^{pos})^2}}{\Delta^{pos}}\right) \cdot \frac{180}{\pi}, & \text{if } v > \frac{2 \cdot \varepsilon^{pos}}{dt^{x,y}}, \\ 180, & \text{if } v \leq \frac{2 \cdot \varepsilon^{pos}}{dt^{x,y}}, \end{cases} \quad (26)$$

$$\Delta^{pos} = v \cdot dt^{x,y}, \quad (27)$$

where  $\varepsilon_{max}^{\phi}$  is the maximal positioning data-based heading error in degrees,  $\varepsilon^{pos}$  is the positioning data error magnitude, and  $\Delta^{pos}$  is the absolute distance, traveled at the given movement speed  $v$  in the delta time period  $dt^{x,y}$  between positioning data samples.

To further represent the potential error of the positioning data-based heading within this work, the Positioning-Noise-to-traveled-Distance Ratio (*PNDR*) metric is introduced. This metric reflects the impact of the positioning data error on the heading estimation at the particular movement speed and positioning data update rate. For the normally distributed positioning data error, it can be devised as follows:

$$PNDR = \frac{\sigma^{pos}}{\Delta^{pos}} = \frac{\sigma^{pos}}{v \cdot dt^{x,y}}, \quad (28)$$

where  $\Delta^{pos}$  represents the absolute distance, traveled at the given movement speed  $v$  in the delta time  $dt^{x,y}$  between the positioning data updates, while  $\sigma^{pos}$  represents the standard deviation of the positioning data noise errors.

To be more representative in case of the real-life data, the *PNDR* metric presumes a normal distribution of positioning errors and thus, is based on the positioning error standard deviation parameter  $\sigma^{pos}$ . The key values of the *PNDR* metric are 0.5 and 1. At  $PNDR \geq 0.5$  two neighboring erroneous positioning data samples may occur at the exact

same coordinate, thus significantly affecting the positioning data-based heading estimation, while the possible heading error may reach 180 degrees. At  $PNDR < 0.5$ , on the other hand, the heading error is primarily not expected to exceed 90 degrees. At  $PNDR$  values beyond 1, the tracked movement potentially becomes indistinguishable from the positioning data noise errors, thus preventing the use of the positioning information for reliable movement direction tracking.

The expected positioning data-based heading error dependence on the  $PNDR$  ratio in case of the normally distributed positioning data errors is depicted in Fig. 12b, along with corresponding mean absolute heading error (magenta), heading RMSE (dark red), and heading error standard deviation (dark blue). The maximal positioning data-based heading error function, previously defined in (26), is shown with a green line. It can be reparametrized as a function of the  $PNDR$  parameter:

$$\varepsilon_{\max}^{\phi} = \begin{cases} \arccos(\sqrt{1 - 4 \cdot PNDR^2}) \cdot \frac{180}{\pi}, & \text{if } PNDR > 0.5 \\ 180, & \text{if } PNDR \leq 0.5 \end{cases} \quad (29)$$

Therefore, the positioning data-based heading error decreases with an increasing movement speed as the impact of the positioning data noise becomes negligible. In the performed simulated testing, the movement speed varies between 1 m/s and 0.1 m/s, which corresponds to the accordingly changing  $PNDR$  ratio between  $N$  and  $N \times 10$ . Further discussed results of the simulation test campaign are provided for the lowest  $PNDR$  value of this range (i.e.,  $N$ ). For example, during simulations performed at a  $PNDR$  of 0.6, the Positioning-Noise-to-Traveled-Distance Ratio varied between 0.6 and 6. A set of 50 simulation iterations was performed for each combination of different positioning data error standard deviation levels and different inertial data drift rates. This results in 16,500 simulations for each of the two tested algorithms and for each of the two simulated movement scenarios, thus totaling 66,000 simulations.

Figure 13 visualizes the averaged median absolute heading error results of 50 simulation iterations for each of the two tested algorithms (column-wise) and at each of the two simulated scenarios (row-wise). Additional results on the achieved mean absolute heading error, heading RMSE, Mean Absolute heading error Deviation (MnAD), Median Absolute heading error Deviation (MdAD), and heading error standard deviation are available in the same format in Appendix 8.

As shown in Fig. 13a, in the case of the first simulated movement scenario of Fig. 11a, the tested drift correction algorithm has demonstrated a rather stabile performance at sub-0.6 levels of  $PNDR$ , by primarily keeping the heading accuracy at below 10 degrees level. In this case, only a minor growth of the median absolute error in the estimated heading can be observed with the growing inertial data drift rates. At the above 0.75  $PNDR$ , the drift correction algorithm has demonstrated a rapid performance drop, which is explained by the consistent false detection of the reverse movement. This overall behavior of the DCA algorithm is caused by its high reliance on positioning data in the gyroscope drift correction.

Figure 13b shows the performance of the ATKF algorithm in the same simulated movement scenario. The obtained results indicate a significant stability of the ATKF algorithm in a wide range of tested gyroscope drift and  $PNDR$  ratios. In this case of moderate maneuvering intensity, the ATKF algorithm was able to consistently estimate the heading of the simulated vehicle with a sub-3.5 degrees median absolute error at  $PNDR$  ratios up to 1 and at the inertial data drift rates up to 0.9 deg/s. At higher positioning data noise ratios and higher inertial drift rates, the ATKF algorithm may experience occasional performance drops, primarily caused by false detections of reverse movement. In comparison with the

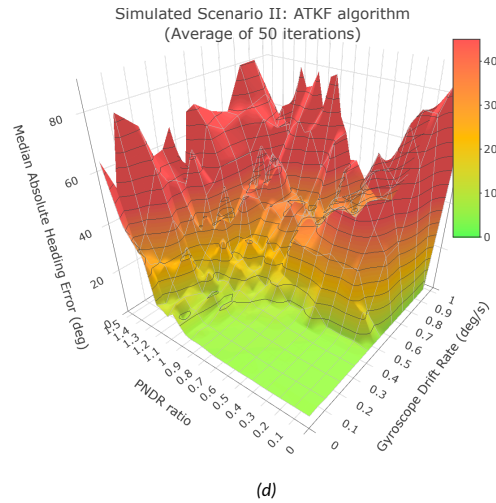
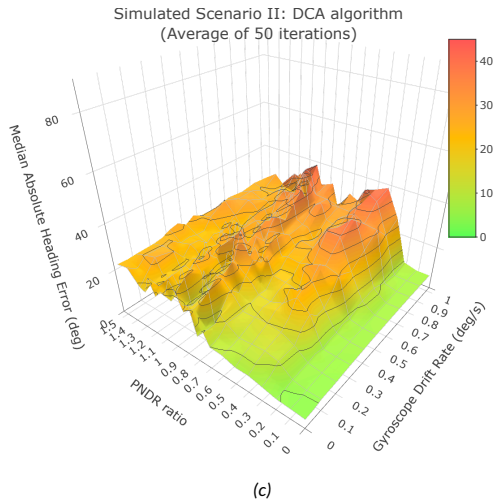
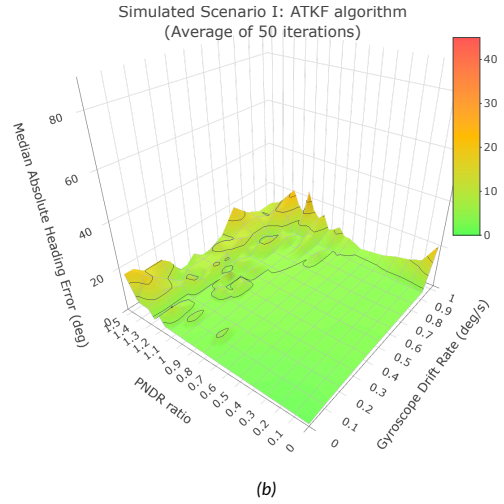
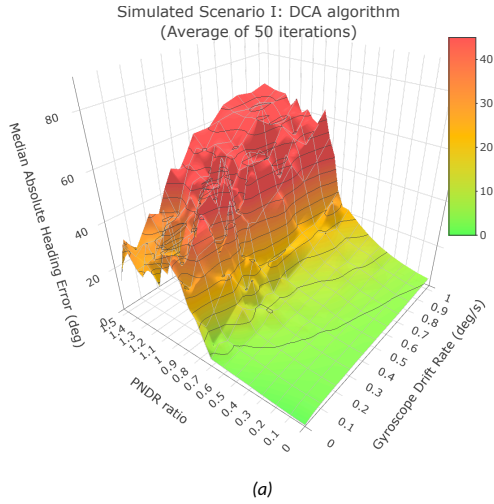


Figure 13: Averaged results on the median absolute error in the simulated vehicle heading estimation by DCA (left) and ATKF (right) algorithms in movement scenarios I (top) and II (bottom), at different combinations of PND ratio and gyroscope drift ratios.

drift correction algorithm, the ATKF algorithm demonstrated exceptional stability and high performance almost at the entire range of covered positioning data noise and gyroscope drift rates.

The second simulated movement scenario, shown in Fig. 11b, represents the vehicle movement with continuous and intense maneuvering to maximize the potential impact of errors present in the positioning and inertial data, thus pushing both tested algorithms to their limits. Figure 13c shows the performance of the drift correction algorithm in this simulated scenario. Similarly to the first simulated scenario, the DCA algorithm shows a stable and consistent performance in the case of low noise positioning data with a below 0.2 *PNDR* ratio, regardless of the inertial data drift error rate. In the case of highly precise positioning information, this algorithm was able to reduce the median absolute error of the tracked heading to the sub-8-degree level. At higher positioning data noise levels of beyond 0.2 *PNDR* rates, the DCA algorithm has shown a significant performance decrease, caused by the combination of even moderate positioning errors and intense maneuvering. It is explained by the high sensitivity of this algorithm to the intense maneuvering, as the inertial heading drift corrections in the DCA algorithm are performed only during the movement in a straight line. Thus, during the intense maneuvering, even relatively moderate positioning errors prevent the effective use of positioning data for reliable heading drift correction. In this case, the drift correction algorithm primarily proceeds with the uncorrected gyroscope heading output. This indicates a significant reliance of this algorithm on positioning data quality and makes it mainly effective in combination with highly precise positioning systems.

The performance results of the ATKF algorithm in the case of the intense maneuvering scenario are reflected in Fig. 13d. This algorithm has demonstrated significant stability, reliability, and high performance in the vehicle heading estimation at the realistically encountered positioning data noise and inertial drift rates. In this scenario, the ATKF algorithm was able to reliably estimate the vehicle heading with a 6-degree median absolute heading error at the gyroscope drift ratio up to 0.4 deg/s and at a sub-1 *PNDR* ratio. As these ranges are noticeably beyond the practically expected positioning and inertial data error rates, this allows to expect the high performance of the ATKF algorithm even in the case of possible drops in positioning and inertial data quality. Due to the intense maneuvering, however, at the inertial data drift rates beyond 0.4 deg/s and at the positioning data noise levels beyond 1.1 *PNDR* ratio, the ATKF algorithm experiences a significant performance decrease. It is caused by the failure of the reverse movement detection mechanism in moments where the intense maneuvering can scarcely be distinguished from extensive positioning errors and gyroscope drift rates. Nevertheless, in the case of highly challenging movement scenarios, the ATKF algorithm has demonstrated significant advantages in stability, reliability, and overall performance over the drift mitigation algorithm.

Figures 14a and 14b respectively show graphs of both ATKF (green) and DCA (blue) algorithms' performance in simulated scenarios I and II, exclusively at realistically expected gyroscope measured heading drift rate of 0.05 deg/s. Results include the averaged median absolute errors in heading estimations by both algorithms, depending on different *PNDR* ratios, along with their respective 95% confidence intervals, depicted with corresponding colored areas. The dashed red line reflects the median absolute error of the sole gyroscope-provided heading. The shaded gray area at *PNDR* ratios above 1 covers the cases when the actual movement of the tracked object becomes occasionally indistinguishable from the positioning data noise, therefore making the positioning data unreliable for heading estimation. These results additionally demonstrate the reliability of the ATKF algorithm at realistic inertial data drift rates, especially in cases of moderate ma-

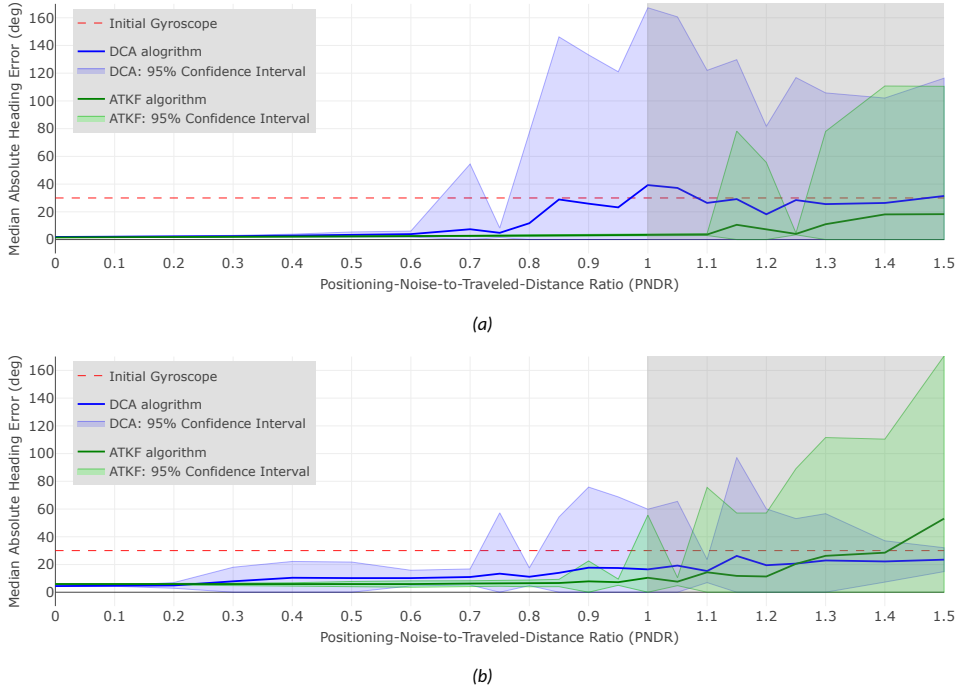


Figure 14: Averaged results on the median absolute Error of the simulated vehicle heading estimations by Drift Correction algorithm (blue) and ATKF algorithm (green) with their corresponding 95% confidence intervals at 0.05 deg/s gyroscope heading drift rate, different  $PNDR$  ratios, and in two different movement scenarios I (a) and II (b).

neuvering intensity and even at the  $PNDR$  ratios beyond 1, as it is shown in Fig. 14a. In cases of highly intense maneuvering, the ATKF algorithm demonstrates similar stability and high performance even at  $PNDR$  ratios up to 0.9. Simulation results, performed at 0.5 and 0.75  $PNDR$  ratios for both tested algorithms and both movement scenarios, were included in Publication III.

#### 4.4.4 Experimental Testing

The proposed ATKF heading estimation algorithm was experimentally tested as part of the full-scale indirect tracking test campaign to validate the results of the simulated tests, described in the Section 4.4.3, and to assess its performance with real-life data and realistic movement scenarios. The thorough description of the conducted  $\sim 14$ -minute-long test campaign in the context of the main research topic is provided further in Section 5.4.1. The movement path of the tested scenario is shown in Fig. 21f in gray. It reflects various aspects of typical forklift operation, including relatively low speeds, varying maneuvering intensity such as sharp turns, instances of reverse movement, occasional stops, and extended periods of idling.

A comprehensive analysis of the proposed ATKF algorithm performance in real forklift heading estimation, along with its comparison against one of the state-of-the-art algorithms, sole gyroscope, and sole magnetometer sensor, is provided in Publication III. This section of the thesis extends the analysis of the results by additional comparison of the ATKF algorithm performance with the earlier mentioned IMU heading drift correction al-



gorithm (DCA), described in Section 4.1.1, as well as a group of additional, magnetometer-based state-of-the-art algorithms, mentioned in Section 2.2.3, such as NMNI algorithm [103], magnetometer-based complementary [223], Madgwick [224, 225] and Mahony [226, 225] filters. To assess the performance of the magnetometer unit and magnetometer-based algorithms in real industrial applications, the corresponding data was collected by using a 13-bit magnetometer sensor available on the BNO055 IMU unit. In suitable environmental conditions, the used magnetometer sensor is expected to provide the heading estimates with a declared accuracy of  $\pm 2.5$  degrees. Tuning parameters of the designed drift correction and ATKF algorithms, used during the test campaign, are provided in Appendix 7. The comprehensive dataset of experimentally collected forklift positioning and IMU data is available at the Taltech database repository [227].

A preliminary evaluation of the positioning and inertial information collected during the test campaign demonstrated the approximate heading drift rate of the used gyroscope at 0.16 deg/s. The collected positioning data demonstrated an approximate error standard deviation of  $\sigma^{pos} \approx 0.022$  m, measured at the moments when the tracked forklift was stationary. The positioning information has also shown an approximate highest movement speed of  $v_{max} \approx 2.2$  m/s, reached by the tracked forklift during the tests. This corresponds to the approximate Positioning-Noise-to-Traveled-Distance Ratio of  $PNDR \approx 0.05$ . According to the simulations' results, discussed earlier in Section 4.4.3, at the above-mentioned parameters of the conducted test campaign (drift rate of 0.16 deg/s and  $PNDR$  ratio of 0.05), both ATKF and Drift correction algorithms are expected to demonstrate a reliable performance at the forklift heading estimation.

### Heading Estimation Results

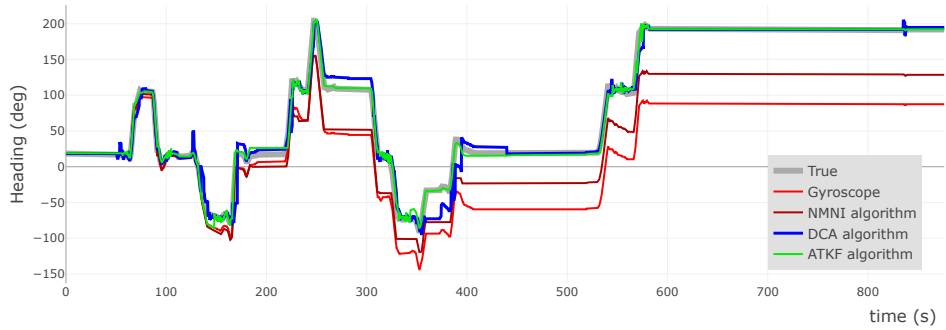
Visualized results on the forklift heading estimation, based on the experimentally collected real-life data and performed by different tested algorithms, are shown in Fig. 15. The corresponding numerical results on the forklift heading estimation accuracy and precision are provided in Table 9 for the entire duration of the test campaign, exclusively for the periods of active forklift movement, as well as at the reference key points. These key points represent locations of specific momentary events, where the forklift was performing payload loading or unloading, and are described in detail in Section 5.4.1.

Figure 15a illustrates heading estimation results provided by the magnetometer-free methods, including the sole gyroscope unit (red), gyroscope-based NMNI algorithm (dark red), as well as positioning and inertial data-based DCA algorithm (blue), and ATKF heading estimation algorithm (green), designed as part of this research. The corresponding numerical results on forklift heading estimation accuracy and precision obtained by these methods are provided in the upper part of Table 9.

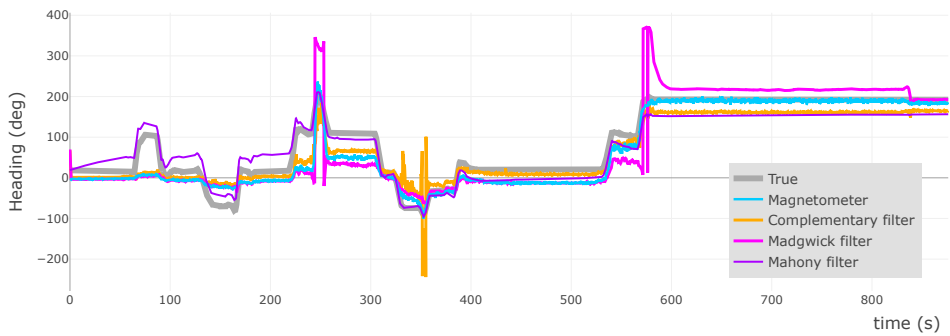
Forklift heading estimation results based on the magnetometer information are illustrated in Fig. 15b. These results include forklift heading estimation performed by the sole magnetometer unit (cyan), as well as magnetometer and inertial (accelerometer & gyroscope) sensor fusion algorithms, such as the complementary filter (orange), Madgwick filter (magenta), and Mahony filter (purple). The corresponding numerical accuracy and precision results are provided in the bottom part of Table 9. The expected true heading graphs on both Fig. 9a and Fig. 9b are illustrated in gray.

#### ***Sole gyroscope-based methods***

The forklift heading, tracked by the sole gyroscope unit, has demonstrated a significant, over 100 degrees drift error by the end of the test campaign, visually observed in Fig. 15a (red). The accumulation of the heading error can be clearly seen at 200<sup>th</sup> second of



(a)



(b)

Figure 15: Graphs of the resulting forklift heading, estimated during the experimental test campaign by magnetometer-free (a) and magnetometer-based (b) methods, including sole gyroscope (red), NMNI algorithm (dark red), DCA algorithm (blue), ATKF algorithm (green), sole magnetometer (light blue), complementary filter (orange), Madgwick filter (magenta), Mahony filter (purple), as well as the expected true heading (grey). Graphs exceed the natural 0 to 360 degrees range for clear visualization purposes.

Table 9: Accuracy and precision results of the experimental data-based forklift heading estimation, performed by the sole gyroscope, gyroscope-based NMNI algorithm, sole magnetometer, magnetometer, and inertial data-based complementary, Mahony & Madgwick filters, as well as designed gyroscope and positioning data-based DCA and ATKF algorithms. Results are provided for the entire test campaign duration, for the periods of active movement, and at the reference key points.

		sole Gyroscope ■			NMNI alg. ■ (Gyro.)			Drift Correction alg. ■ (Gyro. & Pos.)			ATKF alg. ■ (Gyro. & Pos.)		
		overall	moving only	at key points	overall	moving only	at key points	overall	moving only	at key points	overall	moving only	at key points
Accuracy metrics	MdAE	78.3	60.4	42.0	46.7	42.1	31.5	1.1	4.4	2.6	0.9	2.3	1.0
	MnAE	65.5	51.6	44.6	42.4	35.8	29.2	6.0	9.2	5.5	2.8	3.8	1.5
	RMSE	76.0	62.5	58.9	47.8	41.8	37.6	11.8	15.2	7.9	4.9	5.8	2.3
Precision metrics	MdAD	26.2	28.6	36.4	16.9	14.8	26.0	1.1	4.1	2.5	0.8	1.8	0.7
	MnAD	33.4	30.7	36.8	18.2	18.9	22.0	6.5	8.4	5.2	2.8	3.2	1.2
	SD	38.6	35.3	38.6	22.1	21.5	23.7	10.2	12.2	5.7	4.0	4.4	1.7
		sole Magnetometer ■			Complementary filter ■ (Gyro. & Accl. & Mag.)			Mahony filter ■ (Gyro. & Accl. & Mag.)			Madgwick filter ■ (Gyro. & Accl. & Mag.)		
		overall	moving only	at key points	overall	moving only	at key points	overall	moving only	at key points	overall	moving only	at key points
Accuracy metrics	MdAE	20.8	25.3	25.7	28.7	22.0	18.3	29.2	24.6	26.4	25.4	31.1	27.4
	MnAE	23.5	31.4	35.5	28.2	30.4	28.7	27.6	23.3	27.4	36.2	45.0	41.2
	RMSE	32.4	39.9	45.6	34.4	39.0	39.5	30.0	25.9	28.6	46.7	57.2	50.0
Precision metrics	MdAD	13.2	13.9	5.4	11.8	12.3	12.2	9.1	9.5	5.3	5.4	13.7	4.2
	MnAD	16.5	18.7	22.3	13.9	18.8	20.6	10.1	9.3	6.5	20.4	27.9	23.9
	SD	22.4	24.6	28.7	19.8	24.4	27.2	11.7	11.2	8.4	29.5	35.3	28.4

the conducted experiment, where it rapidly exceeds 50 deg. However, in cases when the forklift remained stationary for longer periods of time, such as within the range of 425-525 seconds or after 600<sup>th</sup> second of the test campaign, the gyroscope-based heading estimations were also stable. This indicates the primary accumulation of the drift error during the periods of active maneuvering. This effect reflects the inconsistency of IMU drift errors and makes their mitigation a more complex task, especially in the case of techniques, such as NMNI, focused on drift mitigation during stationary periods.

Numerically, the sole gyroscope unit has demonstrated a significant median absolute error of 78 degrees in the estimated forklift heading with RMSE of 76 degrees and standard deviation of 38.6 deg, which indicates a systematic nature of errors, not caused by occasional outliers. Relatively similar results were achieved exclusively in the case of active movement and at the selected key points. The impact of this level of heading errors on the performance of the indirect tracking method is additionally investigated in the corresponding Publication IV.

The performance of the NMNI algorithm is shown in Fig. 15a with dark red. It can be seen that this algorithm has only mitigated the drift errors that occurred during slow maneuvering or stationary periods, for instance, at the 260<sup>th</sup> second of the test campaign, while the presence of major errors caused by active maneuvering remains the same. However, the inability of the NMNI algorithm to differentiate a correctly measured slow maneuvering from accumulated drift error leads to the mitigation of both components, as for example it can be observed at 190<sup>th</sup>, 370<sup>th</sup>, and 390<sup>th</sup> seconds of the test campaign. This algorithm has reduced the initial drift error of the gyroscope-measured heading down to ~70 deg by the end of the test campaign. As it can be seen from Table 9, the NMNI algorithm has reduced the median absolute heading error of the gyroscope-measured heading down to 46.7 degrees with 22.1 degrees of error standard deviation. Similar to the results of the sole gyroscope, the RMSE results of 47.8 degrees, close to the achieved median absolute error, confirm the systematic nature of heading errors.

#### ***Proposed positioning data-based methods***

In the conducted experimental testing, the proposed drift correction algorithm was able to mitigate the median error of the sole gyroscope-based heading by over 98% down to 1.1 degrees, which additionally confirms the practical performance of this algorithm. The achieved RMSE and standard deviation metrics of 11.8 deg and 10.2 deg accordingly indicate the presence of relatively short-term outliers in the resulting heading estimation. The blue graph in Fig. 15a visually shows the performance of this algorithm, and clearly demonstrates the presence of two distinct outlier types. Momentary peaks, such as those observed at 55<sup>th</sup> and 125<sup>th</sup> second of the test campaign, may be caused by the combination of insufficient movement speed with noisy positioning data (e.g., in cases when *PNDR* ratio is slightly below or close to 1), or significant maneuvering. Momentary peak errors, which occurred during the forklift's gradual slowdown before a complete stop, may persist for the entire stationary period of the forklift. For instance, it can be visually observed at 260<sup>th</sup>, 360<sup>th</sup>, and 390<sup>th</sup> second of the test campaign, where the forklift remained stationary after a gradual slowdown and significant maneuvering. This effect occurs, as the sufficient movement speed is one of the prerequisites for the successful heading error correction in the DCA algorithm.

Numerically, the proposed ATKF algorithm has demonstrated a forklift heading estimation with sub-1 degree median absolute error during the overall test campaign. Achieved sub-5 degree RMSE and standard deviation results also indicate a minor presence of outlier errors in the estimated heading, which reflects the stability of this algorithm. The

performance of this algorithm is visualized with the green line in Fig. 15a. Minor presence of short-term outliers can be seen at 145<sup>th</sup>, 190<sup>th</sup>, 345<sup>th</sup>, and 390<sup>th</sup> seconds of the test campaign, potentially caused by the same factors as in the case of the drift correction algorithm. This confirms the high robustness of this algorithm against poor positioning data, which is essential in real-life applications. A detailed analysis of the ATKF algorithm performance is also available in Publication III. Sub-2 degree accuracy and precision metrics, achieved by this algorithm at the key points, directly reflect a remarkable performance of this algorithm in the context of indirect tracking of industrial products. The corresponding impact of the ATKF heading estimation inaccuracy in the context of the indirect tracking method is further investigated in Section 5.4.2, as well as in Publication IV.

### ***Magnetometer-based methods***

The performance of the sole magnetometer during the experimental testing in the industrial environment is visualized with the cyan graph in Fig. 15b. The magnetometer demonstrated a major, up to 90 degrees, systematic error in the forklift heading estimation, caused by a significant environmental magnetic interference in the industrial area. Occasional accurate heading measurements, however, can be observed at 360<sup>th</sup> and after 580<sup>th</sup> seconds of the test campaign. Additionally, the magnetometer demonstrated a major inconsistency during the first half of the experimental campaign, as it was unable to properly detect the significant maneuvering events, occurred at 70<sup>th</sup>, 140<sup>th</sup>, and 220<sup>th</sup> seconds of the test campaign. The stability of the magnetometer-based heading estimation is also affected by a significant and visually recognizable noise with an approximate magnitude of 10 degrees. Numerical results show a 20.8 deg median absolute error, 32.4 deg RMSE, and 22.4 deg standard deviation, which confirm the presence of a systematic heading error in the magnetometer data. Even though, in comparison with the sole gyroscope, the magnetometer has demonstrated a better performance in heading estimation, the high inconsistency in its response to maneuvering events makes this sensor unreliable for use in the industrial environment.

The performance of magnetometer-based state-of-the-art heading estimation methods is visually demonstrated in Fig. 15b. These methods include complementary (orange), Mahony (purple), and Madgwick (magenta) filter algorithms for magnetometer, accelerometer, and gyroscope fusion. Madgwick and complementary filters visually demonstrate the presence of the overall noise, systematic heading errors, and heading estimation inconsistency, similar to the sole magnetometer. This indicates the primary reliance of these algorithms on the magnetometer data. Mahony filter algorithm demonstrates a more balanced and consistent preference in the forklift heading estimation. Unlike the complementary and Madgwick filter algorithms, this method does not demonstrate the presence of magnetometer noise or provide inconsistent response to the ground truth movement, which may indicate its more gyroscope-reliant nature. Mahony filter, however, shows a significant systematic error of up to 50 deg, especially before 250<sup>th</sup> second of the test campaign, potentially introduced by the magnetometer measurements. Numerical performance results of the corresponding algorithms are provided in the bottom part of Table 9. The aforementioned algorithms have shown relatively similar results in the median absolute heading estimation accuracy in the range of 25-29 deg. The significant presence of systematic error and minor presence of outliers in the Mahony filter heading is also confirmed by lower RMSE and standard deviation metrics of 30 deg and 11.7 deg, respectively. Complementary and Madgwick filters, on the other hand, have respectively demonstrated 34.4 deg and 46.7 deg of estimated heading RMSE, as well as 19.8 deg and 29.5 deg of standard deviation.

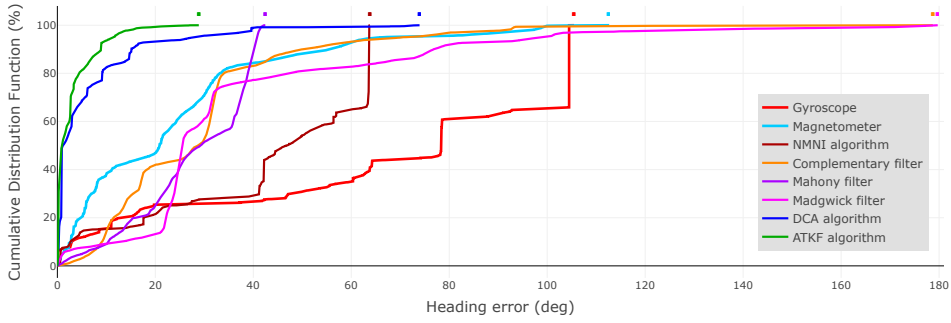


Figure 16: Cumulative error distribution functions of the experimentally tracked forklift heading by the sole gyroscope (red), sole magnetometer (cyan), gyroscope-based NMNI algorithm (dark red), proposed gyroscope and positioning data based drift correction (blue) and ATKF (green) algorithms, as well as magnetometer and inertial data-based of complementary filter (orange), Mahony filter (purple) and Madgwick filter (magenta) algorithms.

Fig. 16 shows cumulative error distribution functions of the experimentally tested forklift heading tracking approaches. The provided graphs are marked with the same color code, as used in Fig. 15 and Table 9. Sole magnetometer and magnetometer-based methods (Madgwick, Mahony & complementary filters) demonstrate a similar overall error presence in their forklift heading estimations, with the slightly lower error presence in the case of the standalone magnetometer. Magnetometer-based fusion algorithms, such as complementary and Madgwick filters, primarily demonstrate a presence of an error pattern, similar to the standalone magnetometer, which also indicates a primary reliance of these algorithms on the magnetometer data. These methods also demonstrate the presence of significant, up to 170-degree momentary errors in the estimated heading. For the Mahony filter, the highest errors in the estimated heading only slightly exceed 40 degrees, which is a significant improvement over the other magnetometer-based methods. The overall slow initial increase of CDF functions in the case of magnetometer and magnetometer-based Mahony, Madgwick, and complementary filters, confirms the presence of significant systematic errors in their heading estimations.

In comparison with other methods, both proposed DCA and ATKF algorithms demonstrate a significantly improved cumulative error distribution. In the case of both algorithms, over 60% of errors in their heading estimations do not exceed 3 degrees. The Drift correction algorithm (blue) demonstrates a higher presence of outlier errors, which do not exceed 75 degrees. Only 7% of errors in the resulting heading exceed 20 degrees, and only 1% exceed the 40-degree level. ATKF heading estimation algorithms demonstrate outstanding performance, where 98% of errors do not exceed 15 degrees with minor outliers reaching sub-29 degrees level.

## 4.5 Discussion

Section 4 covered the main subtopic of this research on the accurate real-time heading estimation of industrial vehicles. With a total of 3 publications, it has answered the research questions **RQ2** & **RQ3**. This section addressed the applicability limitations of the existing state-of-the-art magnetometer-based methods, as well as investigated the effectiveness of positioning and inertial data fusion in reliable and accurate vehicle heading tracking.

The first section of this research has contributed with an algorithmic method for IMU

heading drift correction, designed for the conceptual validation of positioning and inertial data-based heading tracking. Experimental testing of the DCA algorithm has verified the applicability and performance of the positioning data-based approach, which has enabled further advancements in this subtopic. As a side contribution, further research on the state-of-the-art methods and algorithms in this field has resulted in the development of the Adaptive Extended Kalman filter algorithm for the UWB positioning system performance optimization. The last part of this research section contributes with the development of the Adaptive Kalman filter-based algorithmic method for the road vehicle heading estimation. The designed algorithm represents an adaptive Kalman filter with a custom tandem structure, which enhances its real-time performance. The developed ATKF algorithm performs a competitive weighted fusion of the inertial and positioning data-based heading estimations to ensure reliable and accurate vehicle heading tracking, robust to possible erroneous input data.

A comprehensive simulated testing and comparison of both developed DCA and ATKF algorithms has defined their expected performance capabilities and limitations in different scenarios and in cases of poor input data. Both algorithms have demonstrated high performance capabilities in vehicle heading estimation, especially in cases of realistic input data quality and movement scenarios. Experimental testing of both algorithms has verified the simulations' outcomes, demonstrating a high performance of the DCA algorithm and remarkable performance of the ATKF algorithm in the case of real-life data. In comparison with tested state-of-the-art magnetometer-based methods, both of the proposed algorithms have shown over 95% improvement in median absolute error of the estimated heading. The ATKF algorithm has also demonstrated a significant, over 83% improvement in heading estimation RMSE in comparison with magnetometer-based methods and over 58% improvement in comparison with the proposed DCA algorithm. These results have validated high performance expectations of the ATKF algorithm and indicate its remarkable reliability and stability in vehicle heading estimation.

These performance results of the proposed ATKF algorithm are also highly comparable with one of the most recent advancements in this field, presented by Oursland *et al.* in [134] in parallel with this research. In their work, they have also proposed an Invariant Extended Kalman Filter for the inertial and positioning data-based drone heading estimation. According to the available information, the proposed ATKF and the referred InEKF algorithms have demonstrated highly similar results of 4.9 deg and 4.6 deg in terms of heading estimation RMSE. However, in case of the ATKF algorithm, these results were achieved in a significantly longer and complex test campaign, conducted in a real and highly obstructed industrial environment. The referred method, on the other hand, was tested by using the available UTIL dataset, collected in the controlled test environment [228]. Additionally, in comparison with the referred InEKF algorithm, the proposed ATKF algorithm provides a noticeably reduced complexity, as well as additional features, such as adaptivity or compensation for the reverse movement.

## 5 Indirect Tracking

This section resumes the description of the developed indirect tracking method by taking into account the methodology, previously introduced in Section 3, results of the sensors' and technology selection, performed in Section 3.2, as well as the outcomes of the vehicle heading estimation subtopic, described in Section 4. Thus, this section provides the resulting structure of the developed markerless indirect tracking method, introduces the developed algorithm for automatic payload pick-up and drop-down detection, as well as discusses the results of conducted preliminary and full-scale experimental tests.

### 5.1 Resulting Structure & Description of the Developed Method

The flowchart, shown in Fig. 17 reflects the resulting structure of the proposed markerless indirect tracking method. It takes into account the main selected technologies and sensors, proposed fusion algorithms, as well as demonstrates the overall data flow, key steps, and main processing units, such as the forklift onboard MCU (Microcontroller Unit), relay unit, and the main server. The onboard setup includes the data forwarding (relay) unit, used to collect the input data stream of the onboard sensors and immediately forward it to the server by using the established wireless connection (e.g., cellular link).

An additional purpose of the data forwarding unit is to ensure a complete synchronization of the collected & transmitted data. As the relay unit represents a junction point for the collected sensors' data, synchronization is achieved by assigning the corresponding UNIX timestamp to every forwarded data input. Since timestamps are assigned to every sensor's data input by the single relay unit, it ensures complete data synchronization on the server side. Due to the UWB positioning system architecture, its positioning information is initially calculated on the server side and not provided by the onboard UWB tag. To ensure the data synchronization, upon the completion of the ranging process, the UWB tag provides the unique identifier of the performed positioning cycle to the relay unit, which is then similarly assigned with the timestamp. On the server side, this synchronized identifier allows to immediately locate the corresponding positioning results, thus synchronizing the UWB positioning system with other sensors.

Selected sensors are divided into two fusion groups, processed by two separate developed fusion algorithms. Competitive fusion of the positioning and inertial units (first fusion group) is performed on the server side by the proposed ATKF algorithm for vehicle heading estimation, previously discussed in Section 4 and Publication III. The resulting forklift heading information is then used to convert the initial positioning data into the accurate 2D location of the forklift tynes, later combined with the measured tynes' elevation for the resulting 3D coordinates of the fork.

Information from both ultrasonic and wire encoder sensors is collected on demand by the onboard MCU unit and transmitted to the server as a single data output. Complementary fusion of the tynes' elevation and occupancy sensors (second fusion group) is performed by using the A-PDD algorithm, proposed as part of this research and described in Section 5.2 and Publication IV. This algorithm detects the occurrence of a payload pick-up or drop-down event and provides its corresponding status information for further use. Due to the incompleteness of the A-PDD algorithm, this fusion may be immediately performed by the onboard MCU unit and followed by the results transmission to the server along with the sensors' data.

These fusion results reflect the exact moment and stage of the detected pick-up or drop-down event, thus allowing to determine the exact 3D location of the occurred event. It is performed on the server side by using the available forklift positioning and heading



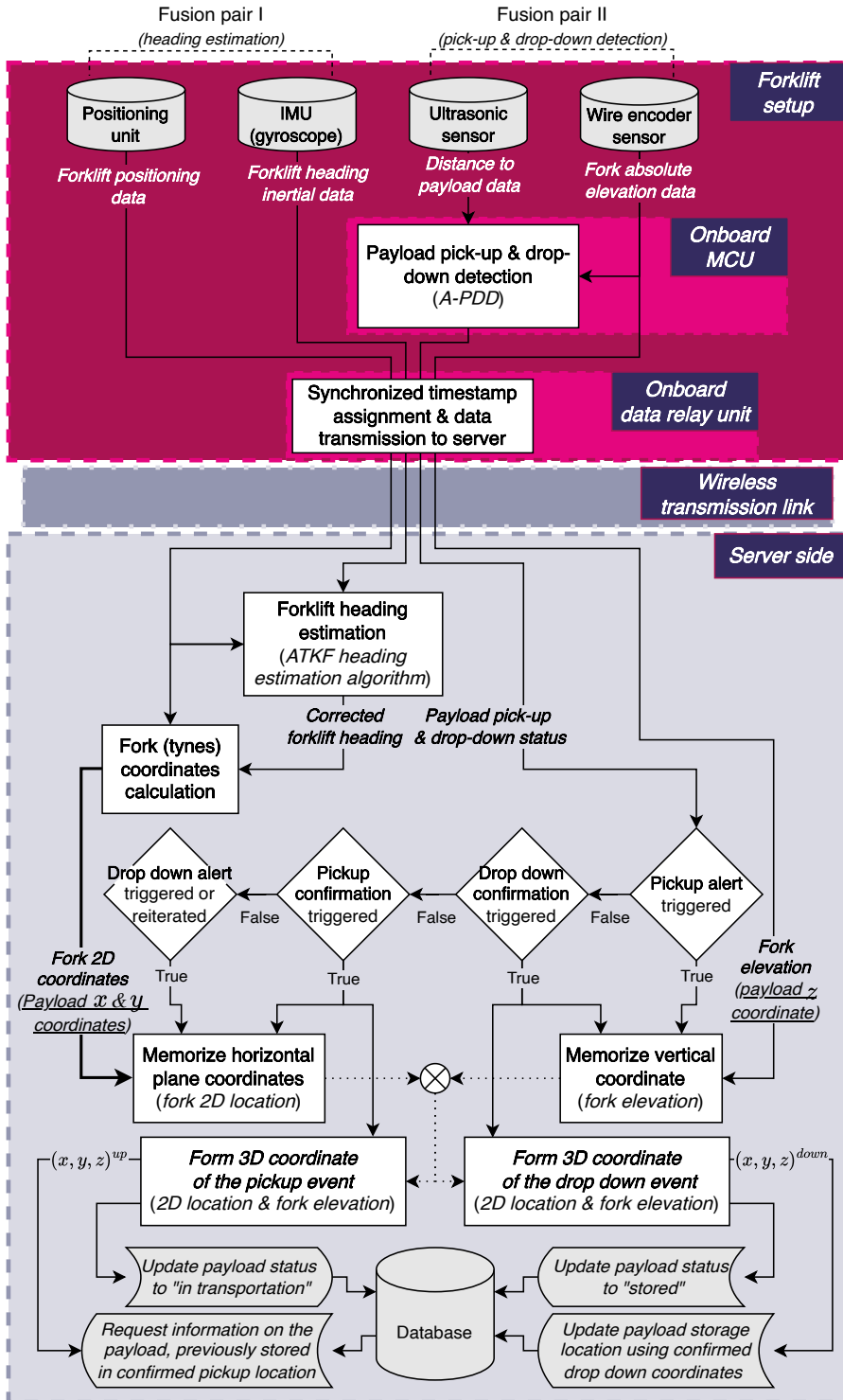


Figure 17: Flowchart of the designed markerless indirect tracking method with sections' separation, based on the components' deployment & processing.



pick-up and drop-down events triggers the corresponding alert, while the second stage confirms the event occurrence. At each stage, the relevant portion of the data is stored and combined into the resulting exact location of the detected event. The flowchart of the A-PDD algorithm is shown in Fig. 18.

The A-PDD algorithm begins with the general filtering of the distance input data sample  $d_k$ , measured by the ultrasonic distance sensor (fork occupancy detection unit). It is done in order to mitigate occasional outliers in the measured distance, caused by minor obstacles and inconsistent ultrasonic signal reflections. Filtering is performed by the introduced hysteresis and is used to distinguish the detected vacancy of the fork area from possible erroneous readings. It is represented with the counter loop, which computes the number of distance measurements  $i_d$  below the distance threshold  $d_{thr}$ , counted within the user-defined range. In this research, the number of distance measurements below the given threshold was counted in the range of 0 to 10. Reaching the maximum or minimum value in the defined range, respectively, indicates consistently and reliably detected presence or absence of the transported payload, while values within the range indicate inconsistent distance measurements. Continuously measured distance below the selected threshold  $d_{thr}$  indicates the object presence within the fork area, thus reflecting tynes' occupancy. Measured absolute tynes' elevation  $h_k$  is used to track momentary elevation changes  $\Delta h$  and detect significant fork movement, which may potentially indicate the particular stage of the payload pick-up or drop-down.

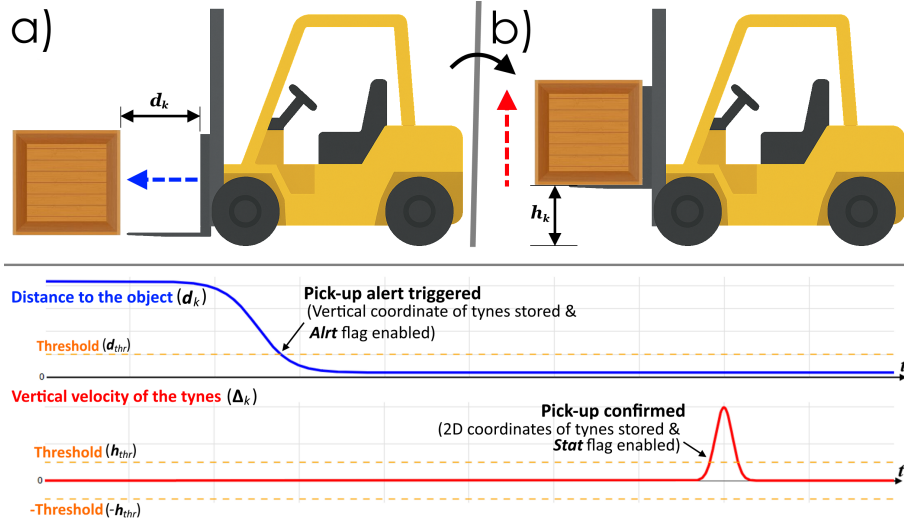


Figure 19: An illustrative example of the payload pick-up sequence, recognized by the A-PDD algorithm, with a graphical representation of the used sensors' data over time: **(a)** Distance to the approached payload, measured by the ultrasonic sensor; **(b)** Payload lifting moment, measured by the wire encoder unit.

Payload transportation status in the A-PDD algorithm is reflected by the **Stat** flag, while the **Alrt** flag indicates the detection of the initial stage of the potential upcoming pick-up or drop-down event. An illustrative example of the pick-up process is shown in Fig. 19 along with the graphs of the corresponding expected inputs from the distance sensor (blue) and elevation sensor (red).

During the pick-up event, the payload is first approached by the forklift with the tynes elevated at the level of pick-up. This stage is detected by the ultrasonic distance sensor,

thus activating the alert flag **Alrt** of the potential pick-up event and initiating the preliminary storage of the ongoing tynes' elevation. In the second stage of the pick-up process, the payload is lifted by the stationary forklift. It is detected by the tynes' elevation sensor, which triggers the merging of the current 2D fork location with its previously measured elevation. This confirms the pick-up event at the resulting 3D coordinates and activates the pick-up status flag **Stat**. Alternatively, instead of lifting the payload, the forklift may move away from it, which is detected by the ultrasonic distance sensor. This cancels the pick-up process, resets the **Alrt** flag, and omits the previously stored tynes' elevation data.

The payload drop-down process is detected in the opposite order. At the first stage of this process, the stationary forklift descends the payload to the storage elevation level, which is detected by the elevation tracking unit. Then the **Alrt** flag is enabled, indicating the potential drop-down event and triggering the 2D drop-down location storage. As the second step of the drop-down process, the forklift moves away from the laid-down payload while the tynes are elevated at the drop-down level, which is simultaneously saved. This confirms the payload drop-down event, combines the previously saved 2D location and elevation of the event for its resulting 3D coordinate, and resets both the **Alrt** and **Stat** flags. The further storage location of the dropped-down payload is updated with the resulting 3D coordinate. Alternatively, triggering the drop-down alert can be canceled by lifting up the payload, whereas the tynes' elevation sensor reports a positive change, which will reset the **Alrt** flag. The continuously updated flags **Alrt** and **Stat** reflect the real-time loading/unloading status of the forklift. These flags represent the output of the proposed A-PDD algorithm and are used in the proposed indirect tracking method. A comprehensive description and detailed truth table for the proposed A-PDD algorithm are available in Publication IV.

### 5.3 Preliminary Testing

The proposed indirect tracking method was initially tested in a down-scaled format to validate the proposed method, as well as to determine the expected performance and possible limitations of this method, prior to its full-scale testing. This section covers the conducted down-scaled preliminary testing and obtained results, which were eventually excluded from Publication IV.

Down-scaled tests were conducted in the outdoor environment by using a moving platform mimicking a forklift maneuvering and payload lifting/transportation functionality, shown in Fig. 20a. The indirect tracking test setup, consisting of sensors previously selected in the Section 3.2, was deployed on the aforementioned platform. The GNSS RTK system with a declared positioning precision of 2 cm was used as a positioning unit [151]. Proposed ATKF and A-PDD fusion algorithms, respectively described in sections 4.4 and 5.2 were used for the real-time heading tracking and automatic detection of payload pick-up & drop-down events accordingly. Two iterations of the same test scenario were performed in the outdoor environment, as shown in Fig. 20b and Fig. 20c. In the test scenario, the down-scaled payload was transported between three predetermined reference spots, marked with magenta roman numerals indicating the sequence of movements, where it was picked up and dropped down. Reference key spots were preliminarily measured by using the laser range finder unit. Results of the indirectly tracked payload pick-up and drop-down locations are respectively shown with green and blue crosses in Fig. 20b and Fig. 20c, while gray reflects the tracked setup itself.

The summarized numerical results of the absolute payload positioning performance achieved during the down-scaled testing are provided in the upper part of Table 10. These results cover the accuracy and precision metrics of the payload's indirect positioning at

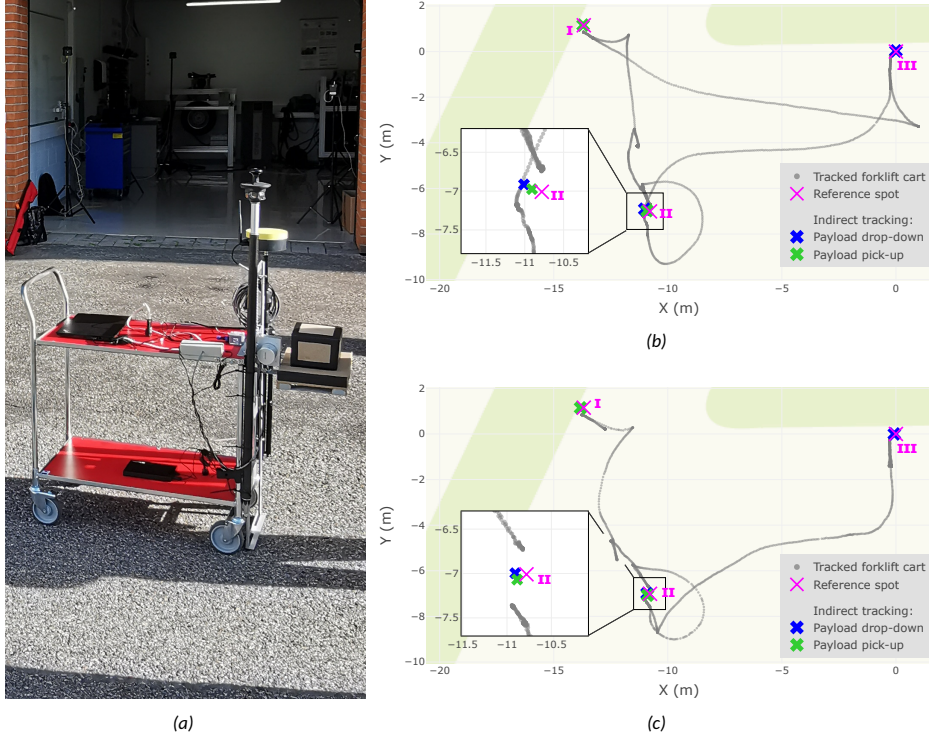


Figure 20: (a) Indirect tracking test setup deployed on the down-scaled forklift platform; Visualized results of the first (b) and second (c) test scenario iterations.

the moments of its pick-up & drop-down. Indirect tracking has demonstrated an average absolute accuracy in the payload positioning of 11 cm with 5 cm of average precision. According to the obtained test results, absolute payload positioning errors of the indirect tracking method have primarily occurred in the two-dimensional plane, with over 70% of these errors caused by external factors. These external factors include the initial error of the used positioning system, which directly impacts the accuracy of indirect tracking, as well as human-related factors, such as the physical misplacement of the payload during its drop-down at the pre-measured reference points. For instance, a noticeable positioning error, primarily caused by the human factor, occurred at reference point II. This error resulted from the absence of a suitable physical marker (reference) to guide accurate payload drop-down, whereas such physical references were present at points I and III. The impact of the human factor at this reference point can be visually observed at the zoomed-in segments on Fig. 20b and Fig. 20c, as well as numerically assessed by using the middle part of the Table 10. At this reference point II, the human factor has caused almost two times higher positioning error in comparison with the results obtained at reference points I & III.

The bottom part of Table 10 shows the obtained repeatability results of the proposed indirect tracking method. Repeatability results reflect the relative positioning error between two indirectly tracked events, which occurred at the same physical location (e.g., pick-up of the earlier dropped-down payload) and thus are not calculated using the true location of the reference point. In the context of the presented preliminary test cam-

Table 10: Averaged results on the absolute (top) and repeatability (bottom) accuracy and precision of the indirect industrial product positioning, including errors caused by the heading estimation and elevation measurement inaccuracy and external factors, as well as performance at each reference spot separately (middle), achieved during the down-scaled testing.

		Accuracy metrics (m)			Precision metrics (m)			Max error (m)
		MnAE	MdAE	RMSE	MnAD	MdAD	SD	
Absolute performance	2D error caused by heading inaccuracy	0.02	0.01	0.03	0.02	0.01	0.02	0.07
	Elevation error	0.02	0.02	0.02	0.01	0.01	0.01	0.03
	2D error caused by external factors	0.11	0.12	0.12	0.04	0.04	0.05	0.18
	<b>3D overall error</b>	<b>0.11</b>	<b>0.13</b>	<b>0.13</b>	<b>0.05</b>	<b>0.03</b>	<b>0.07</b>	<b>0.25</b>
Averaged 3D error	at Reference spot I	0.09	0.09	0.1	0.05	0.05	0.05	0.14
	at Reference spot II	0.16	0.13	0.17	0.05	0	0.05	0.25
	at Reference spot III	0.05	0.05	0.06	0.02	0.02	0.02	0.08
Repeatability performance	2D error caused by heading inaccuracy	0.05	0.05	0.06	0.03	0.03	0.03	0.08
	Elevation error	0.02	0.02	0.02	0.01	0.01	0.01	0.02
	2D error caused by external factors	0.06	0.06	0.07	0.02	0.02	0.02	0.08
	<b>3D overall error</b>	<b>0.1</b>	<b>0.1</b>	<b>0.1</b>	<b>0.02</b>	<b>0.02</b>	<b>0.02</b>	<b>0.12</b>

paign, a pair of pick-up and drop-down events has only occurred at reference point II, and therefore, the repeatability performance was calculated exclusively for these events. Provided results cover the method repeatability accuracy and precision in the overall 3D payload positioning, errors caused by external factors, and inaccuracies in both tracked setup heading and payload elevation. As the repeatability performance is not bound to the ground truth (reference point coordinates), it reflects the expected permanence of the proposed method in real-life applications while neglecting absolute human factor errors.

Since the repeatability performance of the proposed method is measured between two indirectly tracked locations, the impact of positioning errors, caused by external factors, heading inaccuracy, and elevation errors, may be noticeably increased in comparison with absolute performance. This effect can be observed in the case of the repeatability performance results, obtained during the preliminary test campaign (bottom part of Table 10), in comparison with the corresponding absolute performance results (upper part of Table 10). A noticeable increase, approximately by a factor of two, can be observed in the positioning error, caused by inaccuracies in heading estimation. The impact of the external factors on the indirect tracking repeatability performance, on the other hand, has shown a noticeable decrease by a factor of two, which is explained by the exclusion of the human factor. In the preliminary test campaign, the designed indirect tracking method has demonstrated an overall average repeatability accuracy of 10 cm in payload localization with a centimeter-level averaged precision. Nevertheless, the conducted preliminary test campaign has successfully validated the performance of the proposed indirect tracking method, and demonstrated promising results on the indirect positioning accuracy of completely unmarked payload. These results have enabled a further full-scale experimental testing of the proposed method, described in the Section 5.4.

## 5.4 Full-Scale Experimental Testing

Once the performance of the designed markerless indirect tracking method was experimentally validated and confirmed in the preliminary down-scaled testing, described in the previous section, the full-scale experimental test campaign was conducted. A full-scale test campaign was conducted in order to validate and evaluate the performance of the designed method in a real industrial application scenario. This section briefly describes the conducted test campaign and essential results from the corresponding Publication IV regarding the achieved absolute and repeatability performance of the designed method, as well as performance comparison with a direct tracking approach. Sections 5.4.5 and 5.4.3 respectively, provide extra results on the positioning quality comparison of tested direct and indirect tracking methods, and demonstrate the sample output of the designed method on indirectly tracked products. These sections were initially excluded from the original publication to meet the manuscript volume regulations of the chosen venue.

### 5.4.1 Full-scale Test Campaign Description

A full-scale experimental test campaign was conducted in the operating industrial wood manufacturing production site, shown in Fig. 21a, by using the forklift as a material handling equipment to transport the tracked industrial products. The forklift was equipped with the necessary indirect tracking sensors' setup, previously defined in Section 3.2. Proposed ATKF and A-PDD algorithms were respectively used to fuse the available sensors for accurate forklift heading estimation and automatic detection of payload pick-up and drop-down events. The A-PDD algorithm was used with the following heuristically chosen threshold parameters:  $d_{thr} = 275$  mm and  $h_{thr} = 62.5$  mm/s. This test campaign was also used to experimentally evaluate the performance of the proposed ATKF algorithm in forklift heading estimation. Performance results of the experimentally tested ATKF algorithm, along with the used tuning parameters, are covered in Section 4.4.4.

The experimental testing of the proposed indirect tracking method was performed in an indoor industrial area by using the deployed Eliko UWB RTLS system as the positioning unit for the tested indirect tracking method [150]. Figures 21b-d respectively demonstrate the deployment of the wire encoder sensor (b), ultrasonic distance sensor (c), as well as UWB tag and IMU unit (d) on the forklift. During the conducted test campaign, the forklift was operating in the industrial environment, performing the necessary maneuvering to transport a total of two industrial products with the size of  $2\text{ m} \times 1\text{ m} \times 0.5\text{ m}$ , shown in Fig. 21e, within the test area. Products were transported between a total of four reference points, used for their storage. Reference points were manually measured during the test campaign by using a separate UWB tag. The laser range finder unit was used for the preliminary calibration of the UWB positioning system to ensure unbiased results. Figure 21e also demonstrates the independent UWB tag, attached directly to one of the tracked payloads for additional assessment of the performance of the direct tracking approach and its comparison against the designed indirect tracking method. The test campaign covers various scenarios, including both separate and stacked transportation and storage of the tracked products. The resulting forklift route during the test campaign is shown in gray in Fig. 21f, while the aforementioned reference points are highlighted with magenta. Product pick-up & drop-down events that occurred at each reference point are respectively marked in Fig. 21f, and include:

- I Payload A picked up from the top of payload B at the reference point REF1
- II Payload A dropped down at the reference point REF2
- III Payload B picked up at the reference point REF1



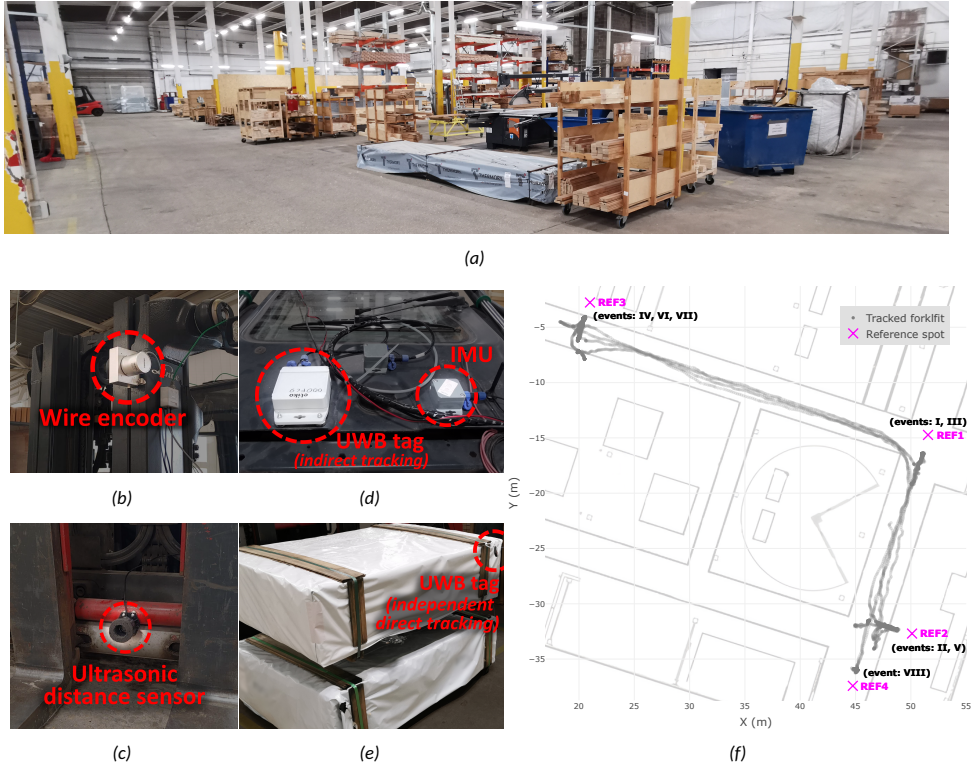


Figure 21: **(a)** Industrial production site environment; Deployment of the indirect tracking sensors' setup on the forklift: **(b)** Wire encoder elevation sensor attached to the forklift mast, **(c)** Ultrasonic distance sensor attached to the base of the forklift tynes (behind the fork area), **(d)** Positioning unit (UWB tag) and IMU attached to the forklift roof; **(e)** Sample industrial products, indirectly tracked during the experimental campaign, and the attached UWB tag to the upper product for its independent direct tracking; **(f)** Visualized forklift route during conducted test campaign (gray) & four reference points (magenta), used for products' storage.

IV Payload B dropped down at the reference point REF3

V Payload A picked up at the reference point REF2

VI Payload A dropped down on top of payload B at the reference point REF3

VII Payloads A & B picked up at the reference point REF3

VIII Payloads A & B dropped down at the reference point REF4

The comprehensive dataset of multi-sensor information collected during the described test campaign is available on the Taltech database repository [230].

#### 5.4.2 Absolute and Repeatability Performance Results

The absolute positioning performance of the proposed indirect tracking method was evaluated at the moments of detected product pick-up & drop-down events, listed in the previous section. Visualized results on the indirect tracking of both industrial products A & B during the full-scale experimental campaign are shown in Fig. 22. Yellow and green dots



respectively depict the measured storage points of payload A & B, while transportation routes of both products are shown with orange and green lines. The dashed yellow-green line represents the simultaneous transportation route of both stacked payloads A & B. Magenta markers represent the pre-measured reference points of payload storage.

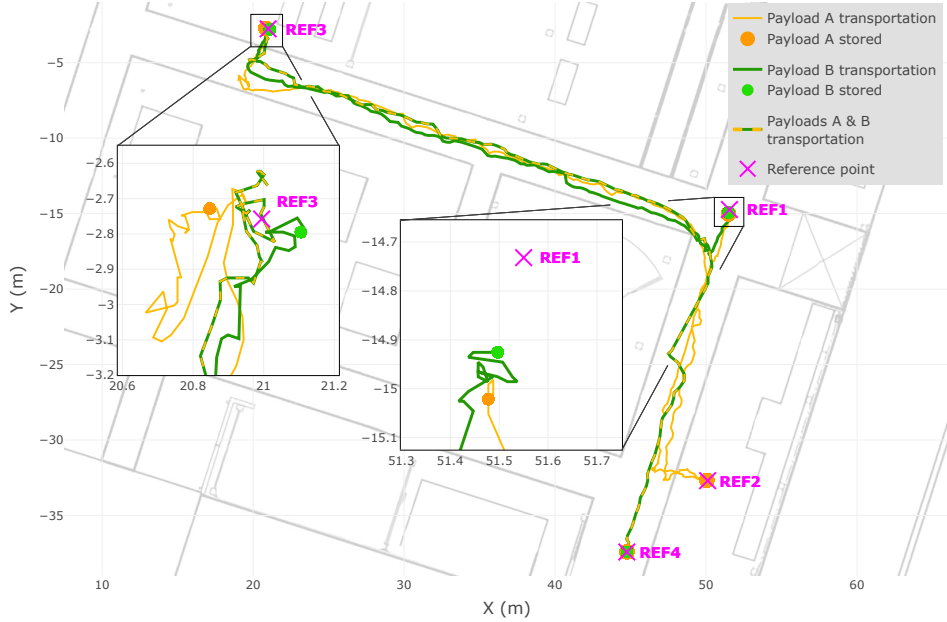


Figure 22: Visualized results on indirectly tracked industrial products A & B during their separate transportation (yellow & green lines), combined (stacked) transportation (dashed yellow-green line), and storage (orange & green dots) at the pre-defined reference points (magenta).

The summarized absolute positioning accuracy and precision results are provided in the upper part of Table 11 along with the corresponding error components, caused by inaccuracies in the heading estimation, elevation measurements, and external factors, such as human factor or the precision errors of the used positioning system. According to the provided numerical results, the designed indirect tracking method was able to localize both industrial products with an average absolute accuracy of 15 cm and an average precision of 8 cm. This method has achieved the absolute positioning RMSE and standard deviation of 18 cm and 9 cm, respectively, resulting in a maximum product positioning error of 30 cm. These achieved errors are primarily caused by external factors, which validates the performance results achieved in the preliminary down-scaled testing and described in Section 5.3. Relatively minor payload positioning errors were caused by inaccuracies in the forklift heading estimations and product elevation measurements. A more detailed evaluation of the forklift heading estimation accuracy during the full-scale test campaign was previously provided in Section 4.4.4.

The bottom part of Table 11 shows the achieved results on the repeatability performance of the proposed indirect tracking method. As it was described for the preliminary tests, the repeatability of the indirect tracking method demonstrates the positioning performance of multiple payload pick-up or drop-down events, which physically occurred in the same location (e.g., pick-up of the earlier dropped-down payload). Since in the presented full-scale test campaign, certain events have occurred at the same location and

Table 11: Averaged results on the experimentally achieved absolute (top) and repeatability (bottom) accuracy and precision of the indirect industrial product positioning, including errors caused by the heading estimation and elevation measurement inaccuracy and external factors, as well as performance at each reference point separately (middle).

		Accuracy metrics (m)			Precision metrics (m)			Max error (m)
		MnAE	MdAE	RMSE	MnAD	MdAD	SD	
Absolute performance	2D error caused by heading inaccuracy	0.04	0.03	0.06	0.03	0.02	0.04	0.14
	Elevation error	0.02	0.02	0.02	0.01	0.01	0.01	0.04
	2D error caused by external factors	0.12	0.08	0.16	0.09	0.07	0.10	0.30
	<b>3D overall error</b>	<b>0.15</b>	<b>0.13</b>	<b>0.18</b>	<b>0.08</b>	<b>0.07</b>	<b>0.09</b>	<b>0.30</b>
Repeatability performance	2D error caused by heading inaccuracy	0.09	0.10	0.11	0.05	0.06	0.06	0.20
	Elevation error	0.04	0.04	0.04	0.02	0.02	0.02	0.06
	2D error caused by external factors	0.13	0.10	0.15	0.06	0.02	0.08	0.29
	<b>2D overall error</b>	<b>0.20</b>	<b>0.18</b>	<b>0.22</b>	<b>0.07</b>	<b>0.08</b>	<b>0.08</b>	<b>0.32</b>

at different elevations (e.g., in case of stacking the payloads), the overall repeatability results are provided for the 2D domain. The proposed indirect tracking method has demonstrated a mean absolute positioning repeatability error of 20 cm with 7 cm of mean absolute deviation and 32 cm of maximal observed positioning error. Similar to the preliminary test campaign, the results of the full-scale testing have shown an expected growth in the repeatability errors in relation to the absolute performance caused by the elevation and heading measurement inaccuracies. This decrease in positioning performance is expected, as instead of the ground truth reference point, the positioning evaluation is performed in relation to coordinates previously measured by the same indirect tracking system. Unlike the results of the preliminary testing, the repeatability and absolute performance comparison did not demonstrate a noticeable decrease in the external factors' impact in the case of the full-scale test campaign.

As the repeatability evaluation primarily neglects the possible human factor, this indicates an impact of different sources of external error, such as the initial precision of the used positioning system. In the case of the conducted full-scale test campaign, the positioning information was provided by the Eliko UWB indoor positioning system with a declared accuracy in the range of 10 cm to 30 cm, which correlates with the obtained absolute external error results [150]. Publication IV provides a more comprehensive evaluation of the absolute and relative performance of the proposed indirect tracking method separately at each pick-up & drop-down event. It also investigates the expected impact of the sole IMU heading drift errors on the indirect tracking performance, thus demonstrating the importance of accurate heading information for the proposed method.

In the optimal/favorable outcome/case scenario, the positioning accuracy results of the proposed indirect tracking method are expected to correspond to the accuracy of the used underlying positioning system. From the perspective of the used positioning system, this will indicate the presence of negligible positioning errors introduced by the proposed method. In the case of the conducted test campaign and the used UWB positioning system, these results were successfully achieved.

From the industrial perspective, the achieved results highly depend on the particular application and the size of the tracked payload. To theoretically eliminate the possibility of the false product pick-up (i.e., pick-up of the neighboring product), the targeted absolute positioning accuracy is expected to remain below a quarter of the payload width (smaller horizontal dimension). In the worst outcome, when the drop-down and later pick-up positioning errors of maximal magnitude align and combine, this corresponds to the highest expected repeatability error below half of the payload width.

Thus, from the perspective of the conducted test campaign, the targeted absolute positioning accuracy results can be estimated from the size of tracked products (2 m × 1 m × 0.5 m) as 0.25 m for horizontal and 0.125 m for vertical positioning. The corresponding theoretically targeted and achieved positioning results are separately provided in Table 12 for vertical and horizontal positioning. These results also include achieved heading estimation accuracy along with the targeted outcome. The targeted heading estimation accuracy corresponds to the targeted horizontal positioning outcome, calculated according to (2) and by using the offset parameter  $\delta_{fork}^{x,y} = 1.52$  m. During the conducted test campaign, the targeted accuracy level was experimentally achieved for the overall horizontal positioning, while the achieved vertical positioning and heading estimation accuracy results have multiple times exceeded the corresponding targeted levels.

Table 12: Theoretically targeted and experimentally achieved absolute and repeatability accuracy results in indirect payload positioning.

	Absolute accuracy		Repeatability accuracy	
	Targeted	Achieved	Targeted	Achieved
2D positioning	25 cm	Avg = 15 cm Max = 30 cm	50 cm	Avg = 20 cm Max = 32 cm
Vertical positioning	12.5 cm	Avg = 2 cm Max = 4 cm	25 cm	Avg = 4 cm Max = 6 cm
Heading estimation	9.4 deg	Avg = 1.5 deg Max = 5.4 deg	18.9 deg	Avg = 4.4 deg Max = 6.1 deg

### 5.4.3 Example of Positioning Information Flow in Indirect Tracking Method

This subsection provides extra information on the output of the proposed indirect tracking method, excluded from Publication IV, and illustrates the updating positioning information of both indirectly tracked payloads during the conducted full-scale test campaign. The key information provided on the indirectly tracked payload is its location at the moment of the detected pick-up or drop-down event, which respectively allows to identify the picked-up product or define the storage location of the dropped-down payload. To cover this side of indirect tracking, location updates for both transported payloads were observed for the sequence of events described in Section 5.4. Three-dimensional locations of each payload were estimated by using their latest available status and location, as well as the location and type of the newly occurred event. Table 13 shows the flow of the payload recognition and location updates by the indirect tracking system during the test campaign. In this example, only the starting coordinates of each payload are initially known, while the further location and status updates of both payloads are fully performed by the indirect tracking method.

Initially, payload A was stacked on top of payload B at the known reference location REF1, as it was previously shown in Fig. 21e. The first detected pick-up event occurred at

Table 13: Over time location update flow of industrial products, indirectly tracked by the designed method during the experimental testing.

Indirect tracking event location & type				Payload A				Payload B			
Event No. & type	x(m)	y(m)	z(m)	Description	x(m)	y(m)	z(m)	Description	x(m)	y(m)	z(m)
0	-	-	-	Starting location:	51.55	-14.73	0.76	Starting location:	51.55	-14.73	0.00
I pick-up	51.48	-15.02	0.77	Distance to event:	0.30 m		-0.01 m	Distance to event:	0.30 m		-0.77 m
				<i>x, y &amp; z match</i> Pick-up confirmed at:	51.48	-15.02	0.77	<i>z below pick-up point</i> Payload remains at:	51.55	-14.73	0.00
II drop-down	50.05	-32.67	1.00	Drop-down confirmed at:	50.05	-32.67	1.00	-	No change		
III pick-up	51.5	-14.93	-0.02	Distance to event:	17.81 m		1.02 m	Distance to event:	0.20 m		0.02 m
				No match Payload remains at:	50.05	-32.67	1.00	<i>x, y &amp; z match</i> Pick-up confirmed at:	51.50	-14.93	-0.02
IV drop-down	21.11	-2.79	-0.02	-	No change			Drop-down confirmed at:	21.11	-2.79	-0.02
V pick-up	50.17	-32.97	1.03	Distance to event:	0.32 m		-0.02 m	Distance to event:	41.89 m		-1.04 m
				<i>x, y &amp; z match</i> Pick-up confirmed at:	50.17	-32.97	1.03	<i>z below pick-up point</i> Payload remains at:	21.11	-2.79	-0.02
VI drop-down	20.85	-2.73	0.75	Drop-down confirmed at:	20.85	-2.73	0.75	-	No change		
VII pick-up	21.01	-2.66	0.04	Distance to event:	0.18 m		0.71 m	Distance to event:	0.16 m		-0.06 m
				<i>z above pick-up point</i> Pick-up in a stack at:	21.01	-2.66	$0.04 + \Delta_z$	<i>x, y &amp; z match</i> Pick-up confirmed at:	21.01	-2.66	0.04
VIII drop-down	44.76	-37.41	-0.02	Drop-down confirmed at:	44.76	-37.41	$-0.02 + \Delta_z$	Drop-down confirmed at:	44.76	-37.41	-0.02

the initial storage location of stacked payloads with slightly below 30 cm horizontal accuracy in relation to the previously saved payload coordinates. In this event, the measured elevation of the corresponding event has matched the elevation of the stored payload A, confirming its pick-up. Even though payload B was also stored at the same 2D coordinate of the detected event, its stored elevation level was significantly below the pick-up location, which has prevented the simultaneous pick-up of the payload B. Payload A was then transported to another storage point REF2, where it was eventually dropped down in event II, which automatically updated its status and location with new storage coordinates.

Coordinates of the detected pick-up and drop-down events III and IV have confirmed the transportation of payload B from the initial location REF1 to another storage point REF3. Similarly, the detected events V and VI have further confirmed the pick-up of the previously dropped-down payload A at reference point REF2, its consequent transportation, and placement on top of payload B at storage location REF3. The coordinates of the detected pick-up event VII have matched the latest storage location of payload B, thus indicating its pick-up. In this case, the location of payload A also matched the pick-up coordinates while its storage elevation was significantly above the pick-up elevation. This indicated the pick-up of payload A as part of the stack for the transportation, and thus, its status and location were correspondingly updated by taking into consideration the elevation difference  $\Delta_z$  between the last known storage locations of stacked payloads. In case of the given example, the elevation difference is  $\Delta_z = |z_{IV}^{payloadB} - z_{VI}^{payloadA}| = 0.75 + 0.02 \approx 0.77$ . The stack of two payloads was then transported and eventually dropped down during event VIII at reference point REF4. Both payloads were assigned with the same drop-down coordinates with consideration of the aforementioned elevation difference in the stack.

#### 5.4.4 Comparison With the Direct Tracking Approach

The conducted test campaign also covers the comparison of the designed indirect tracking method to the direct positioning approach, performed by an independent UWB tag, attached to payload B, as shown in Fig. 21e. Results on a single industrial product positioning by both direct and the proposed indirect tracking methods are shown in Fig. 23. Blue and green lines respectively demonstrate the payload, tracked by direct and indirect methods during its transportation, while blue & green dots reflect the direct and indirect positioning of the payload, stored at reference points (magenta).

Numerical results on the payload positioning accuracy and precision, achieved by both tested methods, are provided in Table 14. The direct tracking method has demonstrated the presence of a significant 50 cm mean error in absolute payload positioning accuracy at a standard deviation of 11 cm. Zoomed-in sections of Fig. 23 visually demonstrate the corresponding positioning performance of the direct tracking approach near reference points REF1 & REF3. The highest observed absolute error of the direct tracking approach at these points reaches 94 cm. During the payload transportation to reference point REF4, the positioning quality of the directly attached tag unit has significantly decreased to an insufficient level for reliable tag localization. For this reason, the positioning of the directly attached tag by UWB positioning system has entirely stopped at the approximate coordinate of (44;-11), and was unable to recover until the end of test campaign. Therefore, the positioning performance of the direct tracking method is only evaluated at reference points REF1 & REF3.

Compared to the direct tracking approach, the proposed indirect tracking method has demonstrated over four times superior absolute payload positioning accuracy. In the case

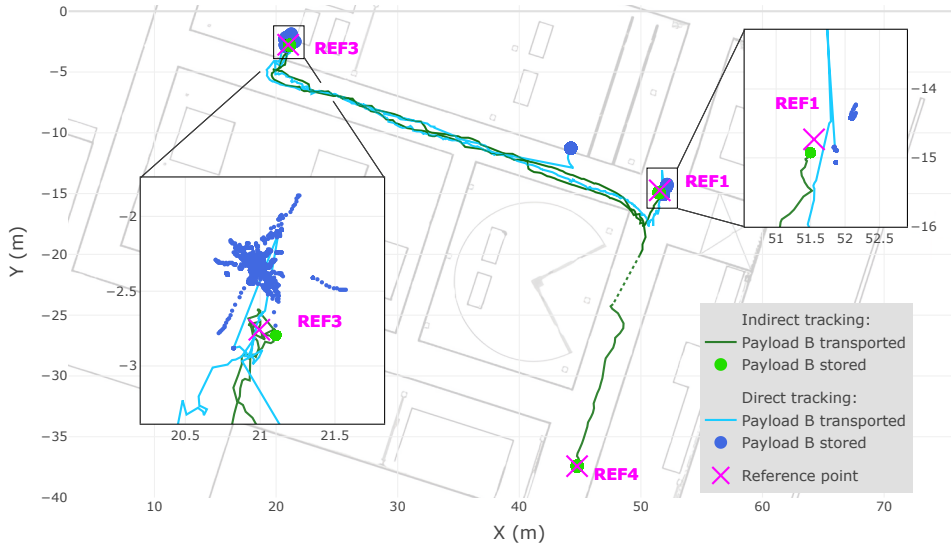


Figure 23: Visualized results on the industrial product B tracking respectively by direct and indirect methods during its transportation (light blue & green lines), and during its storage (blue & green dots) at the pre-defined reference points (magenta).

of tracked payload B, this method has achieved the mean absolute positioning accuracy of 12 cm along with a 7 cm error standard deviation. The highest observed absolute positioning error in the case of the indirect tracking method was 21 cm. A detailed comparison of both methods at each reference point is provided in Publication IV.

Table 14: Results of the industrial product B absolute positioning performance, experimentally achieved by the direct and proposed indirect tracking methods.

	Accuracy metrics (m)			Precision metrics (m)			Max error (m)
	MnAE	MdAE	RMSE	MnAD	MdAD	SD	
Indirect tracking	0.12	0.12	0.13	0.05	0.05	0.07	0.21
Direct tracking (at REF1 & REF3)	0.50	0.50	0.52	0.08	0.06	0.06	0.94

#### 5.4.5 Positioning Quality of Direct and Indirect Tracking Methods

This section provides extensive results on both tested indirect and direct tracking methods' positioning quality evaluation, excluded from Publication IV. This analysis was aimed at further investigation of significant performance differences between these methods observed in the previous section. In the UWB indoor positioning system used for both direct and indirect tracking methods, successful tag localization depends on accurate ranging by a sufficient number of infrastructural UWB units—anchors. The multilateration technique is then used to calculate the resulting coordinate of the tracked tag unit from the obtained ranging information (distances from the tag unit to the available anchors).

In the case of the direct tracking approach, the successful 3D localization of the tag unit requires ranging data from at least four anchor units [231, 232]. It represents the

minimal sufficient number of available rangings needed to successfully calculate the resulting payload location. In the proposed indirect tracking method, on the other hand, the underlying UWB positioning system is only used for two-dimensional forklift location tracking, while the elevation of the mounted UWB tag remains effectively constant due to its fixed position on the vehicle's roof. In this case, the successful forklift positioning in a two-dimensional plane only requires the ranging information from a minimum of three anchor units [231]. These lowered requirements for the available ranging information in case of the indirect tracking method provide increased stability and reliability during possible positioning quality drops, thus representing a significant advantage of the indirect tracking method.

Table 15: Successful positioning rate and availability of UWB anchor units in direct and indirect tracking methods during the entire test campaign and separately at the covered reference points

		REF1	REF3	REF4	Total
Indirect tracking	<b>Successful positioning rate</b>	100%	100%	100%	99.93%
	Average number of anchors used in ranging	5.3	8	5.9	6.7
	Minimal sufficient number of anchors (3) use rate	97.4%	100%	99.8%	99.2%
Direct tracking	<b>Successful positioning rate</b>	3.2%	31.3%	0%	20.8%
	Average number of anchors used in ranging	2.5	3	1.7	2.5
	Minimal sufficient number of anchors (4) use rate	2.9%	5.6%	1.3%	8.5%

Numerical results on the UWB system positioning quality in the case of both direct and indirect tracking methods are provided in the top and the bottom parts of Table 15, accordingly. The table includes the successful UWB system positioning rates, average number of anchor units in line-of-sight (LoS) with UWB tag, as well as the presence rates of a sufficient number of anchors in LoS with the UWB tag throughout the overall experimental test campaign, as well as at each reference point separately.

The indirect tracking method demonstrates the remarkable results of 100% of the successful positioning rate at each covered reference point and 99.93% throughout the entire test campaign. The remaining 0.07% of the unsuccessful positioning rate represents the short-term positioning quality drop which occurred during the payload transportation to reference point REF4 and was visually demonstrated with the dashed green line in Fig. 23 at the approximate coordinates (49;-22). UWB tag, used as part of the indirect tracking method, was successfully positioned by a sufficient number of at least three anchors during 99.2% of the entire test campaign time. On average, this UWB tag was positioned by 6.7 anchor units during the test campaign, which corresponds to 233% of the minimal requirement for the indirect tracking method. Depending on the particular reference point, this UWB tag was successfully positioned by an average number of 5.3 to 8 anchors, which corresponds to beyond 177% of the minimal requirement for this method. Between 97.4% and 100% of the time at the reference points, this tag was positioned by a sufficient number of at least three anchors. Minor occasions of insufficient anchor ranging data were successfully compensated by internal filters and algorithms of the used UWB system. This explains the observed 100% of successful positioning rate at reference points REF1 and

REF4, even though the presence of a sufficient number of anchors in line of sight was not observed in 100% of the campaign time. The heatmap representation of the achieved ranging coverage of the UWB positioning system infrastructure in case of the proposed indirect tracking method is shown in Fig. 30a in Appendix 9.

The direct tracking method, on the other hand, has demonstrated a successful positioning rate of 20.8% throughout the test campaign. According to the obtained results, in only 8.5% of the test campaign time, the UWB positioning infrastructure was able to successfully obtain sufficient ranging information on the UWB tag used for direct product tracking. During the test campaign, the UWB tag, used for direct tracking, was positioned by an average of 2.5 anchors, or 62.5% of the minimal requirement for this method. Depending on the reference point, the UWB tag of the direct tracking method was positioned by 1.7 to 3 anchor units, which represents 42.5% to 75% of the minimal requirement for successful positioning. At reference points REF1 & REF3, the directly attached UWB tag was successfully positioned by a sufficient number of four anchors for only 2.9% and 5.6% of the time, respectively. This has resulted in the respective successful positioning rates of 3.2% and 31.3%. At the reference spot REF4, this UWB tag was occasionally ranged by a sufficient number of anchors for a total of 1.3% of the time, which, however, was insufficient to reestablish the positioning of this tag, and therefore, resulted in 0% of a successful positioning rate. The heatmap of the achieved UWB positioning system ranging coverage in case of the direct tracking method is shown in Fig. 30b in Appendix 9.

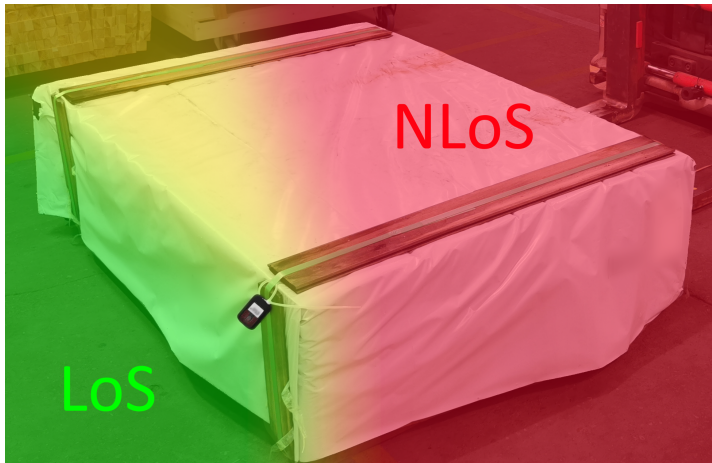


Figure 24: Visualized line of sight limitation of the directly attached UWB tag in the corresponding tracking method, caused by the tracked product.

The poor positioning quality of the direct tracking approach is generally caused by numerous LoS blocking obstacles present in the vicinity of the directly attached tracking unit. Among others, these obstacles also include the used industrial machinery (i.e., fork-lift) and primarily, the tracked product itself as illustrated in Fig. 24. Additionally, these surrounding obstacles also cause a notable factor of the UWB signal reflections, potentially causing significant distortions and errors even in the successfully measured ranging data and affecting the positioning precision [233]. This causes a major decrease in the successful positioning rate of the direct tracking method, which, along with the increased minimum number of required UWB anchor units in the line of sight with the tracked tag, significantly affects the reliability and performance of the direct tracking method, especially in obstructed industrial areas.



The indirect tracking method, on the other hand, has demonstrated an advantage in the overall positioning performance and quality, explained by the physical deployment of the UWB tag. In this method, the UWB tag is installed on top of the  $\sim 2$  m high forklift, above the majority of the potential line of sight obstacles for the UWB anchor infrastructure. An additional advantage of this method is the reduced requirement for the minimum number of anchor units for successful positioning, as the elevation of the forklift-deployed tag remains constant and only requires 2D localization. This ensures a more stable and robust UWB positioning quality for the indirect tracking method.

## 5.5 Discussion

The research described in this section addresses the industrial need for the indirect tracking method, allowing the real-time localization of fully markerless products, payloads & equipment. This work answers the research question **RQ1** and has resulted in the development of a novel method for an accurate real-time 3D localization of industrial products, which takes into consideration different aspects of its real-life application. The developed indirect tracking method is based on widely available and reliable technologies & techniques while avoiding the use of auxiliary, high-data-volume, or computationally complex methods. Since in the proposed method all of the tracked products remain fully unmarked and require no additional hardware or equipment for their localization, this method provides high, theoretically unlimited scalability and minimizes the maintenance requirements with only the equipment deployed on the used industrial machinery. The flexibility of this method also allows for its possible modifications and use with a variety of different industrial machinery, including different lifters, cranes, or other loading & transportation equipment. Additionally, this research also demonstrates the development of the working prototype of the designed indirect tracking setup, as well as its experimental testing in a real application environment, which has demonstrated exceptional performance results. This research has also contributed with the sensor fusion A-PDD algorithm for automatic detection of the payload pick-up and drop-down by the forklift, which may see possible applications in the industry.

## 6 Conclusions & Future Work

This research has addressed the industry need for an accurate real-time indirect localization of fully markerless industrial products, materials & equipment by significantly advancing state-of-the-art in indirect tracking approaches. Based on the research questions, this work has assessed the available indirect tracking techniques to define their existing limitations and gaps, as well as proposed a novel, practically applicable, and fully markerless indirect tracking approach. This work has resulted in the development of a novel method for fully markerless indirect localization of industrial products, materials, and equipment in modern intelligent warehousing and industry. In this method, tracked products do not require the direct attachment of any tracking or identification tags, thus remaining fully unmarked. This provides significant advantages in cost efficiency, energy efficiency, and theoretically unlimited scalability, along with significantly reduced maintenance and computational requirements. Additionally, this research has further contributed to the aforementioned advantages of the developed method by focusing on the use of a minimal set of cost-efficient, computationally incomplex, and reliable sensors and techniques.

In order to fully automate the proposed indirect tracking method, this research has also contributed with the algorithmic sensor fusion method for the automatic detection of payload pick-up & drop-down events, which was effectively used throughout a series of experimental tests. This work has also covered a prototype implementation for the proposed markerless indirect tracking method, its experimental testing and assessment in a real industrial application environment, as well as its comparison with a direct positioning approach. In a series of down-scaled and full-scale experimental tests, the proposed method has demonstrated remarkable results in industrial product positioning accuracy, comparable to the declared performance of the underlying positioning system. Comparison of the proposed indirect tracking method with an equivalent direct positioning approach has also revealed additional advantages of the developed method in overall positioning quality, reliability, and stability. The achieved results have fully validated the performance capabilities of the proposed method, as well as its high potential for practical applicability.

The research on the indirect tracking topic has also demonstrated the necessity of a reliable and accurate vehicle heading estimation, suitable for use in the industrial environment, which has introduced the main subtopic for this research. The primary subtopic of this work has addressed the essential limitation of gyroscope sensors, represented by a significant over time accumulated drift error. This work has also addressed the main limitations of the available and widely used (e.g., magnetometer-based) drift mitigation techniques, preventing their use in certain scenarios and applications, such as industrial land machinery. This research has investigated the possible use of positioning and inertial data fusion for robust vehicle heading estimation. It has resulted in the development of multiple algorithms, including the positioning data-based IMU heading drift correction algorithm (DCA) and the Adaptive Tandem Kalman Filter (ATKF) algorithm for vehicle heading estimation.

The performance of both algorithms was verified and evaluated in a series of simulated and experimental tests, conducted to reflect realistic and challenging movement scenarios of highly maneuverable industrial machinery. Both of the proposed algorithms have experimentally shown a high performance and reliability in real-life data-based heading estimation with over 95% improvement in median absolute heading error over the state-of-the-art magnetometer-based algorithms. The tested magnetometer-based state-of-the-art orientation tracking algorithms, on the other hand, have additionally confirmed their inapplicability in industrial vehicle heading tracking applications. ATKF algorithm has

additionally shown over 83% improvement in the heading estimation RMSE in comparison with tested state-of-the-art algorithms, and beyond 58% improvement over the proposed DCA algorithm. ATKF algorithm has confirmed its overall high stability and robustness in case of poor input data quality, and was eventually used as part of the designed markerless indirect product tracking method.

## 6.1 Research Questions

From the perspective of this research, the defined research questions can be addressed and answered as follows:

- **RQ1:** *What method should be developed in order to provide accurate automatic real-time 3D positioning of markerless industrial products/assets?*

The real-time and accurate localization of fully markerless industrial products is possible during their transportation by the industrial material handling equipment (e.g., forklifts). The real-time location of any transported payload is directly reflected by the real-time location of the product handling unit (i.e., forklift tynes), thus requiring no direct tagging of the transported payload. The real-time tynes' location can be accurately estimated by using the forklift position and heading information, respectively provided by the positioning unit (e.g., indoor or outdoor positioning system) and heading tracking unit (e.g., gyroscope sensor). An algorithmic method is required for the accurate heading estimation and mitigation of the drift errors accumulated by the inertial sensor.

To enable a reliable and precise three-dimensional payload localization, the deployed setup also requires an additional sensor for a continuous measurement of the tynes' elevation. A real-time monitoring of the fork occupancy status also enables the automatic payload loading and unloading detection, thus leading to the entire indirect tracking method automation. An algorithmic sensor fusion method is required to combine the tynes' elevation and occupancy status information for a reliable and real-time recognition of the exact payload pick-up & drop-down moment. The exactly detected location of the pick-up event allows to identify the picked up markerless product by using its latest known storage coordinates, while the exactly detected location of the payload drop-down event represents its further storage location.

*The chosen approach is expected to meet the following criteria:*

- *Cost-efficiency*  
Markerless indirect product tracking should be primarily based on widely available and cost-efficient sensors, and does not require the use of high-end hardware (e.g., military grade inertial sensors, specialized image processing equipment, etc). Although the cost can still vary depending on the chosen positioning system (e.g., UWB, BLE, GNSS, GNSS-RTK, etc).
- *Minimized computational complexity and data processing requirements*  
Markerless indirect product tracking can rely entirely on techniques and sensors that generate low data volumes and require minimal processing complexity—unlike vision- and ML/AI-based methods or computationally intensive algorithms such as Particle Filters.
- *Minimal integration into the mechanisms of industrial machinery*  
Markerless indirect product tracking can be based on sensors requiring minimal integration and adjustments to the used machinery. Sensors and units,

requiring invasive integration into the industrial machinery mechanisms, such as wheel and steering encoders, should be avoided.

- *Seamless deployment with minimal adjustments in an industrial environment or its natural workflow.*

Markerless indirect product tracking requires no adjustments in the industrial environment, such as dedicated storage points and transportation routes, or additional interfering infrastructure (e.g., scanning gates). Indirectly tracked payloads must only be transported by the industrial machinery, equipped with the indirect tracking setup, which represents a potential minor limitation to the natural workflow.

- **RQ2:** *Can the positioning data be reliably used in combination with inertial data for accurate **vehicle heading estimation** in an industrial environment? Will this approach be sufficient for accurate heading tracking of highly maneuverable industrial vehicles?*

Generally, the positioning information can be used for the vehicle heading estimation. However, similarly to other heading tracking methods, the sole positioning information cannot be effectively used for accurate heading tracking due to method-specific limitations. In the case of positioning information, this limitation is represented by its high sensitivity to the movement speed of the tracked vehicle, which prevents a reliable heading estimation at lower movement speeds and especially in stationary cases. Nevertheless, unlike other heading tracking methods, such as drift error accumulating inertial sensors, magnetic interference-sensitive magnetometers, or computationally complex and environmentally sensitive vision & laser-based methods, the positioning data-based approach may be used in any environment and does not accumulate errors over time. This represents a significant advantage of the positioning data-based heading estimation approach in the industrial environment, as well as in the context of the proposed indirect tracking method.

- **RQ3:** *What sensor fusion method should be developed to utilize benefits and overcome limitations/shortcomings of positioning and inertial data in **vehicle heading estimation**? Are the extra/additional supporting sensors required in this method? What is a suitable sensor fusion algorithm for inertial and positioning data-based real-time vehicle heading estimation?* A fusion of the positioning data with a supporting inertial (gyroscope) information allows to compensate the disadvantages and limitations of each separate method and achieve a reliable performance in the heading tracking. In this case, the accumulated errors of the inertial sensor are mitigated by the positioning information, while the gyroscope's immunity to the varying movement speed provides an effective support during intense maneuvering or stationary periods. Minimal environmental sensitivity of this method provides a reliable heading estimation in real-life industrial applications, and requires no additional auxiliary sensors for a reliable heading estimation of industrial machinery.

The required inertial and positioning sensor fusion algorithm must provide a real-time heading estimation with possibly minimal delays to back up scenarios of intense maneuvering, which leads to the required computational incomplexity and immediate use of the newly arriving information. Thus, the positioning and inertial information samples must be processed and applied within a single algorithm iteration. Another key requirement for the fusion algorithm is its possible real-time adaptivity to the ongoing movement speed to effectively mitigate the disadvantages of the positioning information at the lower speeds. Due to the gradually changing

nature of the vehicle heading, the developed fusion method may be based on the estimator algorithms, such as the Kalman filter, additionally enabling the estimation of upcoming heading changes, based on the previous information. Thus, the resulting fusion algorithm may be based on the adaptive variation of the widely used Kalman filter algorithm, or its non-linear extended Kalman filter version. An additional key functionality of the developed vehicle heading estimation algorithm is the capability to reliably recognize the possible reverse movement.

## 6.2 Future Perspectives

This research has proposed and developed a sensor fusion method for the indirect localization of fully markerless industrial products, focused on the use with industrial forklifts. Although the proposed method has achieved remarkable results during the experimental performance validation, its further development may start with thorough and long-term testing of this approach to define possible improvement requirements. As the scope of this research was exclusively focused on the use of industrial forklifts, further work may investigate the extended area of applications for the indirect tracking method and propose necessary sensor & algorithm presets, suitable for different industrial machinery and material handling equipment, such as cranes, lifters, excavators, or other loading & transportation equipment. This may also include the development of a simplified indirect tracking setup version to effectively integrate smaller industrial equipment, such as manual pallet jacks, into the indirect tracking process.

As different passive identification technologies remain widely used in the industry, the further development of the proposed method may include the support for the optional integration of various case-specific or auxiliary sensors, such as cameras or passive identification scanners (e.g., RFID or QR codes). This will allow a seamless integration of the proposed indirect tracking method in production and warehousing processes, where product identification markers remain widely used. This may also utilize the benefits of these technologies to further enhance the performance of the proposed indirect tracking method. Additional features may also include the possible compatibility of the proposed method with pre-deployed sensor setups. These include the available setups, from forklift CAN bus (Controller Area Network) and up to numerous high-performance sensor networks of different industrial robots, unmanned vehicles and platforms. The field of unmanned vehicles and robots may reciprocally benefit from the integration of the presented methods to potentially improve the effective use of sensors, thus reducing the number of required sensors and increasing overall efficiency. Future research may also cover the enhancement and optimization of the proposed automatic pick-up & drop-down detection (A-PDD) algorithm.

Future research perspectives in the field of industrial vehicle heading estimation may also cover the further enhancement of the proposed positioning data-based method on both the algorithmic and the hardware side. Future work may focus on the additional integration of the accelerometer unit - a second inertial sensor, widely available in IMU units. This unit may potentially provide extended information on the real-time vehicle movement, thus enhancing the performance of proposed positioning and gyroscope data-based heading estimation methods. Further development may also be focused on the improvement of the proposed ATKF algorithm by its optimization and tuning for different scenarios and machinery, as well as the possible integration of auxiliary sensors or algorithmic solutions. Further improvement of the ATKF algorithm may include the integration of different machine learning techniques into its adaptivity or estimation mechanisms for the automatic fine-tuning of the algorithm.

Additionally, the future work may also include the data collection and composition of the comprehensive dataset, containing positioning information of multiple sources, such as UWB and GNSS, inertial information of multiple gyroscope and accelerometer sensors, as well as magnetometer information. This synchronized data, accompanied by highly accurate ground truth data on the real-time position and orientation, and collected in different environments and various movement scenarios, may then be used as an easily accessible benchmark dataset for further research advancements. This may gradually lead to more controlled and standardized validation of various algorithms and techniques in the field of navigation and orientation tracking.

## List of Figures

1	Conceptual illustration of indirect tracking method .....	38
2	Geometric interpretation for the fork positioning error caused by the erroneous heading estimation .....	39
3	Illustrative precision of positioning data-based heading at varying movement speed .....	46
4	Flowchart of the proposed IMU heading drift correction algorithm.....	55
5	Visualized results of experimentally tested drift correction algorithm, forklift and sensors setup, used in the test campaign .....	56
6	CDF function of the experimentally tested DCA algorithm .....	57
7	Flowchart of the implemented A-EKF algorithm for AP-TWR UWB positioning	61
8	Visualized dependence of the exponential and logistic weight functions on their input parameters .....	63
9	Illustrative dependence of input data weights on the movement speed in the ATKF algorithm .....	64
10	Flowchart of the designed ATKF algorithm.....	65
11	Visualized simulated movement scenarios I and II .....	68
12	Visualized dependence of the positioning data-based heading error on the movement speed and PNDR ratio .....	69
13	Averaged median absolute error results of simulated ATKF and DCA testing in different scenarios, at different input data error configurations .....	71
14	Averaged median absolute error results of simulated ATKF and DCA testing at varying positioning data error and constant inertial data error .....	73
15	Visualized results of the forklift heading estimation by the proposed algorithms, state-of-the-art algorithms and raw data sources.....	75
16	CDF functions of the forklift heading, estimated by sole sensors, state-of-the-art and proposed algorithms .....	79
17	Flowchart of the designed indirect tracking method .....	82
18	Flowchart of the proposed A-PDD algorithm .....	83
19	An illustrative example of a payload pick-up pattern, recognized by the A-PDD algorithm .....	84
20	Indirect tracking down-scaled test setup & visualized results .....	86
21	Deployment of the indirect tracking test setup, test environment & visualized test scenario .....	89
22	Visualized results industrial payloads' indirect positioning .....	90
23	Visualized results of the payload tracking by indirect and direct methods...	95
25	Averaged mean absolute error results of simulated ATKF and DCA algorithms testing at different positioning and inertial data error rates .....	192
26	Averaged root mean squared error results of simulated ATKF and DCA algorithms testing at different positioning and inertial data error rates .....	193
27	Averaged median absolute error deviation results of simulated ATKF and DCA algorithms testing at different positioning and inertial data error rates	194
28	Averaged mean absolute error deviation results of simulated ATKF and DCA algorithms testing at different positioning and inertial data error rates	195
29	Averaged error standard deviation results of simulated ATKF and DCA algorithms testing at different positioning and inertial data error rates .....	196
30	Heatmaps of UWB anchors' ranging coverage in indirect and direct tracking methods .....	198

## List of Tables

1	Research questions answered in published works .....	17
2	Key aspects and gaps in state-of-the-art indirect tracking methods .....	22
3	Key aspects and gaps in state-of-the-art heading estimation methods .....	33
4	Algorithms used in gyroscope drift correction methods .....	35
5	Summary on underlying positioning system selection .....	44
6	Summary on heading tracking unit selection .....	47
7	Summary on tynes' elevation tracking unit selection .....	50
8	Summary on fork occupancy detection unit selection .....	53
9	Numerical heading estimation accuracy and precision results, experimentally achieved by sole sensors, state-of-the-art and proposed algorithms ...	76
10	Averaged absolute and relative payload positioning results of the down-scaled testing .....	87
11	Averaged absolute and relative payload positioning results of the full-scale test campaign .....	91
12	Targeted and achieved absolute and repeatability results in indirect positioning and heading estimation accuracy .....	92
13	Over time location update of indirectly tracked industrial products .....	93
14	Absolute positioning results of indirect and direct payload tracking .....	95
15	UWB positioning system performance quality in direct and indirect tracking methods .....	96
16	Tuning parameters of proposed ATKF and drift correction algorithms .....	189



## References

- [1] A. Fjodorov, S. Ulp, M. M. Alam, and A. Kuusik, "Inertial and Positioning Sensors Fusion for Indirect Location Tracking in Warehouse Inventory Management," *2023 International Conference on Control, Automation and Diagnosis (ICCAD)*, pp. 1–7, 2023.
- [2] T. Laadung, S. Ulp, A. Fjodorov, M. M. Alam, and Y. Le Moullec, "Adaptive Extended Kalman Filter Position Estimation Based on Ultra-Wideband Active-Passive Ranging Protocol," *IEEE Access*, 2023.
- [3] A. Fjodorov, S. Ulp, T. Laadung, M. M. Alam, and A. Kuusik, "Vehicle Heading Estimation Using Positioning and Inertial Data-Based Adaptive Tandem Kalman Filter," *IEEE Transactions on Intelligent Vehicles*, 2025.
- [4] A. Fjodorov, S. Ulp, T. Laadung, M. M. Alam, and A. Kuusik, "Accurate Indirect 3D Localization of Markerless Industrial Products," *IEEE Sensors Journal*, *Accepted: 18.09*, 2025.
- [5] A. Fjodorov, A. Masood, M. M. Alam, and S. Päränd, "5G Testbed Implementation and Measurement Campaign for Ground and Aerial Coverage," *2022 18th Biennial Baltic Electronics Conference (BEC)*, pp. 1–6, 2022.
- [6] I. Mürsepp, A. Fjodorov, and M. M. Alam, "Non-Line of Sight Detection Based on 5G Signal Strength-and Quality Measurements and its Impact on Mobile Positioning Accuracy," in *2024 International Wireless Communications and Mobile Computing (IWCMC)*, pp. 256–261, IEEE, 2024.
- [7] "10 Benefits of Industrial Automation in Manufacturing." <https://www.amoriabond.com/en/insights/blog/10-benefits-of-industrial-automation-in-manufacturing/>. Accessed: 2024-03-11.
- [8] "Warehouse Automation Explained: Types, Benefits & Best Practices." <https://www.netsuite.com/portal/resource/articles/inventory-management/warehouse-automation.shtml>. Accessed: 2024-03-11.
- [9] F. Piccialli, N. Bessis, and J. J. Jung, "Data Science Challenges in Industry 4.0," *IEEE Transactions on Industrial Informatics*, 2020.
- [10] M. Qi, X. Li, X. Yan, and C. Zhang, "On the Evaluation of AGVS-based Warehouse Operation Performance," *Simulation Modelling Practice and Theory*, vol. 87, pp. 379–394, 2018.
- [11] G. Deak, K. Curran, and J. Condell, "A survey of active and passive indoor localisation systems," *Computer Communications*, vol. 35, no. 16, pp. 1939–1954, 2012.
- [12] T. Ahmad *et al.*, "An improved accelerated frame slotted aloha (afsa) algorithm for tag collision in rfid," *arXiv preprint arXiv:1405.6217*, 2014.
- [13] S. Shyam, S. Juliet, and K. Ezra, "A UWB Based Indoor Asset Tracking Architecture for Industry 4.0," in *2022 4th International Conference on Smart Systems and Inventive Technology (ICSSIT)*, pp. 501–506, IEEE, 2022.
- [14] A. Volpi, L. Tebaldi, G. Matrella, R. Montanari, and E. Bottani, "Low-Cost UWB Based Real-Time Locating System: Development, Lab Test, Industrial Implementation and Economic Assessment," *Sensors*, vol. 23, no. 3, p. 1124, 2023.

- [15] E. Evizal, T. A. Rahman, and S. K. A. Rahim, "Active RFID Technology for Asset Tracking and Management System," *TELKOMNIKA (Telecommunication Computing Electronics and Control)*, vol. 11, no. 1, pp. 137–146, 2013.
- [16] U. Ahmad, K. Poon, A. M. Altayyari, and M. R. Almazrouei, "A Low-cost Localization System for Warehouse Inventory Management," in *2019 International Conference on Electrical and Computing Technologies and Applications (ICECTA)*, pp. 1–5, IEEE, 2019.
- [17] C. K. M. Lee, C. Ip, T. Park, and S. Y. Chung, "A Bluetooth Location-based Indoor Positioning System for Asset Tracking in Warehouse," in *2019 IEEE International Conference on Industrial Engineering and Engineering Management (IEEM)*, pp. 1408–1412, IEEE, 2019.
- [18] H. Vietz, H. B. H. Ammar, S. Baum, N. Jazdi, and M. Weyrich, "5G Indoor Positioning for Manufacturing using Convolutional Neural Networks," *Procedia CIRP*, vol. 120, pp. 1191–1196, 2023.
- [19] S. Alyahya, Q. Wang, and N. Bennett, "Application and Integration of an RFID-enabled Warehousing Management System—a Feasibility Study," *Journal of Industrial Information Integration*, vol. 4, pp. 15–25, 2016.
- [20] D. Saha, G. S. B. Udayagiri, P. Agarwal, B. Ghosh, and S. Kumar, "Warehouse Management Using Real-Time QR-Code and Text Detection," in *11th International Micro Air Vehicle Competition and conference*, 2019.
- [21] K. Sangsane and A. Vanichchinchai, "Improvement of Warehouse Storage Area and System: an Application of Visual Control and Barcode," in *2021 IEEE 8th International Conference on Industrial Engineering and Applications (ICIEA)*, pp. 444–448, IEEE, 2021.
- [22] T. Poon, K. L. Choy, H. K. Chow, H. C. Lau, F. T. Chan, and K. Ho, "A RFID Case-based Logistics Resource Management System for Managing Order-picking Operations in Warehouses," *Expert systems with applications*, vol. 36, no. 4, pp. 8277–8301, 2009.
- [23] A. Motroni, A. Buffi, and P. Nepa, "A Durvey on Indoor Vehicle Localization Through RFID Technology," *IEEE Access*, vol. 9, pp. 17921–17942, 2021.
- [24] D. Wei, W. Hung, and K.-L. Wu, "A Real Time RFID Locationing System Using Phased Array Antennas for Warehouse Management," in *2016 IEEE International Symposium on Antennas and Propagation (APSURSI)*, pp. 1153–1154, IEEE, 2016.
- [25] S. Jeon, M. Choi, G. Kim, and B. Hong, "Localization of Pallets Based on Passive RFID Tags," in *2010 Seventh International Conference on Information Technology: New Generations*, pp. 834–839, 2010.
- [26] P. Nepa, A. Motroni, A. Congi, E. Ferro, M. Pesi, G. Giorgi, A. Buffi, M. Lazzarotti, J. Bellucci, S. Galigani, *et al.*, "I-READ 4.0: Internet-of-READers for an Efficient Asset Management in Large Warehouses With High Stock Rotation Index," in *2019 IEEE 5th International forum on Research and Technology for Society and Industry (RTSI)*, pp. 67–72, IEEE, 2019.
- [27] G. Kapoor, Y. S. Lee, R. Sikora, and S. Piramuthu, "Drone-based Warehouse Inventory Management of Perishables," *International Journal of Production Economics*, vol. 278, p. 109437, 2024.

- [28] C. Li, E. Tanghe, P. Suanet, D. Plets, J. Hoebeke, E. De Poorter, and W. Joseph, "ReLoc 2.0: UHF-RFID Relative Localization for Drone-based Inventory Management," *IEEE Transactions on Instrumentation and Measurement*, vol. 70, pp. 1–13, 2021.
- [29] A. Motroni, P. Nepa, V. Magnago, A. Buffi, B. Tellini, D. Fontanelli, and D. Macii, "SAR-based Indoor Localization of UHF-RFID Tags via Mobile Robot," in *2018 International Conference on Indoor Positioning and Indoor Navigation (IPIN)*, pp. 1–8, IEEE, 2018.
- [30] A. Buffi, A. Motroni, P. Nepa, B. Tellini, and R. Cioni, "A SAR-based Measurement Method for Passive-tag Positioning With a Flying UHF-RFID Reader," *IEEE Transactions on Instrumentation and Measurement*, vol. 68, no. 3, pp. 845–853, 2018.
- [31] A. A. Tubis and J. Rohman, "Intelligent warehouse in industry 4.0—systematic literature review," *Sensors*, vol. 23, no. 8, p. 4105, 2023.
- [32] A. K. Grover and M. H. Ashraf, "Autonomous and iot-driven intralogistics for industry 4.0 warehouses: A thematic analysis of the literature," *Transportation Journal*, vol. 63, no. 1, pp. 42–61, 2024.
- [33] P. Li, W. Wu, Z. Zhao, and G. Q. Huang, "Indoor positioning systems in industry 4.0 applications: Current status, opportunities, and future trends," *Digital Engineering*, p. 100020, 2024.
- [34] K. Zhao, M. Zhu, B. Xiao, X. Yang, C. Gong, and J. Wu, "Joint RFID and UWB Technologies in Intelligent Warehousing Management System," *IEEE Internet of Things Journal*, vol. 7, no. 12, pp. 11640–11655, 2020.
- [35] A. Frankó, G. Vida, and P. Varga, "Reliable Identification Schemes for Asset and Production Tracking in Industry 4.0," *Sensors*, vol. 20, no. 13, p. 3709, 2020.
- [36] H. Borstell, J. Kluth, M. Jaeschke, C. Plate, B. Gebert, and K. Richter, "Pallet Monitoring System Based on a Heterogeneous Sensor Network for Transparent Warehouse Processes," in *2014 Sensor Data Fusion: Trends, Solutions, Applications (SDF)*, pp. 1–6, IEEE, 2014.
- [37] F. Belloni, "Driving Innovation: Creating A Hybrid RTLS Positioning Ecosystem," Jul 2023.
- [38] N. S. Rosli, A. Y. B. Hashim, and Z. Jamaludin, "Tracking of Pallets in Manufacturing Environment Using RFID System," *American Journal of Industrial Engineering*, vol. 1, no. 2, pp. 36–40, 2013.
- [39] A. Motroni, A. Buffi, P. Nepa, M. Pesì, and A. Congi, "An Action Classification Method for Forklift Monitoring in Industry 4.0 Scenarios," *Sensors*, vol. 21, no. 15, p. 5183, 2021.
- [40] M. Li, S. Gu, G. Chen, and Z. Zhu, "A RFID-based Intelligent Warehouse Management System Design and Implementation," in *2011 IEEE 8th International Conference on e-Business Engineering*, pp. 178–184, IEEE, 2011.
- [41] "RFID Asset Management System." <https://www.arizontw.com/msg/rfid-intelligent-forklift.html>. Accessed: 2024-12-13.
- [42] "Warehouse RFID Forklift System." <https://www.cirfid.com/applications/warehouse-management/forklift-system/>. Accessed: 2025-01-05.

- [43] E. S. Kesuma, P. H. Rusmin, and D. A. Maharani, "Pallet Detection and Distance Estimation With YOLO and Fiducial Marker Algorithm in Industrial Forklift Robot," in *2023 International Conference on Artificial Intelligence in Information and Communication (ICAIIIC)*, pp. 270–275, IEEE, 2023.
- [44] N. Bellomo, E. Marcuzzi, L. Baglivo, M. Pertile, E. Bertolazzi, and M. De Cecco, "Pallet Pose Estimation With LiDAR and Vision for Autonomous Forklifts," *IFAC Proceedings Volumes*, vol. 42, no. 4, pp. 612–617, 2009.
- [45] I. S. Mohamed, *Detection and Tracking of Pallets Using a Laser Rangefinder and Machine Learning Techniques*. PhD thesis, European Master on Advanced Robotics+(EMARO+), University of Genova, Italy, 2017.
- [46] I. S. Mohamed, A. Capitanelli, F. Mastrogiovanni, S. Rovetta, and R. Zaccaria, "Detection, Localisation and Tracking of Pallets Using Machine Learning Techniques and 2D Range Data," *Neural Computing and Applications*, vol. 32, pp. 8811–8828, 2020.
- [47] I. Vipperi, "Laoliikumiste Tuvastamine ja Jalgimine Turvakaamerate Abil," 2021.
- [48] J. Zhao, B. Li, X. Wei, H. Lu, E. Lü, and X. Zhou, "Recognition and Location Algorithm for Pallets in Warehouses Using RGB-D Sensor," *Applied Sciences*, vol. 12, no. 20, p. 10331, 2022.
- [49] J. Rutinowski, H. Youssef, A. Gouda, C. Reining, and M. Roidl, "The Potential of Deep Learning Based Computer Vision in Warehousing Logistics," *Logistics Journal: Proceedings*, vol. 2022, no. 18, 2022.
- [50] L. Santoro, M. Nardello, D. Eccher, M. Sittoni, D. Brunelli, and D. Fontanelli, "A Tag-less Ultrawide-band Passive Tracking System," in *2023 IEEE International Workshop on Metrology for Industry 4.0 & IoT (MetroInd4.0&IoT)*, pp. 287–292, IEEE, 2023.
- [51] M. Elsayeh, M. Haroon, B. Tawfik, and A. S. Fahmy, "RFID-based Indoors Localization of Tag-less Objects," in *2010 5th Cairo International Biomedical Engineering Conference*, pp. 61–65, IEEE, 2010.
- [52] A. Tsujii, T. Kasashima, H. Hatano, and T. Yamazato, "Position Estimation of Slowly Moving Obstacles Using Ultrasonic Sensor Array," in *2022 IEEE International Ultrasonics Symposium (IUS)*, pp. 1–4, IEEE, 2022.
- [53] A. Ramezani Akhmareh, M. T. Lazarescu, O. Bin Tariq, and L. Lavagno, "A Tagless Indoor Localization System Based on Capacitive Sensing Technology," *Sensors*, vol. 16, no. 9, p. 1448, 2016.
- [54] L.-o. Kovavisaruch, K. Maneerat, T. Sanpechuda, K. Chinda, T. Wongsatho, S. Wisadsud, S. Lim, and K. Kaemarangsi, "UWB Tracking for Forklift in Near-Automate Warehouse," in *2024 5th Technology Innovation Management and Engineering Science International Conference (TIMES-iCON)*, pp. 1–5, IEEE, 2024.
- [55] V. Barral, P. Suárez-Casal, C. J. Escudero, and J. A. García-Naya, "Multi-sensor Accurate Forklift Location and Tracking Simulation in Industrial Indoor Environments," *Electronics*, vol. 8, no. 10, p. 1152, 2019.
- [56] A. Motroni, A. Buffi, and P. Nepa, "Forklift Tracking: Industry 4.0 Implementation in Large-scale Warehouses Through UWB Sensor Fusion," *Applied Sciences*, vol. 11, no. 22, p. 10607, 2021.

- [57] S. Konatowski, P. Kaniewski, and J. Matuszewski, "Comparison of Estimation Accuracy of EKF, UKF and PF Filters," *Annual of Navigation*, no. 23, pp. 69–87, 2016.
- [58] W. Wei, S. Gao, Y. Zhong, C. Gu, and G. Hu, "Adaptive Square-root Unscented Particle Filtering Algorithm for Dynamic Navigation," *Sensors*, vol. 18, no. 7, p. 2337, 2018.
- [59] "Sewio Tag-less Tracking Project Prakab 2.0: Case Study." <https://www.sewio.net/wp-content/uploads/2023/02/Case-Study-Prakab-2.0-v4.pdf>. Accessed: 2024-09-06.
- [60] R. Juráš, P. Mlýnek, and A. Čech, "A System for the Real-time Indirect Monitoring of Objects," July 2024. Accessed: 2025-02-07.
- [61] J. G. Webster and H. Eren, *Measurement, instrumentation, and sensors handbook: spatial, mechanical, thermal, and radiation measurement*. CRC press, 2017.
- [62] J. H. Wall, D. M. Bevy, et al., "Characterization of Various IMU Error Sources and the Effect on Navigation Performance," in *Proceedings of the 18th international technical meeting of the satellite division of the institute of navigation (ION GNSS 2005)*, pp. 967–978, 2005.
- [63] M. N. Armenise, C. Ciminelli, F. Dell'Olio, and V. M. Passaro, *Advances in Gyroscope Technologies*. Springer Science & Business Media, 2010.
- [64] V. M. Passaro, A. Cuccovillo, L. Vaiani, M. De Carlo, and C. E. Campanella, "Gyroscope Technology and Applications: A Review in the Industrial Perspective," *Sensors*, vol. 17, no. 10, p. 2284, 2017.
- [65] "Getting Started With Inertial Measurement Units | Exploring Degrees Of Freedom." <https://core-electronics.com.au/guides/getting-started-with-inertial-measurement-units-exploring-degrees-of-freedom/>. Accessed: 2024-04-05.
- [66] "What is the Definition of AHRS?." <https://www.advancednavigation.com/glossary/ahrs>. Accessed: 2024-05-27.
- [67] L. Wöhle and M. Gebhard, "SteadEye-Head—Improving MARG-Sensor Based Head Orientation Measurements Through Eye Tracking Data," *Sensors*, vol. 20, no. 10, p. 2759, 2020.
- [68] F. Wang, L. Ling, and Z. Qi, "Research on Data Drift Suppression Method of Gyroscope Sensor Based on First-Order Inertia and Low Pass Filter," in *2020 Chinese Control And Decision Conference (CCDC)*, pp. 1237–1241, IEEE, 2020.
- [69] B. Suwandi, T. Kitasuka, and M. Aritsugi, "Vehicle Vibration Error Compensation on IMU-Accelerometer Sensor Using Adaptive Filter and Low-pass Filter Approaches," *Journal of Information Processing*, vol. 27, pp. 33–40, 2019.
- [70] N. H. Ariffin, N. Arsad, and B. Bais, "Low Cost MEMS Gyroscope and Accelerometer Implementation Without Kalman Filter for Angle Estimation," in *2016 International Conference on Advances in Electrical, Electronic and Systems Engineering (ICAEEES)*, pp. 77–82, IEEE, 2016.

- [71] H. G. Min and E. T. Jeung, "Complementary Filter Design for Angle Estimation Using MEMS Accelerometer and Gyroscope," *Department of Control and Instrumentation, Changwon National University, Changwon, Korea*, pp. 641–773, 2015.
- [72] M. L. Hoang and A. Pietrosanto, "A New Technique on Vibration Optimization of Industrial Inclinator for MEMS Accelerometer Without Sensor Fusion," *Ieee Access*, vol. 9, pp. 20295–20304, 2021.
- [73] M. Long Hoang, *Industry-Oriented Enhancement of Inertial Platform Performance*. PhD thesis, Università degli studi di Salerno, 2022.
- [74] M. L. Hoang, M. Carratù, V. Paciello, and A. Pietrosanto, "Fusion Filters Between the No Motion No Integration Technique and Kalman Filter in Noise Optimization on a 6DoF Drone for Orientation Tracking," *Sensors*, vol. 23, no. 12, p. 5603, 2023.
- [75] M. L. Hoang and A. Pietrosanto, "Yaw/Heading Optimization by Drift Elimination on MEMS Gyroscope," *Sensors and Actuators A: Physical*, vol. 325, p. 112691, 2021.
- [76] R. I. Alfian, A. Ma'arif, and S. Sunardi, "Noise Reduction in the Accelerometer and Gyroscope Sensor With the Kalman Filter Algorithm," *Journal of Robotics and Control (JRC)*, vol. 2, no. 3, pp. 180–189, 2021.
- [77] J. Abbasi, M. Hashemi, and A. Alasty, "A Memory-based Filter for Long-term Error De-noising of MEMS-gyros," *IEEE Transactions on Instrumentation and Measurement*, vol. 71, pp. 1–8, 2022.
- [78] Y. Bai, X. Wang, X. Jin, T. Su, J. Kong, and B. Zhang, "Adaptive Filtering for MEMS Gyroscope With Dynamic Noise Model," *ISA transactions*, vol. 101, pp. 430–441, 2020.
- [79] M. Wang, X. Dong, C. Qin, and J. Liu, "Adaptive  $H_{\infty}$  Kalman filter Based Random Drift Modeling and Compensation Method for Ring Laser Gyroscope," *Measurement*, vol. 167, p. 108170, 2021.
- [80] Z. Wang, L. Shan, Z. Wu, J. Yan, and J. Li, "MEMS Gyro Signal Processing based on Improved-Sage-Husa Adaptive Filtering Method," in *2021 33rd Chinese Control and Decision Conference (CCDC)*, pp. 5029–5035, IEEE, 2021.
- [81] H. M. Abdelzaher, I. M. El-Dokany, S. A. El-Dolil, O. A. Oraby, M. I. Dessouky, A. S. El-Fishawy, E.-S. M. El-Rabaie, and F. E. Abd-El-Samie, "Noise Reduction in Optical Gyroscope Signals Based on Hybrid Approaches," *Journal of Optics*, vol. 51, no. 1, pp. 5–21, 2022.
- [82] W. Chen, Z. Cao, Z. Yang, and M. Yang, "Research on Sway Detection Method of Subway Train Based on MEMS Gyroscope Technology," in *2022 5th International Conference on Advanced Electronic Materials, Computers and Software Engineering (AEMCSE)*, pp. 19–22, IEEE, 2022.
- [83] C. Zhu, S. Cai, Y. Yang, W. Xu, H. Shen, and H. Chu, "A Combined Method for MEMS Gyroscope Error Compensation Using a Long Short-term Memory Network and Kalman Filter in Random Vibration Environments," *Sensors*, vol. 21, no. 4, p. 1181, 2021.

- [84] J. Mi, Q. Wang, and X. Han, "Low-cost MEMS Gyroscope Performance Improvement Under Unknown Disturbances Through Deep Learning-based Array," *Sensors and Actuators A: Physical*, vol. 368, p. 115086, 2024.
- [85] P. Wang, G. Li, and Y. Gao, "A Compensation Method for Gyroscope Random Drift Based on Unscented Kalman Filter and Support Vector Regression Optimized by Adaptive Beetle Antennae Search Algorithm," *Applied Intelligence*, vol. 53, no. 4, pp. 4350–4365, 2023.
- [86] Z. Li, Y. Cui, Y. Gu, G. Wang, J. Yang, K. Chen, and H. Cao, "Temperature Drift Compensation for Four-mass Vibration MEMS Gyroscope Based on EMD and Hybrid Filtering Fusion Method," *Micromachines*, vol. 14, no. 5, p. 971, 2023.
- [87] R. K. R. Damagatla and M. Atia, "A Novel Approach for IMU Denoising Using Machine Learning," in *2023 IEEE Sensors Applications Symposium (SAS)*, pp. 1–6, IEEE, 2023.
- [88] R. K. R. Damagatla and M. Atia, "Improving EKF Based IMU/GNSS Fusion Using Machine Learning for IMU Denoising," *IEEE Access*, 2024.
- [89] R. K. R. Damagatla, *Improved IMU/GNSS EKF fusion using Machine Learning*. PhD thesis, Carleton University, 2024.
- [90] R. K. R. Damagatla and M. Atia, "Improved IMU/GNSS EKF Fusion Using XGBoost Machine Learning Algorithm," in *2024 14th International Conference on Electrical Engineering (ICEENG)*, pp. 276–281, IEEE, 2024.
- [91] J. Du, C. Gerdtnan, and M. Lindén, "Signal quality improvement algorithms for mems gyroscope-based human motion analysis systems: A systematic review," *Sensors*, vol. 18, no. 4, p. 1123, 2018.
- [92] X. Shi, Z. Wang, H. Zhao, S. Qiu, R. Liu, F. Lin, and K. Tang, "Threshold-free Phase Segmentation and Zero Velocity Detection for Gait Analysis Using Foot-mounted Inertial Sensors," *IEEE Transactions on Human-Machine Systems*, vol. 53, no. 1, pp. 176–186, 2022.
- [93] S. Y. Cho, J. H. Lee, and C. G. Park, "A Zero-velocity Detection Algorithm Robust to Various Gait Types for Pedestrian Inertial Navigation," *IEEE Sensors Journal*, vol. 22, no. 6, pp. 4916–4931, 2021.
- [94] T. Zhao and M. J. Ahamed, "Pseudo-Zero Velocity Re-Detection Double Threshold Zero-Velocity Update (ZUPT) for Inertial Sensor-Based Pedestrian Navigation," *IEEE Sensors Journal*, vol. 21, no. 12, pp. 13772–13785, 2021.
- [95] R. Zhang, H. Yang, F. Höflinger, and L. M. Reindl, "Adaptive Zero Velocity Update Based on Velocity Classification for Pedestrian Tracking," *IEEE Sensors journal*, vol. 17, no. 7, pp. 2137–2145, 2017.
- [96] G. Aristizábal Pla, D. N. Martini, M. V. Potter, and W. Hoogkamer, "Assessing the Validity of the Zero-velocity Update Method for Sprinting Speeds," *Plos one*, vol. 19, no. 2, p. e0288896, 2024.
- [97] W. Zhang, L. Wang, and Y. Zu, "The Zero-Velocity Correction Method for Pipe Jacking Automatic Guidance System Based on Fiber Optic Gyroscope," *Sensors*, vol. 24, no. 18, p. 5911, 2024.

- [98] Y. Wang and X. Li, "The IMU/UWB Fusion Positioning Algorithm Based on a Particle Filter," *ISPRS International Journal of Geo-Information*, vol. 6, no. 8, p. 235, 2017.
- [99] M. Li, W. Nie, V. Suvorkin, A. Rovira-Garcia, W. Zhang, T. Xu, and G. Xu, "Stationary Detection for Zero Velocity Update of IMU Based on the Vibrational FFT Feature of Land Vehicle," *Remote Sensing*, vol. 16, no. 5, p. 902, 2024.
- [100] L. An, X. Pan, M. Wang, Z. Chen, Z. Tu, and C. Chu, "A Zero-velocity Detection Algorithm for Pedestrian Navigation Based on LSTM," in *2021 International Symposium on Computer Science and Intelligent Controls (ISCSIC)*, pp. 361–367, IEEE, 2021.
- [101] Q. Li, K. Li, and W. Liang, "A Zero-velocity Update Method Based on Neural Network and Kalman Filter for Vehicle-mounted Inertial Navigation System," *Measurement Science and Technology*, vol. 34, no. 4, p. 045110, 2023.
- [102] T. Wang, "Heading Attitude Drifts Controlled by the Angular Accelerations Instead of Using Magnetometers," in *2018 IEEE International Conference on Mechatronics and Automation (ICMA)*, pp. 563–567, IEEE, 2018.
- [103] M. L. Hoang, A. Pietrosanto, S. D. Iacono, and V. Paciello, "Pre-processing Technique for Compass-less Madgwick in Heading Estimation for Industry 4.0," in *2020 IEEE International Instrumentation and Measurement Technology Conference (I2MTC)*, pp. 1–6, IEEE, 2020.
- [104] Y. Zhu, J. Liu, R. Yu, Z. Mu, L. Huang, J. Chen, and J. Chen, "Attitude Solving Algorithm and FPGA Implementation of Four-rotor UAV Based on Improved Mahony Complementary Filter," *Sensors*, vol. 22, no. 17, p. 6411, 2022.
- [105] A. Akbari, F. Rahemi, M. J. Khosrowjerdi, and S. Ebadollahi, "Roll and Pitch Estimation from IMU Data Using an LPV  $H_\infty$  Filter," *IEEE Transactions on Instrumentation and Measurement*, vol. 72, pp. 1–10, 2023.
- [106] J. Luo, S. Chen, Y. Lv, W. Sun, F. Yang, and R. Xu, "An IMU Error Correction Method Based on Multithreshold ZV Detection and SRCKF," in *2023 International Conference on Cyber-Physical Social Intelligence (ICCSI)*, pp. 622–627, IEEE, 2023.
- [107] M. Nazarahari and H. Rouhani, "40 Years of Sensor Fusion for Orientation Tracking via Magnetic and Inertial Measurement units: Methods, Lessons Learned, and Future Challenges," *Information Fusion*, vol. 68, pp. 67–84, 2021.
- [108] F. Wittmann, O. Lambercy, and R. Gassert, "Magnetometer-based Drift Correction During Rest in IMU Arm Motion Tracking," *Sensors*, vol. 19, no. 6, p. 1312, 2019.
- [109] E. M. Diaz, F. de Ponte Müller, A. R. Jiménez, and F. Zampella, "Evaluation of AHRS Algorithms for Inertial Personal Localization in Industrial Environments," in *2015 IEEE International Conference on Industrial Technology (ICIT)*, pp. 3412–3417, IEEE, 2015.
- [110] S. A. Ludwig, K. D. Burnham, A. R. Jiménez, and P. A. Touma, "Comparison of Attitude and Heading Reference Systems Using Foot Mounted MIMU Sensor Data: Basic, Madgwick, and Mahony," in *Sensors and Smart Structures Technologies for Civil, Mechanical, and Aerospace Systems 2018*, vol. 10598, pp. 644–650, SPIE, 2018.



- [111] S. A. Ludwig and K. D. Burnham, "Comparison of Euler Estimate Using Extended Kalman Filter, Madgwick and Mahony on Quadcopter Flight Data," in *2018 International Conference on Unmanned Aircraft Systems (ICUAS)*, pp. 1236–1241, IEEE, 2018.
- [112] J. Justa, V. Šmídl, and A. Hamáček, "Fast AHRS Filter for Accelerometer, Magnetometer, and Gyroscope Combination With Separated Sensor Corrections," *Sensors*, vol. 20, no. 14, p. 3824, 2020.
- [113] Q. Zhou, Z. Li, G. Yu, H. Li, and N. Zhang, "A Novel Adaptive Kalman Filter for Euler-angle-based MEMS IMU/Magnetometer Attitude Estimation," *Measurement Science and Technology*, vol. 32, no. 4, p. 045104, 2021.
- [114] S. B. Farahan, J. J. Machado, F. G. de Almeida, and J. M. R. Tavares, "9-DOF IMU-based Attitude and Heading Estimation Using an Extended Kalman Filter With Bias Consideration," *Sensors*, vol. 22, no. 9, p. 3416, 2022.
- [115] A. A. Badawy, M. A. Hassan, A. H. Hassaballa, and Y. Z. Elhalwagy, "Real Time Integration GPS with Gyro-Compassing Using Two Cascaded EKF with Free RTOS," in *2024 6th International Conference on Computing and Informatics (ICCI)*, pp. 307–314, IEEE, 2024.
- [116] R. V. Vitali, R. S. McGinnis, and N. C. Perkins, "Robust Error-state Kalman Filter for Estimating IMU Orientation," *IEEE Sensors Journal*, vol. 21, no. 3, pp. 3561–3569, 2020.
- [117] C. Hajiyev and D. Cilden-Guler, "Attitude and Gyro Bias Estimation by SVD-aided EKF," *Measurement*, vol. 205, p. 112209, 2022.
- [118] X. Chen, A. Bettens, Z. Xie, Z. Wang, and X. Wu, "Kalman Filter and Neural Network Fusion for Fault Detection and Recovery in Satellite Attitude Estimation," *Acta Astronautica*, vol. 217, pp. 48–61, 2024.
- [119] E. D'Amato, V. A. Nardi, I. Notaro, and V. Scordamaglia, "A Particle Filtering Approach for Fault Detection and Isolation of UAV IMU Sensors: Design, Implementation and Sensitivity Analysis," *Sensors*, vol. 21, no. 9, p. 3066, 2021.
- [120] J. Kaltenthaler, H. A. Lauterbach, D. Borrmann, and A. Nüchter, "Pose Estimation and Mapping Based on IMU and LiDAR," *IFAC-PapersOnLine*, vol. 55, no. 8, pp. 71–76, 2022.
- [121] A. Nazemipour, M. T. Manzuri, D. Kamran, and M. Karimian, "MEMS Gyro Bias Estimation in Accelerated Motions Using Sensor Fusion of Camera and Angular-rate Gyroscope," *IEEE Transactions on Vehicular Technology*, vol. 69, no. 4, pp. 3841–3851, 2020.
- [122] X. Tao, P. Meng, B. Zhu, and J. Zhao, "A Fast and Accurate Camera-IMU Calibration Method for Localization System," *Insight-Automatic Control*, vol. 6, no. 1, p. 578, 2023.
- [123] X. Xia, L. Xiong, Y. Huang, Y. Lu, L. Gao, N. Xu, and Z. Yu, "Estimation on IMU Yaw Misalignment by Fusing Information of Automotive Onboard Sensors," *Mechanical Systems and Signal Processing*, vol. 162, p. 107993, 2022.

- [124] G. Park, S. B. Choi, D. Hyun, and J. Lee, "Integrated Observer Approach Using In-vehicle Sensors and GPS for Vehicle State Estimation," *Mechatronics*, vol. 50, pp. 134–147, 2018.
- [125] M. Bersani, M. Vignati, S. Mentasti, S. Arrigoni, and F. Cheli, "Vehicle State Estimation Based on Kalman Filters," in *2019 AEIT International Conference of Electrical and Electronic Technologies for Automotive (AEIT AUTOMOTIVE)*, pp. 1–6, IEEE, 2019.
- [126] R. Song and Y. Fang, "Vehicle State Estimation for INS/GPS Aided by Sensors Fusion and SCKF-Based Algorithm," *Mechanical Systems and Signal Processing*, vol. 150, p. 107315, 2021.
- [127] A. Ramezanifard, M. Hashemi, H. Salarieh, and A. Karmozdi, "Mems-based Gyro Denoising via AUV Dynamic for Enhancing Navigation," *IEEE Transactions on Intelligent Vehicles*, 2024.
- [128] L. Xiong, X. Xia, Y. Lu, W. Liu, L. Gao, S. Song, and Z. Yu, "IMU-based Automated Vehicle Body Sideslip Angle and Attitude Estimation Aided by GNSS Using Parallel Adaptive Kalman Filters," *IEEE Transactions on Vehicular Technology*, vol. 69, no. 10, pp. 10668–10680, 2020.
- [129] M. N. Cahyadi, T. Asfihani, R. Mardiyanto, and R. Erfianti, "Performance of GPS and IMU Sensor Fusion Using Unscented Kalman Filter for Precise I-Boat Navigation in Infinite Wide Waters," *Geodesy and Geodynamics*, vol. 14, no. 3, pp. 265–274, 2023.
- [130] Z. Xu, R. Zhu, T. Zheng, and L. Yang, "The Fusion of GPS and Gyroscope Based on Kalman Filter," in *2021 International Conference on Intelligent Transportation, Big Data & Smart City (ICITBS)*, pp. 205–208, IEEE, 2021.
- [131] M. Zhang, Q. Wang, Y. Dai, J. Yang, and Z. Li, "A GPS/Gyroscope Real Time Heading Fusion Algorithm for Unmanned Ground Vehicle," in *2018 International Conference on Sensing, Diagnostics, Prognostics, and Control (SDPC)*, pp. 107–112, IEEE, 2018.
- [132] Z. Li and Y. Tang, "Attitude Determination for Land Vehicles Based on Low Cost GPS/MEMS-IMU," in *2018 Eighth International Conference on Instrumentation & Measurement, Computer, Communication and Control (IMCCC)*, pp. 1510–1513, IEEE, 2018.
- [133] Z. Wu, D. Yuan, F. Zhang, and M. Yao, "Low-cost Attitude Estimation Using GPS/IMU Fusion Aided by Land Vehicle Model Constraints and Gravity-based Angles," *IEEE Transactions on Intelligent Transportation Systems*, vol. 23, no. 8, pp. 13386–13402, 2021.
- [134] J. Oursland and M. Mehrabian, "An Invariant Extended Kalman Filter for IMU-UWB Sensor Fusion," in *2024 33rd IEEE International Conference on Robot and Human Interactive Communication (ROMAN)*, pp. 154–159, IEEE, 2024.
- [135] B. V. Krishnaveni, K. S. Reddy, and P. R. Reddy, "Indoor Tracking by Adding IMU and UWB Using Unscented Kalman filter," *Wireless Personal Communications*, vol. 123, no. 4, pp. 3575–3596, 2022.
- [136] D. Feng, J. Peng, Y. Zhuang, C. Guo, T. Zhang, Y. Chu, X. Zhou, and X.-G. Xia, "An Adaptive IMU/UWB Fusion Method for NLOS Indoor Positioning and Navigation," *IEEE Internet of Things Journal*, vol. 10, no. 13, pp. 11414–11428, 2023.

- [137] P. Ji, Z. Duan, and W. Xu, "A Combined UWB/IMU Localization Method with Improved CKF," *Sensors*, vol. 24, no. 10, p. 3165, 2024.
- [138] S. Y. Alaba, "GPS-IMU Sensor Fusion for Reliable Autonomous Vehicle Position Estimation," *arXiv preprint arXiv:2405.08119*, 2024.
- [139] S. Paul and T. Maiti, "Accurate Kinematic-Parameters Estimation Using IMU and GPS Sensors Fusion," *IEEE Sensors Journal*, 2024.
- [140] T. Zhang, M. Yuan, L. Wang, H. Tang, and X. Niu, "A Robust and Efficient IMU Array/GNSS Data Fusion Algorithm," *IEEE Sensors Journal*, 2024.
- [141] S. Hayward, K. van Lopik, C. Hinde, and A. A. West, "A Survey of Indoor Location Technologies, Techniques and Applications in Industry," *Internet of Things*, vol. 20, p. 100608, 2022.
- [142] A. Sesyuk, S. Ioannou, and M. Raspopoulos, "A Survey of 3D Indoor Localization Systems and Technologies," *Sensors*, vol. 22, no. 23, p. 9380, 2022.
- [143] P. Pascacio, S. Casteleyn, J. Torres-Sospedra, E. S. Lohan, and J. Nurmi, "Collaborative Indoor Positioning Systems: A Systematic Review," *Sensors*, vol. 21, no. 3, p. 1002, 2021.
- [144] P. Hou, J. Zha, T. Liu, and B. Zhang, "Recent advances and perspectives in gnss ppp-rtk," *Measurement Science and Technology*, vol. 34, no. 5, p. 051002, 2023.
- [145] P. S. Farahsari, A. Farahzadi, J. Rezazadeh, and A. Bagheri, "A Survey on Indoor Positioning Systems for IoT-based Applications," *IEEE Internet of Things Journal*, vol. 9, no. 10, pp. 7680–7699, 2022.
- [146] N. H. A. Wahab, N. Sunar, S. H. Ariffin, K. Y. Wong, Y. Aun, *et al.*, "Indoor Positioning System: A Review," *International Journal of Advanced Computer Science and Applications*, vol. 13, no. 6, 2022.
- [147] F. Zafari, A. Gkelias, and K. K. Leung, "A Survey of Indoor Localization Systems and Technologies," *IEEE Communications Surveys & Tutorials*, vol. 21, no. 3, pp. 2568–2599, 2019.
- [148] L. Mainetti, L. Patrono, and I. Sergi, "A Survey on Indoor Positioning Systems," in *2014 22nd international conference on software, telecommunications and computer networks (SoftCOM)*, pp. 111–120, IEEE, 2014.
- [149] G. Ouyang and K. Abed-Meraim, "A Survey of Magnetic-field-based Indoor Localization," *Electronics*, vol. 11, no. 6, p. 864, 2022.
- [150] "Eliko UWB RTLS." <https://eliko.tech/uwb-rtls-ultra-wideband-real-time-location-system/>. Accessed: 2024-02-18.
- [151] "FieldBee GNSS RTK." <https://www.fieldbee.com>. Accessed: 2025-01-22.
- [152] "Best Autonomous Vehicle Navigation Data Products." <https://www.techsalerator.com/sub-data-categories/autonomous-vehicle-navigation-data>. Accessed: 2024-04-04.
- [153] "Exploring the Application of Gyroscopes." <https://www.ceva-ip.com/ourblog/exploring-the-application-of-gyroscopes/>. Accessed: 2024-11-29.

- [154] A. Burg, A. Meruani, B. Sandheinrich, and M. Wickmann, "MEMS Gyroscopes and Their Applications," *Northwestern University*, <http://clifton.mech.northwestern.edu/~me381/project/done/Gyroscope.pdf>, 2004.
- [155] H. P. Robertson, "Postulate Versus Observation in the Special Theory of Relativity," *Reviews of modern Physics*, vol. 21, no. 3, p. 378, 1949.
- [156] L. Page, "Introduction to Electrodynamics," *Nucleus*, 2007.
- [157] H. C. Lefevre, *The Fiber-optic Gyroscope*. Artech house, 2022.
- [158] L. Mosconi, F. Farroni, A. Sakhnevych, F. Timpone, and F. S. Gerbino, "Adaptive Vehicle Dynamics State Estimator for Onboard Automotive Applications and Performance Analysis," *Vehicle System Dynamics*, vol. 61, no. 12, pp. 3244–3268, 2023.
- [159] M. Viehweger, C. Vaseur, S. van Aalst, M. Acosta, E. Regolin, A. Alatorre, W. Desmet, F. Naets, V. Ivanov, A. Ferrara, *et al.*, "Vehicle State and Tyre Force Estimation: Demonstrations and Guidelines," *Vehicle system dynamics*, vol. 59, no. 5, pp. 675–702, 2021.
- [160] P. Ripka, *Magnetic Sensors and Magnetometers*. Artech house, 2021.
- [161] T. S. Wibowo and P. H. Rusmin, "Heading Estimation Based on Magnetometer Measurement Using LSTM," in *2022 International Conference on Information Technology Systems and Innovation (ICITSI)*, pp. 340–345, IEEE, 2022.
- [162] Z. Ning, J. Fu, Y. Chang, and T. Lyu, "Improved MEMS Magnetometer Adaptive Filter Noise Reduction and Compensation Method," *IEEE Sensors Journal*, vol. 22, no. 2, pp. 1252–1264, 2021.
- [163] X. Li and Y. Qi, "Multi-antenna and geometry-based differential gnss positioning for vehicles," *IEEE Transactions on Intelligent Transportation Systems*, vol. 25, no. 5, pp. 3389–3401, 2023.
- [164] W. Ding, W. Sun, H. Yan, W. Li, Y. Jiang, and Y. Gao, "Low-cost Dual-antenna GNSS-based Heading and Pitch Angles Estimation Considering Baseline Length Constraint," *Measurement*, vol. 239, p. 115492, 2025.
- [165] W. Jin, W. Gong, T. Hou, X. Sun, and H. Ma, "A Dual-antenna Heading Determination Method for Single-frequency GNSS Antennas With Large Phase Pattern Variations," *GPS Solutions*, vol. 27, no. 2, p. 96, 2023.
- [166] D. C. Hernández, V.-D. Hoang, A. Filonenko, and K.-H. Jo, "Vision-based heading angle estimation for an autonomous mobile robots navigation," in *2014 IEEE 23rd International Symposium on Industrial Electronics (ISIE)*, pp. 1967–1972, IEEE, 2014.
- [167] A. Mikov, A. Cloitre, and I. Prikhodko, "Stereo-vision-aided Inertial Navigation for Automotive Applications," *IEEE Sensors Letters*, vol. 5, no. 2, pp. 1–4, 2021.
- [168] F. Xu, Z. Wang, H. Wang, L. Lin, and H. Liang, "Dynamic Vehicle Pose Estimation and Tracking Based on Motion Feedback for LiDARs," *Applied Intelligence*, vol. 53, no. 2, pp. 2362–2390, 2023.
- [169] B. Anbarasu, "Vision-based heading estimation for navigation of a micro-aerial vehicle in gnss-denied staircase environment using vanishing point," *Aerospace Systems*, vol. 7, no. 2, pp. 395–418, 2024.

- [170] "BNO055 Intelligent 9-axis Absolute Orientation Sensor datasheet." [https://cdn-shop.adafruit.com/datasheets/BST\\_BNO055\\_DS000\\_12.pdf](https://cdn-shop.adafruit.com/datasheets/BST_BNO055_DS000_12.pdf). Accessed: 2024-02-18.
- [171] G. Jie, Z. Hao, and Y. Huadong, "High-precision Elevation Sensor Based on Atmospheric Pressure," *Sensors and Materials*, vol. 35, no. 12, pp. 3985–3996, 2023.
- [172] G. Scarmana, "Back to the Future: Revisiting Barometric Levelling," *The International Archives of the Photogrammetry, Remote Sensing and Spatial Information Sciences*, vol. 48, pp. 403–408, 2024.
- [173] J. B. Young, "Modern Altimeter and Barometer System Using the MPL115A," *NXP*, vol. 7, 2022.
- [174] J. Yun and B. Park, "A GNSS/Barometric Altimeter Tightly Coupled Integration for Three-Dimensional Semi-Indoor Mapping With Android Smartphones," *IEEE Geoscience and Remote Sensing Letters*, vol. 21, pp. 1–5, 2024.
- [175] F. Aliew, "An Approach for Precise Distance Measuring Using Ultrasonic Sensors," *Engineering Proceedings*, vol. 24, no. 1, p. 8, 2022.
- [176] T. S. R. Pereira, T. P. de Carvalho, T. A. Mendes, and K. T. M. Formiga, "Evaluation of Water Level in Flowing Channels Using Ultrasonic Sensors," *Sustainability*, vol. 14, no. 9, p. 5512, 2022.
- [177] A. J. Patton and R. C. Braun, "Measurement of Turf Height and Growth Using a Laser Distance Device," *Crop Science*, vol. 61, no. 5, pp. 3110–3123, 2021.
- [178] R. Kosarat and A. Wongjan, "Laser Distance Measuring and Image Calibration for Robot Walking Using Mean Shift Algorithm," *International Journal of Advanced Computer Science & Applications*, vol. 15, no. 12, 2024.
- [179] "The IR Distance Sensors." <https://micromelon.com.au/resources/ir-sensor>. Accessed: 2025-03-15.
- [180] "Types of Distance Sensors and How to Select One?." [https://www.seeedstudio.com/blog/2019/12/23/distance-sensors-types-and-selection-guide/?srsltid=AfmB0ormB7t1TpmjFJdNvtFzcSh2MlzWY-5chPmZ7qITM5SGigUZnN\\_a](https://www.seeedstudio.com/blog/2019/12/23/distance-sensors-types-and-selection-guide/?srsltid=AfmB0ormB7t1TpmjFJdNvtFzcSh2MlzWY-5chPmZ7qITM5SGigUZnN_a). Accessed: 2025-03-15.
- [181] "Difference Between IR Sensor and Ultrasonic Sensor." [https://maxbotix.com/blogs/blog/ultrasonic-or-infrared-sensors?srsltid=AfmB0or7inwyKQx2QLJ0oMGfsS-iEqs4gV\\_eILREziDMX\\_29Vbci0gLZ](https://maxbotix.com/blogs/blog/ultrasonic-or-infrared-sensors?srsltid=AfmB0or7inwyKQx2QLJ0oMGfsS-iEqs4gV_eILREziDMX_29Vbci0gLZ). Accessed: 2025-03-15.
- [182] H. Yun, H. Jeon, S. Yang, and M. B. Jun, "Calibration of Industrial Robots with Spherical Joint Using Single Wire Encoder," *Manufacturing Letters*, vol. 33, pp. 46–50, 2022.
- [183] G. Boschetti and T. Sinico, "A Novel Step-by-step Procedure for the Kinematic Calibration of Robots Using a Single Draw-wire Encoder," *The International Journal of Advanced Manufacturing Technology*, vol. 131, no. 7, pp. 4129–4147, 2024.
- [184] "Encoder Resolution, Encoder Accuracy and System Repeatability." [https://www.dynapar.com/Knowledge/Encoder\\_Resolution\\_Encoder\\_Accuracy\\_Repeatability/](https://www.dynapar.com/Knowledge/Encoder_Resolution_Encoder_Accuracy_Repeatability/). Accessed: 2025-03-15.

- [185] "Draw Wire Leine Linde." [https://pdb-media.leinelinde.se/media/file/9654/Draw\\_wire\\_datasheet\\_en.pdf](https://pdb-media.leinelinde.se/media/file/9654/Draw_wire_datasheet_en.pdf). Accessed: 2025-05-20.
- [186] E. Kim and D. Choi, "A UWB Positioning Network Enabling Unmanned Aircraft Systems Auto Land," *Aerospace science and Technology*, vol. 58, pp. 418–426, 2016.
- [187] J. Li, Y. Wang, Z. Chen, L. Ma, and S. Yan, "Improved Height Estimation Using Extended Kalman Filter on UWB-Barometer 3D Indoor Positioning System," *Wireless Communications and Mobile Computing*, vol. 2021, no. 1, p. 7057513, 2021.
- [188] M. G. Wing and J. Frank, "Vertical measurement accuracy and reliability of mapping-grade gps receivers," *Computers and electronics in agriculture*, vol. 78, no. 2, pp. 188–194, 2011.
- [189] N. Naciri, D. Yi, S. Bisnath, F. J. de Blas, and R. Capua, "Assessment of galileo high accuracy service (has) test signals and preliminary positioning performance," *GPS solutions*, vol. 27, no. 2, p. 73, 2023.
- [190] S. Morichika, H. Sekiya, Y. Zhu, S. Hirano, and O. Maruyama, "Estimation of Displacement Response in Steel Plate Girder Bridge Using a Single MEMS Accelerometer," *IEEE sensors journal*, vol. 21, no. 6, pp. 8204–8208, 2021.
- [191] Y.-C. Yang, L.-J. Tang, X. Zhao, and T.-X. Han, "A Method of Field Elevation Measurement in Distribution Network Work Based on Combination of Barometric Altimetry and Motion Detection," *IEEJ Transactions on Electrical and Electronic Engineering*, vol. 19, no. 4, pp. 576–585, 2024.
- [192] Y. Shi, L. Fang, D. Guo, Z. Qi, J. Wang, and J. Che, "Research on Distance Measurement Method Based on Micro-accelerometer," *AIP Advances*, vol. 11, no. 5, 2021.
- [193] "Miran MPS Series Draw Wire Potentiometers." [http://www.miransensor.com/english/cpzx/37/list\\_1633.html](http://www.miransensor.com/english/cpzx/37/list_1633.html). Accessed: 2024-02-17.
- [194] Q. Meng, Y. Lu, J. Wang, D. Chen, and J. Chen, "A Piezoresistive Pressure Sensor With Optimized Positions and Thickness of Piezoresistors," *Micromachines*, vol. 12, no. 9, p. 1095, 2021.
- [195] Y.-W. Chen, P. P. Pancham, A. Mukherjee, E. Martincic, and C.-Y. Lo, "Recent Advances in Flexible Force Sensors and Their Applications: A Review," *Flexible and Printed Electronics*, vol. 7, no. 3, p. 033002, 2022.
- [196] V. Kamble, V. shinde, and J. Kittur, "Overview of Load Cells," *Journal of Mechanical and Mechanics Engineering*, 10 2021.
- [197] "Load Cells vs. Strain Gauges: Exploring the Differences and Benefits." <https://www.measurex.com.au/load-cells-vs-strain-gauges/>. Accessed: 2025-04-10.
- [198] Z. Lei, K. Ohno, M. Tsubota, E. Takeuchi, and S. Tadokoro, "Transparent Object Detection Using Color Image and Laser Reflectance Image for Mobile Manipulator," in *2011 IEEE International Conference on Robotics and Biomimetics*, pp. 1–7, IEEE, 2011.
- [199] D. Amarasinghe, G. K. Mann, and R. G. Gosine, "Moving Object Detection in Indoor Environments Using Laser Range Data," in *2006 IEEE/RSJ International Conference on Intelligent Robots and Systems*, pp. 802–807, IEEE, 2006.

- [200] D. Yi, H. Jin, M. C. Kim, and S. C. Kim, "An Ultrasonic Object Detection Applying the ID Based on Spread Spectrum Technique for a Vehicle," *Sensors*, vol. 20, no. 2, p. 414, 2020.
- [201] J. N. Yasin, S. A. Mohamed, M.-H. Haghbayan, J. Heikkonen, H. Tenhunen, and J. Plosila, "Low-cost Ultrasonic Based Object Detection and Collision Avoidance Method for Autonomous Robots," *International Journal of Information Technology*, vol. 13, pp. 97–107, 2021.
- [202] G. Arun Francis, M. Arulselvan, P. Elangkumaran, S. Keerthivarman, and J. Vijaya Kumar, "Object Detection Using Ultrasonic Sensor," *Int. J. Innov. Technol. Explor. Eng.*, vol. 8, pp. 207–209, 2020.
- [203] X. Dai, X. Yuan, and X. Wei, "TIRNet: Object Detection in Thermal Infrared Images for Autonomous Driving," *Applied Intelligence*, vol. 51, no. 3, pp. 1244–1261, 2021.
- [204] A. Shokrollahi, J. A. Persson, R. Malekian, A. Sarkheyli-Hägele, and F. Karlsson, "Passive Infrared Sensor-based Occupancy Monitoring in Smart Buildings: a Review of Methodologies and Machine Learning Approaches," *Sensors*, vol. 24, no. 5, p. 1533, 2024.
- [205] N. Bustos, M. Mashhadi, S. K. Lai-Yuen, S. Sarkar, and T. K. Das, "A Systematic Literature Review on Object Detection Using Near Infrared and Thermal Images," *Neurocomputing*, vol. 560, p. 126804, 2023.
- [206] H. Wang, B. Cui, X. Wen, Y. Jiang, C. Gao, and Y. Tian, "Pallet Detection and Estimation With RGB-D Salient Feature Learning," in *2023 China Automation Congress (CAC)*, pp. 8914–8919, IEEE, 2023.
- [207] Y.-Y. Li, X.-h. Chen, G.-Y. Ding, S. Wang, W.-C. Xu, B.-B. Sun, and Q. Song, "Pallet Detection and Localization With RGB Image and Depth Data Using Deep Learning Techniques," in *2021 6th International Conference on Automation, Control and Robotics Engineering (CACRE)*, pp. 306–310, IEEE, 2021.
- [208] R. Iinuma, Y. Hori, H. Onoyama, T. Fukao, and Y. Kubo, "Pallet Detection and Estimation for Fork Insertion with RGB-D Camera," in *2021 IEEE International Conference on Mechatronics and Automation (ICMA)*, pp. 854–859, IEEE, 2021.
- [209] B. George, H. Zangl, T. Bretterklieber, and G. Brasseur, "A Combined Inductive–Capacitive Proximity Sensor for Seat Occupancy Detection," *IEEE transactions on instrumentation and measurement*, vol. 59, no. 5, pp. 1463–1470, 2010.
- [210] Y. Xie, S. Wang, S. Zhang, H. Zhang, and H. Shi, "Dual Inductive–Capacitive Detection Cell: A Promising Tool for Distinguishing Mixed Metal Particles," *IEEE Sensors Journal*, vol. 23, no. 18, pp. 21163–21171, 2023.
- [211] T. Zhu, X. Yin, C. Deng, M. Mwelango, Z. Zhang, X. Yuan, W. Li, and G. Chen, "A Dual Mode Nondestructive Evaluation Sensor With Simultaneous Inductive and Capacitive Outputs," *IEEE Sensors Journal*, vol. 23, no. 6, pp. 6214–6224, 2023.
- [212] "Weatherproof Ultrasonic Sensor SEN0208." [https://wiki.dfrobot.com/Weatherproof\\_Ultrasonic\\_Sensor\\_With\\_Separate\\_Probe\\_SKU\\_SEN0208](https://wiki.dfrobot.com/Weatherproof_Ultrasonic_Sensor_With_Separate_Probe_SKU_SEN0208). Accessed: 2024-02-18.

- [213] R. E. Kalman, "A New Approach to Linear Filtering and Prediction Problems," *Journal of Basic Engineering*, 1960.
- [214] D. Simon, *Optimal State Estimation: Kalman, H Infinity, and Nonlinear Approaches*. John Wiley & Sons, 2006.
- [215] R. R. Labbe Jr, *Kalman and Bayesian Filters in Python*. GitHub, 2020.
- [216] A. Becker, *Kalman Filter from the Ground Up*. KilmanFilter.NET, 2023.
- [217] M. Hossain, M. Haque, and M. T. Arif, "Kalman filtering techniques for the online model parameters and state of charge estimation of the li-ion batteries: A comparative analysis," *Journal of Energy Storage*, vol. 51, p. 104174, 2022.
- [218] M. Mallick, X. Tian, and J. Liu, "Evaluation of Measurement Converted KF, EKF, UKF, CKF, and PF in GMTI Filtering," in *2021 International Conference on Control, Automation and Information Sciences (ICCAIS)*, pp. 21–27, IEEE, 2021.
- [219] W. Elmenreich, "An Introduction to Sensor Fusion," *Vienna University of Technology, Austria*, vol. 502, no. 1-28, p. 37, 2002.
- [220] B. Fariña, J. Toledo, and L. Acosta, "Augmented Kalman Filter Design in a Localization System Using Onboard Sensors With Intrinsic Delays," *IEEE Sensors Journal*, vol. 23, no. 11, pp. 12105–12113, 2023.
- [221] A. Popovici, P. Zaal, and D. M. Pool, "Dual Extended Kalman Filter for the Identification of Time-varying Human Manual Control Behavior," in *AIAA Modeling and Simulation Technologies Conference*, p. 3666, 2017.
- [222] M. Demirci, H. Gözde, and M. C. Taplamacioglu, "Improvement of Power Transformer Fault Diagnosis by Using Sequential Kalman Filter Sensor Fusion," *International Journal of Electrical Power & Energy Systems*, vol. 149, p. 109038, 2023.
- [223] "AHRS: Attitude Estimators, Complementary Filter." <https://ahrs.readthedocs.io/en/latest/filters/complementary.html>. Accessed: 2024-09-03.
- [224] S. O. Madgwick *et al.*, "An Efficient Orientation Filter for Inertial and Inertial/Magnetic Sensor Arrays," 2010.
- [225] "Open Source IMU and AHRS Algorithms." <https://x-io.co.uk/open-source-imu-and-ahrs-algorithms/>. Accessed: 2024-09-03.
- [226] R. Mahony, T. Hamel, and J.-M. Pflimlin, "Nonlinear Complementary Filters on the Special Orthogonal Group," *IEEE Transactions on automatic control*, vol. 53, no. 5, pp. 1203–1218, 2008.
- [227] A. Fjodorov, T. Laadung, M. Tommingas, and S. Ulp, "Forklift Positioning and Inertial Data Collected in the Industrial Environment," *TalTech Data Repository*, 2024.
- [228] W. Zhao, A. Goudar, X. Qiao, and A. P. Schoellig, "Util: An ultra-wideband time-difference-of-arrival indoor localization dataset," *The International Journal of Robotics Research*, vol. 43, no. 10, pp. 1443–1456, 2024.
- [229] S. Haag and R. Anderl, "Digital Twin – Proof of Concept," *Manufacturing letters*, vol. 15, pp. 64–66, 2018.



- [230] A. Fjodorov, T. Laadung, M. Tommingas, and S. Ulp, "Dataset of Forklift-Deployed Multi-Sensor Setup for Indirect Tracking of Markerless Industrial Products," *TalTech Data Repository*, 2024.
- [231] R. Kapoor, S. Ramasamy, A. Gardi, C. Bieber, L. Silverberg, and R. Sabatini, "A novel 3d multilateration sensor using distributed ultrasonic beacons for indoor navigation," *Sensors*, vol. 16, no. 10, p. 1637, 2016.
- [232] F. Malivert, O. Labbani-Igbida, and H. Boeglen, "Comparison and improvement of 3d-multilateration for solving simultaneous localization of drones and uwb anchors," *Applied Sciences*, vol. 13, no. 2, p. 1002, 2023.
- [233] A. Pastrav, R. Simedroni, T. Palade, P. Dolea, D. Popescu, and E. Puschita, "Evaluation of uwb transmissions in highly reflective environments," in *2020 13th International Conference on Communications (COMM)*, pp. 527–532, IEEE, 2020.

## Acknowledgements

I would like to express my gratitude to the Thomas Johann Seebeck Department of Electronics at Tallinn University of Technology and Eliko Tehnoloogia Arenduskeskus OÜ for the opportunity to pursue a PhD degree.

I would like to thank and acknowledge the assistance of my supervisors, Professor Muhammad Mahtab Alam and Dr. Alar Kuusik from Tallinn University of Technology, as well as Dr. Taavi Laadung and Dr. Sander Ulp from Eliko Tehnoloogia Arenduskeskus OÜ, for the invaluable supervision, guidance, and support throughout the entire process of research. Their guidance allowed me to arrange and finalize my research, as well as eventually write, organize, and shape my thesis at the end of my studies.

I would like to thank all of my colleagues at Eliko Tehnoloogia Arenduskeskus OÜ for their highly qualified and professional guidance and assistance in various technical aspects of my research. I would like to thank all of my colleagues at Tallinn University of Technology, and particularly Professor Yannick Le Moullec, for his active help and guidance during the entire study process.

Additionally, I would like to express my personal gratitude to my colleagues Dr. Mihkel Tommingas and Dr. Taavi Laadung for their invaluable help in the widest range of research aspects, from technical and academic discussions to practical assistance in data collection and conducted test campaigns. Also, I would like to thank my family and friends for all the support, encouragement, and patience during this journey of PhD studies.

I would like to acknowledge the financial support provided for this research by:

- „Increasing the knowledge intensity of Ida-Viru entrepreneurship“ project, co-funded by the European Union, subproject "AloT\*5G - Artificial intelligence, edge computing and IoT solutions in distributed systems"
- European Union's Horizon Europe Research Program under grant agreement No.101058505 - 5G-TIMBER
- Development of an industrial digital control system based on precise positioning technology, ELIKO TAK and Atemix Automatika nr. 2014-2020.4.02.21-0311.

## **Abstract**

### **Advancements in Sensor Fusion Enabled Indirect Positioning Methods**

This thesis addresses the industrial need and investigates a method to enable accurate and real-time localization of completely markerless industrial products. The key motivation behind the investigated method is to enable the identification and accurate tracking of various industrial products in a cost-effective manner without the direct attachment of any tracking or identification units. Thus, the key criterion for the targeted method is to fully avoid the direct attachment of any positioning or identification tags, including QR codes, barcodes, or other markers to localized payloads, leaving them fully unmarked. This dissertation starts by investigating the available indirect tracking methods to evaluate their key features, performance capabilities, and assess their applicability for markerless product localization. Afterward, this thesis introduces a proposed fully markerless indirect tracking method along with its key components, including proposed vehicle heading estimation methods.

As a first contribution, this research assesses the applicability of the available inertial data-based heading estimation methods in the context of an industrial environment. It also investigates the applicability of the positioning and inertial data-based approach in industrial vehicle heading estimation and proposes a corresponding gyroscope heading drift correction algorithm (DCA). This algorithm is focused on the use of the positioning data as supplementary information to occasionally mitigate the accumulated drift errors. One of the main goals of this algorithm is to verify the reliability of positioning information in accurate vehicle heading estimation, as well as define its primary advantages and limitations. In the full-scale experimental test campaign, the proposed DCA algorithm is used for the heading tracking of a highly maneuverable forklift in the industrial area, where it demonstrates a significant reduction of the gyroscope median absolute heading error from 44.1 degrees down to a sub-6 degree level. This confirms the effectiveness of the positioning and inertial data fusion for the reliable industrial vehicle heading estimation and enables further research in this field.

The second contribution focuses on the implementation of the Adaptive Extended Kalman Filter (A-EKF) algorithm for the UWB AP-TWR (Active-Passive Two-Way Ranging) protocol-based positioning. In the context of this research, this contribution assesses the performance of a non-linear state-of-the-art Kalman filter algorithm in real-life applications, as well as investigates the implementation methods and advantages of the adaptive Kalman filter algorithm for its further use in the field of vehicle heading estimation. In experimental testing, the implemented A-EKF algorithm has demonstrated a significant improvement of the AP-TWR-based UWB positioning over sole SS-TWR (Single-Sided Two-Way Ranging) and AP-TWR based positioning in obstructed industrial areas. The A-EKF algorithm has shown a reduction of the peak positioning errors RMS by a factor of three in stationary 3D testing, and a ninefold RMSE reduction in the movement test scenario. These results highlight the significance of the Kalman filter adaptivity feature, especially in real-life applications, which is eventually used in later contributions.

As a third contribution, this research proposes an Adaptive Tandem Kalman Filter (ATKF) algorithmic method for an accurate and reliable vehicle heading estimation. This algorithm represents an adaptive version of the Kalman filter algorithm with a non-conventional tandem structure. It performs a competitive fusion of inertial and positioning information for the real-time vehicle heading estimation in different scenarios, including intense maneuvering and reverse movement. The proposed DCA and ATKF algorithms are tested in

a series of simulations to define their expected performance capabilities and reliability limits. Simulated tests confirm a significant robustness of the DCA algorithm against high inertial data drift rates, along with high sensitivity to the positioning data quality and cases of intense maneuvering. ATKF algorithm demonstrates a balanced reliability and stability in case of both poor positioning data quality and high inertial drift rates, even in cases of intense maneuvering.

This contribution also covers an experimental validation of the obtained simulations' results in a live industrial environment by using a highly maneuverable forklift. The DCA algorithm demonstrates the median absolute error reduction in IMU tracked forklift heading down to 1 degree level with moderate to high stability. The proposed ATKF algorithm, on the other hand, experimentally achieves a sub-1 degree accuracy in forklift heading estimation with exceptional stability and high robustness even in cases of poor input data quality. In the same test campaign, both of the proposed algorithms outperform the tested state-of-the-art magnetometer-based heading estimation algorithms, such as Mahony, Madgwick, and complementary filters.

A fourth contribution of this research proposes a novel method for a sensor fusion-based automatic and three-dimensional tracking of fully unmarked industrial products. The proposed method prioritizes the positioning accuracy, cost- and energy efficiency, reduced computational complexity and processing requirements, while achieving high scalability. Additionally, the proposed method focuses on the seamless integration into the industrial environment and machinery to minimize its interference in the natural workflow. To fully automate the proposed indirect tracking method, this contribution also proposes a sensor fusion algorithm for automatic payload pick-up & drop-down detection (A-PDD). This algorithm performs a complementary fusion of multi-sensor information to detect the exact moment of the payload loading or unloading. This enables an indirect identification of the picked up product and allows to determine the exact storage location of the dropped down payload.

Conducted down-scaled and full-scale experimental tests of the proposed indirect tracking method demonstrate its high absolute and repeatability accuracy in product positioning, closely comparable to the performance of the underlying positioning system. Thus, in the full-scale test campaign, the industrial product was positioned by the UWB-based indirect tracking method with sub-30 cm accuracy, which closely corresponds to the initial declared 10-30 cm accuracy of the underlying UWB positioning system.

Due to its high scalability, cost- and energy efficiency, as well as reduced maintenance requirements and high potential for modifications, the proposed markerless indirect tracking method is expected to be widely applicable in industry and warehousing, utilizing different industrial machinery and material handling equipment, such as forklifts, lifters, or cranes. The developed A-PDD algorithm for automatic pick-up & drop-down detection may also find its use in the industry and warehousing automation. Presented contributions in the field of vehicle heading tracking, including a developed positioning data-based DCA algorithm for IMU drift correction and ATKF algorithm for vehicle heading estimation, may find their use in a wide variety of fields, such as robotics, autonomous vehicles, as well as industry and logistics automation.

## Kokkuvõte

### Andurisulandusel põhinevate kaudsete positsioneerimismetodite edasiarendused

Käesolev doktoritöö käsitleb tööstuslikku vajadust ja uurib meetodit, mis võimaldaks täielikult markeriteta tööstustoodete täpset ja reaalaajalist positsioneerimist. Uuritava meetodi peamine motivatsioon on võimaldada erinevate tööstustoodete tuvastamist ja täpset jälgimist kuluefektiivsel viisil ilma jälgimis- või identifitseerimisüksuste otsese kinnitamiseta. Antud meetodi disainikriteerium tagab positsioneerimis- või identifitseerimiseadmete vältimist, sealhulgas QR-koodide, triipkoodide või muude markerite otsest kinnitamist tootele, jättes need täielikult märgistamata. Käesolev töö algab olemasolevate kaudse jälgimise meetodite uurimisega, et hinnata nende põhiomadusi, jõudlust ning hinnata nende rakendatavust markeriteta toodete positsioneerimiseks. Seejärel tutvustatakse käesolevas doktoritöö raames väljapakutud täielikku markeriteta kaudset jälgimismetodit koos selle põhikomponentidega, sealhulgas kavandatud sõiduki suuna hindamise meetodeid.

Esmalt pakub doktoritöö hinnangut olemasolevate ja laialt kasutatavate meetodite rakendatavust inertsiaalandurite põhinevate suuna jälgimiseks tööstuskeskkonna kontekstis ja kaudse jälgimise meetodi osana. Samuti uuritakse positsioneerimis- ja inertsiaalandmetel põhineva lähenemisviisi rakendatavust tööstussõidukite suuna jälgimisel ning pakutakse välja vastav güroskoobi suuna triivi korrigeerimise algoritm (DCA). See algoritm keskendub positsioneerimisandmete kasutamisele lisateabena, aja jooksul kogunenud triivivigade aegajaliseks leevendamiseks. Selle algoritmi peamine eesmärk on kontrollida positsioneerimisteabe usaldusväärsust sõiduki suuna täpsel jälgimisel, samuti määratleda rakendatud algoritmi peamised eelised ja piirangud. Mõõtekatsetes kasutatakse pakutud DCA-algoritmi manööverdatava tõstuki suuna jälgimiseks tööstuspiirkonnas, kus rakendatud algoritm näitas güroskoobi absoluutse mediaani suunavea olulist vähenemist 44,1 kraadilt alla 6 kraadini. See kinnitab positsioneerimis- ja inertsiaal andmete liitmise tõhusust tööstussõidukite usaldusväärse suuna hindamiseks ning võimaldab selles valdkonnas edasisi uuringuid.

Teine doktoritöö põhipanus keskendub adaptiivse laiendatud Kalmani filtri (A-EKF) algoritmi rakendamisele UWB AP-TWR (Active-Passive Two-Way Ranging) protokollipõhise asukoha arvutamise ja filtreerimise jaoks. Selle uurimistöö kontekstis hinnatakse selles panuses mittelineaarse tipptasemel Kalmani filtrialgoritmi toimivust reaalses rakenduses, samuti uuritakse adaptiivse Kalmani filtrialgoritmi rakendusmeetodeid ja eeliseid selle edasiseks kasutamiseks sõiduki suuna jälgimise valdkonnas. Eksperimentaalsetes katsetes on rakendatud A-EKF algoritm näidanud AP-TWR-põhise UWB positsioneerimise olulist paranemist võrreldes ainsuse SS-TWR-i (Single-Sided Two-Way Ranging) ja AP-TWR-põhise positsioneerimisega takistatud tööstuspiirkondades. A-EKF-i algoritm on näidanud tippositsioneerimisvigade RMS-i kolmekordset vähenemist statsionaarses 3D-testimises ning üheksakordset RMSE vähenemist liikumistesti stsenaariumis. Need tulemused rõhutavad Kalmani filtri adaptiivsuse funktsiooni olulisust reaalses rakenduses, mille lõpuks kasutatakse hilisemates kaastöodes.

Järgmisena pakub käesolev doktoritöö välja Adaptiivse Tandem Kalmani Filtri (ATKF) algoritmilise meetodi täpseks usaldusväärseks ja reaalaajaliseks sõiduki suuna jälgimiseks. Väljapakutud algoritm põhineb Kalmani filtril, võttes ebakonventsionaalse adaptiivse tandemstruktuuriga vormi. ATKF algoritm teostab inertsiaalse ja positsioneerimisteabe andurite liitmist täpse, usaldusväärse, ja reaalaajalise sõiduki suuna jälgimiseks erinevate stsenaariumides, nagu näiteks intensiivse manööverdamise ja tagurdamise korral. Kavandatud DCA- ja ATKF-algoritme testitakse arvutikatsete seerias, et määratleda nende eelda-

tavad jõudlusvõimalused ja töökindluse piirid. Arvutikatsete abil kinnitati DCA algoritmi märkimisväärselt vastupidavust andmete inertsaalse triivimise vastu kannatades samas positsioneerimisandmete müradest tingitud tundlikkuse all, eriti intensiivse manööverdamise korral. Väljapakutud ATKF algoritm seevastu näitab tasakaalustatud töökindlust ja stabiilsust nii halva positsioneerimisteabe kui ka suure inertsaalse triivikiiruse korral, isegi intensiivse manööverdamise korral.

See panus hõlmab ka saadud arvutitestide tulemuste katselist valideerimist reaalses tööstuskeskkonnas rohkelt manööverdatavat tõstuki kasutades. DCA algoritm näitab IMU suuna jälgimise absoluutse vea mediaanväärtust 1 kraadi tasemele ning mõõdukat kuni kõrget stabiilsust. Väljapakutud ATKF algoritm seevastu saavutab kahveltõstuki suuna jälgimisel alla 1-kraadise täpsuse, kõrge stabiilsuse ja vastupidavusega isegi halva sisendandmete kvaliteedi korral. Samas katsekampaanias ületavad mõlemad pakutud algoritmid testitud tiiptasemelisi magnetomeetritel põhinevaid suuna jälgimise algoritme, seal hulgas Mahony, Madgwick ja Complementary filter.

Viimasena pakub antud doktoritöö välja uudse andurisulandusel põhineva meetodi täielikult märgistamata tööstustoodete, varade ja seadmete automaatseks reaalaaja kolmemõõtmeliseks jälgimiseks. Pakutud meetod seab esikohale positsioneerimise täpsuse, kulu- ja energiatõhususe, töökindluse, väiksema arvutusliku keerukuse ja töötlemisnõuded, ning seekaudu tagab kõrge laiendatavuse. Lisaks keskendub kavandatud meetod selle sujuvale integreerimisele tööstuskeskkonda ja kasutatud masinatesse, et minimeerida selle mõju tööstusprotsessidele ja loomulikule töövoogudele. Pakutud kaudse jälgimismeetodi täielikuks automatiseerimiseks on pakutud ka andurisulandusel põhinev algoritmiline meetod toote automaatse ülesvõtmise ja mahapaneku tuvastamiseks (A-PDD). See algoritm teostab mitme anduriga teabe täiendava liitmise, et tuvastada tõstuki käitumise järgi tööstustootte peale- või mahalaadimise täpne hetk. See võimaldab võimaldab kaudsel jälgimismeetodil määratlada tööstustootte täpse asukoha.

Pakutud kaudse positsioneerimismeetodi praktilised katsed näitavad selle suurt absoluutset ja korratavuse täpsust toote positsioneerimisel, võrdluse aluseks oleva positsioneerimissüsteemi jõudlusega. Seega pakutud UWB-põhinev kaudne positsioneerimismeetod sooritatud katsekampaanias näitas tööstustootte jälgimist alla 30 cm täpsusega, mis lähidalt vastab aluseks oleva UWB positsioneerimissüsteemi deklareeritud 10–30 cm täpsusele.

Tänu suurele laiendatavusele, kulu- ja energiatõhususele, samuti väiksematele hoolitusvajadustele ning suurele muudatavusele pakutud markeriteta kaudne positsioneerimismeetod on laialdaselt rakendatav tööstuses ja laonduses kasutatavate erinevate tööstusmasinatel ja materjalikäitlusseadmetel, näiteks kahveltõstukite, tõstukite või kraanade puhul. Doktoritöö raames väljatöötatud automaatse pealevõtmise ja mahapaneku tuvastamisalgoritm (A-PDD) võib leida oma kasutust ka tööstuses ja laoautomaatikas. Avaldatud teadusartiklid sõiduki suuna jälgimise valdkonnas, sealhulgas väljatöötatud positsioneerimisandmetel põhinevad DCA ja ATKF algoritmid sõiduki suuna jälgimiseks võivad leida oma kasutust paljudes valdkondades, nagu robotika, autonoomsed sõidukid, ning tööstus ja logistika automatiseerimine.



## Appendix 1

### I

A. Fjodorov, S. Ulp, M. M. Alam, and A. Kuusik, "Inertial and Positioning Sensors Fusion for Indirect Location Tracking in Warehouse Inventory Management," *2023 International Conference on Control, Automation and Diagnosis (ICCAD)*, pp. 1–7, 2023





# Inertial and positioning sensors fusion for indirect location tracking in warehouse inventory management

Aleksei Fjodorov<sup>†</sup> ‡, Sander Ulp<sup>‡</sup>, Muhammad Mahtab Alam<sup>†</sup>, Alar Kuusik<sup>†</sup>

<sup>†</sup> Thomas Johann Seebeck Department of Electronics

Tallinn University of Technology

<sup>‡</sup> Eliko Tehnoloogia Arenduskeskus OU

Tallinn, Estonia

{aleksei.fjodorov1, muhammad.alam, alar.kuusik}@taltech.ee, sander.ulp@eliko.ee

**Abstract**—This paper proposes a heading drift correction algorithm for inertial and positioning sensor fusion for indirect localization of industrial products in warehouse management. The tracking of objects is performed indirectly during their transportation by constantly tracked industrial machinery (e.g., forklift). The fusion of inertial and positioning units provide real-time information on position and heading of industrial machinery, which is transformed into real-time position of the carried payload. Within this work, a test setup was assembled and based on the proposed inertial measurement unit (IMU) heading correction algorithm. The performance of the solution was assessed in an industrial production environment. Results show that the proposed algorithm was able to reduce the heading median error from 44.1 degrees to 5.9 degrees, which is 86.5% improvement in measured heading accuracy. This results in an improvement of the positioning accuracy from 1.91 m median error to 0.26 m median error for the indirectly tracked object.

**Index Terms**—Tagless, indirect, tracking, IMU, GNSS, UWB RTLS, forklift, warehousing

## I. INTRODUCTION

In recent years, all aspects of industries become more efficient through integration of various complex and smart solutions aimed to improve its performance and assist the working personnel in all possible ways. For instance, as part of integrating Industry 4.0. Intelligent warehousing for instance, is aimed to simplify, automatize and increase the awareness of various aspects of management processes at warehouses and production sites, especially where the manual, reliable and real time product tracking can be challenging [1].

Variety of different publications propose different smart solutions for products tracking in warehouses, production and other industrial areas. Majority of them describe localization solutions with the use of portable tracking units – tags. Direct industrial products marking with active (e.g., UWB (Ultra Wide-band) [2], [3]), or passive (RFID (Radio-Frequency Identification) [4]) positioning tags, allows them to be tracked in real-time by the corresponding infrastructure [5]. These technologies are also often assisted with different identification technologies used for asset recognition. It is often done with directly attached passive RFID tags [6], barcodes or QR codes

[7]. As these technologies were originally designed for identification, they are often used to assist a primary positioning system (e.g. UWB [8], [9]). Their use as primary technologies for objects' localization would require significantly more complicated and expensive infrastructure to provide a base level of objects' localization [10].

Some sources also propose assets' identification via recognition of reference objects (e.g., forklift pallets) by using LiDARs (Light Detection and Ranging) [11] or visual (camera based) sensing [12], or RGB-D (Red Green Blue-Depth) cameras [13]. Unfortunately, fragile parts of optical sensors are naturally sensitive to minor environmental pollution (e.g., dust or moisture), typically encountered in industrial environments.

Unfortunately, certain products cannot be directly marked with tags, due to different environmental or physical processes these products go through, where any attached positioning tags have a high possibility to be physically damaged or destroyed. For instance, in metal production sites material goes through high temperature and physical formation processes during its life cycle, which will instantly destroy any attached tag [14].

Industrial products can be indirectly tracked during their transportation together with constantly tracked industrial machinery. In this case, location of the carried object measured during its drop down event represents its storage location until it is picked up for a further transportation. In this approach, a real-time position of transported payload corresponds to the position of payload carrying unit (e.g., forklift tynes). The exact position of load carrying unit in its turn can be determined from continuously measured position and heading of the used carrier machinery. Tracking of this carrier machinery heading can be performed in several different ways. For example, positioning the industrial vehicle with several positioning units and calculating the heading vector from measured coordinates. However, this will double the number or increase the complexity of the required positioning units and increase the cost of the solution. This cost is further increased when the tracked vehicle is tracked both indoors and outdoors [15].

This paper proposes a novel approach for indirect products

localization within warehousing, production and industrial areas without their direct tagging. Focus is on using an inertial measurement unit (IMU) to obtain a real-time industrial machinery heading information. Using IMU data for heading information requires compensating for drift which is typical for inertial measurement units [16]. IMU drift correction is usually compensated with assistance of magnetometer sensors [17], [18]. However, magnetometer data becomes unreliable to use for drift compensation in industrial environments due to its high sensitivity to magnetic interference [19]. This paper proposes a novel coordinates-based heading correction algorithm to compensate for the heading drift without requiring magnetometer data. The paper is divided into 4 sections. The first section defines main the problem addressed in this work with proposed methodology. The second section describes the proposed algorithm for heading data drift compensation. The third section specifies the experimental setup, describes the performed live experiments and demonstrates the results. The last section concludes the paper.

## II. PROBLEM

The main problem to be solved within this work is the fusion of positioning data with IMU data for reliable real-time industrial vehicle tracking in terms of its location and orientation. The location and orientation of the vehicle are used for indirect localization of completely tagless assets in an industrial area (e.g. warehouse). During payload pick-up, transportation and drop-down events the payload location directly corresponds to the location of the payload carrying location (e.g., on the forklift tynes). The positioning units in most cases cannot be attached directly to the location of the payload on the vehicle due to risk of damaging the unit or obstructing the unit with the payload or environment. Therefore, the location of the positioning unit needs to be transformed to the location of the payload carrying location. The heading information and known offset is utilized to define the exact location of the payload carrying location, and consequently, a transported payload in relation to the deployed positioning unit.

A direct use of IMU measured heading information has poor reliability due to a presence of drift, which is the continuous accumulation of angular errors over time. The drift of the measurements is caused by gyroscope bias instabilities and internal noise [16]. Several methods are often used to minimize IMU drift including gyroscope and accelerometer output data filtering with the use of complementary filter [20] and its improved variations of Mahony and Madgwick filters [21]. Different variations of linear and non-linear Kalman filters are also widely used for IMU fusion with and its drift elimination [22]–[24].

Particularly the heading rotation (*yaw* Euler angle), which corresponds to a machinery heading, is represented/described with integrated angular velocity readings of gyroscope in two-dimensional plane around vertical Z-axis. While the angular drift present in IMU measured *roll* and *pitch* Euler angles can be relatively effectively compensated with assistance of

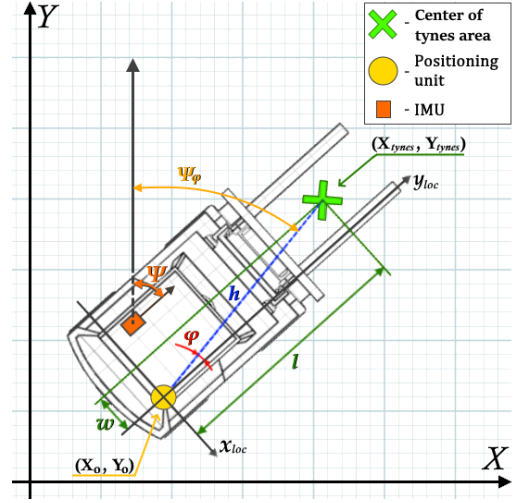


Fig. 1. Schematic illustration of the forklift tynes' area center relation to the deployed setup components within forklift local ( $x_{loc}, y_{loc}$ ) and main coordinate systems ( $X, Y$ ).

accelerometer data, a similarly effective *yaw* angle drift compensation requires a use of magnetometer [17], [18]. Magnetometers in their turn are naturally sensitive to environmental magnetic interference [19]. It makes this sensor unreliable for a proper *yaw* angle correction in industrial environmental conditions and attached to the heavy industrial machinery [19]. For this reason, the use of magnetometer is avoided in this work.

### A. Methodology

In the case of a forklift, during the payload transportation process, the exact location of the transported payload directly corresponds to the position of the forklift tynes' center. Geometrically, the position of the forklift tynes' center in relation to the deployed positioning unit has a known constant offset and depends on a placement of measurement units on the forklift (i.e. their location in the local coordinate system of the forklift body frame). As it is shown on Fig. 1, the exact location of the tynes' area center  $X_{tynes}$  and  $Y_{tynes}$  in the main coordinate system ( $X, Y$ ) can be calculated with the use of measured heading and positioning data as follows:

$$\begin{cases} X_{tynes} = X_o + \sin(\Psi_\varphi) \cdot h \\ Y_{tynes} = Y_o + \cos(\Psi_\varphi) \cdot h \end{cases} \quad (1)$$

where  $X_o$  and  $Y_o$  are the measured coordinates of the positioning unit in the main coordinate system;  $h$  is the known constant offset between the positioning unit and the center of the forklift tynes area.  $\Psi_\varphi$  is the tynes' direction from the perspective of the positioning unit in the main coordinate system.  $\Psi_\varphi$  represents the IMU measured heading of the setup  $\Psi$  combined with the constant angular offset  $\varphi$  within forklift

body frame (local) coordinate system  $(x_{loc}, y_{loc})$  between the direction of the tynes' center from the positioning unit perspective, and the positive  $y_{loc}$  axis of local coordinates system. These parameters are calculated in the following way:

$$h = \sqrt{w^2 + l^2} \quad (2)$$

$$\Psi_\varphi = \Psi + \varphi, \quad \text{where } \varphi = \text{atan2}(w, l), \quad (3)$$

where  $w$  and  $l$  are tynes' location offsets from the  $(x_{loc}, y_{loc})$  coordinate system origin respectively in  $x_{loc}$  and  $y_{loc}$  axes. The forklift local coordinate system  $(x_{loc}, y_{loc})$  describes the relation of the forklift to the deployed sensors and location of payload carrying unit (i.e. tynes). The origin of the local coordinate system corresponds to the location of the positioning unit  $(X_o, Y_o)$  in the main coordinate system.

The tynes' position error depends on the heading error, which can be calculated as follows:

$$\varepsilon_{tynes} = 2 \cdot \sin\left(\frac{\varepsilon_\Psi}{2}\right) \cdot h, \quad (4)$$

where  $\varepsilon_{tynes}$  is the tynes' position error calculated from the heading error  $\varepsilon_\Psi$ . Therefore, with this approach, a 1 degree setup heading error will cause 1.75 cm error per 1 m of offset in  $h$ .

### III. PROPOSED IMU HEADING CORRECTION ALGORITHM

This section describes the proposed IMU heading correction algorithm. The algorithm performs corrections to the over-time accumulative errors present in the IMU measured heading.

The proposed algorithm iteratively compensates for the angular drift present in the measured IMU heading based on the positioning data. Within the algorithm, the measured IMU heading (*yaw* Euler angle) is combined with a conditionally updated correction value, which is only calculated from the positioning data when the requirements are met for a certain type of movement behaviour. Recent positioning data samples are stored in limited size FIFO (first in, first out) buffer. To calculate an updated correction value for the IMU heading, the stored positioning data is required to indicate a relatively straight movement above the defined minimal speed. Actual parameters of the required movement are preliminarily defined depending on the specific use case. These movement requirements separate an actual movement in clearly determined direction from possible noise present in data and directional readings during manoeuvring. Once these movement requirements are met the coordinates based calculated heading is considered as valid. The change in dynamics in valid heading data is also tracked to detect a possible reverse movement event. In this case the coordinates based heading is expected to show a rapid change to the opposite direction with a minor change in IMU measured heading. The difference between valid movement direction calculated from the positioning data and the raw heading provided by IMU module is then considered as the approximately accurate correction for the IMU measured heading. The described IMU heading correction algorithm is demonstrated in Algorithm 1.

---

#### Algorithm 1: Horizontal plane coordinates based IMU heading correction

---

**Parameters:** Minimal movement speed:  $v_{min}$  [m/s]  
Maximal heading range:  $\alpha_{max}$  [deg]  
FIFO buffer fixed length:  $\mu$   
Reverse movement threshold:  $\beta$  [deg]  
Previous or initial correction value:  $\delta_0$  [deg]  
Previous or initial valid coordinates based heading:  $\theta_0$  [deg]  
Previous or initial IMU heading:  $\psi_0$  [deg], measured together with  $\theta_0$  [deg]

**Input Data:** Measured setup coordinates:  $(X_o, Y_o)$  [m]

IMU measured heading:  $\psi$  [deg]

**Outputs :** Corrected heading:  $\Psi$  [deg]

Heading correction value:  $\delta$  [deg]

- 1 Apply previously calculated correction to the received IMU heading  $\Psi = \psi + \delta_0$
  - 2 Save the new coordinate reading  $(X_o, Y_o)$  in the FIFO buffer  $W$  with length  $\mu$
  - 3 **foreach** consecutive coordinates pair  $k \in W$  **do**
  - 4     Calculate the set of movement velocities  $v(k)$
  - 5     Calculate the set of heading angles  $\alpha(k)$
  - 6 **end**
  - 7 Calculate the range  $R_\alpha$  of heading angles' set  $\alpha(k)$
  - 8 **if**  $\forall v \in v(k) > v_{min} \ \&\& \ R_\alpha \leq \alpha_{max}$  **then**
  - 9     Calculate the mean heading  $\hat{\theta}_\alpha$  from heading angles set  $\alpha(k)$
  - 10    **if**  $|\hat{\theta}_\alpha - \theta_0| > 2\beta \ \&\& \ |\hat{\psi} - \psi_0| < \beta$  **then**
  - 11     Apply the detected reverse movement correction:  $\hat{\theta}_\alpha = \hat{\theta}_\alpha + 180$
  - 12    **end**
  - 13    Update the previous valid coordinates based heading:  $\theta_0 = \hat{\theta}_\alpha$
  - 14    Update the last corresponding IMU measured heading:  $\psi_0 = \hat{\psi}$
  - 15    Calculate the new correction value for IMU heading:  $\delta = \hat{\theta}_\alpha - \psi$
  - 16 **else**
  - 17     $\delta = \delta_0$
  - 18 **end**
- 

### IV. DESCRIPTION OF THE SETUP

In order to experimentally test the proposed heading drift compensation algorithm with the proposed sensor combination approach for industrial vehicle position and heading tracking a test setup was assembled and deployed on the forklift. The 9-DOF 32-bit cortex M0+ microcontroller assisted Inertial Measurement Unit BNO055 was used as the inertial measurement unit for the real-time heading tracking setup [25]. As a source of positioning information on the tracked setup it was individually used one of two separate high accuracy

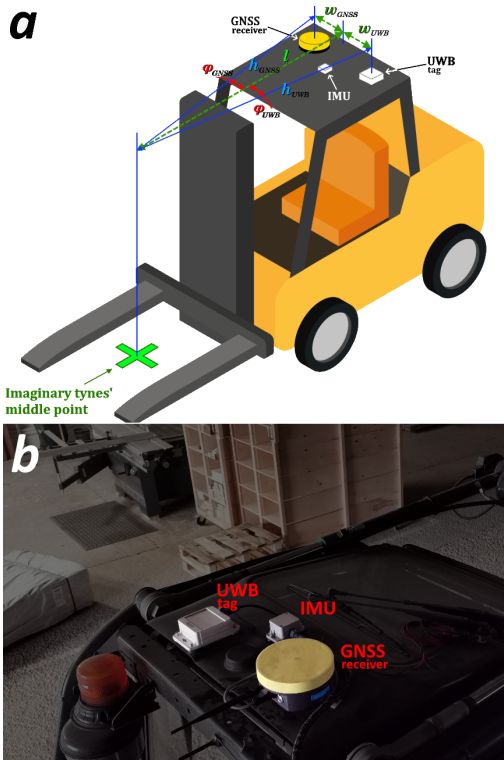


Fig. 2. Illustrative (a) and practical (b) test setup deployment on a forklift for testing in real warehouse environment. The deployment includes an IMU unit, a GNSS positioning unit for outdoor positioning and an UWB tag for indoor localization.

positioning systems depending on indoor or outdoor environment. These systems are respectively UWB indoor positioning system [26] represented with Eliko UWB RTLS system [27], and GNSS-RTK (Global Navigation Satellite System - Real Time Kinematic) [28], represented with and Fieldbee RTK GNSS system [29].

An illustrative setup deployment topology for performed experiments is shown on a Fig. 2 (a) with corresponding offsets explained earlier on Fig. 1, as well as its deployment on the actual forklift shown on Fig. 2 (b). All the gathered positioning and heading data was then transmitted to the main server for necessary calculations as heading corrections and resulting tynes' position, and further data storage. Approximate setup heading error and corresponding correction were calculated from collected data with the use of proposed algorithm.

#### A. Tests

The practical experiments were conducted using a forklift operating in an industrial production and warehousing environment. The tests were intended to evaluate the overall capability of proposed approach to track a position and heading of



Fig. 3. Sample images of the forklift used for practical testing (a), and sample of payload, meant to be tracked with proposed indirect tracking approach (b).

the forklift in real-time, and more particularly, evaluate a capability of the proposed algorithm to define and apply valid positioning data based corrections to the IMU measured heading. Fig. 3 (a) demonstrates the forklift with the deployed setup of sensor units during the live tests. Fig. 3 (b) shows an example payload from the production site, which cannot be localized with directly attached tag and is meant to be tracked indirectly with the proposed approach.

While constantly being tracked the forklift was moving around the industrial production facility performing its usual payload transportation procedures followed by corresponding manoeuvring between different obstacles in both indoor and outdoor areas. The real-time position and the heading of the forklift were simultaneously tracked using the IMU unit and one of the two deployed positioning units depending on the operating environment. In order to properly test the performance of the proposed approach and the IMU drift correction algorithm the experimental movement path was altered by different manoeuvring patterns of the forklift including a three-point turn, short term reverse movements, an approximate 720 degrees turnaround, straight movements at different speeds and stops.

#### B. Results

Fig. 4 shows the corresponding data collected during the aforementioned test. The tracked coordinates with both raw and the corrected forklift heading information are represented with blue dots, red and blue arrows, respectively. The results

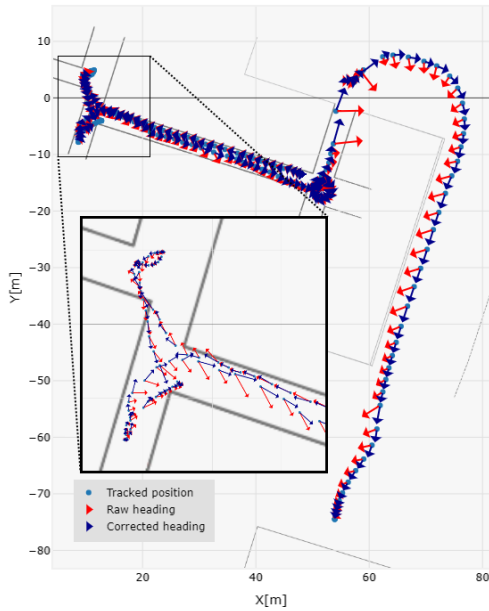


Fig. 4. Visualized sample data of the position and orientation of the forklift collected during the live test. The tracked forklift coordinates are represented with blue dots; red and blue arrows indicate the setup heading simultaneously measured by the onboard IMU respectively before and after applying the proposed correction algorithm.

demonstrate the significant and visually observable improvement of the IMU measured heading after the proposed algorithm was applied. Result show that the performance of the proposed algorithm is able to define and apply a proper correction to IMU heading drift in real-time and in practical experiments.

In order to evaluate the performance of the proposed heading correction algorithm, the IMU heading errors were compared to the corresponding heading data from the ground truth before and after the proposed algorithm was applied. Fig. 5 shows graphs of averaged errors of IMU provided forklift heading directly (colour coded with red) and the processed heading with correction algorithm (colour coded with green). The dashed lines demonstrate the overall median errors for both cases. Results show that during this test the IMU has provided the forklift orientation data with accumulated median error of 44.1 degrees. According to (4) this heading error would translate to potential 1.914 m error in the payload pick up or drop down location. Nearly 2 meters error in payload interaction location could be critical for the indirect tracking problem. Depending on the asset size, this error can cause a critical position error and can be misinterpreted as potential pick up of neighbour package or error in identifying the location of the asset.

The proposed heading correction algorithm, in its turn, has

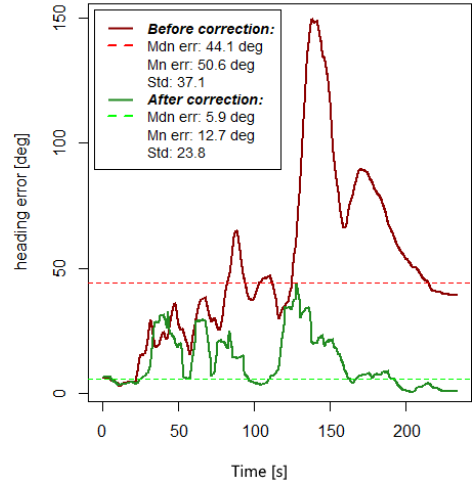


Fig. 5. Graphs of averaged errors in IMU provided setup heading with the corresponding error mean, median and standard deviation results before (red) and after (green) the IMU heading correction algorithm was applied.

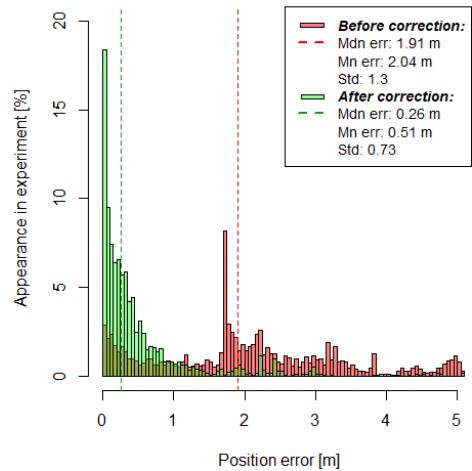


Fig. 6. Histogram of the tynes position errors percentage distribution obtained during the performed test with (green) and without (red) the use of the proposed correction algorithm. Median errors for both cases are marked with dashed lines of respective colors.

reduced the median error of IMU heading to 5.9 degrees, which is approximately 86.8 % of IMU heading accuracy improvement. The 5.9 degrees error corresponds to 0.262 m error in package pick up location in accordance with (4) for this particular forklift sensor deployment. This improvement of error in package pick up & drop down location allows a relatively precise tracking of interacted payloads. The 26 cm positioning error can be neglected in the case of payload sizes, which are expected to be carried by forklifts. The corresponding histogram of the percentage distribution of tynes position errors obtained during the performed test is shown on Fig. 6. The tynes positioning errors before and after the correction algorithm was applied are color-coded with red and green respectively. The median errors, the mean errors and the standard deviations of the errors are provided for both cases. The median errors are marked on the histogram with the dashed lines of the corresponding colors.

## V. CONCLUSIONS

In this paper, a correction algorithm was proposed to provide heading drift compensation based on the positioning data and IMU data for indirect localization of industrial products in warehouse management. In this approach, the objects are localized during their transportation by precise tracking of position and heading of corresponding industrial machinery. The position and heading of the industrial machine is transformed into the location of the object being transported. The capability of the sensor combination alongside with the proposed algorithm to track the orientation of a forklift during its routine movement and manoeuvring was practically tested in an industrial environment. Experimental results show that the proposed algorithm was able to estimate and apply valid positioning data based corrections to the IMU measured heading reducing accumulative IMU heading error by 86.5 % from 44.1 degrees to 5.9 degrees. This improvement corresponds to reduction of the tracked object's position median error from 1.9 m down to 0.26 m. Experimental results have demonstrated that the proposed method with IMU & positioning fusion is able to be used in real industrial conditions to perform product indirect tracking.

## ACKNOWLEDGMENT

This project has received funding from the European Union's Horizon 2020 Research programme under grant agreement No 101058505. Development of an industrial digital control system based on precise positioning technology ELIKO TAK and Atemix Automatika nr. 2014-2020.4.02.21-0311. This research has also been supported in part by the Internet of Intelligent Things project of Estonian IT Academy program and Estonian Research Council under Grant PUT-PRG424.

## REFERENCES

- [1] M. van Geest, B. Tekinerdogan, and C. Catal, "Design of a reference architecture for developing smart warehouses in industry 4.0," *Computers in industry*, vol. 124, p. 103343, 2021.
- [2] S. Shyam, S. Juliet, and K. Ezra, "A UWB Based Indoor Asset Tracking Architecture for Industry 4.0," in *2022 4th International Conference on Smart Systems and Inventive Technology (ICSSIT)*. IEEE, 2022, pp. 501–506.
- [3] A. Volpi, L. Tebaldi, G. Matrella, R. Montanari, and E. Bottani, "Low-Cost UWB Based Real-Time Locating System: Development, Lab Test, Industrial Implementation and Economic Assessment," *Sensors*, vol. 23, no. 3, p. 1124, 2023.
- [4] A. Frankó, G. Vida, and P. Varga, "Reliable identification schemes for asset and production tracking in industry 4.0," *Sensors*, vol. 20, no. 13, p. 3709, 2020.
- [5] A. Motroni, A. Buffi, P. Nepa, M. Pesi, and A. Congi, "An Action Classification Method for Forklift Monitoring in Industry 4.0 Scenarios," *Sensors*, vol. 21, no. 15, p. 5183, 2021.
- [6] S. Jeon, M. Choi, G. Kim, and B. Hong, "Localization of Pallets Based on Passive RFID Tags," in *2010 Seventh International Conference on Information Technology: New Generations*, 2010, pp. 834–839.
- [7] H. Borstell, J. Kluth, M. Jaeschke, C. Plate, B. Gebert, and K. Richter, "Pallet monitoring system based on a heterogeneous sensor network for transparent warehouse processes," in *2014 Sensor Data Fusion: Trends, Solutions, Applications (SDF)*, 2014, pp. 1–6.
- [8] A. Motroni, A. Buffi, and P. Nepa, "Forklift Tracking: Industry 4.0 Implementation in Large-Scale Warehouses through UWB Sensor Fusion," *Applied Sciences*, vol. 11, no. 22, p. 10607, 2021.
- [9] K. Zhao, M. Zhu, B. Xiao, X. Yang, C. Gong, and J. Wu, "Joint RFID and UWB Technologies in Intelligent Warehousing Management System," *IEEE Internet of Things Journal*, vol. 7, no. 12, pp. 11 640–11 655, 2020.
- [10] A. Motroni, A. Buffi, and P. Nepa, "A survey on indoor vehicle localization through RFID technology," *IEEE Access*, vol. 9, pp. 17 921–17 942, 2021.
- [11] N. Bellomo, E. Marcuzzi, L. Baglivo, M. Pertile, E. Bertolazzi, and M. De Cecco, "Pallet pose estimation with LIDAR and vision for autonomous forklifts," *IFAC Proceedings Volumes*, vol. 42, no. 4, pp. 612–617, 2009.
- [12] I. Vipper, "Laoliikumiste tuvastamine ja jalgimine turvakaamerate abil," 2021. [Online]. Available: <https://digikogu.taltech.ee/Item/41b80a70-73fd-4c08-997a-c6bea3375c94>
- [13] J. Zhao, B. Li, X. Wei, H. Lu, E. Lü, and X. Zhou, "Recognition and Location Algorithm for Pallets in Warehouses Using RGB-D Sensor," *Applied Sciences*, vol. 12, no. 20, p. 10331, 2022.
- [14] "How is aluminium made?" Norsk Hydro, accessed December 29, 2022. [Online]. Available: <https://www.hydro.com/en/aluminium/about-aluminium/how-its-made/>
- [15] K. Mannay, N. Benhadjyoussef, M. Machhout, and J. Urena, "Location and positioning systems: Performance and comparison," in *2016 4th International Conference on Control Engineering & Information Technology (CEIT)*. IEEE, 2016, pp. 1–6.
- [16] J. H. Wall, D. M. Bevy et al., "Characterization of various IMU error sources and the effect on navigation performance," in *Proceedings of the 18th international technical meeting of the satellite division of the institute of navigation (ION GNSS 2005)*, 2005, pp. 967–978.
- [17] M. L. Hoang and A. Pietrosanto, "Yaw/Heading optimization by drift elimination on MEMS gyroscope," *Sensors and Actuators A: Physical*, vol. 325, p. 112691, 2021.
- [18] S. A. Ludwig, K. D. Burnham, A. R. Jiménez, and P. A. Touma, "Comparison of attitude and heading reference systems using foot mounted MIMU sensor data: Basic, Madgwick, and Mahony," in *Sensors and Smart Structures Technologies for Civil, Mechanical, and Aerospace Systems 2018*, vol. 10598. SPIE, 2018, pp. 644–650.
- [19] E. M. Diaz, F. de Ponte Müller, A. R. Jiménez, and F. Zampella, "Evaluation of AHRS algorithms for inertial personal localization in industrial environments," in *2015 IEEE International Conference on Industrial Technology (ICIT)*. IEEE, 2015, pp. 3412–3417.
- [20] M. S. Listiyana et al., "Tracking Object based on GPS and IMU Sensor," in *2018 5th International Conference on Information Technology, Computer, and Electrical Engineering (ICITACEE)*. IEEE, 2018, pp. 214–218.
- [21] M. L. Hoang, A. Pietrosanto, S. D. Iacono, and V. Paciello, "Pre-processing technique for compass-less madgwick in heading estimation for industry 4.0," in *2020 IEEE International Instrumentation and Measurement Technology Conference (I2MTC)*. IEEE, 2020, pp. 1–6.

- [22] U. Ahmad, K. Poon, A. M. Altayyari, and M. R. Almazrouei, "A Low-cost Localization System for Warehouse Inventory Management," in *2019 International Conference on Electrical and Computing Technologies and Applications (ICECTA)*. IEEE, 2019, pp. 1–5.
- [23] R. Ali, R. Liu, A. Nayyar, B. Qureshi, and Z. Cao, "Tightly Coupling Fusion of UWB Ranging and IMU Pedestrian Dead Reckoning for Indoor Localization," *IEEE Access*, vol. 9, pp. 164 206–164 222, 2021.
- [24] S. Gupta, A. P. Singh, D. Deb, and S. Ozana, "Kalman Filter and Variants for Estimation in 2DOF Serial Flexible Link and Joint Using Fractional Order PID Controller," *Applied Sciences*, vol. 11, no. 15, p. 6693, 2021.
- [25] "BNO055 Intelligent 9-axis absolute orientation sensor." [Online]. Available: <https://www.bosch-sensortec.com/media/boschsensortec/downloads/datasheets/bst-bno055-ds000.pdf>
- [26] J. Kunthoth, A. Karkar, S. Al-Maadeed, and A. Al-Ali, "Indoor positioning and wayfinding systems: a survey," *Human-centric Computing and Information Sciences*, vol. 10, no. 1, pp. 1–41, 2020.
- [27] "Eliko UWB RTLS - the most accurate and reliable tracking," Nov 2022. [Online]. Available: <https://eliko.tech/uwb-rtls-ultra-wideband-real-time-location-system/>
- [28] "Introduction to RTK," accessed December 29, 2022. [Online]. Available: [https://base.xsens.com/s/article/Introduction-to-RTK?language=en\\_US](https://base.xsens.com/s/article/Introduction-to-RTK?language=en_US)
- [29] "RTK GPS system for Agriculture," Nov 2022. [Online]. Available: <https://www.fieldbee.com/product/rtk-gps-system/>





## Appendix 2

### II

T. Laadung, S. Ulp, A. Fjodorov, M. M. Alam, and Y. Le Moullec, "Adaptive Extended Kalman Filter Position Estimation Based on Ultra-Wideband Active-Passive Ranging Protocol," *IEEE Access*, 2023



Received 3 August 2023, accepted 13 August 2023, date of publication 25 August 2023, date of current version 31 August 2023.

Digital Object Identifier 10.1109/ACCESS.2023.3308696

## RESEARCH ARTICLE

# Adaptive Extended Kalman Filter Position Estimation Based on Ultra-Wideband Active-Passive Ranging Protocol

TAAVI LAADUNG<sup>1,2</sup>, SANDER ULP<sup>2</sup>, ALEKSEI FIODOROV<sup>1,2</sup>,  
MUHAMMAD MAHTAB ALAM<sup>1</sup>, (Senior Member, IEEE),  
AND YANNICK LE MOULLEC<sup>1</sup>, (Senior Member, IEEE)

<sup>1</sup>Thomas Johann Seebeck Department of Electronics, Tallinn University of Technology, 12616 Tallinn, Estonia

<sup>2</sup>ÕÜ Eliko Tehnoloogia Arenduskeskus, 12918 Tallinn, Estonia

Corresponding author: Taavi Laadung (taavi.laadung@taltech.ee)

This work has received funding partly from the European Union's Horizon 2020 Research and Innovation Program under Grant 951867 '5G-ROUTES' and Grant 101058505 '5G-TIMBER'. This research has also been supported by the European Regional Development Fund and Estonian Research Council under Grant PUT-PRG424 as well as TUT development program for the years 2016-2022" no. 2014-2020.4.01.16-0032, financed by the Regional Development Fund of the European Union.

**ABSTRACT** This paper first presents a comprehensive analysis of Non-Line-of-Sight (NLoS) error cases in the Ultra-Wideband (UWB) Active-Passive Two-Way Ranging (AP-TWR) protocol. Based on this analysis, we then propose the Adaptive Extended Kalman Filter (A-EKF) positioning method, utilizing variances calculated from AP-TWR range estimates, which are adapted based on the distance and intermittency of the range estimates. The proposed method needs no training data, nor any additional information about the environment the system is deployed in and does not yield any additional time delays. Based on experiments conducted in an industrial environment, the results show that the proposed method outperforms standard non-adaptive AP-TWR and active-only Single-Sided Two-Way Ranging (SS-TWR) methods in both stationary and movement tests. The stationary tests show that on average the proposed A-EKF method provides more than three times lower Root-Mean-Square-Error (RMSE) than the next best method (AP-TWR) in 3D positioning, while SS-TWR consistently performs worse by about 0.4 m in the z-axis. Additionally, the movement tests confirm the findings of the stationary tests and show that the challenging propagation conditions of the testing environment cause maximum errors at about 4.5 m for AP-TWR and SS-TWR, whereas the proposed A-EKF managed to mitigate these effects and reduce the error by 9 times, resulting in a maximum error of 0.5 m.

**INDEX TERMS** A-EKF, AP-TWR, EKF, position estimation, SS-TWR, UWB.

## I. INTRODUCTION

Ultra-Wideband (UWB) is a term used for radio communication that covers a bandwidth of over 500 MHz or 20% of the carrier center frequency. With the IEEE 802.15.4a-2007 amendment to the original IEEE 802.15.4-2006 standard, additional physical layers were introduced, which enabled precise ranging for UWB devices [1].

Utilizing UWB technology provides several benefits. The first one is the reduced interference with other narrowband wireless technologies thanks to the low transmission power

of the wideband signal [2]. Another benefit of UWB is the nanosecond-range duration of the signal pulses, which reduces the effect of multipath as the signals from multiple propagation paths can be determined and filtered out accordingly [3]. Additionally, the high temporal resolution allows for centimeter-level ranging by utilizing Time of Flight (ToF) estimation by various Two-Way Ranging methods or using the Time Difference of Arrival (TDoA) method [4].

Like Bluetooth or WiFi, UWB also relies on the propagation of Radio Frequency (RF) waves, allowing it to function effectively even in Non-Line-of-Sight (NLoS) situations, although with diminished performance [2], [5]. In contrast,

The associate editor coordinating the review of this manuscript and approving it for publication was Mohamed Kheir<sup>1</sup>.

indoor positioning systems based on light, vision, or infrared technologies are unable to operate in these conditions [6].

To reduce the accuracy/precision penalties induced by NLoS propagation conditions, numerous NLoS detection and/or mitigation methods have been proposed [7]. In the literature, these strategies typically fall into three distinct but not mutually exclusive categories which are briefly discussed in the following paragraphs.

Firstly, channel statistics-based methods exploit the additional information about the propagation channel itself. These methods may use the various channel state parameters directly supplied by UWB transceiver chips (i.e. Qorvo DW1000 [8]) or the raw Channel Impulse Response (CIR) values. The former provides quickly accessible values, while the latter entails more time-consuming processes to extract the CIR [9].

Krishnan et al. employed machine learning (ML) methods (Multi-Layer Perceptron and Boosted Decision Trees) with the DW1000 supplied parameters of first path power and total received power to achieve a classification accuracy of up to 87% [10]. Similarly, [11] utilized readily available signal parameters reported by the DW1000 transceiver chip and proposed classifiers based on Gaussian Distribution and Generalized Gaussian Distribution models, outperforming multiple state-of-the-art ML techniques. The authors of [12] put forward a Neural Network model, which was trained on distance measurements, the running standard deviation of these measurements, and several received signal parameters. The purpose was to derive weights for a weighted least squares position estimator, aiming to minimize the impact of NLoS. In addition to ML, various other methods have been researched, such as fuzzy inference of NLoS parameters combined with adaptive Kalman filtering [13], utilizing logistic regression for NLoS detection [14], and devising a power-performance metric based on the estimated first path power and the total received power [15].

A sizable amount of research has been conducted by using the raw CIR: NLoS detection via Capsule Networks [16], proposing an NLoS-induced outlier-aware positioning method based on multilayer perception [17], signal decomposition by One-Dimensional Wavelet Packet Analysis in conjunction with Convolutional Neural Networks (CNN) [18], Transformer deep learning model [19], combining the Multilayer Perceptron with CNN to reduce calculation complexity [20], overcoming the problem of site-specific models by conducting Long Short-Term Memory training to predict NLoS error magnitude and variance of measurements [21], to name a few of the latest. In addition to ML and deep learning, other methods utilizing the raw CIR are explored: NLoS detection using fuzzy comprehensive evaluation [22], a weighted particle filter based on probability density functions of Line-of-Sight (LoS)/NLoS correlation coefficients [23], and adaptively selecting the optimal anchors based on the channel quality indicators [24].

Although the methods based on raw CIR typically offer higher accuracy than methods based on the readily available channel parameters, they propose a drawback on the scalability of a positioning system as the extraction of the raw CIR values from the transceiver is a time-consuming process [9]. Moreover, employing ML models requires large amounts of high-quality training data, which makes the data-gathering process tedious, while the training and implementation of models could turn out computationally expensive [20], [25].

Secondly, the position estimate-based category is with the broadest reach, covering methods that use position estimation residuals, redundancy of ranging estimates, environment (geometrical and propagation) data, or time series of position estimates.

In [26], Chen proposed the seminal Residual Weighting (Rwgh) algorithm, in which the position estimates and their residuals are calculated with every possible range estimate combination. The final position estimate is found as a residual-weighted linear combination of the intermediate position estimates. Jiao et al. improved on the work of Chen, lowering the computational cost by introducing an iterative approach to residual weighting [27]. Given  $N$  range estimates, this method calculates position estimates and residuals with  $N - 1$  combinations, choosing the one with the lowest average residual. It then selects the subsets until possible and calculates the final weighted position estimate based. Even though the computational complexity is reduced compared to Chen's algorithm, the method still requires in the order of tens of intermediate position estimate calculations to provide a final estimate.

Similar to the previous methods, [28] utilized the ranging residuals to propose an iterative residual test to identify and use only the detected LoS distances for positioning. Excluding NLoS distances, particularly in situations where multiple anchors are affected by the NLoS conditions, may lead to the inadvertent dismissal of crucial data for accurate positioning. In [29], the authors detected the presence of NLoS from statistical parameters calculated from the ranging residuals. While the general detection of Non-Line-of-Sight (NLoS) presence in positioning demonstrated high accuracy, discerning individual NLoS range estimates became more challenging as the accuracy decreased.

In [30] the authors addressed NLoS-corrupted measurements by detecting points of intersection with known obstacles present in a room. Subsequently, they computed correction terms based on these intersections to rectify the inaccuracies caused by NLoS effects. Similarly, Silva et al. utilized the geometric floor plan of the positioning environment, alongside information about the surrounding walls' composition, to propose a through-the-wall ranging model for positioning [31]. As this information is highly specific to the positioning environment, the setup of such a positioning system needs extra steps, such as acquiring floor plans or site surveying and matching them to the specific refractive indices of the walls of the positioning environment.

Thirdly, range-based methods utilize the time series of ranging values to detect and mitigate NLoS-induced position errors, for example by using the running variance of range estimates or a known probability density function for LoS/NLoS detection [32]. Applying such methods requires *a priori* error distributions or introduces time latency to the detection [22]. Furthermore, without additional constraints, the running variance method could lead to false classification if the tag is moving during the estimation process [33]. Momtaz et al. proposed a statistical method of detecting and eliminating the NLOS errors with lower computational complexity and increased accuracy [34], allowing for a more scalable solution than the previously mentioned Rwgh algorithm. As a downside, this method requires a specific online training phase, in which the noise term has to be measured. In order to circumvent some of the restrictions caused by extracting the CIR samples from the transceiver chip, Barral et al. opted to use the received signal value in conjunction with ranging data as features for multiple ML techniques for LoS/NLoS classification [9].

#### A. CONTRIBUTIONS

The advent of the UWB Active-Passive Two-Way Ranging (AP-TWR) protocol researched in [35] and [36] opens up a new way of providing robust positioning in the presence of NLoS conditions. The following paragraphs outline the contributions of this paper.

While previous studies have focused on the performance of AP-TWR ranging, this paper goes further to examine how AP-TWR range estimates affect positioning accuracy. The proposed AP-TWR-based positioning method is validated and benchmarked in a real industrial environment to assess its performance.

The formulation of the proposed positioning method involves a thorough analysis of different NLoS error cases of AP-TWR, a novel contribution that has not been explored in the existing literature. Utilizing the redundant range estimates of AP-TWR allows for the calculation of range estimate noise variances, which is based on the previous analysis representative of NLoS propagation conditions. The noise variance is coupled with the proposed distance and intermittency penalties and used as input parameters to an Extended Kalman Filter (EKF) to provide a novel NLoS-robust and accurate positioning method.

The uniqueness of the proposed method lies in its avoidance of computationally expensive iterative NLoS detection techniques, lack of reliance on channel statistics or CIR information, independence from acquiring large datasets and labeling for model training, retention of all ranging data by not discarding any information, absence of latency issues typically found in methods computing running parameters, and the ability to operate without any knowledge about the environment, such as the composition and placement of walls or obstructions in a room. The proposed method stands out as a scalable, relatively easy-to-implement, and

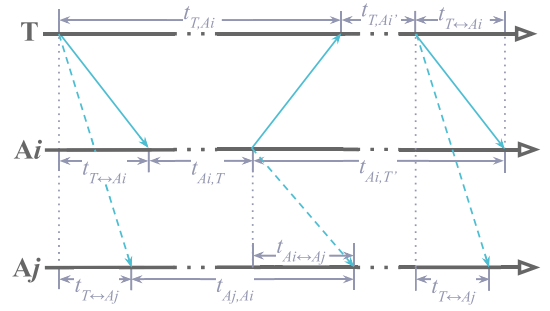


**FIGURE 1.** The Active-Passive Two-Way Ranging protocol. Tag T starts the ranging process by transmitting a packet, to which the active anchor  $A_i$  responds, after which T finishes the ranging sequence with a final transmitted packet. The passive anchor  $A_j$  listens to the active transmission in the air and calculates its passive range estimate.

accurate NLoS-robust positioning solution, capable of efficiently adapting to various environments and ensuring reliable performance even in challenging propagation conditions.

The rest of the paper is organized as follows: Section II gives the theoretical background of the AP-TWR protocol, Section III presents the effects of NLoS on the AP-TWR range estimates and formulates the proposed method based on it, Section IV describes the environment and the parameter values used in the experiments, Section V provides the analysis of the results, and Section VI concludes this paper.

#### II. ACTIVE-PASSIVE TWO-WAY RANGING

The AP-TWR protocol packet exchange diagram is pictured in Fig. 1, where the mobile device (tag T) starts the ranging sequence by transmitting a ranging request packet. Upon receiving that packet, the current active anchor  $A_i$  responds after its processing time  $t_{A_i,T}$ , which T promptly receives and records the round trip time interval  $t_{T,A_i}$ . The final ranging report packet sent by T is irrelevant from the standpoint of producing time interval values; rather it is used to communicate the  $t_{T,A_i}$  values back to the anchors for final range calculation. Meanwhile, the passive anchor  $A_j$  listens to the packet exchange of T and  $A_i$  and records the time interval between receiving T's first packet and  $A_i$ 's response,  $t_{A_j,A_i}$ .

The resulting values are used in calculating the AP-TWR Time of Flight (ToF) estimates via:

$$t_{T \leftrightarrow A_j|A_i} = \begin{cases} \frac{t_{T,A_i} - t_{A_i,T}}{2}, & \text{for } i = j \\ \frac{t_{T,A_i} + t_{A_i,T}}{2} + t_{A_i \leftrightarrow A_j} - t_{A_j,A_i}, & \text{for } i \neq j, \end{cases} \quad (1)$$

where the first part corresponds to the active ranging by Single-Sided Two-Way Ranging (SS-TWR), and the second part is used to calculate the passive range estimates, hence the name AP-TWR. The resulting term  $t_{T \leftrightarrow A_j|A_i}$  is the estimated ToF between T and  $A_j$ , calculated with the

information acquired from listening to  $A_i$ 's active ranging. The ToF between  $A_i$  and  $A_j$ ,  $t_{A_i \leftrightarrow A_j}$ , is considered known as the anchors are part of a fixed infrastructure, with known coordinates. Therefore  $t_{A_i \leftrightarrow A_j}$  can be measured by ranging between the anchors or calculated theoretically.

The values of the active anchor index are in the range of  $1 \leq i \leq m$  and the index for passive anchors is  $1 \leq j \leq n$ , where the total number of additional passive-only anchors is  $l = n - m$ , such that  $n \geq m$ , meaning that the active anchors act as passive anchors while they are not actively transmitting.

The resulting ToF estimates are converted to range estimates via the expression  $d_{j|i} = c \cdot t_{T \leftrightarrow A_j|A_i}$ , where  $c$  is the wave velocity in the propagation medium. In this case, we assume the velocity to be the speed of light in vacuum  $c \approx 3 \cdot 10^8$  m/s, as UWB is based on radio-frequency electromagnetic waves. Designating  $k$  as the temporal measure i.e. the ranging sequence number, we get the AP-TWR range estimate measurement matrix at time step  $k$  as  $\mathbf{T}_{d,k}$ :

$$\mathbf{T}_{d,k} = \begin{bmatrix} d_{1|1,k} & \dots & d_{1|m,k} \\ \vdots & \ddots & \vdots \\ d_{n|1,k} & \dots & d_{n|m,k} \end{bmatrix}. \quad (2)$$

Previous studies [35], [36] have solely focused on evaluating the performance of the AP-TWR, based on the ranging Root-Mean-Square Error (RMSE). However, in this paper, we extend the evaluation to include the precision of position estimates as the primary consideration. Additionally, a novel position estimation algorithm based on the EKF is proposed, aiming to further enhance the performance. The specific contributions of this paper were explained in more detail in Section I.

### III. PROPOSED METHOD

This section provides the theoretical background and formulation of the proposed AP-TWR-based Adaptive Extended Kalman Filter (A-EKF) positioning system. The following subsections present the essential information about the effects of NLoS on AP-TWR range estimates, the mechanisms for penalizing the inputs based on the distance and the intermittency of the range estimates, and finally the theory and the algorithm formulation of the proposed method.

#### A. EFFECT OF NLoS TO AP-TWR ESTIMATES

In order to quantify the effect of NLoS on AP-TWR estimates, (1) is analytically observed when arbitrary NLoS one-way bias factors  $\beta$  are introduced into the equations, depending on the severity of the NLoS case. Noting that for the formulation of this specific AP-TWR NLoS analysis, all other sources of errors are omitted. Table 1 presents the seven cases of errors possible for the trio of T,  $A_i$ , and  $A_j$ . The different NLoS propagation paths are viewed as separate cases between the tag and active anchor ( $T \leftrightarrow A_i$ ), the tag and the passive anchor ( $T \leftrightarrow A_j$ ), the active and passive anchors

( $A_i \leftrightarrow A_j$ ), and all possible combinations thereof. Each case introduces a specific set of bias factors  $\beta$  to the propagation times  $t_{T \leftrightarrow A_i}$ ,  $t_{T \leftrightarrow A_j}$ , and  $t_{A_i \leftrightarrow A_j}$ .

In the context of Table 1, the variables with the hat ( $\hat{\cdot}$ ) are affected by the NLoS bias, whereas the equivalent variables without the hat ( $\cdot$ ) are the true values, unaffected by the bias. The fourth column presents the NLoS-affected term(s) of Eq. (1), referenced to Fig. 1. The final two columns present the net effect of NLoS on the active and passive range estimates of AP-TWR, respectively.

The results of Table 1 show that in Cases 1, 4, 6, and 7, the active range estimate is additively impaired by a factor  $\beta_{T \leftrightarrow A_i}$  due to the existing NLoS path between T and  $A_i$ . Interestingly, the passive range estimates are unaffected by the NLoS between T and  $A_i$ , as its bias term cancels out in the calculation of the passive range estimates.

On the other hand, the passive range estimates are similarly affected by NLoS in pairwise Cases 2 & 4, 3 & 6, and 5 & 7. Noting that an obstruction between  $A_i$  and  $A_j$  (Cases 3, 5, 6, 7) causes a negative  $\beta_{A_i \leftrightarrow A_j}$  NLoS term to emerge, which could translate to an altogether negative NLoS bias in the passive range estimates, as opposed to a strictly positive NLoS bias for standard active ranging protocols [37], [38].

The effects of NLoS presented in Table 1 align with the observed error cases for TDoA defined by Zandian and Witkowski in [39], while also expanding on it by adding the NLoS link between the active and passive anchor.

The presence of variable NLoS biases in the AP-TWR estimates can be used to one's advantage, as the rows of (2) may contain estimates from many anchors with various propagation conditions between them and the tag. This translates into fluctuating range estimates in the rows of the measurement matrix, the measure of which can be expressed by the row variances  $\sigma_{j|1:m,k}^2$  corresponding to each time step  $k$ , expressed in matrix form:

$$\mathbf{S}_k = \left[ \sigma_{1|1:m,k}^2 \quad \sigma_{2|1:m,k}^2 \quad \dots \quad \sigma_{n|1:m,k}^2 \right]^T. \quad (3)$$

Previous research [36] has shown that taking the medians of the AP-TWR measurement matrix rows provides robust range estimates for positioning, therefore we denote the final range estimates of each time step  $k$  in matrix form as:

$$\mathbf{N}_k = [\tilde{d}_{1|1:m,k} \quad \tilde{d}_{2|1:m,k} \quad \dots \quad \tilde{d}_{n|1:m,k}]^T, \quad (4)$$

where the tilde markers denote the mathematical operation of median across each row  $d_{1|1:m,k} \dots d_{n|1:m,k}$  of (2). The values of (4) act as the input to the EKF position estimation.

#### B. DISTANCE PENALTY

Research has shown that the accuracy of position estimation may be impaired because the ranging error magnitude has a distance-dependent component [7], [21]. However, some results show that this relationship is not exactly linear [5].

**TABLE 1.** The AP-TWR errors in various NLoS cases between the devices.

Case	NLoS path	Bias factor(s)	Affected term in equations	Calculation of $\hat{t}_{T \leftrightarrow Ai Ai}$	Calculation of $\hat{t}_{T \leftrightarrow Aj Ai}$
1	T $\leftrightarrow$ Ai	$\beta_{T \leftrightarrow Ai}$	$\hat{t}_{T,Ai} = t_{T,Ai} + 2\beta_{T \leftrightarrow Ai}$ , $\hat{t}_{Aj,Ai} = t_{Aj,Ai} + \beta_{T \leftrightarrow Ai}$	$t_{T \leftrightarrow Ai Ai} + \beta_{T \leftrightarrow Ai}$	-
2	T $\leftrightarrow$ Aj	$\beta_{T \leftrightarrow Aj}$	$\hat{t}_{Aj,Ai} = t_{Aj,Ai} - \beta_{T \leftrightarrow Aj}$	-	$t_{T \leftrightarrow Aj Ai} + \beta_{T \leftrightarrow Aj}$
3	Ai $\leftrightarrow$ Aj	$\beta_{Ai \leftrightarrow Aj}$	$\hat{t}_{Aj,Ai} = t_{Aj,Ai} + \beta_{Ai \leftrightarrow Aj}$	-	$t_{T \leftrightarrow Aj Ai} - \beta_{Ai \leftrightarrow Aj}$
4	T $\leftrightarrow$ Ai, T $\leftrightarrow$ Aj	$\beta_{T \leftrightarrow Ai}$ , $\beta_{T \leftrightarrow Aj}$	$\hat{t}_{T,Ai} = t_{T,Ai} + 2\beta_{T \leftrightarrow Ai}$ , $\hat{t}_{Aj,Ai} = t_{Aj,Ai} - \beta_{T \leftrightarrow Aj} + \beta_{T \leftrightarrow Ai}$	$t_{T \leftrightarrow Ai Ai} + \beta_{T \leftrightarrow Ai}$	$t_{T \leftrightarrow Aj Ai} + \beta_{T \leftrightarrow Aj}$
5	T $\leftrightarrow$ Aj, Ai $\leftrightarrow$ Aj	$\beta_{T \leftrightarrow Aj}$ , $\beta_{Ai \leftrightarrow Aj}$	$\hat{t}_{Aj,Ai} = t_{Aj,Ai} - \beta_{T \leftrightarrow Aj} + \beta_{Ai \leftrightarrow Aj}$	-	$t_{T \leftrightarrow Aj Ai} - \beta_{Ai \leftrightarrow Aj} + \beta_{T \leftrightarrow Aj}$
6	T $\leftrightarrow$ Ai, Ai $\leftrightarrow$ Aj	$\beta_{T \leftrightarrow Ai}$ , $\beta_{Ai \leftrightarrow Aj}$	$\hat{t}_{T,Ai} = t_{T,Ai} + 2\beta_{T \leftrightarrow Ai}$ , $\hat{t}_{Aj,Ai} = t_{Aj,Ai} + \beta_{Ai \leftrightarrow Aj} + \beta_{T \leftrightarrow Ai}$	$t_{T \leftrightarrow Ai Ai} + \beta_{T \leftrightarrow Ai}$	$t_{T \leftrightarrow Aj Ai} - \beta_{Ai \leftrightarrow Aj}$
7	T $\leftrightarrow$ Ai, T $\leftrightarrow$ Aj, Ai $\leftrightarrow$ Aj	$\beta_{T \leftrightarrow Ai}$ , $\beta_{T \leftrightarrow Aj}$ , $\beta_{Ai \leftrightarrow Aj}$	$\hat{t}_{T,Ai} = t_{T,Ai} + 2\beta_{T \leftrightarrow Ai}$ , $\hat{t}_{Aj,Ai} = t_{Aj,Ai} + \beta_{Ai \leftrightarrow Aj} + \beta_{T \leftrightarrow Ai} - \beta_{T \leftrightarrow Aj}$	$t_{T \leftrightarrow Ai Ai} + \beta_{T \leftrightarrow Ai}$	$t_{T \leftrightarrow Aj Ai} - \beta_{Ai \leftrightarrow Aj} + \beta_{T \leftrightarrow Aj}$

As a way to give higher weights to shorter distances, we propose a parametric exponential scaling coefficient  $e^{s_c \cdot \tilde{d}_{j|1:m,k}}$ , where the scaling constant is defined as  $s_c = \frac{\ln s_m}{s_d}$ . It is calculated via user-set parameters  $s_m$  and  $s_d$  such that the exponential scaler provides a multiplier of  $s_m$  at distance  $s_d$ .

The resulting values corresponding to each distance are then expressed as the exponential scaling vector:

$$\mathbf{B}_k = \left[ e^{s_c \cdot \tilde{d}_{j|1:m,k}} \ e^{s_c \cdot \tilde{d}_{2|1:m,k}} \ \dots \ e^{s_c \cdot \tilde{d}_{n|1:m,k}} \right]^T, \quad (5)$$

which is used to modify the measurement noise vector in the AP-TWR A-EKF positioning scheme. The usage of the scaling vector is further explained in Section III-D.

### C. INTERMITTENCY PENALTY

The UWB range estimates can be impaired by intermittent noise, multipath, and obstacles in the environment the system is operating in [40]. As a result of some or many of the aforementioned effects, the range estimates supplied by the UWB system might arrive intermittently.

To establish the intermittency penalty method, we hypothesize that the intermittent values are inherently less accurate, as the intermittent values show that the system works on the edge of its detection limit in the ranging process. We set forward two parameters, a positive integer  $l_s$  and a non-negative real number  $l_m$ , i.e., the time history length, and the intermittency multiplier, respectively.

Representing all the historical ranging values as sets on numbers with a cardinality of  $l_s$ , corresponding to all anchors in the system  $A_1, A_2, \dots, A_N$  at time step  $k$ , we get:

$$\begin{aligned} A_{1,k} &= \{d_{A_1,k}, d_{A_1,k-1}, \dots, d_{A_1,k-l_s+2}, d_{A_1,k-l_s+1}\} \\ A_{2,k} &= \{d_{A_2,k}, d_{A_2,k-1}, \dots, d_{A_2,k-l_s+2}, d_{A_2,k-l_s+1}\} \\ &\vdots \\ A_{N,k} &= \{d_{A_N,k}, d_{A_N,k-1}, \dots, d_{A_N,k-l_s+2}, d_{A_N,k-l_s+1}\}. \end{aligned}$$

The elements of the sets of time history values assume the value of 0 in the case where a specific anchor does not produce a range estimate at that time instance. So, at each time instance, we get the number of missing range estimates

in the history window for each anchor:

$$\begin{aligned} r_{A_1,k} &= |x_1 \in A_{1,k} : x_1 = 0| \\ r_{A_2,k} &= |x_2 \in A_{2,k} : x_2 = 0| \\ &\vdots \\ r_{A_N,k} &= |x_N \in A_{N,k} : x_N = 0|. \end{aligned}$$

The resulting numbers of missing values are in turn used to calculate the total set of intermittency penalty multipliers for each anchor in the system, for each time step value  $k$ :

$$L_k = \left\{ 1 + \frac{l_m}{l_s} \cdot r_{A_1,k}, \dots, 1 + \frac{l_m}{l_s} \cdot r_{A_N,k} \right\}. \quad (6)$$

Similar to (5), the intermittency penalty multiplier vector at time instance  $k$  is then formulated as:

$$\mathbf{C}_k = [l_{i_1,k} \ l_{i_2,k} \ \dots \ l_{i_n,k}]^T, \quad (7)$$

such that the values  $l_{i_1,k}, l_{i_2,k}, \dots, l_{i_n,k}$  are elements of the subset of  $L_k$  and  $i_1, i_2, \dots, i_n$  are the indices of the subset elements, marking the specific anchors providing their corresponding range estimates at time instance  $k$ .

Since only the intermittency penalty magnitude and not the input positioning data is dependent on time series history, no extra time-domain latency is introduced to the positioning process.

### D. EXTENDED KALMAN FILTER

The literature encompasses a wide range of position estimation algorithms, spanning various Linear Least Squares (LLS), Nonlinear Least Squares (NLS), and multiple Bayesian Filter approaches, to name a few [41]. Among these methods, the EKF has demonstrated excellent performance in LoS scenarios while outperforming other methods in NLoS conditions, on par with the performance of the Unscented Kalman Filter (UKF) [42]. Furthermore, the EKF exhibits lower complexity, resulting in calculation times that are more than three times shorter than those of the UKF [39]. Considering these factors, the EKF was selected as the foundation for the method proposed in this paper.

Furthermore, in the scope of this paper, a single-model approach is utilized due to the absence of information



regarding whether the tag is moving or stationary. However, incorporating sensors that provide additional information on the tag's movement/stationary state could enable adopting a multi-model approach. For instance, the switch to a zero-velocity model could be considered for cases where the tag is detected to be stationary [43].

Following previous works [21], [44], we expand the position, velocity, and acceleration model of EKF to three dimensions (3D). We do so by expressing the corresponding values at each time step as  $\mathbf{X}_k$ , and tying them with information from the previous time step  $k-1$  using the appropriate kinematics equations:

$$\mathbf{X}_k = \begin{bmatrix} x_k \\ y_k \\ z_k \\ v_k^x \\ v_k^y \\ v_k^z \\ a_k^x \\ a_k^y \\ a_k^z \end{bmatrix} = \begin{bmatrix} x_{k-1} + T_s \cdot v_{k-1}^x + \frac{T_s^2}{2} a_{k-1}^x + \frac{T_s^3}{6} w_{k-1}^x \\ y_{k-1} + T_s \cdot v_{k-1}^y + \frac{T_s^2}{2} a_{k-1}^y + \frac{T_s^3}{6} w_{k-1}^y \\ z_{k-1} + T_s \cdot v_{k-1}^z + \frac{T_s^2}{2} a_{k-1}^z + \frac{T_s^3}{6} w_{k-1}^z \\ v_{k-1}^x + T_s \cdot a_{k-1}^x + \frac{T_s^2}{2} w_{k-1}^x \\ v_{k-1}^y + T_s \cdot a_{k-1}^y + \frac{T_s^2}{2} w_{k-1}^y \\ v_{k-1}^z + T_s \cdot a_{k-1}^z + \frac{T_s^2}{2} w_{k-1}^z \\ a_{k-1}^x + T_s \cdot w_{k-1}^x \\ a_{k-1}^y + T_s \cdot w_{k-1}^y \\ a_{k-1}^z + T_s \cdot w_{k-1}^z \end{bmatrix}, \quad (8)$$

where at time step  $k$  the coordinates, velocities, and acceleration values for each of the three axes are defined as  $\{x_k, y_k, z_k\}$ ,  $\{v_k^x, v_k^y, v_k^z\}$ , and  $\{a_k^x, a_k^y, a_k^z\}$ , respectively. The kinematics equations and sampling time  $T_s$  are used to express the dependency of values at time step  $k$  from values at  $k-1$ . The last terms of each row represent the position  $(T_s^3/6)w_{k-1}$ , velocity  $(T_s^2/2)w_{k-1}$ , and acceleration  $(T_s \cdot w_{k-1})$  noise of the model, respectively.

The process noise can be rewritten as a vector  $\mathbf{w}_{k-1} = [w_{k-1}^x, w_{k-1}^y, w_{k-1}^z]^T$  with a covariance matrix  $\mathbf{Q}_{k-1} = \text{diag}(\sigma_{jx}^2, \sigma_{jy}^2, \sigma_{jz}^2)$ . Therefore, the state vector (8) can be expressed as a series of matrix calculations, such that:

$$\mathbf{X}_k = \mathbf{A}\mathbf{X}_{k-1} + \mathbf{G}\mathbf{w}_{k-1}, \quad (9)$$

where matrix  $\mathbf{A}$  is the state transition matrix and is written as:

$$\mathbf{A} = \begin{bmatrix} 1 & 0 & 0 & T_s & 0 & 0 & \frac{T_s^2}{2} & 0 & 0 \\ 0 & 1 & 0 & 0 & T_s & 0 & 0 & \frac{T_s^2}{2} & 0 \\ 0 & 0 & 1 & 0 & 0 & T_s & 0 & 0 & \frac{T_s^2}{2} \\ 0 & 0 & 0 & 1 & 0 & 0 & T_s & 0 & 0 \\ 0 & 0 & 0 & 0 & 1 & 0 & 0 & T_s & 0 \\ 0 & 0 & 0 & 0 & 0 & 1 & 0 & 0 & T_s \\ 0 & 0 & 0 & 0 & 0 & 0 & 1 & 0 & 0 \\ 0 & 0 & 0 & 0 & 0 & 0 & 0 & 1 & 0 \\ 0 & 0 & 0 & 0 & 0 & 0 & 0 & 0 & 1 \end{bmatrix}, \quad (10)$$

and  $\mathbf{G}$  represents the noise transition matrix as:

$$\mathbf{G} = \begin{bmatrix} \frac{T_s^3}{6} & 0 & 0 \\ 0 & \frac{T_s^3}{6} & 0 \\ 0 & 0 & \frac{T_s^3}{6} \\ \frac{T_s^2}{2} & 0 & 0 \\ 0 & \frac{T_s^2}{2} & 0 \\ 0 & 0 & \frac{T_s^2}{2} \\ T_s & 0 & 0 \\ 0 & T_s & 0 \\ 0 & 0 & T_s \end{bmatrix}. \quad (11)$$

The AP-TWR range estimates  $z_{j,k}$  are placed in the observation/measurement vector  $\mathbf{Z}_k$ , which consists of the sum of the true distance vector  $\mathbf{D}_k = [d_{1,k}, d_{2,k}, \dots, d_{n,k}]^T$  and the observation noise vector  $\mathbf{V}_k = [v_{1,k}, v_{2,k}, \dots, v_{n,k}]^T$ . The latter of which has a covariance matrix of  $\mathbf{R}_k = \text{diag}(\sigma_{d1,k}^2, \sigma_{d2,k}^2, \dots, \sigma_{dn,k}^2)$ :

$$\mathbf{Z}_k = \begin{bmatrix} z_{1,k} \\ z_{2,k} \\ \vdots \\ z_{n,k} \end{bmatrix} = \begin{bmatrix} d_{1,k} + v_{1,k} \\ d_{2,k} + v_{2,k} \\ \vdots \\ d_{n,k} + v_{n,k} \end{bmatrix} = \mathbf{D}_k + \mathbf{V}_k = \mathbf{H}_k \mathbf{X}_k + \mathbf{V}_k. \quad (12)$$

The vector  $\mathbf{D}_k$  can be rewritten in the form of circle equations, where the centers are defined by the anchor coordinates  $\{x_j, y_j, z_j\}$ :

$$\mathbf{D}_k = \begin{bmatrix} \sqrt{(x_k - x_1)^2 + (y_k - y_1)^2 + (z_k - z_1)^2} \\ \sqrt{(x_k - x_2)^2 + (y_k - y_2)^2 + (z_k - z_2)^2} \\ \vdots \\ \sqrt{(x_k - x_n)^2 + (y_k - y_n)^2 + (z_k - z_n)^2} \end{bmatrix}. \quad (13)$$

Because the resulting equations are nonlinear, the first-order Taylor expansion is utilized for linearization, to produce the Jacobian matrix  $\mathbf{H}_k$ :

$$\mathbf{H}_k = \begin{bmatrix} \frac{\partial d_{1,k}}{\partial x_k} & \frac{\partial d_{1,k}}{\partial y_k} & \frac{\partial d_{1,k}}{\partial z_k} & 0 & 0 & 0 & 0 & 0 & 0 \\ \frac{\partial d_{2,k}}{\partial x_k} & \frac{\partial d_{2,k}}{\partial y_k} & \frac{\partial d_{2,k}}{\partial z_k} & 0 & 0 & 0 & 0 & 0 & 0 \\ \vdots & \vdots & \vdots & \vdots & \vdots & \vdots & \vdots & \vdots & \vdots \\ \frac{\partial d_{n,k}}{\partial x_k} & \frac{\partial d_{n,k}}{\partial y_k} & \frac{\partial d_{n,k}}{\partial z_k} & 0 & 0 & 0 & 0 & 0 & 0 \end{bmatrix}, \quad (14)$$

such that the partial derivatives are calculated at each time step  $k$  as:

$$\frac{\partial d_{j,k}}{\partial x_k} = \frac{x_k - x_j}{\sqrt{(x_k - x_j)^2 + (y_k - y_j)^2 + (z_k - z_j)^2}} \quad (15a)$$

$$\frac{\partial d_{j,k}}{\partial y_k} = \frac{y_k - y_j}{\sqrt{(x_k - x_j)^2 + (y_k - y_j)^2 + (z_k - z_j)^2}} \quad (15b)$$

$$\frac{\partial d_{j,k}}{\partial z_k} = \frac{z_k - z_j}{\sqrt{(x_k - x_j)^2 + (y_k - y_j)^2 + (z_k - z_j)^2}}. \quad (15c)$$

### E. PROPOSED ADAPTIVE EKF METHOD

The proposed positioning method is described in the algorithm's pseudocode in Alg. 1, which consists of three distinct phases: AP-TWR ranging, EKF prediction, and EKF correction. The algorithm is also visualized as a flowchart in Fig. 2.

As a first step, the EKF initial state and state covariance matrices need to be initialized; this part is described in more detail in Section IV. After initialization, the first phase is launched, where the AP-TWR measurement matrix is acquired. Since the coordinate is calculated for three axes, a minimum of four input range estimates is needed. Otherwise, the position estimation process is skipped for this time step.

When the number of columns of the measurement matrix is larger than one i.e.,  $m > 1$ , the row medians (4) and variances (3) are calculated. In the other case, the measurement matrix is directly taken as the observation vector and an appropriately-sized row variance vector  $\mathbf{S}_k$  is constructed by repeating a default observation noise variance,  $\sigma_d^2$ . Then the distance and intermittency penalty vectors are calculated, and the observation covariance matrix  $\mathbf{R}_k$  is formed as a diagonal matrix composed of the Hadamard product of vectors  $\mathbf{S}_k$ ,  $\mathbf{B}_k$ , and  $\mathbf{C}_k$ .

In the following phase, the state and its covariance matrices are predicted, noting that the predicted values are marked with a "minus" superscript. Finally, the Kalman gain is computed and used to correct the state estimate and covariance providing a position estimate for that time step.

We adopt the naming convention used in previous studies [45], [46] that refer to the Kalman Filter as adaptive when the covariance matrices  $\mathbf{Q}$  and  $\mathbf{R}$  are dynamically modified. Accordingly, we introduce our approach as the Active-Passive Two-Way Ranging Adaptive Extended Kalman Filter (AP-TWR A-EKF) positioning method.

### IV. EXPERIMENTAL SETUP

This section provides an overview of the experiments to validate the proposed AP-TWR A-EKF positioning method.

The experiments were conducted using the AP-TWR protocol implemented in the Eliko UWB RTLS system [47], which is based on the Qorvo DW1000 UWB transceiver chip [8]. The true coordinates of the anchors' and tag's locations were surveyed using the Leica DISTO S910 laser distance meter, which provides three-dimensional coordinates [48].

The Eliko UWB RTLS was deployed in an industrial environment, at the premises of Krah Pipes OÜ [49] which specializes in producing large thermoplastic pipes. The factory premises were selected for conducting the experiments as they provide challenging conditions for the positioning system and the proposed method. These conditions include 1) restrictions on the placement of the anchors: most of the anchors have to be mounted near the ceiling, thus the tag is almost always positioned outside the 3D convex hull of

### Algorithm 1 EKF Positioning for AP-TWR Protocol

**Input:**  $\mathbf{T}_{d,k} \in \mathbb{R}^{n \times m}$ ,  $\{s_d, \sigma_d^2, \sigma_{jx}^2, \sigma_{jy}^2, \sigma_{jz}^2\} \in \mathbb{R}_{>0}$ ,  $\{s_m, l_m\} \in \mathbb{R}_{\geq 0}$ ,  $l_s \in \mathbb{Z}_{>0}$   
**Output:**  $\hat{\mathbf{X}}_k$   
**Initialize:**  $\hat{\mathbf{X}}_0, \mathbf{P}_0$

- 1: **for**  $k = 1, 2, \dots, \infty$  **do**
- AP-TWR ranging
- 2:   **if**  $n < 4$  **then**                    $\triangleright$  Less than 4 distances in input
- 3:     **skip**
- 4:   **end if**
- 5:   **if**  $m > 1$  **then**
- 6:      $\mathbf{Z}_k = \mathbf{N}_k$                     $\triangleright$  Observation vector
- 7:     Calculate  $\mathbf{S}_k$                     $\triangleright$  Row variances
- 8:   **else**
- 9:      $\mathbf{Z}_k = \mathbf{T}_{d,k}$
- 10:     $\mathbf{S}_k = [\sigma_d^2 \dots \times n]^T$     $\triangleright$  Assign default variance
- 11:   **end if**
- 12:   Calculate  $\mathbf{B}_k$                     $\triangleright$  Distance penalty
- 13:   Calculate  $\mathbf{C}_k$                     $\triangleright$  Intermittency penalty
- 14:    $\mathbf{R}_k = \text{diag}(\mathbf{S}_k \odot \mathbf{B}_k \odot \mathbf{C}_k)$     $\triangleright$  Hadamard product
- EKF Prediction
- 15:    $\hat{\mathbf{X}}_k^- = \mathbf{A}\hat{\mathbf{X}}_{k-1}$                     $\triangleright$  Predict state
- 16:    $\mathbf{P}_k^- = \mathbf{A}\mathbf{P}_{k-1}\mathbf{A}^T + \mathbf{G}\mathbf{Q}_{k-1}\mathbf{G}^T$     $\triangleright$  Predict state cov.
- EKF Correction
- 17:    $\mathbf{K}_k = \mathbf{P}_k^- \mathbf{H}_k^T (\mathbf{H}_k \mathbf{P}_k^- \mathbf{H}_k^T + \mathbf{R}_k)^{-1}$     $\triangleright$  Kalman gain
- 18:    $\hat{\mathbf{X}}_k = \hat{\mathbf{X}}_k^- + \mathbf{K}_k (\mathbf{Z}_k - \mathbf{D}_k^-)$     $\triangleright$  Correct state estimate
- 19:    $\mathbf{P}_k = \mathbf{P}_k^- - \mathbf{K}_k \mathbf{H}_k \mathbf{P}_k^-$                     $\triangleright$  Correct state cov.
- 20:   **return**  $\hat{\mathbf{X}}_k, \mathbf{P}_k$
- 21: **end for**

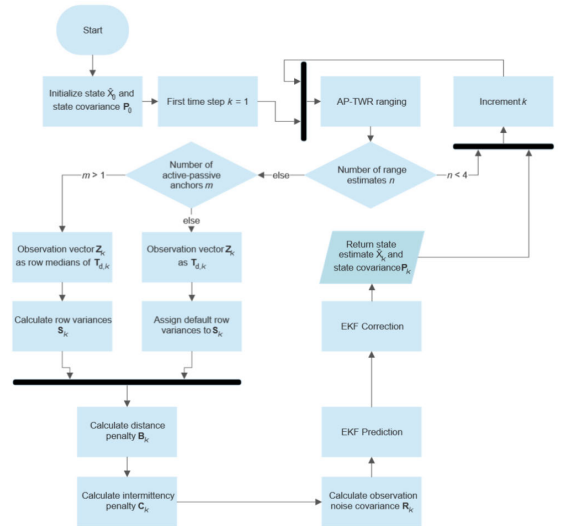


FIGURE 2. The flowchart of the proposed AP-TWR A-EKF method.

the anchors; and 2) the presence of large metal and concrete objects obstructing the propagation path, etc.

**TABLE 2.** The coordinates of the anchors used in the experiments.

Anchor	x (m)	y (m)	z (m)
A <sub>1</sub>	0.17	-0.05	4.50
A <sub>2</sub>	47.52	-6.67	10.5
A <sub>3</sub>	29.63	0.10	4.50
A <sub>4</sub>	23.62	10.37	10.05
A <sub>5</sub>	41.59	4.28	9.98
A <sub>6</sub>	17.65	0.51	7.50
A <sub>7</sub>	47.52	14.66	10.68
A <sub>8</sub>	11.32	4.46	9.99

The factory environment of the experiments can be seen in Fig. 3 where the Leica Disto S910 is marked in cyan, the two visible anchors in red, and the tag in dark blue color. Additionally, an industrial crane is mounted on rails on the ceiling, but it cannot be seen clearly: only the hook block of the crane is visible in the upper center part of the photo. The Leica DISTO S910 was installed on a concrete mezzanine floor, with a height of about 4.5 meters from the ground floor, such that it could provide the tag and anchor's true location across the whole area. The locations of the anchors, measured with the Leica DISTO S910, are given in Table 2.

The first set of tests was conducted with a stationary tag, mounted on a tripod, at 30 separate test points across the factory. The locations of the test points (TP), anchors (A), and the Leica DISTO S910 can be seen in Fig. 4. At each of the 30 test points the AP-TWR range estimates were captured for 30 seconds, using a tag with an update rate of 10 Hz, providing data from approximately 300 ranging sequences.

The second set of experiments was conducted to validate the results of the stationary tests. The experiment was performed with a moving tag which was mounted on a tripod, attached to a shelf trolley. The tag was moved throughout the factory with reference to the printed lines on the floor, where the critical points, i.e. turning points, are previously surveyed to provide a reference true track. The shelf trolley and the reference lines are also visible in Fig. 3. The data was captured throughout the movement process for 99 seconds, resulting in data of 990 separate ranging sequences.

The parameter values of the AP-TWR A-EKF used in the experiments are given in Table 3. The Eliko UWB RTLS was configured such that the maximum number of active anchors  $m_{\max}$  of AP-TWR protocol is 6. Although the intermittency and distance penalty parameters were chosen heuristically, it is likely that the chosen values are sub-optimal, not providing the best achievable positioning performance for the proposed method. Finding the optimal parameter values could be considered in future work.

The default observation noise variance  $\sigma_d^2$  and the process noise covariance values of  $\mathbf{Q}_{k-1}$  are inferred from [21]. The sampling time  $T_s$  was extracted from the tag's internal clock during each ranging sequence.

The very first step of the EKF process requires initializing the values of the initial state vector  $\mathbf{X}_0$  and the state covariance matrix  $\mathbf{P}_0$ . The initial coordinates  $\{x_0, y_0, z_0\}$  of the state vector are given as the true coordinate measured by

**TABLE 3.** The parameters for the proposed AP-TWR A-EKF positioning method used in the experiments.

Parameter	Value
$m_{\max}$	6
$s_d$	100 m
$l_s$	6
$l_m$	100
$\sigma_d^2$	0.01 m <sup>2</sup>
$\sigma_{jx}^2, \sigma_{jy}^2, \sigma_{jz}^2$	0.01 m <sup>2</sup> /s <sup>6</sup>
$T_s$	from tag clock
$x_0, y_0, z_0$	from true position
$v_0^x, v_0^y, v_0^z$	0 m/s
$a_0^x, a_0^y, a_0^z$	0 m/s <sup>2</sup>
$\mathbf{P}_0$	$I_9$

the DISTO S910 for all of the tested EKF variants, which are discussed in the following paragraphs. This is done to give all the methods the same initial conditions and to eliminate the additional errors from converging to the correct location when the initial position is set to the coordinate origin, for example. The initial speed and acceleration values for each axis are set to zero. The initial state covariance matrix  $\mathbf{P}_0$  is set as a 9-by-9 identity matrix, corresponding to the size of the state vector.

The proposed A-EKF positioning method is compared to the baseline EKF methods, accordingly using standard AP-TWR range estimates (4) and SS-TWR active-only range estimates as input. The same exact dataset is utilized for all of the compared methods, as both the SS-TWR and AP-TWR range estimates are inherently present in it, making the results of different methods directly comparable. The initial state, initial covariance, and  $\mathbf{Q}_{k-1}$  matrix values are the same as stated in Table 3, whereas the diagonal of the appropriately-sized  $\mathbf{R}_k$  matrix is filled with the default variance  $\sigma_d^2$  values.

The data acquisition was performed via a custom Python script that interfaces with the Eliko UWB RTLS server, extracts the required UWB range estimate packets, and saves them to a text file. Then a custom script written in R was used to parse and process the data, as well as to calculate the range estimates and the metrics for all three methods. Although this specific implementation provides the results by post-processing the range estimates, the proposed system is able to work in real-time applications.

The comprehensive dataset with supplemental materials and detailed explanations is uploaded to the IEEE Dataport repository and can be found in [50].

## V. RESULTS

This section provides the results of the stationary and moving experiments and the analysis thereof.

### A. STATIONARY TESTS

The results of the stationary experiments are given in Fig. 5, where the 2D and 3D Root-Mean-Square-Error (RMSE) of the SS-TWR, standard AP-TWR EKF, and the proposed A-EKF positioning methods are given across all of the 30 test points.



**FIGURE 3.** Setup for the movement tests in the industrial environment. Visible anchors  $A_1$  and  $A_6$  are circled in red, the Leica DISTO S910 in cyan, and the tripod-mounted tag on the shelf trolley in dark blue. The tag is moved in reference to the lines on the factory floor.

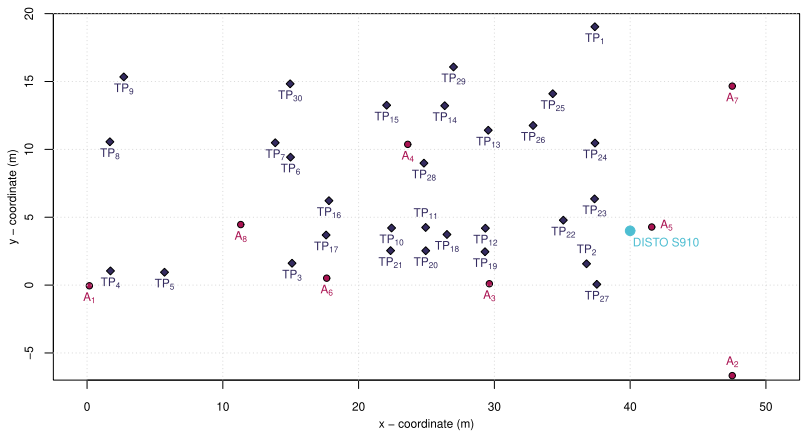


**FIGURE 4.** The test setup plan. Test point locations are marked with numbered “TP” markers in dark blue, anchor locations with numbered “A” markers in red, and the location of the Leica DISTO S910 laser distance meter is marked with a cyan circle.

Firstly, focusing on the 2D results, it can be seen that for most cases all of the tested methods provide comparable performance at approximately 0.15 m RMSE. The SS-TWR EKF shows a more uniform performance across the test points, with an exception at TP<sub>1</sub> and TP<sub>8</sub>, where the 2D RMSE is significantly higher than usual, obtaining values of 0.49 m and 1.97 m, respectively. The higher RMSE of TP<sub>8</sub> is

a result of the blocking of the LoS of the tag and  $A_1$ ,  $A_6$  due to large pipe mandrels made of metal, visible in the upper-left side of Fig. 3, while in TP<sub>1</sub>, the direct propagation path to anchor  $A_7$  is obstructed by the mezzanine floor.

The differences for the standard AP-TWR EKF are more diverse, as in test points 1, 3, 5, 8, 9, and 29 the 2D RMSE obtains significantly higher values than normal, ranging from

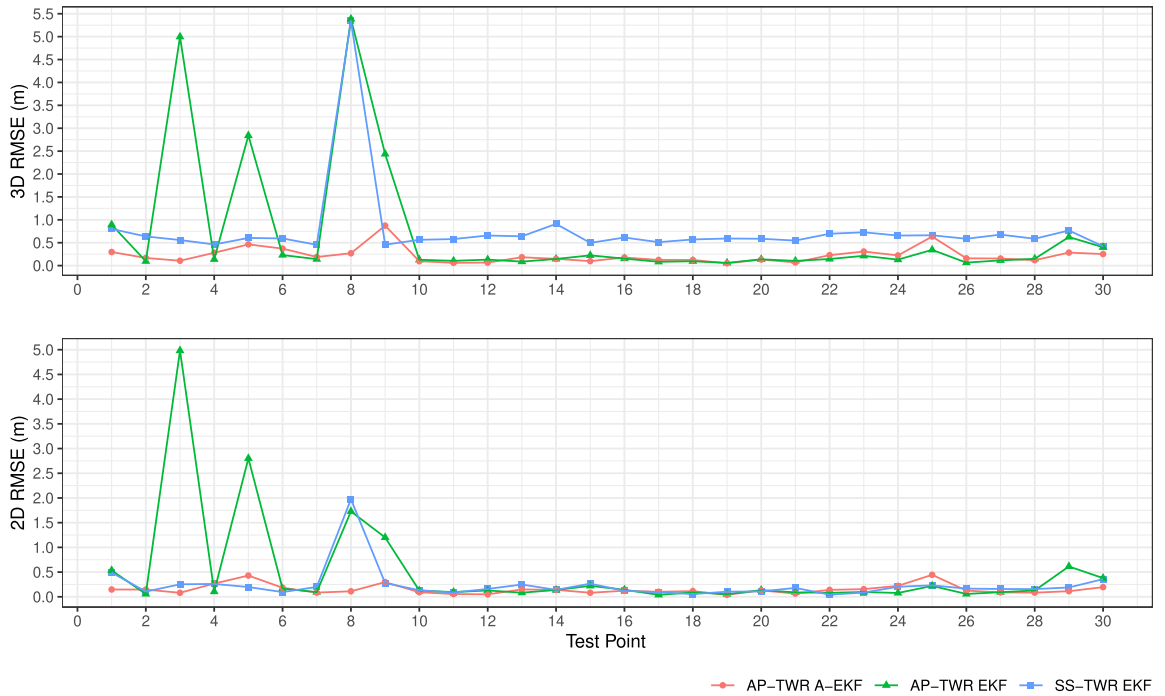


FIGURE 5. The 2D and 3D RMSE results across all the stationary test points.

0.53 m (TP<sub>1</sub>) up to 4.98 m (TP<sub>3</sub>). Although the reasons are not as evident as for SS-TWR EKF, the analysis presented in Table 1 suggests that AP-TWR range estimates are impaired because of the compound NLoS effects of different propagation paths encountered during each ranging sequence. The effects could be a result of a combination of the aforementioned pipe mandrels, the overhead crane blocking propagation paths between anchors, all of the assets in the factory, etc.

As both, the standard AP-TWR and SS-TWR, methods do not provide the EKF with any additional information on the measurement noise that may be present, the input distances are treated as equal and the distances with larger error contribute to an increase in the positioning error.

The proposed AP-TWR A-EKF positioning method, on the other hand, is robust against the adverse propagation conditions present in the industrial environment. The proposed method typically performs at a similar or lower error level than the baseline methods, whereas the largest differences come into play at the previously mentioned high error test points of the baselines. The following analysis gives an overview of the behavior of A-EKF compared to other methods in the most significant test points.

At the high-error test points 1, 3, 5, 8, 9, and 29 of AP-TWR, the proposed A-EKF method reduces the RMSE respectively by 0.387, 4.902, 2.370, 1.617, 0.904, and

0.501 m, providing a large reduction in the absolute values of errors in every one of the high error test points. One minor drawback can be identified at test point 25, where the proposed method provides slightly lower performance than the baseline AP-TWR, with according RMSE of 0.445 m and 0.220 m. In terms of 2D RMSE, the proposed method performs better than AP-TWR in 18 of the 30 test points.

Comparing the proposed method to the SS-TWR in terms of 2D RMSE, it can be observed that the errors at TP<sub>1</sub> and TP<sub>8</sub> are reduced by 0.343 m and 1.863 m, correspondingly. Even though the proposed method provides slightly higher 2D errors at TP<sub>5</sub> and TP<sub>25</sub>, the opposite is true for the 3D case where the A-EKF provides slightly better RMSE performance than SS-TWR. In conclusion, the proposed method provides a lower RMSE than SS-TWR at 17 of the 30 test points.

Although the test points show rather similar trends in the 3D RMSE, we see that in typical cases not involving the large error test points, the proposed method alongside the AP-TWR consistently provides about 0.4 m lower RMSE.

All of the high error test points 1, 3, 5, 8, 9, and 29 of AP-TWR are again subsequently reduced by 0.597, 4.890, 2.378, 5.117, 1.565, and 0.340 m using the proposed method. Comparing the 3D results, it is evident that the proposed A-EKF method provides a reduction in RMSE at half of the test points when compared to AP-TWR, including the



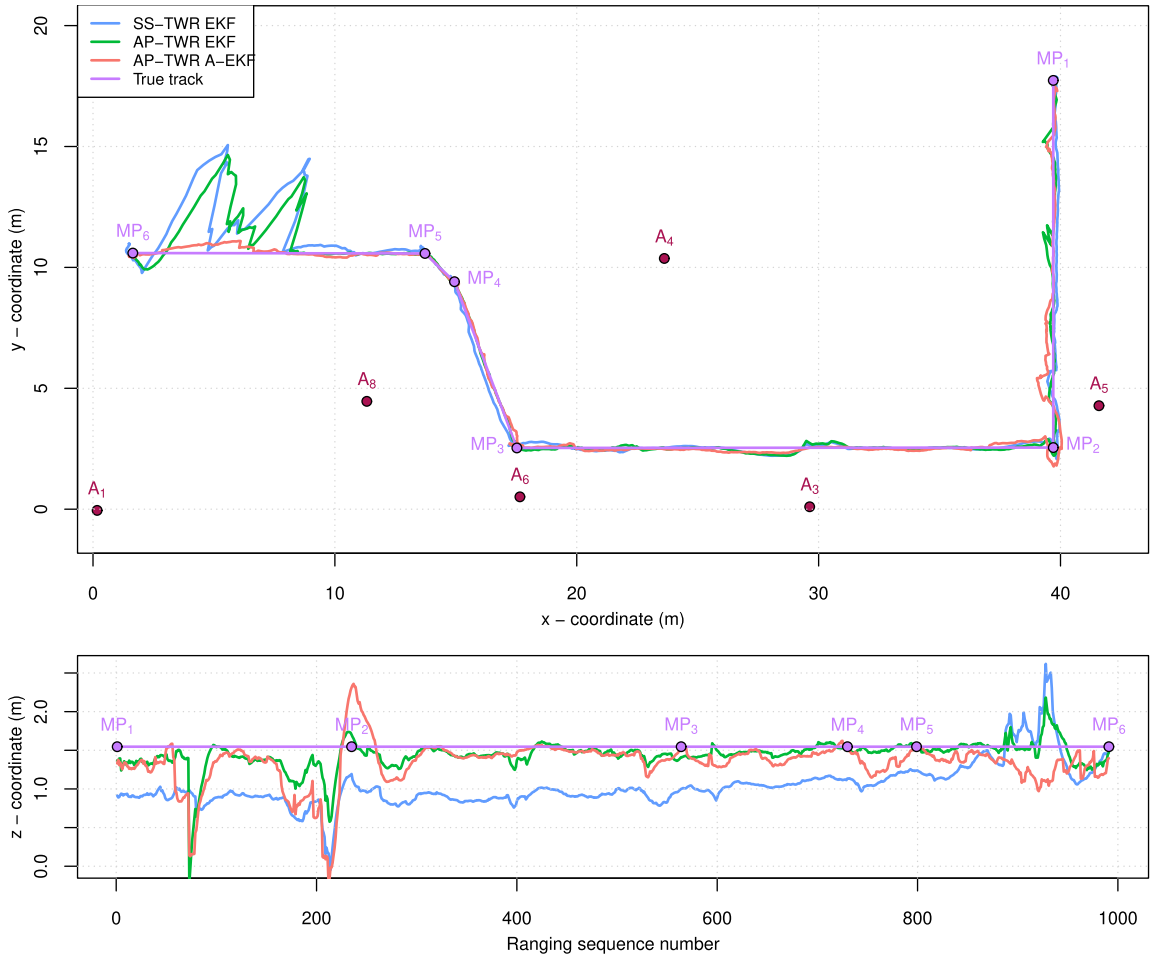


**FIGURE 6.** The movement paths of the second set of tests. The upper figure displays the tested methods' x and y coordinates, while the lower figure displays the z-coordinate across the ranging sequences. The critical points of the true movement path are marked with consecutive purple dots noted as MP on the respective figures. Note that on the z-coordinate plot, the movement path critical points are marked approximately in regards to the sequence number, as the shelf trolley needed to be stopped and its direction adjusted for the next segment of the movement.

previously mentioned points where the error magnitude was reduced significantly.

Similarly, the high error points 8 and 14 of SS-TWR are also mitigated by the proposed method, which reduces 3D RMSE by 5.074 and 0.763 m, correspondingly. Moreover, the A-EKF outperformed the SS-TWR positioning in 29 out of the 30 test points, providing moderately higher RMSE at only TP<sub>9</sub>.

On average, the tested methods achieved the following RMSE in 2D positioning: AP-TWR 0.492 m, SS-TWR 0.238 m, and A-EKF 0.149 m, meaning that the proposed method achieved almost 1.6 times better performance in 2D as the next best method, the SS-TWR. The 3D results showed the average RMSE of the methods to be AP-TWR 0.693 m, SS-TWR 0.765 m, and A-EKF 0.224 m, showing that the

proposed method achieved over 3 times lower RMSE than the next best method i.e., AP-TWR.

## B. MOVEMENT TESTS

The experiments with a moving tag were conducted to validate the results achieved by the stationary tests to show that the initialization of the methods does not affect the position estimates. Due to the inherent requirement of knowing the true coordinate of the tag at each time step, the calculation of objective error metrics becomes infeasible as the necessary devices to acquire an accurate time series reference track were unfortunately unavailable to the authors. As a consequence, the resulting analysis should be approached with caution as it solely presents the visual movement paths of the tested methods without calculating objective

performance parameters in regards to the true movement track.

Fig. 6 presents the results of the movement tests, which were described in detail in Section IV. Noting that although the x-y coordinate plot is zoomed in for clarity such that  $A_2$  is not visible, the anchor still took part in the experiments. To facilitate the presentation of the 3D data, it was partitioned into two distinct graphs: a two-dimensional representation depicting the x-y plane of the factory floor, and a depiction of the z-coordinate variation corresponding to the ranging sequence number.

The previously surveyed critical movement points are marked with numbered purple dots (MP), connected by purple lines to indicate the true track of the movement. The approximate locations of arrival at the critical points are marked with corresponding purple dots in the z-coordinate graph. The locations on the z-coordinate figure are approximate because at each critical point, the shelf trolley was stopped to re-position it for the next section of the movement, so parts of the plots also correspond to brief stationary moments during the movement.

The movement traces in Fig. 6 support the results achieved in the stationary test, where the proposed A-EKF and the standard AP-TWR method consistently provide more accurate results in the z-axis, as was evident in the 3D RMSE graphs in Fig. 5.

In the first segment of the movement, all of the methods show slightly higher deviation from the true track, especially in the z-axis. This increased noise can be explained by the presence of the mezzanine floor on the right side, since in the first segment the tag is moved in parallel and almost under the mezzanine floor, obstructing the LoS paths to anchors 2, 5, and 7.

The next 3 movement segments show rather similar performance for all of the methods, keeping in mind that the SS-TWR method consistently shows about 0.5 m lower z-coordinate value compared to the true track, than other methods.

The final movement segment is impaired by the same pipe mandrels discussed in the previous section, as can be seen by the large deviations from the true track of the SS-TWR and AP-TWR methods. These fluctuations achieve a maximum of about 4.5 m in the x-y plane and about 1 m in the z-axis, whereas the proposed A-EKF positioning method deviates by a maximum of 0.5 m in both the x-y plane and the z-axis, reducing the maximum errors by about 9 times.

## VI. CONCLUSION

This paper presented a comprehensive overview and analysis of the possible NLoS error cases that may be encountered with the usage of the UWB AP-TWR protocol. This analysis was the basis for the proposed A-EKF method, which was experimentally tested in an industrial environment and benchmarked against EKF position estimators based on active-only SS-TWR and standard AP-TWR range estimates. The proposed method can be used in real-time applications and does

not require any additional information on the environment, signal properties, error models, statistics, or training data, or cause any additional time delays in the position estimation process.

Although in 2D the tested methods typically operated with the same performance, a part of the test points provided unfavorable propagation conditions for the UWB system, inducing large errors for standard AP-TWR (maximum about 5 m error) and SS-TWR (maximum about 2 m error), which the proposed A-EKF method mitigated, reducing errors with a maximal of less than 0.5 m. On average, the A-EKF provided almost 1.6 times lower RMSE than the next best i.e., the SS-TWR positioning method.

Similar trends were apparent in the 3D RMSE results as well, with the exception that the SS-TWR method provided consistently about 0.4 m inferior results than the other methods. The large errors of some test points are also present in the 3D results, with a maximum of about 5.4 m for both the SS-TWR and AP-TWR methods, while the A-EKF provided a maximum error of only 0.9 m. Across all of the test points, the average RMSE of the proposed method was more than 3 times lower than the next method, AP-TWR.

The movement tests confirmed the validity of A-EKF stationary tests by showing that the largest errors of AP-TWR and SS-TWR, caused by the presence of various assets in the factory, are reduced ninefold. Both sets of experiments showed the robustness of the proposed A-EKF positioning method with its ability to drastically reduce large errors caused by the propagation conditions.

While the current study has demonstrated the effectiveness of the A-EKF method, further investigation is warranted to identify and determine the optimal parameters for this approach. In-depth analyses and experimentations should be conducted to explore the impact of different parameter configurations on the method's performance, accuracy, and robustness. This exploration will contribute to refining the A-EKF algorithm.

The current paper has presented an overview of AP-TWR NLoS error cases. However, a more comprehensive and detailed analysis is required to identify and characterize specific NLoS error scenarios. In-depth investigations should be conducted to explore the possibilities of developing strategies to detect and mitigate these specific NLoS cases effectively. This analysis should encompass a broader range of environmental conditions, and diverse deployment scenarios to enhance the understanding and mitigation of AP-TWR NLoS errors.

## REFERENCES

- [1] *IEEE Standard for Information Technology—Local and Metropolitan Area Networks—Specific Requirements—Part 15.4: Wireless Medium Access Control (MAC) and Physical Layer (PHY) Specifications for Low-Rate Wireless Personal Area Networks (WPANs): Amendment 1: Add Alternate PHYs*, IEEE Standard 802.15.4a-2007, 2007.
- [2] J. Kuntho, A. Karkar, S. Al-Maadeed, and A. Al-Ali, "Indoor positioning and wayfinding systems: A survey," *Hum.-Centric Comput. Inf. Sci.*, vol. 10, no. 1, Dec. 2020, doi: [10.1186/s13673-020-00222-0](https://doi.org/10.1186/s13673-020-00222-0).

- [3] T. Savic, X. Vilajosana, and T. Watteyne, "Constrained localization: A survey," *IEEE Access*, vol. 10, pp. 49297–49321, 2022.
- [4] M. Ridolfi, A. Kaya, R. Berkvens, M. Weyn, W. Joseph, and E. D. Poorter, "Self-calibration and collaborative localization for UWB positioning systems: A survey and future research directions," *ACM Comput. Surv.*, vol. 54, no. 4, pp. 1–27, May 2021, doi: [10.1145/3448303](https://doi.org/10.1145/3448303).
- [5] N. Smaoui, O. Gnawali, and K. Kim, "Study and mitigation of platform related UWB ranging errors," in *Proc. Int. Conf. Commun. Syst. Netw. (COMSNETS)*, Jan. 2020, pp. 346–353.
- [6] L. Mainetti, L. Patrono, and I. Sergi, "A survey on indoor positioning systems," in *Proc. 22nd Int. Conf. Softw., Telecommun. Comput. Netw. (SoftCOM)*, Sep. 2014, pp. 111–120.
- [7] I. Guvenç and C.-C. Chong, "A survey on TOA based wireless localization and NLOS mitigation techniques," *IEEE Commun. Surveys Tuts.*, vol. 11, no. 3, pp. 107–124, 2nd Quart., 2009.
- [8] Decawave. *DW1000 User Manual V2.18*. Accessed: Dec. 21, 2022. [Online]. Available: <https://www.decawave.com/dw1000/usermanual/>
- [9] V. Barral, C. J. Escudero, J. A. García-Naya, and R. Maneiro-Catoira, "NLOS identification and mitigation using low-cost UWB devices," *Sensors*, vol. 19, no. 16, p. 3464, Aug. 2019.
- [10] S. Krishnan, R. X. M. Santos, E. R. Yap, and M. T. Zin, "Improving UWB based indoor positioning in industrial environments through machine learning," in *Proc. 15th Int. Conf. Control, Autom., Robot. Vis. (ICARCV)*, Nov. 2018, pp. 1484–1488.
- [11] F. Che, Q. Z. Ahmed, J. Fontaine, B. Van Herbruggen, A. Shahid, E. De Poorter, and P. I. Lazaridis, "Feature-based generalized Gaussian distribution method for NLOS detection in ultra-wideband (UWB) indoor positioning system," *IEEE Sensors J.*, vol. 22, no. 19, pp. 18726–18739, Oct. 2022.
- [12] M. Shalihan, R. Liu, and C. Yuen, "NLOS ranging mitigation with neural network model for UWB localization," in *Proc. IEEE 18th Int. Conf. Autom. Sci. Eng. (CASE)*, Aug. 2022, pp. 1370–1376.
- [13] J. Wu, Z. Zhang, S. Zhang, Z. Kuang, and L. Zhang, "UWB positioning algorithm based on fuzzy inference and adaptive anti-NLOS Kalman filtering," *Appl. Sci.*, vol. 12, no. 12, p. 6183, Jun. 2022. [Online]. Available: <https://www.mdpi.com/2076-3417/12/12/6183>
- [14] R. Zandian and U. Witkowski, "Differential NLOS error detection in UWB-based localization systems using logistic regression," in *Proc. 15th Workshop Positioning, Navigat. Commun. (WPNC)*, Oct. 2018, pp. 1–6.
- [15] K. Gururaj, A. K. Rajendra, Y. Song, C. L. Law, and G. Cai, "Real-time identification of NLOS range measurements for enhanced UWB localization," in *Proc. Int. Conf. Indoor Positioning Indoor Navigat. (IPIN)*, Sep. 2017, pp. 1–7.
- [16] Z. Cui, T. Liu, S. Tian, R. Xu, and J. Cheng, "Non-line-of-sight identification for UWB positioning using capsule networks," *IEEE Commun. Lett.*, vol. 24, no. 10, pp. 2187–2190, Oct. 2020.
- [17] C. Liu, Y. Cao, C. Sun, W. Shen, X. Li, and L. Gao, "An outlier-aware method for UWB indoor positioning in NLoS situations," in *Proc. IEEE 25th Int. Conf. Comput. Supported Cooperat. Work Design (CSCWD)*, May 2022, pp. 1504–1509.
- [18] J. Wang, K. Yu, J. Bu, Y. Lin, and S. Han, "Multi-classification of UWB signal propagation channels based on one-dimensional wavelet packet analysis and CNN," *IEEE Trans. Veh. Technol.*, vol. 71, no. 8, pp. 8534–8547, Aug. 2022.
- [19] S. Tomovic, K. Bregar, T. Javornik, and I. Radusinovic, "Transformer-based NLoS detection in UWB localization systems," in *Proc. 30th Telecommun. Forum (TELFOR)*, Nov. 2022, pp. 1–4.
- [20] M. Si, Y. Wang, H. Sijjak, C. Seow, and H. Yang, "A lightweight CIR-based CNN with MLP for NLOS/LOS identification in a UWB positioning system," *IEEE Commun. Lett.*, vol. 27, no. 5, pp. 1332–1336, May 2023.
- [21] D.-H. Kim, A. Farhad, and J.-Y. Pyun, "UWB positioning system based on LSTM classification with mitigated NLOS effects," *IEEE Internet Things J.*, vol. 10, no. 2, pp. 1822–1835, Jan. 2023.
- [22] K. Yu, K. Wen, Y. Li, S. Zhang, and K. Zhang, "A novel NLOS mitigation algorithm for UWB localization in harsh indoor environments," *IEEE Trans. Veh. Technol.*, vol. 68, no. 1, pp. 686–699, Jan. 2019.
- [23] Z. Zeng, R. Bai, L. Wang, and S. Liu, "NLOS identification and mitigation based on CIR with particle filter," in *Proc. IEEE Wireless Commun. Netw. Conf. (WCNC)*, Apr. 2019, pp. 1–6.
- [24] C. Chen, Z. Huang, J. Wang, L. Yuan, J. Bao, and Z. Chen, "Channel-quality-evaluation-based anchor node selection for UWB indoor positioning," *Electronics*, vol. 11, no. 3, p. 436, Jan. 2022. [Online]. Available: <https://www.mdpi.com/2079-9292/11/3/436>
- [25] C. Jiang, J. Shen, S. Chen, Y. Chen, D. Liu, and Y. Bo, "UWB NLOS/LOS classification using deep learning method," *IEEE Commun. Lett.*, vol. 24, no. 10, pp. 2226–2230, Oct. 2020.
- [26] P.-C. Chen, "A non-line-of-sight error mitigation algorithm in location estimation," in *Proc. IEEE Wireless Commun. Netw. Conf.*, Mar. 1999, pp. 316–320.
- [27] L. Jiao, J. Xing, X. Zhang, C. Zhao, and J. Zhang, "LCC-RWGH: A NLOS error mitigation algorithm for localization in wireless sensor network," in *Proc. IEEE Int. Conf. Control Autom.*, May 2007, pp. 1354–1359.
- [28] Y. T. Chan, W. Y. Tsui, H. C. So, and P.-C. Ching, "Time-of-arrival based localization under NLOS conditions," *IEEE Trans. Veh. Technol.*, vol. 55, no. 1, pp. 17–24, Jan. 2006.
- [29] B. J. Silva and G. P. Hancke, "Non-line-of-sight identification without channel statistics," in *Proc. 46th Annu. Conf. IEEE Ind. Electron. Soc.*, Oct. 2020, pp. 4489–4493.
- [30] Q.-T. Ngo, P. Roussel, B. Denby, and G. Dreyfus, "Correcting non-line-of-sight path length estimation for ultra-wideband indoor localization," in *Proc. Int. Conf. Localization GNSS (ICL-GNSS)*, Jun. 2015, pp. 1–6.
- [31] B. Silva and G. P. Hancke, "Ranging error mitigation for through-the-wall non-line-of-sight conditions," *IEEE Trans. Ind. Informat.*, vol. 16, no. 11, pp. 6903–6911, Nov. 2020.
- [32] J. Borras, P. Hatrack, and N. B. Mandayam, "Decision theoretic framework for NLOS identification," in *Proc. 48th IEEE Veh. Technol. Conf., Pathway Global Wireless Revolution*, Mar. 1998, pp. 1583–1587.
- [33] J. Schroeder, S. Galler, K. Kyamakyaa, and K. Jobmann, "NLOS detection algorithms for ultra-wideband localization," in *Proc. 4th Workshop Positioning, Navigat. Commun.*, Mar. 2007, pp. 159–166.
- [34] A. A. Momtaz, F. Behnia, R. Amiri, and F. Marvasti, "NLOS identification in range-based source localization: Statistical approach," *IEEE Sensors J.*, vol. 18, no. 9, pp. 3745–3751, May 2018.
- [35] T. Laadung, S. Ulp, M. M. Alam, and Y. L. Moullec, "Novel active-passive two-way ranging protocols for UWB positioning systems," *IEEE Sensors J.*, vol. 22, no. 6, pp. 5223–5237, Mar. 2022.
- [36] T. Laadung, S. Ulp, M. M. Alam, and Y. L. Moullec, "Performance evaluation of UWB active-passive two-way ranging distance estimation matrix weighting methods," in *Proc. 12th Int. Conf. Indoor Positioning Indoor Navigat.*, Sep. 2022, pp. 1–5.
- [37] S. Wu, Y. Ma, Q. Zhang, and N. Zhang, "NLOS error mitigation for UWB ranging in dense multipath environments," in *Proc. IEEE Wireless Commun. Netw. Conf.*, Mar. 2007, pp. 1565–1570.
- [38] G. Shen, R. Zetik, O. Hirsch, and R. S. Thomä, "Range-based localization for UWB sensor networks in realistic environments," *EURASIP J. Wireless Commun. Netw.*, vol. 2010, no. 1, pp. 1–12, Dec. 2009.
- [39] R. Zandian and U. Witkowski, "Non-line of sight error mitigation in Bayesian differential localization systems," in *Proc. 15th Workshop Positioning, Navigat. Commun. (WPNC)*, Oct. 2018, pp. 1–6.
- [40] C. K. Toth, G. Jozkow, Z. Koppányi, and D. Grejner-Brzezinska, "Positioning slow-moving platforms by UWB technology in GPS-challenged areas," *J. Surveying Eng.*, vol. 143, no. 4, Nov. 2017, Art. no. 04017011.
- [41] S. A. R. Zekavat and R. M. Buehrer, *Handbook of Position Location: Theory, Practice, and Advances*, 2nd ed. Hoboken, NJ, USA: Wiley, 2019.
- [42] C. L. Sang, M. Adams, M. Hesse, T. Hörmann, T. Korthals, and U. Rückert, "A comparative study of UWB-based true-range positioning algorithms using experimental data," in *Proc. 16th Workshop Positioning, Navigat. Commun. (WPNC)*, Oct. 2019, pp. 1–6.
- [43] Q. Li, K. Li, and W. Liang, "A zero-velocity update method based on neural network and Kalman filter for vehicle-mounted inertial navigation system," *Meas. Sci. Technol.*, vol. 34, no. 4, Jan. 2023, Art. no. 045110, doi: [10.1088/1361-6501/acabde](https://doi.org/10.1088/1361-6501/acabde).
- [44] D. Feng, C. Wang, C. He, Y. Zhuang, and X.-G. Xia, "Kalman filter-based integration of IMU and UWB for high-accuracy indoor positioning and navigation," *IEEE Internet Things J.*, vol. 7, no. 4, pp. 3133–3146, Apr. 2020. [Online]. Available: <https://ieeexplore.ieee.org/document/8954658/>
- [45] S. Akhlaghi, N. Zhou, and Z. Huang, "Adaptive adjustment of noise covariance in Kalman filter for dynamic state estimation," in *Proc. IEEE Power Energy Soc. Gen. Meeting*, Jul. 2017, pp. 1–5.
- [46] Y.-W. Chen and K.-M. Tu, "Robust self-adaptive Kalman filter with application in target tracking," *Meas. Control*, vol. 55, nos. 9–10, pp. 935–944, Nov. 2022, doi: [10.1177/00202940221083548](https://doi.org/10.1177/00202940221083548).
- [47] Eliko Tehnologgia Arenduskeskus OÜ. *Eliko UWB RTLS*. Apr. 11, 2023. [Online]. Available: <https://eliko.ee/uwb-rtls-ultra-wideband-real-time-location-system/>



- [48] Leica Geosystems AG. (Apr. 11, 2023). *Leica DISTO S910 User Manual*. [Online]. Available: <https://shop.leica-geosystems.com/sites/default/files/2019-04/leica-disto-s910-user-manual-805080-808183-806677-en.pdf>
- [49] (Apr. 11, 2023). *Krah Pipes OÜ*. [Online]. Available: <http://www.krah-pipes.ee/eng/>
- [50] T. Laadung, S. Ulp, "UWB active-passive two-way ranging protocol data captured in an industrial environment," IEEE Dataport, Jun. 2023, doi: 10.21227/4f5b-gx15.



**TAAVI LAADUNG** was born in Tallinn, Estonia, in 1990. He received the B.Sc. and M.Sc. degrees in telecommunication from the Tallinn University of Technology, Tallinn, in 2013 and 2016, respectively, where he is currently pursuing the Ph.D. degree in information and communication technology. From 2015 to 2016, he was a Course Practical Work Supervisor with the Tallinn University of Technology. From 2017 to 2019, he was a Communication Systems Research and Development Specialist with Estonian Defence Forces. Since 2019, he has been a Researcher with OÜ Eliko Tehnoloogia Arenduskeskus, Tallinn. His current research interests include the improvement of algorithms and methods utilized in wireless indoor tracking, positioning, and object-locating systems.



**SANDER ULP** received the M.Sc. degree in telecommunication and the Ph.D. degree in information and communication technology from the Tallinn University of Technology, in 2013 and 2019, respectively. In 2018, he was a Researcher with OÜ Eliko Tehnoloogia Arenduskeskus. Since 2019, he has been held the position of Chief Technology Officer (CTO) at this technology competence center, which is dedicated to pioneering advancements in indoor positioning research and technologies. His current research interests include distributed estimation, learning and adaptation over networks, digital signal processing, localization technologies, and indoor positioning.



**ALEKSEI FIODOROV** was born in Tallinn, Estonia, in 1995. He received the B.Sc. and M.Sc. degrees in telecommunication from the Tallinn University of Technology (TUT), Estonia, in 2017 and 2021, respectively, where he is currently pursuing the Ph.D. degree in telecommunication. Since 2021, he has been a Researcher with OÜ Eliko Tehnoloogia Arenduskeskus, Tallinn. His current research interests include sensor fusion-enabled indoor positioning and tracking, the IoT, and electronics and communication technologies.



**MUHAMMAD MAHTAB ALAM** (Senior Member, IEEE) received the M.Sc. degree in electrical engineering from Aalborg University, Denmark, in 2007, and the Ph.D. degree in signal processing and telecommunication from the INRIA Research Center, University of Rennes 1, France, in 2013. From 2014 to 2016, he was Post-Doctoral Research at the Qatar Mobility Innovation Center, Qatar. In 2016, he joined as the European Research Area Chair and as an Associate Professor with the Thomas Johann Seebeck Department of Electronics, Tallinn University of Technology, where he was elected as a Professor in 2018 and Tenured Full Professor in 2021. Since 2019, he has been the Communication Systems Research Group Leader. He has over 15 years of combined academic and industrial multinational experiences while working in Denmark, Belgium, France, Qatar, and Estonia. He has several leading roles as PI in multimillion Euros international projects funded by European Commission (Horizon Europe LATEST-5GS, 5G-TIMBER, H2020 5G-ROUTES, NATOSPS (G5482), Estonian Research Council (PRG424), Telia Industrial Grant etc. He is an author and co-author of more than 100 research publications. He is actively supervising a number of Ph.D. and Postdoc Researchers. He is also a contributor in two standardization bodies (ETSI SmartBAN, IEEE-GeenICT-EECH), including "Rapporteur" of work item: DTR/ SmartBAN-0014. His research focuses on the fields of wireless communications—connectivity, mobile positioning, 5G/6G services and applications.



**YANNICK LE MOULLEC** (Senior Member, IEEE) received the M.Sc. degree from Université de Rennes I, France, in 1999, and the Ph.D. and H.D.R. (accreditation to supervise research) degrees from Université de Bretagne Sud, France, in 2003 and 2016, respectively. From 2003 to 2013, he was a Postdoctoral Researcher, an Assistant Professor, and an Associate Professor with the Department of Electronic Systems, Aalborg University, Denmark. Then, he joined the Thomas Johann Seebeck Department of Electronics, Tallinn University of Technology, Estonia, where he was a Senior Researcher, from 2013 to 2016, and has been a Professor, since 2017. He has supervised or co-supervised more than 50 M.Sc. students and 11 Ph.D. students. He has been involved in more than 20 projects, including five as the PI and the co-PI or the co-main applicant; one such notable project was the H2020 COEL ERA-Chair Project, from 2015 to 2019. His current research interests include embedded systems, reconfigurable systems, the IoT, and the application thereof. He is a member of the IEEE Sustainable ICT Technical Community and the IEEE Circuits and Systems Society.

...

## Appendix 3

### III

A. Fjodorov, S. Ulp, T. Laadung, M. M. Alam, and A. Kuusik, "Vehicle Heading Estimation Using Positioning and Inertial Data-Based Adaptive Tandem Kalman Filter," *IEEE Transactions on Intelligent Vehicles*, 2025



# Vehicle Heading Estimation Using Positioning and Inertial Data-Based Adaptive Tandem Kalman Filter

Aleksei Fjodorov<sup>✉</sup>, Sander Ulp<sup>✉</sup>, Taavi Laadung<sup>✉</sup>, Alar Kuusik<sup>✉</sup>, *Senior Member, IEEE*, Muhammad Mahtab Alam<sup>✉</sup>, *Senior Member, IEEE*

**Abstract**—This paper proposes an Adaptive Tandem Kalman Filter (ATKF) algorithmic method for accurate, robust, and magnetometer-free heading estimation through the competitive fusion of inertial and positioning data. It aims to mitigate the angular heading drift, typically present in MEMS IMU (Micro-Electromechanical Systems Inertial Measurement Unit) sensors, without the use of environmentally sensitive magnetometers. Due to its adaptive nature, the ATKF algorithm is capable of iterative estimation of the input data significance, based on the tracked vehicle behavior, and performing a corresponding weighted fusion. A novel tandem structure allows to perform a series of consecutive data processing steps within a single Kalman filter iteration, thus minimizing the delay in algorithmic response to the input data. Series of simulated comparison tests with one of the state-of-the-art algorithms have demonstrated the high stability and robustness of the proposed algorithm. It has shown a consistent 40% to 90% improvement in the estimated heading accuracy and precision, depending on the maneuvering intensity and the data quality. Simulation results were experimentally validated during the full-scale test campaign, conducted in the industrial environment using a highly maneuverable forklift. Real-time forklift heading was tracked by the proposed ATKF algorithm with a 1° overall median error and 2.3° median error during the active movement periods. The proposed method has respectively shown 95% and 93% improvement in initial IMU heading accuracy and precision. Experimental performance evaluation of the magnetometer-based heading estimation methods has practically confirmed their unreliability and inconsistency in industrial applications. The proposed ATKF heading estimation algorithm may find a variety of possible applications in the field of robotics and intelligent vehicles. It is expected to be especially useful in magnetometer-denied environments.

**Index Terms**—Gyroscope, Heading estimation, IMU, Kalman filter, Magnetometer-free, Positioning, Sensor fusion, Vehicle application.

## I. INTRODUCTION

**H**EADING information is one of the key aspects of vehicle navigation, along with its position and speed information [1]. Accurate heading information plays an important role in various fields of vehicle control and is essential for self-navigation and collision avoidance in the field of autonomous vehicles [2]–[4].

A variety of different real-time vehicle heading tracking methods exist. Relatively straightforward methods are based on the measurement of the Earth's magnetic field by using magnetometers (i.e., a compass) [5]. Magnetometers, however, are also naturally sensitive to random distortions in the Earth's magnetic field and the interference caused by the surrounding ferromagnetic objects in the vicinity [6], [7]. Even though a

variety of calibration techniques are often used to improve the magnetometer performance in a given environment, they are only capable of compensating for the constant surrounding magnetic distortions [8], [9]. Compensation for dynamic magnetic interference, on the other hand, represents a major challenge in this field. For this reason, magnetometers become highly unreliable in a variety of land applications and especially in industrial environments [10]–[14]. More complex solutions, such as optical flow or LiDAR (Light Detection and Ranging) based methods, provide the real-time mapping of the surrounding environment for self-navigation [15], [16].

Inertial data-based methods (i.e., gyroscopes) allow real-time measurements of the rotational motion and are widely used in real-time orientation tracking applications [17]. Among other gyroscope types, MEMS (Micro-Electro-Mechanical Systems) gyroscopes provide unique benefits of high portability, efficiency, and availability. MEMS gyroscopes are often encountered as part of 6-DOF (Degrees of Freedom) inertial measurement units (IMUs) along with accelerometer sensors [18]. 9-DOF IMU units, sometimes also referred to as MARG (Magnetic, Angular Rate, and Gravity) or AHRS (Attitude and Heading Reference System), additionally include a magnetometer sensor [19], [20]. Bias instabilities and internal noise of MEMS gyroscopes, however, naturally cause overtime accumulated error in the tracked heading, also known as a drift or angular random walk (ARW) [21]. Gyroscope drift mitigation is essential for successful real-time orientation tracking, especially in different vehicle tracking applications.

## A. Related Works

A variety of different gyroscope fusion techniques, aimed for its drift mitigation and further heading estimation, exist in the literature. Some of them use complementary filtering of the initial gyroscope and accelerometer data of the IMU, as, for example, proposed by Wang *et al.* [22]. This approach provides processing simplicity and does not require additional auxiliary sensors. Inertial data noise filtering, however, also inevitably impacts the data itself, which becomes the limitation of this method. This mainly affects the inertial data on the minor movement and rotation, due to its low, close to the noise level magnitude.

Certain case-specific methods, such as NMNI (No Motion, No Integration), used by Hoang *et al.* offer an even simpler approach for gyroscope drift elimination without assisting sensors [10], [23]. In this method, any sensor input below the

noise magnitude is disregarded. This consequently eliminates a significant part of the drift component along with minor heading adjustments, thus limiting the applicability of this method, especially in vehicle heading tracking. A similar ZUPT (Zero Velocity Update) method is frequently used in human motion tracking [24]. The inability of these methods to spot minor adjustments in vehicle heading makes them unsuitable for vehicle heading tracking.

State-of-the-art heading drift elimination techniques propose a gyroscope fusion with assisting sensors, by using state-of-the-art fusion algorithms, such as Madgwick, Mahony, or Kalman filters, as, for instance, described by Ludwig *et al.* and Hoang *et al.* [10], [12], [13], [25]. Depending on the application, these methods often provide state-of-the-art performance in angular drift elimination. Specifically for the heading drift elimination, these methods rely on the environmentally sensitive magnetometer units [10], [12], [13], [25].

Vehicle heading tracking is also covered in the field of vehicle state estimation, which covers a detailed tracking of different vehicle dynamic parameters for its stability control applications [26]–[29]. In this field, inertial units are mainly assisted by various field-specific sensors, such as steering or wheel speed sensors. Even though the diversity of sensors allows an accurate vehicle heading estimation, it also leads to increased computational complexity, cost, and energy consumption.

An algorithmic method for IMU heading drift mitigation was proposed in the author's earlier studies [30]. This method performs the IMU heading error correction, based on the vehicle positioning information, and avoids the use of environmentally sensitive magnetometers. Even though this algorithm has experimentally demonstrated a good performance in IMU drift mitigation, it also contains certain performance limitations. These include high sensitivity to the positioning data quality and the requirement for episodic movement in a straight line.

## B. Contributions

This work offers an algorithmic method for accurate vehicle heading estimation, based on the adaptive version of the state-of-the-art Kalman filter algorithm with the tandem structure. It performs a competitive fusion of inertial and positioning data for heading estimation. Competitive configuration of the sensor fusion combines multiple data sources of the same property to provide an increased robustness and fault tolerance [31].

The proposed algorithm adapts to real-time vehicle movement behavior by iteratively estimating the input data significance and performing a corresponding weighted fusion of heading data. The designed tandem structure of the algorithm allows to perform a series of consecutive data processing steps within a single algorithm iteration. In comparison with the traditional Kalman filter structure, this minimizes the delay of the algorithm's response to the input data. This algorithm avoids the use of environmentally sensitive magnetometers or other auxiliary sensors. This allows the proposed method to be used on ground vehicles without the need for extra supporting sensors for heading estimation. This article provides

a performance comparison of the proposed algorithm with the algorithm from the state-of-the-art literature in a series of simulations. Simulations cover different data quality levels and vehicle movement scenarios. This work also covers full-scale experimental testing and evaluation of the proposed algorithm by using a highly maneuverable forklift, naturally operating in the industrial environment.

The remaining paper is organized as follows: Section II describes the structure and key aspects of the proposed heading estimation algorithm. Section III demonstrates the direct performance comparison of the proposed algorithm with one of the state-of-the-art algorithms in a series of simulated tests. Section IV describes the conducted experimental test campaign and the used sensors. Section V describes the results of the experimental testing. Section VI concludes this paper.

## II. ADAPTIVE TANDEM KALMAN FILTER FOR HEADING ESTIMATION

The proposed algorithmic method represents an adaptive version of the state-of-the-art Kalman filter fusion algorithm with the custom tandem structure. It performs a competitive fusion of the inertial and positioning data for a vehicle heading estimation. The Adaptive Tandem Kalman Filter (ATKF) algorithm, proposed in this work, represents an adaptive version of the state-of-the-art Kalman filter fusion algorithm with the proposed tandem structure. In this algorithm, vehicle heading information is separately obtained from the inertial and positioning data and further fused by using the competitive configuration. This configuration provides an increased robustness of the resulting heading and allows to avoid critical flaws of the initial data sources (e.g., gyroscope drift).

The proposed ATKF algorithm is based on the features of the Adaptive Kalman filter version. These features are essential in real-life applications, as they allow the algorithm to flexibly adapt its response to any external changes. In this work, the adaptivity features are used for a real-time choice of a more trusted source of heading information, depending on the current vehicle movement behavior. Adaptivity of the ATKF algorithm is represented with iteratively recalculated noise covariance parameters by using a proposed weight function.

In the proposed ATKF algorithm, the standard Kalman filter correction part is separated into three consecutive correction steps. With this structure, the algorithm is capable of performing three consecutive processing steps of the input positioning data within a single algorithm iteration, where the results of the earlier correction step are immediately used in the next correction step. In this work, this structure is referred to as a tandem structure. It allows the ATKF algorithm to perform multiple consecutive data correction steps within a single Kalman filter iteration. This structure ensures a complete and real-time use of the newly arrived data, thus possibly reducing its relevance loss.

A flowchart of the proposed Adaptive Tandem Kalman filter algorithm for the heading estimation is shown in Fig. 1, reflecting the main processing steps and changes to the key parameters. Algorithm 1 demonstrates the corresponding pseudo-code of the proposed ATKF algorithm. In this work,

---

**Algorithm 1:** Positioning and inertial data-based Adaptive Tandem Kalman Filter (ATKF) algorithm for vehicle heading estimation

---

<b>Parameters:</b>	Movement speed thresholds : $v_{thr}^x, v_{thr}^y, v_{thr}^z$ , $v_{thr}^{\psi}$
	Weight function coefficients : $a^x, a^y, a^z, a^{\psi}$
	Estimation model noise covariance parameters : $q^{pos}, q^x, q^y, q^{\psi}, q_{min}^x, q_{min}^y, q_{max}$
	Measurement noise covariance parameters : $r^{pos}, r^x, r^y, r^{\psi}, r_{min}^x, r_{min}^y, r_{max}$
<b>Initialize</b>	Initial state vector : $\mathbf{X}_0$
	Initial state covariance matrix : $\mathbf{P}_0 = \mathbf{I}_7$
<b>Input Data</b>	Positioning data input : $(x, y)_k^{meas}$
	Delta time of the positioning data : $dt_k^{xy}$
	Yaw angular velocity input : $\omega_k$
	Delta time of the gyroscope input data ( $\omega_k$ ) : $dt_k^{\omega}$
<b>Outputs</b>	Resulting heading : $\Psi_k$

```

for  $k \leftarrow 1$  to inf  $do$  // Estimation
    if  $v_{k-1} > v_{thr}^0$  then
         $\hat{\mathbf{X}}_k = \mathbf{A}_k \cdot \mathbf{X}_{k-1} + \mathbf{B}_k \cdot \mathbf{u}_k$ 
    else
         $\hat{\mathbf{X}}_k = \mathbf{A}_k \cdot \mathbf{X}_{k-1}$ 
    end

     $q_k^\phi = f^W(v_{k-1}, v_{thr}^\phi, a^\phi, q_{min}^\phi, q_{max})$ 
     $q_k^\psi = f^W(v_{k-1}, v_{thr}^\psi, a^\psi, q_{min}^\psi, q_{max})$ 

    Compose  $\mathbf{Q}_k$  matrix,  $\forall i: (\mathbf{Q}_k)_{ii} \in \{q^{pos}, q^v, q^v, q_k^\phi, q_k^\psi\}$ 

     $\hat{\mathbf{P}}_k = \mathbf{A}_k \cdot \mathbf{P}_{k-1} \cdot \mathbf{A}_k^T + \mathbf{Q}_k$ 

    if New  $(x, y)_k^{meas}$  input available then // Correction 1
         ${}^1\mathbf{K}_k = \hat{\mathbf{P}}_k \cdot {}^1\mathbf{H}^T \cdot ({}^1\mathbf{H} \cdot \hat{\mathbf{P}}_k \cdot {}^1\mathbf{H}^T + {}^1\mathbf{R})^{-1}$ 
         ${}^1\mathbf{X}_k = \hat{\mathbf{X}}_k + {}^1\mathbf{K}_k \cdot ({}^1\mathbf{Z}_k - {}^1\mathbf{H} \cdot \hat{\mathbf{X}}_k)$ 
         ${}^1\mathbf{P}_k = (\mathbf{I}_7 - {}^1\mathbf{K}_k \cdot {}^1\mathbf{H}) \cdot \hat{\mathbf{P}}_k$ 

        // Correction 2
         $\hat{v}_k = \sqrt{(v_k^x)^2 + (v_k^y)^2}$ 
         $\hat{\phi}_k = \text{atan2}(-v_k^x, -v_k^y) \cdot \frac{180}{\pi} + 180$ 
         $\hat{\phi}_k = \begin{cases} \hat{\phi}_k + 360, & \hat{\phi}_k - \phi_{k-1} < -180 \\ \hat{\phi}_k - 360, & \hat{\phi}_k - \phi_{k-1} > 180 \end{cases}$ 

        Compose  ${}^2\mathbf{z}_k$  vector,  ${}^2\mathbf{z}_k = [\hat{v}_k \quad \hat{\phi}_k]^T$ 

         $r_k^\phi = f^W(v_{k-1}, v_{thr}^\phi, -a^\phi, r_{min}^\phi, r_{max})$ 
        Compose  ${}^2\mathbf{R}_k$  matrix,  ${}^2\mathbf{R}_k = \text{diag}(r^v, r_k^\phi)$ 

         ${}^2\mathbf{K}_k = {}^1\mathbf{P}_k \cdot {}^2\mathbf{H}^T \cdot ({}^2\mathbf{H} \cdot {}^1\mathbf{P}_k \cdot {}^2\mathbf{H}^T + {}^2\mathbf{R}_k)^{-1}$ 
         ${}^2\mathbf{X}_k = {}^1\mathbf{X}_k + {}^2\mathbf{K}_k \cdot ({}^2\mathbf{z}_k - {}^2\mathbf{H} \cdot {}^1\mathbf{X}_k)$ 
         ${}^2\mathbf{P}_k = (\mathbf{I}_7 - {}^2\mathbf{K}_k \cdot {}^2\mathbf{H}) \cdot {}^1\mathbf{P}_k$ 

         $\phi_k = \phi_k \bmod 360$ 

        // Correction 3
         $\text{rng} = \{\phi_k, (\phi_k + 180) \bmod 360\}$ 
         $\phi_k = \arg \min_{\alpha \in \text{rng}} (|\alpha - \hat{\Psi}_k|)$ 

         $\phi_k = \begin{cases} \phi_k + 360, & \phi_k - \phi_{k-1} < -180 \\ \phi_k - 360, & \phi_k - \phi_{k-1} > 180 \end{cases}$ 

        Compose  ${}^3\mathbf{z}_k$  vector,  ${}^3\mathbf{z}_k = [\phi_k]$ 

         $r_k^\psi = f^W(v_{k-1}, v_{thr}^\psi, -a^\psi, r_{min}^\psi, r_{max})$ 
        Compose  ${}^3\mathbf{R}_k$  matrix,  ${}^3\mathbf{R}_k = \text{diag}(r_k^\psi)$ 

         ${}^3\mathbf{K}_k = {}^2\mathbf{P}_k \cdot {}^3\mathbf{H}^T \cdot ({}^3\mathbf{H} \cdot {}^2\mathbf{P}_k \cdot {}^3\mathbf{H}^T + {}^3\mathbf{R}_k)^{-1}$ 
         $\mathbf{X}_k = {}^2\mathbf{X}_k + {}^3\mathbf{K}_k \cdot ({}^3\mathbf{z}_k - {}^3\mathbf{H} \cdot {}^2\mathbf{X}_k)$ 
         $\mathbf{P}_k = {}^2\mathbf{P}_k \cdot (\mathbf{I}_7 - {}^3\mathbf{K}_k \cdot {}^3\mathbf{H}) \cdot {}^2\mathbf{P}_k$ 

         $\Psi_k = \Psi_k \bmod 360$ 
    else
         $\mathbf{X}_k = [(\mathbf{X}_{k-1})_{1:6} \quad (\hat{\mathbf{X}}_{k-1})_7]^T$ 
    end

    Output heading  $\Psi_k$ 
end

```

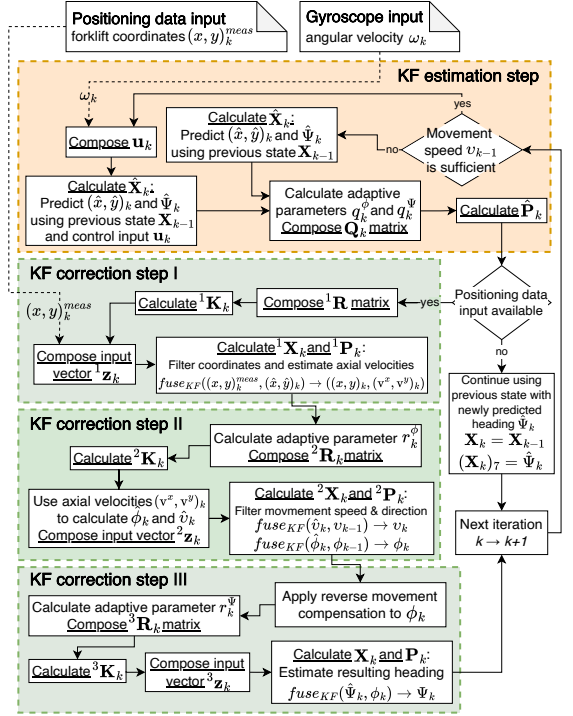


Fig. 1. Flowchart of the proposed ATKF algorithm for vehicle heading estimation.

the angular data is measured in degrees ( $^{\circ}$ ) for improved comprehensibility.

The algorithm starts with the estimation step, aimed to extrapolate the state estimation vector  $\hat{\mathbf{X}}_k$  for the current iteration  $k$ :

$$\hat{\mathbf{X}}_k = \begin{bmatrix} \hat{x}_k \\ \hat{y}_k \\ \mathbf{v}_{k-1}^x \\ \mathbf{v}_{k-1}^y \\ v_{k-1} \\ \phi_{k-1} \\ \hat{\Psi}_k \end{bmatrix} = \begin{bmatrix} x_{k-1} + dt_{k-1}^{xy} \cdot \mathbf{v}_{k-1}^x \\ y_{k-1} + dt_{k-1}^{xy} \cdot \mathbf{v}_{k-1}^y \\ \mathbf{v}_{k-1}^x \\ \mathbf{v}_{k-1}^y \\ v_{k-1} \\ \phi_{k-1} \\ \Psi_{k-1} + dt_{k-1}^\omega \cdot \omega_k \end{bmatrix}. \quad (1)$$

It contains algorithm estimations for the new positioning data coordinates  $(\hat{x}, \hat{y})_k$  and resulting heading  $\hat{\Psi}_k$ , along with the results of the previous iteration  $k - 1$ , including positioning data  $(x, y)_{k-1}$ , its axial velocities  $(v^x, v^y)_{k-1}$ , overall movement speed  $v_{k-1}$ , direction  $\phi_{k-1}$ , and the resulting heading  $\Psi_{k-1}$ . Heading angular velocity measurement is represented as  $\omega_k$ , while  $dt_k^{xy}$  and  $dt_k^\omega$  respectively are delta-time values of the positioning and inertial data measurements.

The state estimation vector is calculated as follows:

$$\hat{\mathbf{X}}_k = \begin{cases} \mathbf{A}_k \cdot \mathbf{X}_{k-1} + \mathbf{B}_k \cdot \mathbf{u}_k & v_{k-1} > v_{thr}^0 \\ \mathbf{A}_k \cdot \mathbf{X}_{k-1} & v_{k-1} \leq v_{thr}^0 \end{cases}, \quad (2)$$

by using the state vector of the previous iteration  $\mathbf{X}_{k-1}$  and the estimation model  $\mathbf{A}_k$ :

$$\mathbf{A}_k = \begin{bmatrix} 1 & 0 & dt_k^{xy} & 0 & 0 & 0 & 0 \\ 0 & 1 & 0 & dt_k^{xy} & 0 & 0 & 0 \\ 0 & 0 & 1 & 0 & 0 & 0 & 0 \\ 0 & 0 & 0 & 1 & 0 & 0 & 0 \\ 0 & 0 & 0 & 0 & 1 & 0 & 0 \\ 0 & 0 & 0 & 0 & 0 & 1 & 0 \\ 0 & 0 & 0 & 0 & 0 & 0 & 1 \end{bmatrix}, \quad (3)$$

as well as the control input model  $\mathbf{B}_k$  and control vector  $\mathbf{u}_k$ :

$$\mathbf{B}_k = [0 \ 0 \ 0 \ 0 \ 0 \ 0 \ dt_k^\omega]^T, \quad (4)$$

$$\mathbf{u}_k = [\omega_k]. \quad (5)$$

In this step, the algorithm extrapolates the expected coordinates  $(\hat{x}, \hat{y})_k$  and resulting heading  $\hat{\Psi}_k$  for the current iteration. The gyroscope input  $\omega_k$  is conditionally introduced, depending on the latest movement speed estimation  $v_{k-1}$  by using the control input  $\mathbf{B}_k \cdot \mathbf{u}_k$ . In case of the negligible movement speed (i.e., below the user-defined threshold  $v_{thr}^0$ ), the gyroscope input is ignored. This allows to avoid a potential impact of the gyroscope noise in completely stationary cases.

Adaptivity of the proposed algorithm to the input data is achieved with a real-time tuning of the model and measurement noise covariance parameters. In this work, these covariance parameters are respectively notated as  $q$  and  $r$  for model and measurement noise covariance matrices  $\mathbf{Q}$  &  $\mathbf{R}$ . These parameters are calculated for every iteration using the exponential weighting function  $f^W$ :

$$f^W(v_k, v_{thr}, a, \sigma_{min}, \sigma_{max}) = e^{a \cdot (v_k + b - v_{thr})} + \sigma_{min}, \quad (6)$$

where the weight function exists in the range between defined upper ( $\sigma_{max}$ ) and lower ( $\sigma_{min}$ ) noise covariance parameters  $f^W \in (\sigma_{min}, \sigma_{max}]$ . The exponential weight function is based on the input value of the ongoing movement speed  $v_k$ , which is an accessible and incomplex parameter, essential in the positioning data-based heading estimation. It determines the distinguishability of the actual movement from the positioning data noise, and thus, defines the reliability of positioning data-based movement direction, which is generally labeled as  $\phi$  later in this work. Within the proposed ATKF algorithm, it justifies the reliability of both positioning and inertial data inputs, thus preventing the fusion of expectedly unreliable sensors. Tuning coefficients of the weight function include the input coefficient  $a$  and internal coefficient  $b$ . The positive or negative sign of the tuning coefficient  $a$  respectively defines the descending or ascending weight function, while its scalar value determines the function ascent/descent rate. The movement speed threshold parameter  $v_{thr}$  defines the moment of the function descent. The internal tuning coefficient  $b$  is calculated as follows:

$$b = \frac{\ln(\sigma_{max} - \sigma_{min})}{a}. \quad (7)$$

The tuning coefficient  $a$  of the opposite sign is used to achieve synchronized and counterbalanced adaptive weighting in model ( $q$ ) and measurement ( $r$ ) noise covariance parameters. This enables a rapid transition between heading data

sources, thus minimizing the use of a momentarily unreliable sensor. The adaptivity of the ATKF algorithm at lower movement speeds may be further fine-tuned by integration of positioning quality analysis methods. This, however, may potentially bind the proposed method to the particular positioning system. Additionally, the use of reliable positioning quality estimation methods, such as channel impulse response (CIR), significantly increases the algorithm complexity, thus making it potentially unsuitable for real-life applications [32].

As demonstrated in the Algorithm 1 lines 7-8, adaptive estimation noise covariance weights  $q_k^\phi$  and  $q_k^\Psi$  are calculated respectively for the positioning data-based movement direction and the resulting heading. These weights are used to compose the estimation model noise covariance matrix  $\mathbf{Q}_k$ :

$$\mathbf{Q}_k = \begin{bmatrix} q^{pos} & 0 & 0 & 0 & 0 & 0 & 0 \\ 0 & q^{pos} & 0 & 0 & 0 & 0 & 0 \\ 0 & 0 & q^v & 0 & 0 & 0 & 0 \\ 0 & 0 & 0 & q^v & 0 & 0 & 0 \\ 0 & 0 & 0 & 0 & q^v & 0 & 0 \\ 0 & 0 & 0 & 0 & 0 & q_k^\phi & 0 \\ 0 & 0 & 0 & 0 & 0 & 0 & q_k^\Psi \end{bmatrix}. \quad (8)$$

State estimation covariance matrix  $\hat{\mathbf{P}}_k$  is then calculated as follows:

$$\hat{\mathbf{P}}_k = \mathbf{A}_k \cdot \mathbf{P}_{k-1} \cdot \mathbf{A}_k^T + \mathbf{Q}_k, \quad (9)$$

by using the previous state covariance matrix  $\mathbf{P}_{k-1}$ , estimation model, and estimation noise covariance matrix. The initial state covariance matrix represents the identity matrix  $\mathbf{I}_7$ .

This algorithm does not require the positioning and inertial data synchronization, thus allowing the inertial unit to have a naturally higher update rate. It is achieved by the capability of the proposed ATKF algorithm to entirely skip the Kalman correction step and operate only with the inertial information until the new positioning data arrives. In this case, the proposed algorithm only updates the resulting heading parameter  $\Psi$  in the state vector. In case of the missing positioning data, the positioning data delta-time  $dt_k^{xy}$  remains naturally unknown and can be replaced with a placeholder value (e.g.,  $dt_k^{xy} = 0$ ), as it is not used until the actual positioning data is available.

Once the positioning data is received, the ATKF algorithm proceeds with the correction part. It performs a total of three consecutive correction steps by calculating the Kalman gain matrix, state vector, and state covariance matrix for each step. The calculated matrices can be generally expressed as follows:

$${}^n\mathbf{K}_k = {}^{n-1}\mathbf{P}_k \cdot {}^n\mathbf{H}^T \cdot ({}^n\mathbf{H} \cdot {}^{n-1}\mathbf{P}_k \cdot {}^n\mathbf{H}^T + {}^n\mathbf{R}_k)^{-1}, \quad (10)$$

$${}^n\mathbf{X}_k = {}^{n-1}\mathbf{X}_k + {}^n\mathbf{K}_k \cdot ({}^n\mathbf{z}_k - {}^n\mathbf{H} \cdot {}^{n-1}\mathbf{X}_k), \quad (11)$$

$${}^n\mathbf{P}_k = (\mathbf{I}_7 - {}^n\mathbf{K}_k \cdot {}^n\mathbf{H}) \cdot {}^{n-1}\mathbf{P}_k, \quad (12)$$

where  $n$  is the sequence number of the correction step, while  $n = 0$  represents the Kalman estimation step. Measurement vector  ${}^n\mathbf{z}_k$ , measurement model  ${}^n\mathbf{H}$  and measurement noise covariance matrix  ${}^n\mathbf{R}_k$  are unique for each step and are prepared prior their use in the algorithm.

In the first correction step, the ATKF algorithm performs the positioning data filtering by using the newly measured positioning data  $(x, y)_k^{meas}$ , introduced in the first measurement vector  ${}^1\mathbf{z}_k$ :

$${}^1\mathbf{z}_k = \begin{bmatrix} x_k^{meas} \\ y_k^{meas} \end{bmatrix}, \quad (13)$$

and updates the positioning data-based axial velocities  $v_k^x$  and  $v_k^y$  in parallel. The first step Kalman gain matrix  ${}^1\mathbf{K}_k$  is calculated as shown in (10) by using the state estimation covariance matrix  $\hat{\mathbf{P}}_k$ , measurement model  ${}^1\mathbf{H}$ :

$${}^1\mathbf{H} = \begin{bmatrix} 1 & 0 & 0 & 0 & 0 & 0 & 0 \\ 0 & 1 & 0 & 0 & 0 & 0 & 0 \end{bmatrix}, \quad (14)$$

and measurement noise covariance matrix  ${}^1\mathbf{R}_k$ :

$${}^1\mathbf{R}_k = \begin{bmatrix} r^{pos} & 0 \\ 0 & r^{pos} \end{bmatrix}. \quad (15)$$

The preliminary state vector of the first step  ${}^1\mathbf{X}_k$  and the corresponding state covariance matrix  ${}^1\mathbf{P}_k$  are then respectively calculated in accordance with (11) and (12).

The second correction step of the ATKF algorithm is aimed at calculating the current movement direction  $\phi_k$  and speed  $v_k$ . The process starts with the estimation of both parameters ( $\hat{v}_k$  and  $\hat{\phi}_k$ ) by using the earlier updated positioning data-based axial velocities  $v_k^x$  and  $v_k^y$ , as demonstrated in the Algorithm 1 lines 15-16. In order to provide a smooth possible transition between  $0^\circ$  and  $360^\circ$ , the corresponding range limitation is temporarily removed for the estimated movement direction  $\hat{\phi}_k$ , as it is demonstrated in the Algorithm 1 line 17. The second measurement vector  ${}^2\mathbf{z}_k$  is then composed as follows:

$${}^2\mathbf{z}_k = \begin{bmatrix} \hat{v}_k \\ \hat{\phi}_k \end{bmatrix} = \begin{bmatrix} \sqrt{(v_k^x)^2 + (v_k^y)^2} \\ \text{atan2}(-v_k^x, -v_k^y) \cdot \frac{180}{\pi} + 180 \end{bmatrix}. \quad (16)$$

The adaptive weight for positioning data-based movement direction filtering  $r_k^\phi$  is calculated and used in the second-step measurement noise covariance matrix  ${}^2\mathbf{R}_k$ :

$${}^2\mathbf{R}_k = \begin{bmatrix} r^v & 0 \\ 0 & r_k^\phi \end{bmatrix}. \quad (17)$$

It is then used together with the measurement model  ${}^2\mathbf{H}$ :

$${}^2\mathbf{H} = \begin{bmatrix} 0 & 0 & 0 & 0 & 1 & 0 & 0 \\ 0 & 0 & 0 & 0 & 0 & 1 & 0 \end{bmatrix}, \quad (18)$$

and the previous step state covariance matrix  ${}^1\mathbf{P}_k$ , to calculate Kalman gain for the second correction step  ${}^2\mathbf{K}_k$ . The state vector  ${}^2\mathbf{X}_k$  and state covariance matrix  ${}^2\mathbf{P}_k$  of the corresponding step are also respectively calculated according to (11) and (12). This results with updated and filtered parameters of movement speed  $v_k$  and direction  $\phi_k$ , respectively available as  $5^{th}$  and  $6^{th}$  elements in the state vector  ${}^2\mathbf{X}_k$ . Movement direction  $\phi_k$  is then normalized back to the default  $0^\circ$  to  $360^\circ$  angular range as shown in the Algorithm 1 line 24.

The third correction step fuses the gyroscope input containing heading estimation  $\hat{\Psi}_k$  and the movement direction  $\phi_k$ , calculated from the positioning data. Correction for a possible case of reverse movement is then applied to the calculated movement direction  $\phi_k$  as shown in the Algorithm 1 lines 25 & 26. This correction prevents a possible sudden  $180^\circ$  flip in

positioning data-based heading, in case of occasional reverse movement. In this algorithm implementation, this correction is done by forming a temporary vector  $\mathbf{rng}$ , which contains the updated movement direction  $\phi_k$  and its counterpart heading with  $180^\circ$  offset  $\phi_k + 180^\circ$ , normalized to the range of  $0^\circ$  to  $360^\circ$ . The nearest value from the vector  $\mathbf{rng}$  to the current heading estimation  $\hat{\Psi}_k$  is then selected as shown in the Algorithm 1 line 26. This calculated movement direction  $\phi_k$  is used as input for the third measurement vector  ${}^3\mathbf{z}_k$ :

$${}^3\mathbf{z}_k = [\phi_k]. \quad (19)$$

The third measurement noise covariance matrix  ${}^3\mathbf{R}_k$  is formed as follows:

$${}^3\mathbf{R}_k = [r_k^\Psi], \quad (20)$$

and contains the adaptive weight for the resulting heading  $r_k^\Psi$ . This adaptive weight is calculated as demonstrated in Algorithm 1 line 29. Kalman gain matrix  ${}^3\mathbf{K}_k$ , state vector  ${}^3\mathbf{X}_k$  and state covariance matrix  ${}^3\mathbf{P}_k$  are then calculated for the third correction step. These matrices are calculated using third step measurement vector  ${}^3\mathbf{z}_k$ , measurement noise covariance matrix  ${}^3\mathbf{R}_k$ , and measurement model  ${}^3\mathbf{H}$ :

$${}^3\mathbf{H} = [0 \ 0 \ 0 \ 0 \ 0 \ 0 \ 1]. \quad (21)$$

The result of this correction step represents an output heading  $\Psi_k$  for the current iteration and requires a final normalization back to the default  $0^\circ$  to  $360^\circ$  angular range as shown in the Algorithm 1 lines 34.

In case of the missing positioning data, the entire correction section of the algorithm, described in Algorithm 1 lines 11 to 35, is skipped. Instead, the algorithm proceeds with the sole gyroscope data-based heading update, performed in the estimation section. The resulting state vector  $\mathbf{X}_k$  is formed as follows:

$$\mathbf{X}_k = \begin{bmatrix} (\mathbf{X}_{k-1})_{1:6} \\ (\hat{\mathbf{X}}_k)_7 \end{bmatrix} = \begin{bmatrix} x_{k-1} \\ y_{k-1} \\ v_{k-1}^x \\ v_{k-1}^y \\ v_{k-1} \\ \phi_{k-1} \\ \hat{\Psi}_k \end{bmatrix}, \quad (22)$$

by using the resulting state vector of the previous iteration  $\mathbf{X}_{k-1}$  and the gyroscope data-based heading estimation  $\hat{\Psi}_k$ , calculated by the algorithm in the estimation step. In the Algorithm 1, this part is demonstrated in line 36.

### III. SIMULATIONS

In a series of simulated tests, the performance of the proposed heading estimation ATKF algorithm was compared to the state-of-the-art IMU drift correction algorithm, further referred to as the benchmark algorithm [30]. The simulated vehicle was moving at varying speeds between 0.1 and 1 m/s, following one of two different movement paths, while performing maneuvering of different intensity and occasional reverse movement. Simulated movement paths I and II are respectively shown in Fig. 2a and Fig. 2b, where black and red arrows respectively indicate forward and reverse movement



directions. To push both tested algorithms to their limits, the positioning data for both simulated paths was generated with internal Gaussian noise of heuristically chosen standard deviation of  $\sigma_{\varepsilon}^{pos} = 0.5$  m and  $\sigma_{\varepsilon}^{pos} = 0.75$  m, thus resulting in four test scenarios. Gyroscope data was generated with a significant drift error of  $0.05^\circ/\text{s}$ , resulting in a  $60^\circ$  error by the end of each simulation. A set of 10 simulations was done for each of the four test scenarios. Both of the tested algorithms were heuristically tuned for each simulated path. ATKF algorithm parameters, used in simulations, are provided in Table III in the Appendix section.

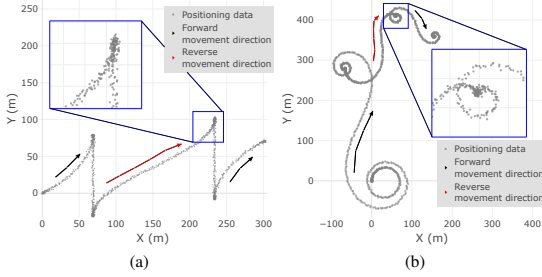


Fig. 2. Generated movement paths I (a) and II (b), used in a series of simulated tests with marked periods of forward and reverse movement.

Simulation results evaluate the heading estimation accuracy and precision of the compared algorithms. Used accuracy metrics include the Median Absolute Error (MdAE):

$$MdAE = \text{Median}(|X_i - X_i^{tru}|), \quad (23)$$

Mean Absolute Error (MnAE):

$$MnAE = \frac{\sum_{i=1}^N |X_i - X_i^{tru}|}{N}, \quad (24)$$

and Root Mean Squared Error (RMSE):

$$RMSE = \sqrt{\frac{\sum_{i=1}^N (X_i - X_i^{tru})^2}{N}}, \quad (25)$$

where  $X_i$  represents  $i^{th}$  observed value,  $X_i^{tru}$  is corresponding expected value, and  $N$  is the total number of samples. Used precision evaluation metrics include Median Absolute Deviation (MdAD):

$$MdAD_{err} = \text{Median}(|\varepsilon_i - MdAE|) \quad (26)$$

Mean Absolute Deviation (MnAD):

$$MnAD_{err} = \frac{\sum_{i=1}^N (\varepsilon_i - MAE)}{N}, \quad (27)$$

and Standard Deviation ( $\sigma$ ):

$$\sigma_{err} = \sqrt{\frac{\sum_{i=1}^N (\varepsilon_i - MAE)^2}{N}}, \quad (28)$$

where the error value  $\varepsilon_i$  of the  $i^{th}$  sample is calculated as:

$$\varepsilon_i = |X_i - X_i^{tru}|. \quad (29)$$

TABLE I  
AVERAGED HEADING ESTIMATION ACCURACY AND PRECISION RESULTS OF BOTH COMPARED ALGORITHMS FOR EVERY SET OF 10 SIMULATIONS.

			Benchmark alg. ( $^\circ$ )	ATKF alg. ( $^\circ$ )	Improvement over benchmark alg.
Path I	$\sigma_{\varepsilon}^{pos} = 0.5$ m	MdAE	3.1	2.1	34.1%
		MnAE	4.1	2.5	40.3%
		RMSE	5.3	3.1	41.4%
		MdAD <sub>err</sub>	2.0	1.3	38.1%
		MnAD <sub>err</sub>	2.8	1.6	44.0%
		$\sigma_{err}$	3.4	1.9	42.9%
	$\sigma_{\varepsilon}^{pos} = 0.75$ m	MdAE	4.2	2.6	39.4%
		MnAE	5.3	3.1	41.8%
		RMSE	6.7	3.9	41.2%
		MdAD <sub>err</sub>	2.7	1.5	43.8%
		MnAD <sub>err</sub>	3.4	1.9	43.5%
		$\sigma_{err}$	4.1	2.4	41.1%
Path II	$\sigma_{\varepsilon}^{pos} = 0.5$ m	MdAE	15.6	5.3	66.2%
		MnAE	52.7	6.6	87.4%
		RMSE	87.9	8.6	90.2%
		MdAD <sub>err</sub>	10.0	3.1	69.3%
		MnAD <sub>err</sub>	60.5	4.2	93.1%
		$\sigma_{err}$	70.3	5.4	92.3%
	$\sigma_{\varepsilon}^{pos} = 0.75$ m	MdAE	14.9	6.2	58.8%
		MnAE	52.0	9.0	82.7%
		RMSE	86.6	12.8	85.2%
		MdAD <sub>err</sub>	10.5	4.0	61.7%
		MnAD <sub>err</sub>	59.3	6.7	88.7%
		$\sigma_{err}$	69.3	9.0	87.0%

#### A. Simulated Path I

Generated movement path I covers a movement scenario with average maneuvering intensity and reverse movement cases. Averaged simulations' results for the movement path I are provided in the upper half of Table I, and demonstrate a good performance of both tested algorithms at both positioning data error levels. Depending on the positioning data quality, the proposed ATKF algorithm has demonstrated  $2.1^\circ$  to  $2.6^\circ$  of a median absolute error, which corresponds to a 34-40% improvement over the benchmark algorithm. Since the median absolute error metric excludes possible short-term error peaks, it depicts the overall accuracy of the evaluated algorithms. Outliers' sensitive RMSE metric has demonstrated a  $3.1^\circ$  to  $3.9^\circ$  error in the case of the ATKF algorithm, which represents a 41% improvement in comparison with the benchmark algorithm. These results indicate the minor presence of significant heading error outliers and confirm the overall stability of the proposed algorithm. Additionally, the ATKF algorithm demonstrates 1.75 times lower dispersion in RMSE results between different positioning data error rates, which indicates its higher robustness to positioning data errors.

The precision evaluation results have demonstrated  $1.3^\circ$  to  $1.5^\circ$  of median absolute deviation in the case of the ATKF algorithm. This represents a 38-43% improvement over the benchmark algorithm and indicates a minor presence of noise errors in the estimated heading. ATKF heading estimation results demonstrate a  $1.9^\circ$  to  $2.4^\circ$  error standard deviation, depending on the positioning data error rate. Both algorithms have shown a relatively negligible impact of the positioning

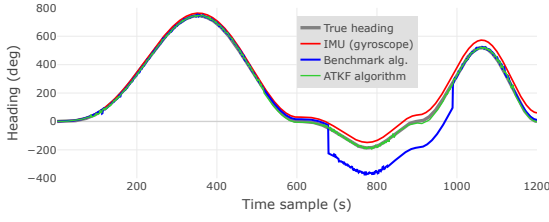


Fig. 3. Visualized vehicle heading, tracked in the sample simulation for the movement path II at 0.5 m positioning data error standard deviation. Graphs exceed the natural  $0^\circ$  to  $360^\circ$  range for clear visualization purposes.

data error on the heading estimation precision.

### B. Simulated Path II

The second generated movement path covers an intense maneuvering scenario, including varying movement speed and reverse movement cases. Averaged results of the second path simulations are shown in the bottom half of Table I. These results demonstrate a dramatic performance improvement in the case of the ATKF algorithm over the benchmark algorithm. The benchmark algorithm has demonstrated the median heading absolute error results between  $14.9^\circ$  and  $15.6^\circ$ , depending on the positioning data quality. The proposed algorithm, on the other hand, was able to keep the median heading absolute error at  $5.3^\circ$  to  $6.2^\circ$ , which corresponds to a 59–66% improvement. RMSE results of the ATKF algorithm, on the other hand, have demonstrated a dramatic 85–90% improvement over the benchmark algorithm. Depending on the positioning data quality, the ATKF algorithm has shown  $8.6^\circ$  to  $12.8^\circ$  RMSE, whereas the benchmark algorithm has demonstrated  $87.9^\circ$  to  $86.6^\circ$  of the same metric. This dramatic difference in RMSE results indicates the presence of major error outliers in the heading, estimated by the benchmark algorithm.

Precision evaluation of both algorithms has shown similar improvement. Depending on the simulated positioning data error scale, the proposed ATKF algorithm has demonstrated 61–69% improvement in heading error median absolute deviation. This corresponds to the reduction from  $10^\circ$  down to the  $3^\circ$  to  $4^\circ$  range in this metric. Heading error standard deviation has shown a dramatic reduction from the  $69^\circ$ – $70^\circ$  range down to the  $5^\circ$ – $9^\circ$  range in the case of the ATKF algorithm. Depending on the positioning data error rate, this represents an 87–92% improvement over the benchmark algorithm.

These results are explained by the nature and structure of both algorithms. The benchmark algorithm is naturally dependent on the occasional movement in a straight line. Thus, the combination of intense maneuvering and poor positioning data of the second simulated path leads to eventual data misinterpretation and false triggering of reverse movement compensation, causing a  $180^\circ$  shift. This effect can be clearly observed on the blue graph in Fig. 3, which demonstrates the heading results of a sample path II simulation. The structure of the proposed ATKF algorithm adapts to the data quality and allows its initial filtering, thus providing higher robustness to intense maneuvering and poor positioning data.

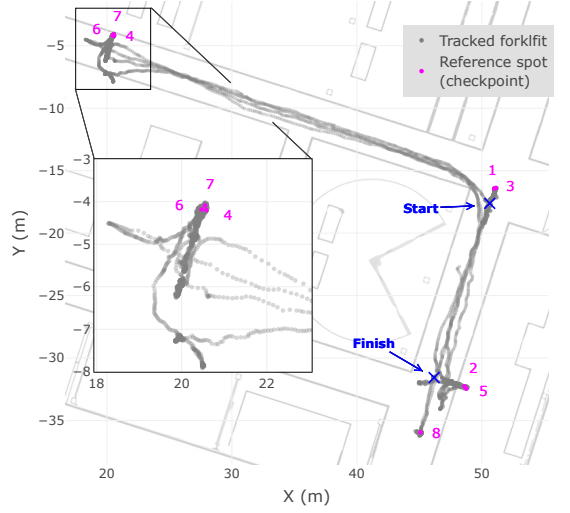


Fig. 4. Visualized forklift movement path within the industrial area during the experimental test campaign, along with marked momentary key spots.

## IV. EXPERIMENTAL TESTING

An experimental test campaign was conducted in order to evaluate the performance of the proposed ATKF algorithm with real data and validate the simulations' results, described in Section III. A test setup of positioning and inertial sensors was deployed on the full-scale forklift, naturally operating in the industrial environment.

The real-time forklift localization was performed by the Eliko UWB indoor positioning system, operating at a 5 Hz update rate [33]. This localization system is expected to provide positioning accuracy from 50 cm and up to 5–10 cm in the best environmental and deployment conditions, with a 1 cm resolution. Since the proposed ATKF algorithm is not bound to any specific localization system, the UWB positioning system can be substituted with any source of positioning information from GNSS (Global Navigation Satellite System) to cellular (e.g., 5G), WiFi, Bluetooth, or other technologies.

The 16-bit gyroscope sensor, available in a 9-DOF Bosh BNO055 inertial measurement unit (IMU), was used as a source of inertial heading data (angular velocity of yaw Euler rotation) [34]. With the declared sensor resolution, it is expected to detect angular velocity down to  $0.03^\circ/\text{s}$ . Data from the onboard 13-bit magnetometer unit was also collected to evaluate its performance in a real industrial application. In suitable environmental conditions, the used magnetometer is expected to allow the heading estimation with the declared accuracy of  $\pm 2.5^\circ$ . Both gyroscope and magnetometer data were collected at a 100 Hz update rate.

Forklift positioning and inertial data were collected during a *sim*14-minute-long test campaign. The forklift was naturally operating in an industrial area, transporting payloads and maneuvering at different speeds, including rapid turns, reverse movements, and occasional stops. Momentary locations, further referred to as key spots, where the forklift was directly

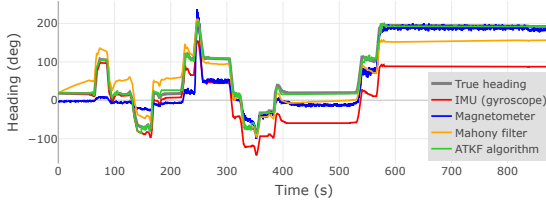


Fig. 5. Visualized forklift heading, tracked in experimental test campaign by the evaluated methods. Graphs exceed the natural  $0^\circ$  to  $360^\circ$  range for clear visualization purposes.

interacting with payloads, were used to investigate the momentary performance of the ATKF algorithm. Figure 4 shows the forklift movement track (grey), its starting and final locations, as well as marked key spots (magenta). The use of a highly maneuverable forklift operating in the magnetometer-denied industrial environment was chosen for proper testing of the ATKF algorithm in realistic conditions, where magnetometer-based state-of-the-art methods are expected to fail.

In order to demonstrate the unreliability of the magnetometer-based heading estimation methods, one of the state-of-the-art algorithms, the Mahony filter, was implemented in this work [35], [36]. The gain parameters  $k_P = 0.05$  and  $k_I = 0$  of this filter were heuristically tuned to achieve better performance with the experimentally collected data. Used tuning parameters for the tested ATKF algorithm are provided in Table III in the Appendix section. The comprehensive dataset of experimentally collected forklift positioning and IMU data is available at the Taltech database repository [37].

## V. EXPERIMENTAL RESULTS

This section covers the experimentally obtained results of the ATKF algorithm performance in the forklift heading estimation. This section also investigates the experimental performance of the initial IMU and the sole magnetometer in the industrial environment. It is done for comparison purposes, to demonstrate and justify the need for an alternative IMU drift mitigation solution. The performance of the initial IMU, sole magnetometer, and ATKF algorithm in heading estimation was evaluated for the overall test campaign, periods of the active forklift movement, and at the momentary key spots.

Figure 5 demonstrates heading graphs of the forklift, initially provided by the IMU unit (red), separate magnetometer unit (blue), heading estimations by the Mahony filter (orange), and the proposed ATKF algorithm (green), as well as the expected true forklift heading (grey).

The graph of the IMU provided heading demonstrates a significant drift error, accumulated during the test campaign, which can be clearly observed after  $200^{th}$  second of the experiment. Heading error rapidly exceeds  $50^\circ$  and reaches over  $100^\circ$  by the end of the experimental campaign. At the time periods of 420–530 s and 580–830 s, when the forklift remained stationary for longer periods of time, the IMU also demonstrates a visually stable heading. This leads to the conclusion that the drift error is primarily accumulated during

the active maneuvering, which indicates the inconsistency of IMU drift errors and makes their mitigation a more complex task.

The magnetometer provided heading, visualized in Fig. 5, demonstrates major inconsistency and poor reliability in the first half of the experimental campaign. The first significant maneuvering events (e.g., rapid  $90^\circ$  turns) occurred at the test campaign time periods of 80–100 s and 120–180 s, and were almost completely disregarded by the magnetometer. The observed significant, over  $20^\circ$ , bias in the magnetometer provided heading is possibly caused by the magnetic interference of the forklift itself, which may be initially compensated. Additionally, the magnetometer-based heading also demonstrates a significant noise with an approximate  $10^\circ$  magnitude. These performance results were expectedly caused by the surrounding magnetic interference in the industrial area.

Heading estimations, performed by the Mahony filter, demonstrate improved consistency and reliability compared to the initial magnetometer-based heading. Throughout the test campaign, the Mahony filter heading estimation demonstrates a proper response to the actual forklift maneuvering, due to the proper fusion of inertial (IMU) data. However, due to significant inconsistency of the magnetometer data, a Mahony filter is unable to properly compensate for the initially present IMU drift effect, which can be clearly observed in Fig. 5. Dynamically varying environmental distortions in the magnetometer data are expressed with a significant drift over-compensation by the Mahony filter at the test campaign time period of 0–250 s, and major drift under-compensation at the period of 400–850 s. These results additionally confirm the unreliability of the magnetometer-based heading estimation methods in a variety of land applications.

Visually, the ATKF algorithm estimated forklift heading almost fully matches the expected heading during the entire period of the test campaign. The highest heading error peaks of approximately  $10^\circ$  can be observed at the test campaign time periods of 140–150 s and 190–210 s. This positively depicts the overall performance of the proposed ATKF algorithm throughout the test campaign.

TABLE II  
FORKLIFT HEADING TRACKING ACCURACY AND PRECISION RESULTS OF THE ENTIRE TEST CAMPAIGN, PERIODS OF ACTIVE MOVEMENT, AND AT THE KEY SPOTS

	Accuracy metrics ( $^\circ$ )			Precision metrics ( $^\circ$ )		
	MdAE	MnAE	RMSE	MdAD	MnAD	$\sigma$
IMU <sub>overall</sub>	78.3	65.5	76.0	26.2	33.4	38.6
IMU <sub>moving</sub>	60.4	51.6	62.5	28.6	30.7	35.3
IMU <sub>key spot</sub>	42.0	44.6	58.9	36.4	36.8	38.6
MAG <sub>overall</sub>	20.8	23.5	32.4	13.2	16.5	22.4
MAG <sub>moving</sub>	25.3	31.4	39.9	13.9	18.7	24.6
MAG <sub>key spot</sub>	25.7	35.5	45.6	5.4	22.3	28.7
Mahony <sub>overall</sub>	29.2	27.6	30	9.1	10.1	11.7
Mahony <sub>moving</sub>	24.6	23.3	25.9	9.5	9.3	11.2
Mahony <sub>key spot</sub>	26.4	27.4	28.6	5.3	6.5	8.4
ATKF <sub>overall</sub>	0.9	2.8	4.9	0.8	2.8	4.0
ATKF <sub>moving</sub>	2.3	3.8	5.8	1.8	3.3	4.4
ATKF <sub>key spot</sub>	1.0	1.5	2.3	0.9	1.3	1.7

Numerical results of the IMU-measured forklift heading are provided in the upper quarter of Table II. These results demonstrate a major, above  $60^\circ$  error presence in accuracy metrics, observed throughout the entire test campaign and during the periods of active forklift movement. These cases are respectively indexed as  $IMU_{overall}$  and  $IMU_{moving}$ . Slightly better accuracy results of above  $40^\circ$  were achieved at the momentary key spots ( $IMU_{key\ spot}$ ). Approximately  $30^\circ$  error in precision metrics was also observed in the mentioned cases. These results clearly demonstrate the significance of the IMU drift problem and the need for its mitigation.

The second quarter of Table II shows the accuracy and precision results of the magnetometer-tracked forklift heading. A sole magnetometer has demonstrated relatively mediocre overall accuracy with above  $20^\circ$  mean and median heading errors. Above  $25^\circ$  error was observed in accuracy metrics during the active forklift movement and at the key spots, respectively indexed as  $MAG_{moving}$  and  $MAG_{key\ spot}$  in the Table II. Above  $13^\circ$  errors were observed in precision metrics during the overall test campaign and periods of active forklift movement. Relatively better results in a median absolute deviation of  $5^\circ$  were achieved at the momentary key spots. These results confirm the presence of a significant heading bias and sensor noise.

The third quarter of Table II demonstrates the accuracy and precision results of the Mahony filter heading estimation. Results demonstrate above  $27^\circ$  mean and median heading errors, which represent a noticeable decrease in overall heading accuracy, in comparison with the sole magnetometer performance. Approximately  $25^\circ$  error in accuracy metrics was observed during the active forklift movement and at the key spots, respectively indexed as  $Mahony_{moving}$  and  $Mahony_{key\ spot}$  in Table II. Slightly above  $9^\circ$  errors can be observed in the mean and median absolute deviation metrics during the overall test campaign and active forklift movement periods. Slightly above  $5^\circ$  errors were observed in the precision metrics at the momentary key spots. This precision improvement over the sole magnetometer-based heading can be explained by a major filtering of the magnetometer data noise, performed by the Mahony filter.

Outstanding results of below  $1^\circ$  median heading error and median error deviation were demonstrated by the ATKF algorithm during the conducted test campaign. Corresponding results are provided in the bottom quarter of the Table II. These metrics demonstrate the overall accuracy and precision in heading estimation and exclude momentary error outliers. The achieved sub- $5^\circ$  heading RMSE and error standard deviation results also indicate a minor presence of significant error outliers in the estimated heading accuracy and precision. A minor expected increase in the heading error results can be expectedly observed in the case of the moving forklift ( $ATKF_{moving}$ ), which indicates the stability of the ATKF algorithm during the active maneuvering. Slightly above  $1^\circ$  accuracy and precision results were achieved at the momentary key spots ( $ATKF_{key\ spot}$ ), which additionally confirms the robustness of the proposed algorithm.

Fig. 6 demonstrates the Cumulative error Distribution Functions (CDF) for the forklift heading, estimated by initial IMU

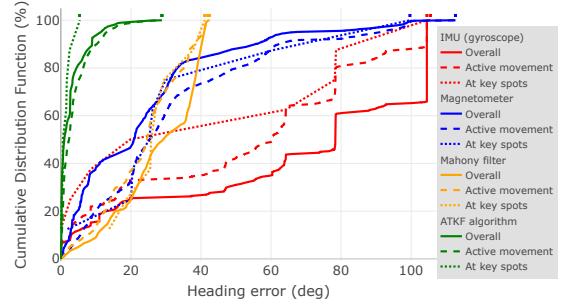


Fig. 6. Cumulative error distribution functions of the experimentally tracked forklift heading during the entire test campaign, during periods of active movement, and at the momentary key spots.

(red), magnetometer (blue), Mahony filter (orange), and the ATKF algorithm (green). These functions are provided for the three above-mentioned cases of the overall test campaign (line), exclusively for the moving forklift (dashed line), and at the key spots (dotted line). According to these results, the ATKF estimated heading did not exceed  $30^\circ$  error throughout the entire test campaign, while above 90% of the time the heading error was kept below  $10^\circ$ . Exceptional performance was demonstrated at the stationary key spots, where errors in the ATKF-provided heading never exceeded  $5^\circ$ . These results additionally confirm the reliability and stability of the proposed ATKF algorithm in accurate vehicle heading tracking. Overall results indicate an approximate 95% improvement in the IMU heading accuracy metrics, and 93% in the precision metrics, provided by the proposed ATKF algorithm. Mahony filter, on the other hand, has demonstrated a nearly linear heading error distribution, slightly exceeding  $40^\circ$  in the maximum observed error. Even though the Mahony filter algorithm was able to mitigate most of the above  $40^\circ$  heading errors, initially present in both fused data sources, it was unable to improve the general performance of the fused data sources.

## VI. CONCLUSIONS

This paper addressed major limitations of the magnetometer-based vehicle heading estimation methods, which prevent their effective use in a variety of applications. This work proposed a robust, accurate, and magnetometer-free algorithmic method for vehicle heading estimation, based on inertial and positioning data. This method represents a custom version of the adaptive Kalman filter algorithm (ATKF) with a novel tandem structure. Its adaptivity features allow an iterative relevance re-estimation of each data source for its weighted fusion, while the tandem structure enables multiple consecutive data processing steps within a single iteration, ensuring immediate use of input data and preventing relevance loss.

The ATKF was compared against a state-of-the-art algorithm in a series of simulated tests, covering diverse movement scenarios and input data quality levels. Depending on the

simulated scenario, the ATKF has shown 40% to 90% improvement over the compared algorithm in real-time heading estimation accuracy. Additionally, it has also demonstrated high stability during intense maneuvering, robustness to noisy positioning data, and resilience to reverse movement. These results were also experimentally validated during the full-scale test campaign by using a highly maneuverable forklift in an industrial environment. The ATKF has respectively demonstrated 95% and 93% improvement in the tracking heading accuracy and precision over the sole gyroscope (IMU), maintaining a median error below  $2.3^\circ$  even in periods of active movement. In contrast, the evaluated magnetometer-based methods, including the sole magnetometer and the Mahony filter algorithm, have confirmed their significant unreliability and inconsistency under industrial conditions.

Future work is focused on long-term testing of the proposed algorithm to identify its practical limitations, as well as its possible improvement by refining the adaptivity process or integration of additional auxiliary sensors, such as an accelerometer. The ATKF has potential applications in robotics, intelligent vehicles, industry automation, and advanced control systems, particularly covering different environments with significant magnetic interference.

## APPENDIX

TABLE III

ATKF TUNING PARAMETERS, USED IN TEST SIMULATIONS AND DURING THE EXPERIMENTAL TEST CAMPAIGN

Parameter	Value		
	Simulations		Experimental tests
	Path I	Path II	
$q^{pos}$	1 m <sup>2</sup>	1 m <sup>2</sup>	1 m <sup>2</sup>
$r^{pos}$	30 m <sup>2</sup>	40 m <sup>2</sup>	3 m <sup>2</sup>
$q^v$	0.1 m <sup>2</sup> /s <sup>2</sup>	5 m <sup>2</sup> /s <sup>2</sup>	10 m <sup>2</sup> /s <sup>2</sup>
$q^v$	1 m <sup>2</sup> /s <sup>2</sup>	1 m <sup>2</sup> /s <sup>2</sup>	1 m <sup>2</sup> /s <sup>2</sup>
$r^v$	0 m <sup>2</sup> /s <sup>2</sup>	1 m <sup>2</sup> /s <sup>2</sup>	0 m <sup>2</sup> /s <sup>2</sup>
$q_{min}^\phi$	1 (°) <sup>2</sup>	1 (°) <sup>2</sup>	0 (°) <sup>2</sup>
$r_{min}^\phi$	100 (°) <sup>2</sup>	10 (°) <sup>2</sup>	0 (°) <sup>2</sup>
$q_{min}^\psi, r_{min}^\psi$	0 (°) <sup>2</sup>	0 (°) <sup>2</sup>	0 (°) <sup>2</sup>
$q_{max}, r_{max}$	100 (°) <sup>2</sup>	100 (°) <sup>2</sup>	10000 (°) <sup>2</sup>
$v_{thr}^0$	0.07 m/s	0.07 m/s	0.1 m/s
$v_{thr}^\phi$	0.3 m/s	0.4 m/s	0.5 m/s
$v_{thr}^\psi$	0.55 m/s	0.75 m/s	1.18 m/s
$a^\phi$	190	230	300
$a^\psi$	33	445	710

## ACKNOWLEDGMENTS

This project has received funding from the European Union's Horizon Europe Research Program under grant agreement No. 101058505 - 5G-TIMBER, and from the Estonian Education and Youth Board ÕÜF11 "AIoT\*5G - Artificial intelligence, edge computing and IoT solutions in distributed systems". Development of an industrial digital control system based on precise positioning technology ELIKO TAK and Atemix Automatika nr. 2014-2020.4.02.21-0311.

## REFERENCES

- [1] "Best Autonomous Vehicle Navigation Data Products," <https://www.techsalerator.com/sub-data-categories/autonomous-vehicle-navigation-data>, accessed: 2024-04-04.
- [2] L. Nastro, "Position and orientation data requirements for precise autonomous vehicle navigation," in *Proceedings of the XXI st ISPRS Congress*, vol. 37, no. 1. Citeseer, 2008, pp. 1237–1242.
- [3] X. Li, L. Guvenc, and B. Aksun-Guvenc, "Vehicle state estimation and prediction for autonomous driving in a round intersection," *Vehicles*, vol. 5, no. 4, pp. 1328–1352, 2023. [Online]. Available: <https://www.mdpi.com/2624-8921/5/4/73>
- [4] Z. Huang, "Application of interval state estimation in vehicle control," *Alexandria Engineering Journal*, vol. 61, no. 1, pp. 911–916, 2022.
- [5] P. Ripka, *Magnetic sensors and magnetometers*. Artech house, 2021.
- [6] J. Haverinen and A. Kempainen, "A global self-localization technique utilizing local anomalies of the ambient magnetic field," in *2009 IEEE International Conference on Robotics and Automation*. IEEE, 2009, pp. 3142–3147.
- [7] K. Yamazaki, K. Kato, K. Ono, H. Saegusa, K. Tokunaga, Y. Iida, S. Yamamoto, K. Ashiho, K. Fujiwara, and N. Takahashi, "Analysis of magnetic disturbance due to buildings," *IEEE Transactions on Magnetics*, vol. 39, no. 5, pp. 3226–3228, 2003.
- [8] S. Bonnet, C. Bassompierre, C. Godin, S. Lesecq, and A. Barraud, "Calibration methods for inertial and magnetic sensors," *Sensors and Actuators A: Physical*, vol. 156, no. 2, pp. 302–311, 2009.
- [9] V. Renaudin, M. H. Afzal, and G. Lachapelle, "Complete triaxis magnetometer calibration in the magnetic domain," *Journal of Sensors*, vol. 2010, no. 1, p. 967245, 2010. [Online]. Available: <https://onlinelibrary.wiley.com/doi/abs/10.1155/2010/967245>
- [10] M. L. Hoang and A. Pietrosanto, "Yaw/Heading optimization by drift elimination on MEMS gyroscope," *Sensors and Actuators A: Physical*, vol. 325, p. 112691, 2021.
- [11] E. M. Diaz, F. de Ponte Müller, A. R. Jiménez, and F. Zampella, "Evaluation of AHRS algorithms for inertial personal localization in industrial environments," in *2015 IEEE International Conference on Industrial Technology (ICIT)*. IEEE, 2015, pp. 3412–3417.
- [12] M. L. Hoang, A. Pietrosanto, S. D. Iacono, and V. Paciello, "Pre-processing technique for compass-less madgwick in heading estimation for industry 4.0," in *2020 IEEE International Instrumentation and Measurement Technology Conference (I2MTC)*. IEEE, 2020, pp. 1–6.
- [13] S. A. Ludwig and K. D. Burnham, "Comparison of euler estimate using extended kalman filter, madgwick and mahony on quadcopter flight data," in *2018 International Conference on Unmanned Aircraft Systems (ICUAS)*. IEEE, 2018, pp. 1236–1241.
- [14] H. Ahmed and M. Tahir, "Accurate attitude estimation of a moving land vehicle using low-cost mems imu sensors," *IEEE Transactions on Intelligent Transportation Systems*, vol. 18, no. 7, pp. 1723–1739, 2016.
- [15] N. Maus and O. W. Layton, "Estimating heading from optic flow: Comparing deep learning network and human performance," *Neural Networks*, vol. 154, pp. 383–396, 2022.
- [16] M. J. Gallant and J. A. Marshall, "The lidar compass: Extremely lightweight heading estimation with axis maps," *Robotics and Autonomous Systems*, vol. 82, pp. 35–45, 2016.
- [17] V. M. Passaro, A. Cuccovillo, L. Vaiani, M. De Carlo, and C. E. Campanella, "Gyroscope technology and applications: A review in the industrial perspective," *Sensors*, vol. 17, no. 10, p. 2284, 2017.
- [18] "Getting Started With Inertial Measurement Units — Exploring Degrees Of Freedom," <https://core-electronics.com.au/guides/getting-started-with-h-inertial-measurement-units-exploring-degrees-of-freedom/>, accessed: 2024-04-05.
- [19] "What is the definition of AHRS?" <https://www.advancednavigation.com/glossary/ahrs>, accessed: 2024-05-27.
- [20] L. Wöhle and M. Gebhard, "Steadyeye-head—improving marg-sensor based head orientation measurements through eye tracking data," *Sensors*, vol. 20, no. 10, p. 2759, 2020.
- [21] J. H. Wall, D. M. Bevilacqua, et al., "Characterization of various IMU error sources and the effect on navigation performance," in *Proceedings of the 18th international technical meeting of the satellite division of the institute of navigation (ION GNSS 2005)*, 2005, pp. 967–978.
- [22] T. Wang, "Heading attitude drifts controlled by the angular accelerations instead of using magnetometers," in *2018 IEEE International Conference on Mechatronics and Automation (ICMA)*. IEEE, 2018, pp. 563–567.
- [23] M. L. Hoang, M. Carratù, V. Paciello, and A. Pietrosanto, "Fusion filters between the no motion no integration technique and kalman filter in



noise optimization on a 6dof drone for orientation tracking,” *Sensors*, vol. 23, no. 12, p. 5603, 2023.

- [24] R. P. Suresh, V. Sridhar, J. Pramod, and V. Talasila, “Zero velocity potential update (zupt) as a correction technique,” in *2018 3rd International Conference On Internet of Things: Smart Innovation and Usages (IoT-SIU)*. IEEE, 2018, pp. 1–8.
- [25] S. A. Ludwig, K. D. Burnham, A. R. Jiménez, and P. A. Touma, “Comparison of attitude and heading reference systems using foot mounted MIMU sensor data: Basic, Madgwick, and Mahony,” in *Sensors and Smart Structures Technologies for Civil, Mechanical, and Aerospace Systems 2018*, vol. 10598. SPIE, 2018, pp. 644–650.
- [26] R. Song and Y. Fang, “Vehicle state estimation for ins/gps aided by sensors fusion and sckf-based algorithm,” *Mechanical Systems and Signal Processing*, vol. 150, p. 107315, 2021.
- [27] L. Xiong, X. Xia, Y. Lu, W. Liu, L. Gao, S. Song, and Z. Yu, “Imu-based automated vehicle body sideslip angle and attitude estimation aided by gnss using parallel adaptive kalman filters,” *IEEE Transactions on Vehicular Technology*, vol. 69, no. 10, pp. 10668–10680, 2020.
- [28] M. Bersani, M. Vignati, S. Mentasti, S. Arrigoni, and F. Cheli, “Vehicle state estimation based on kalman filters,” in *2019 AEIT International Conference of Electrical and Electronic Technologies for Automotive (AEIT AUTOMOTIVE)*. IEEE, 2019, pp. 1–6.
- [29] G. Park, S. B. Choi, D. Hyun, and J. Lee, “Integrated observer approach using in-vehicle sensors and gps for vehicle state estimation,” *Mechatronics*, vol. 50, pp. 134–147, 2018.
- [30] A. Fjodorov, S. Ulp, M. M. Alam, and A. Kuusik, “Inertial and positioning sensors fusion for indirect location tracking in warehouse inventory management,” in *2023 International Conference on Control, Automation and Diagnosis (ICCAD)*. IEEE, 2023, pp. 1–7.
- [31] W. Elmenreich, “An introduction to sensor fusion,” *Vienna University of Technology, Austria*, vol. 502, pp. 1–28, 2002.
- [32] M. Tommingas, M. M. Alam, I. Mürsepp, and S. Ulp, “Uwb positioning integrity estimation using ranging residuals and ml augmented filtering,” *IEEE Journal of Indoor and Seamless Positioning and Navigation*, vol. 2, pp. 205–218, 2024.
- [33] “Eliko UWB RTLS,” <https://eliko.tech/uwb-rtls-ultra-wideband-real-time-location-system/>, accessed: 2024-02-18.
- [34] “BNO055 Intelligent 9-axis absolute orientation sensor datasheet,” [https://cdn-shop.adafruit.com/datasheets/BST\\_BNO055\\_DS000\\_12.pdf](https://cdn-shop.adafruit.com/datasheets/BST_BNO055_DS000_12.pdf), accessed: 2024-02-18.
- [35] R. Mahony, T. Hamel, and J.-M. Pfimlin, “Nonlinear complementary filters on the special orthogonal group,” *IEEE Transactions on automatic control*, vol. 53, no. 5, pp. 1203–1218, 2008.
- [36] “Open source IMU and AHRS algorithms,” <https://x-io.co.uk/open-source-imu-and-ahrs-algorithms/>, accessed: 2024-09-03.
- [37] A. Fjodorov, T. Laadung, M. Tommingas, and S. Ulp, “Forklift Positioning and Inertial Data Collected in the Industrial Environment,” *TalTech Data Repository*, 2024. [Online]. Available: <https://doi.org/10.48726/xwy13-cfd98>



**Aleksei Fjodorov** was born in Tallinn, Estonia in 1995. He received his B.Sc. and M.Sc. degrees in telecommunication and electronics from the Tallinn University of Technology (TUT), Estonia in 2017 and 2021, respectively. Currently, he is pursuing a Ph.D. degree in information and communication technology from Tallinn University of Technology. Since 2021, he has been working as a Researcher at Eliko Tehnoloogia Arenduskeskus OÜ, Tallinn. His current research covers sensor fusion methods and algorithms, sensor fusion-enabled indoor positioning and tracking, IoT, electronics, and communication technologies.



sitioning.

**Sander Ulp** received the M.Sc. degree in telecommunication and the Ph.D. degree in information and communication technology from Tallinn University of Technology, in 2013 and 2019, respectively. In 2018 he started working as a researcher at Eliko Tehnoloogia Arenduskeskus OÜ. Since 2019 he is the CTO of the competence center which develops novel indoor positioning research and technologies. His research interests are in distributed estimation, learning and adaptation over networks, digital signal processing, localization technologies, and indoor po-



**Taavi Laadung** was born in Tallinn, Estonia, in 1990. He received his M.Sc. and Ph.D. degrees in telecommunication from the Tallinn University of Technology in 2016 and 2023, respectively. From 2015 to 2016, he served as a Practical Coursework Supervisor at the Tallinn University of Technology. From 2017 to 2019, he worked as a Communication Systems Research and Development Specialist with the Estonian Defence Forces. Since 2019, he has been a Researcher at OÜ Eliko Tehnoloogia Arenduskeskus in Tallinn, focusing on research regarding ranging protocols and improving the robustness of the Eliko UWB RTLS positioning system. His current research interests include the enhancement of algorithms and methodologies for wireless indoor tracking, positioning, and object-locating systems.



Vice-Coordinator of the GAC of IEEE Computer Society in Region 8.

**Alar Kuusik** (Member, IEEE) received the Ph.D. degree in IT from the Tallinn University of Technology (TalTech), Estonia, in 2001. He is currently a Senior Research Scientist with the T. J. Seebeck Institute of Electronics, TalTech, focusing on the IoT, data acquisition, and networking technologies. He has been involved with several international research and innovation projects related to smart environments, smart cities, and wearable technologies. He has published more than 50 peer-reviewed articles and is the author of five patent families. He is the



**Muhammad Mahtab Alam** (Senior Member, IEEE) received the M.Sc. degree in electrical engineering from Aalborg University, Denmark, in 2007, and the Ph.D. degree in signal processing and telecommunication from the University of Rennes I France (INRIA Research Center), in 2013. He did his post-doctoral research (2014–2016) at the Qatar Mobility Innovation Center, Qatar. In 2016, he joined as the European Research Area Chair and as an Associate Professor with the Thomas Johann Seebeck Department of Electronics, Tallinn University of

Technology, where he was elected as a Professor in 2018 and Tenured Full Professor in 2021. Since 2019, he has been the Communication Systems Research Group Leader. His research focuses on the fields of wireless communications—connectivity, mobile positioning, 5G/6G services and applications. He has over 15 years of combined academic and industrial multinational experiences while working in Denmark, Belgium, France, Qatar, and Estonia. He has several leading roles as PI in multimillion Euros international projects funded by European Commission (Horizon Europe LATEST-5GS, 5G-TIMBER, H2020 5G-ROUTES, NATOSPS (G5482), Estonian Research Council (PRG424), Telia Industrial Grant etc. He is an author and co-author of more than 100 research publications. He is actively supervising a number of Ph.D. and Postdoc Researchers. He is also a contributor in two standardization bodies (ETSI SmartBAN, IEEE-GeenICT-EECH), including “Rapporteur” of work item: DTR/ SmartBAN-0014”.



## Appendix 4

### IV

A. Fjodorov, S. Ulp, T. Laadung, M. M. Alam, and A. Kuusik, "Accurate Indirect 3D Localization of Markerless Industrial Products," *IEEE Sensors Journal*, Accepted: 18.09, 2025



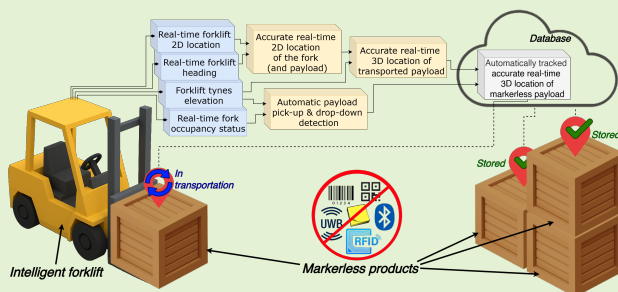


# Accurate Indirect 3D localization of Markerless Industrial Products

Aleksei Fjodorov<sup>1</sup>, Sander Ulp<sup>2</sup>, Taavi Laadung<sup>3</sup>, Alar Kuusik<sup>4</sup>, *Senior Member, IEEE*, Muhammad Mahtab Alam<sup>5</sup>, *Senior Member, IEEE*

**Abstract**—This paper proposes a novel method for the indirect, automatic, real-time, and three-dimensional tracking of industrial products. The motivation behind the proposed method is to fully avoid the direct product marking with active or passive tags. This method combines the tracked forklift position and heading data with the real-time fork elevation to obtain a complete 3D location of the transported product. This work also proposes a fusion algorithm for automatic product pick-up and drop-down event detection (A-PDD). It is based on the fusion of the fork elevation and occupancy sensors, used for the automatic recognition of the forklift behavior patterns during the payload pick-up or drop-down events. This work experimentally validates the performance of the proposed markerless indirect tracking method in an operating industrial production site. The proposed method was able to indirectly track two industrial products with below 30 cm absolute and repeatability errors. The experimental comparison of the proposed indirect tracking method with the traditional direct product localization approach has shown a major advantage of the proposed method in terms of product positioning stability, reliability, and quality, along with approximately four times higher product positioning accuracy. The proposed indirect tracking method offers high scalability, significantly increased cost- and energy efficiency, and reduced maintenance requirements in comparison with the direct tracking methods. It is expected to be widely applicable to different industrial machinery and material handling equipment, from forklifts and various lifters to cranes.

**Index Terms**—Indirect tracking, industrial product positioning, sensor fusion, UWB, IMU, ultrasonic distance sensor, wire encoder, intelligent warehousing



## I. INTRODUCTION

**A**UTOMATION is one of the key aspects of industry advancement, especially in the field of warehousing and manufacturing. It improves the quality, efficiency, and profitability of manufacturing, increases process transparency and scalability, as well as improves workplace safety, and reduces the risk of human error [1]. Different intelligent warehouse management solutions are demanded in the industry nowadays, including direct and indirect tracking methods as part of

warehousing and Industry 4.0 [2], [3].

A wide variety of different solutions for product localization are presented in the literature. One of the most straightforward methods is direct product tracking using active positioning systems, such as an Ultra-Wideband (UWB) indoor positioning system [4]. Even though this approach allows direct and real-time product localization, it offers limited scalability and remains an inefficient method in cost, computational complexity, and maintenance requirements. The widely used method of direct product marking with passive identification units, such as RFID (Radio-Frequency Identification) tags [5], on the other hand, offers a relative cost-efficiency and high scalability. However, the real-time passive tag-based product positioning requires a complex infrastructure, such as massive scanning grids, deployed around the localization area [6].

Unfortunately, certain industrial products (e.g., wood, metal, or stone materials) face frequent physical processing or extreme environmental conditions (e.g., high temperatures or accelerations), which completely prohibit their direct marking with any type of tags. Thus, the real-time localization of these products requires indirect methods, which fully avoid their direct marking.

This project has received funding from the European Union's Horizon Europe Research Program under grant agreement No. 101058505 - 5G-TIMBER, from the Estonian Education and Youth Board ÕÜ11 "AIoT\*5G - Artificial intelligence, edge computing and IoT solutions in distributed systems", and "Increasing the knowledge intensity of Ida-Viru entrepreneurship" co-funded by the European Union. Development of an industrial digital control system based on precise positioning technology ELIKO TAK and Atemix Automatika nr. 2014-2020.4.02.21-0311.

Aleksei Fjodorov, Muhammad Mahtab Alam and Alar Kuusik are with Thomas Johann Seebeck Department of Electronics, Tallinn University of Technology, Tallinn, Estonia. (e-mails: {aleksei.fjodorov1, muhammad.alam, alar.kuusik}@taltech.ee)

Aleksei Fjodorov, Taavi Laadung and Sander Ulp are with Eliko Tehnoloogia Arenduskeskus OÜ, Tallinn, Estonia. (e-mails: {aleksei.fjodorov, taavi.laadung, sander.ulp}@eliko.ee).

Certain quasi-indirect methods in this field offer product identification and localization through reference objects, such as industrial pallets. Pallets can be either marked directly (e.g., with UWB tags [7]) or recognized by using intelligent vision [8]. In this approach, however, products remain bound to their objects of reference. On the other hand, visual recognition of the product directly may be considered an indirect identification method, which, however, is limited by the variety of supported object shapes [9]. Nontraditional use of common technologies may also be utilized for tagless object localization, such as radar principle-based UWB positioning [10], RFID-based proximity detection [11], or capacitive sensing-based positioning [12].

### A. Related Works

In the literature, the "indirect tracking" term presumes that the tracked object is not marked with active positioning units, while accepting the use of passive units, such as RFID tags, QR-, or barcodes [13]–[16]. This subsection covers the latest available state-of-the-art works in the field of indirect asset localization to the author's best knowledge.

Motroni *et al.* have proposed a solution for indirect asset tracking, based on UWB positioning, inertial measurement unit (IMU), and Optical Flow (OFS) sensor, aided with laser distance sensors [17]. Sensor fusion is performed by using a reliable and computationally expensive variation of the Kalman filter algorithm - the Unscented Kalman Filter (UKF) [18]. Their method, however, relies on the direct asset marking with passive RFID tags for its identification purposes. Asset loading & unloading detection is performed by using an ultrasonic sensor.

Frankó *et al.* [13] and Zhao *et al.* [14] have proposed relatively similar approaches for indirect asset tracking. In their approaches, direct asset marking with passive RFID tags becomes essential, as it is used for both asset identification and pick-up detection. A continuous detection of a particular RFID tag within the fork area is considered as a pick-up of the corresponding product. The location of a transported asset is then associated with the real-time forklift coordinates, tracked by the indoor UWB RTLS (Real-Time Locating System). In the forklift body frame, the positioning unit is physically deployed with a certain offset from the transported product, which, in this case, becomes a constant, beyond-meter error in the asset location. Frankó *et al.* in their work additionally use the geofencing technique, in which assets are only transported between predetermined storage areas. The RFID scanning routine in their method is only triggered by the accelerometer unit during the moments of the forklift movement.

The pallet tracking approach, proposed by Kovavisaruch *et al.*, is only based on the forklift-deployed UWB positioning unit [19]. Similarly, the transported pallet location is directly associated with the forklift position, while the pick-up & drop-down detection routine is performed manually. Pallets are identified by manual scanning of the directly attached barcodes and tracked with the claimed average precision of 47 cm. The tracked forklift location is also used to identify one of the possible predefined forklift routes.

Barral *et al.* in their work have proposed a simulated multi-sensor accurate forklift tracking method, based on the UWB positioning system, IMU, and computationally heavy PX4 smart optical flow camera [20]. Even though their work does not contribute to the product localization or indirect tracking topics directly, the theoretical possibility of pallet localization by using the forklift-deployed sensors is mentioned. However, possible methods for the product localization, as well as their loading and unloading detection, are not addressed in their work.

Borstell *et al.* have proposed a pallet monitoring system using vehicle and asset localization, based on a passive planar Markers-based Local Positioning System (MarLO) [15]. This approach is assisted by specialized gates with integrated RFID and depth sensors, installed between sections of the industrial area, for pallet identification and dimension measurement. In their method, the detection of the payload pick-up & drop-down is performed manually.

Zealabs and Sewio have developed a tagless method for industrial coils localization in Prokab cabling factory [21], [22]. By using the pressure sensor, their method offers automatic product pick-up detection, while for identification purposes, it still relies on direct product marking with QR codes. Similar to methods proposed by Frankó *et al.*, Zhao *et al.*, and Kovavisaruch *et al.*, the transported product location is directly associated with the UWB positioning system provided forklift coordinates. This is expected to cause an earlier-mentioned beyond-meter offset error in the product location. Unlike other methods, this method also allows for three-dimensional product positioning through its real-time elevation tracking.

The majority of available state-of-the-art works mainly propose indirect asset localization methods without providing experimental evaluation and qualitative performance results. Available methods still fully or partially rely on direct product marking with passive identification tags, primarily cover only two-dimensional product positioning, and in some cases, require more complex data processing [20]. Additionally, the majority of the available methods associate the product location with the forklift coordinate, which leads to a potentially significant error in product positioning.

### B. Contributions

This paper addresses the field of indirect methods for industrial product localization in advancing areas of automated industry and warehousing. It proposes the following contributions:

- A novel indirect tracking method for automatic and real-time 3D localization of fully markerless industrial products. In comparison to the available indirect tracking approaches, the proposed method does not require the direct marking of tracked products with either active or passive tags. Thus, the required sensor setup does not depend on the growing number of tracked products, which leads to a potentially unlimited scalability, and high cost- and energy efficiency of the proposed method. It offers a highly accurate and three-dimensional positioning of any product, as well as covers possible product shelving and stacking scenarios. This method avoids the use

of computationally heavy or additional auxiliary sensors to reduce its complexity and minimize the number of required sensors.

- A sensor fusion algorithm for automatic payload pick-up & drop-down detection (A-PDD), based on the elevation and distance sensors. This algorithm recognizes the forklift behavior patterns during the payload pick-up & drop-down events to define their exact moment and location.
- Experimental testing, validation, and performance evaluation of the proposed indirect tracking method in an operating industrial environment. The evaluation covers different performance aspects of the proposed method, including the absolute accuracy and repeatability of indirect product positioning, as well as its quality and reliability in the industrial area. Additionally, this paper provides a performance comparison of the proposed method with the UWB-based direct product localization approach.

## II. PROPOSED MARKERLESS INDIRECT TRACKING METHOD

The key hypothesis behind the proposed markerless method for indirect tracking is that a completely unmarked industrial object can be localized in real-time during its transportation by any material handling equipment, such as a regular forklift. During the product transportation process, its real-time location can be naturally associated with the location of the forklift tynes (i.e., the center of the fork area). Therefore, by tracking the real-time position, elevation, and occupancy of the forklift tynes, a fully unmarked product can be indirectly tracked in the industrial area with the following key assumptions:

- Indirectly tracked products are only transported by specialized transportation machinery (e.g., forklift), which is equipped with the necessary sensors for indirect tracking.
- When stored, the indirectly tracked products remain stationary until their pick-up by transportation machinery.

The proposed method is primarily focused on the larger industrial products, which transportation naturally requires the use of material handling equipment (MHE), such as forklifts. These assumptions are aimed at minimizing the unauthorized transportation of markerless products by MHE without the deployed indirect tracking setup. Nevertheless, in the case of occasional unregistered product displacement (e.g., by widely used manual pallet jacks), their location may be manually updated. Further planned advancements in the proposed method also include the development of a simplified indirect tracking setup to cover manual transportation options, such as manual pallet jacks.

The proposed indirect tracking approach is illustrated in Fig. 1. The tynes area of the forklift, however, cannot be directly marked with the positioning unit, as it may be damaged by any heavy payload. For this reason, the positioning unit should be installed in the safer areas of the forklift's body frame. This, however, leads to the physical offset  $\delta_{fork}$  between the positioning unit provided coordinates  $(x, y)_0$  and the actual location of the tynes area  $(x, y)_{fork}$ , and thus, the location of the indirectly tracked payload. To eliminate this offset and estimate the exact real-time location of the forklift tynes,

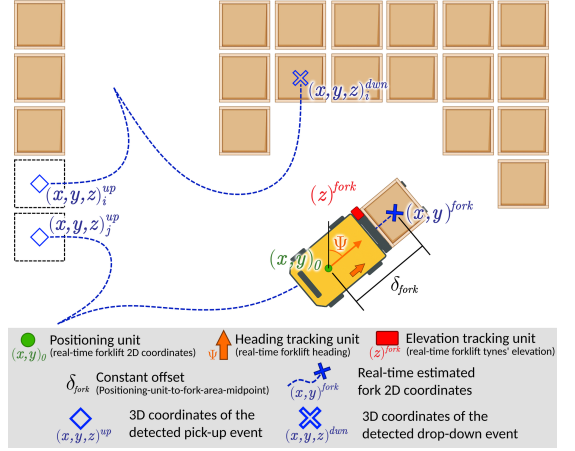


Fig. 1. Illustrative conceptual example of the proposed indirect tracking method from the 2D perspective

the accurate forklift heading information  $\Psi$  is required. This information, together with the known offset  $\delta_{fork}$  between the installed positioning unit and fork area, can then be geometrically translated to the exact desired coordinates of the fork area as follows:

$$\begin{cases} x^{fork} = x_0 + \sin(\Psi) \cdot \delta_{fork} \\ y^{fork} = y_0 + \cos(\Psi) \cdot \delta_{fork} \end{cases} \quad (1)$$

Accurate tracking of the forklift heading is essential, as it directly impacts the calculated location of the fork and, thus, the location of the tracked payload. The forklift heading error can be translated into the error in the tracked payload position by using the following equation:

$$\varepsilon_{fork}^{x,y} = 2 \cdot \sin\left(\frac{\varepsilon_{\Psi}}{2}\right) \cdot \delta_{fork}, \quad (2)$$

where  $\varepsilon_{fork}^{x,y}$  is the positioning error of the forklift tynes', and hence, of the tracked payload, and  $\varepsilon_{\Psi}$  is the heading error. The context of this approach was briefly described in the author's preliminary research [23].

Accurate forklift heading estimation can be performed by widely available, highly portable, and cost-efficient MEMS (Micro-Electromechanical Systems) gyroscope units. MEMS gyroscopes, however, are prone to the drift effect, represented by over-time accumulated heading errors [24]. In the majority of the state-of-the-art IMU drift mitigation methods, inertial units are fused with environmentally sensitive magnetometers, particularly unreliable in industrial areas [25]. In this work, the accurate forklift heading estimation is performed by an alternative magnetometer-free algorithmic method, developed in one of the author's preliminary works [26]. This algorithm, further referred to as the ATKF (Adaptive Tandem Kalman Filter), represents an adaptive Kalman filter algorithm for vehicle heading estimation, which is based on the inertial and positioning data. It avoids the use of environmentally sensitive magnetometers, thus making it suitable for industrial areas.

The time- and space complexity of this algorithm corresponds to a regular linear Kalman filter.

The corresponding article covers the simulated testing of the ATKF algorithm, which includes different vehicle movement scenarios with moderate and high maneuvering intensities, occasional reverse movement, and various input data error rates. The ATKF algorithm has demonstrated high heading estimation accuracy and stability results, even in the case of highly intense maneuvering scenario. Used techniques and reliance on the absolute positioning information are expected to enable the long-term performance of this algorithm and prevent unwanted error accumulation during the stationary periods.

Positioning unit placement outside of the fork area also prohibits its use for fork elevation tracking, thus requiring a separate sensor to fulfill this task. Real-time tracking of the fork elevation ( $z$ )<sub>fork</sub> extends the product positioning capabilities of the proposed method into complete 3D. Three-dimensional positioning capability additionally allows to cover a variety of product stacking and shelving scenarios. With automatic detection of the payload pick-up and drop-down events, this method allows a complete, real-time, and automatic three-dimensional localization of any object in the area without its direct tagging with any positioning or identification unit. In this work, the automatic payload pick-up and drop-down detection is performed by an additionally developed A-PDD fusion algorithm. This algorithm is further described in section III and combines the aforementioned fork elevation and occupancy sensors to recognize the forklift behavior during payload pick-up or drop-down routine.

The following set of sensors is needed to provide the necessary information for the proposed indirect tracking method:

- *Underlying positioning unit*: Provides the real-time location of the industrial transportation machinery (i.e., forklift). The secondary purpose of this unit is the role of the supporting sensor for the forklift heading estimation by the ATKF algorithm. Even though in this work, the proposed indirect tracking method implementation is based on the UWB indoor positioning system, it may also be replaced with any suitable alternative positioning system, such as GNSS, 5G-, Wi-Fi-, and Bluetooth-based localization methods, as well as their combinations.
- *Heading tracking unit*: Provides the real-time heading tracking of the industrial machinery (e.g., forklift). This work focuses on the use of the MEMS gyroscope unit due to its wide availability, portability, and low processing complexity.
- *Fork elevation tracking unit*: Provides the real-time and accurate absolute elevation of the forklift tynes, and therefore, the elevation of the transported product. As the fork elevation change also reflects the forklift behavior during payload interaction events, the assistance in the payload pick-up and drop-down detection is the secondary role of this unit. In this work, the absolute fork elevation is tracked by using the industrial wire encoder sensor due to its reliability in industrial applications.
- *Fork occupancy sensor*: Provides the real-time fork occupancy status and detects the payload emergence within the

forklift tynes area. This unit is fused with the aforementioned elevation sensor by using the A-PDD algorithm, proposed in section III. This work focuses on the use of the ultrasonic distance sensor primarily for its reliability in industrial applications.

The sensors setup for the proposed indirect tracking method was chosen to minimize the required number of sensors, while effectively using their combination. The use of extra supporting, cost-inefficient, or computationally complex sensors, such as cameras, LiDARs, or military-grade inertial sensors, is avoided in this work. It is done to reduce the computational complexity, data processing time, and maintenance requirements of the proposed method while keeping a possibly high cost-efficiency, product positioning accuracy, and setup robustness in the industrial environment. These attributes allow for a potential future modification and upscaling of the proposed method for different applications and scenarios.

In the proposed indirect tracking method, the payload positioning is directly determined by the performance of the underlying positioning system. Therefore, the proposed method expects a satisfactory performance of the underlying positioning system (e.g., ensured by the appropriate deployment of UWB infrastructure). Nevertheless, to address this aspect, the proposed method supports the use of any positioning system suitable for a particular application, such as GNSS or cellular positioning, and is not bound to a specific option. This also includes combined methods, such as GNSS & UWB system for multi-environmental coverage, as well as a variety of available state-of-the-art approaches for the positioning performance enhancement, such as (machine learning) ML-enhanced, vision & inertial data-supported sensor fusion methods. The expected horizontal ( $\varepsilon_{indir}^{x,y}$ ) and vertical ( $\varepsilon_{indir}^z$ ) positioning errors of the proposed indirect tracking method can be expressed as functions, containing the following error components:

$$\begin{cases} \varepsilon_{indir}^{x,y} = f(\varepsilon_{pos}^{x,y}, \varepsilon_{fork}^{x,y}, \varepsilon_t^{x,y}, \varepsilon_{external}^{x,y}) \\ \varepsilon_{indir}^z = f(\varepsilon_{fork}^z, \varepsilon_t^z) \end{cases}, \quad (3)$$

where  $\varepsilon_{pos}^{x,y}$  is the horizontal error of the used underlying positioning system,  $\varepsilon_{fork}^{x,y}$  is the payload horizontal positioning error, caused by error in the forklift heading estimation and determined in (2), and  $\varepsilon_{fork}^z$  is the absolute error in the tynes' elevation measurement. Horizontal and vertical errors, caused by a potential timing error in the payload pick-up or drop-down event detection are respectively denoted as  $\varepsilon_t^{x,y}$  and  $\varepsilon_t^z$ , while  $\varepsilon_{external}^{x,y}$  is the horizontal error, caused by external factors, such as human error. Functional representation is used as the included error components are not linearly additive, and may occasionally compensate for each other.

Figure 2 shows the flow chart of the proposed indirect tracking method process. Data processing performed by the deployed sensor setup is highlighted in green, and processing performed on the server side is highlighted in blue. The data, collected and processed on the forklift setup side, is transmitted to the server using a wireless (e.g., cellular) link, highlighted in gray. The used sensors are divided into two fusion pairs. Competitive fusion of positioning and inertial in-

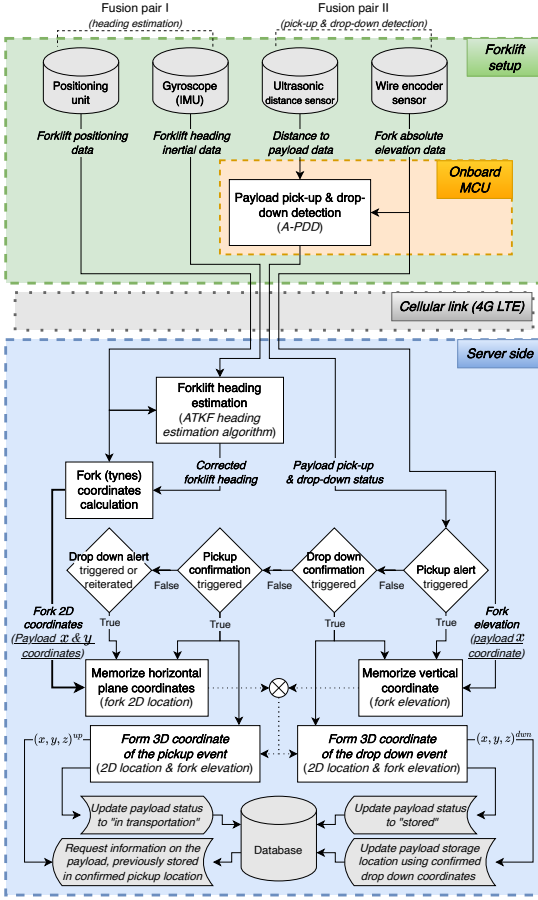


Fig. 2. Flowchart of proposed indirect tracking method, separated into sections, depending on the components' deployment/processing side.

formation is performed by using the ATKF heading estimation algorithm. The accurate forklift heading information is then combined with the forklift positioning data to calculate the exact horizontal location of the forklift tyres, thus minimizing the error component  $\varepsilon_{fork}^{x,y}$  in (3). Complementary fusion of the fork occupancy and elevation sensors is performed to detect the exact moment of the payload pick-up or drop-down event. This fusion is performed by the proposed pick-up detection algorithm, described in Section III. Detection of one of the mentioned events triggers the saving of the current tyres' position and elevation, which represents the current three-dimensional payload location.

In the case of the pick-up, the current tyres' position is compared to the locations of available products, previously stored in the database. The matching payload is then labeled as "in transportation", while its coordinates are bound to the forklift tyres' coordinates. Products, which are stacked on top of the picked-up payload, will also be labeled as "in transportation" with their respective elevation offsets. Automatic pick-

up of the above-located products can be disabled in predefined shelving areas. In the case of the detected drop-down event, the payload is labeled as "stored" at the latest 3D tyres' coordinates.

In the proposed indirect tracking method, the product identification information is bound to its current coordinates, updated in the database, and does not require any identification markers. Thus, this method suffices for the starting coordinates assignment to the newly arrived product during its initial registration routine. This, for instance, may be seamlessly and automatically performed by geofencing the specific unloading zones with exactly defined coordinates, where the product is eventually unloaded from the transportation vehicle (e.g., truck) upon arrival. Depending on the particular industrial site preferences, a wide variety of different methods may be used for the digital product registration routine, from manual input or logistics tag scanning up to the AI-enhanced vision. Assigning the obtained product information to the particular unloading zone finalizes the initial registration and enables the markerless tracking for the newly arrived product.

Depending on the various factors, such as the used positioning system, its configurations and specific limitations, used server and/or onboard processing units, the proposed indirect tracking method is expected to support dozens of simultaneously operating material handling equipment units (e.g., forklifts). In case of the tested indirect tracking setup, the number of simultaneously supported forklifts may reach 15-20 units, theoretically limited by the processing capacity of the used server unit. A distributed data processing (e.g., by forklift onboard processing units) or the use of a server unit with higher computational power may significantly increase the number of simultaneously supported forklifts.

### III. ALGORITHM FOR AUTOMATIC PICK-UP & DROP-DOWN DETECTION (A-PDD)

This section describes a proposed algorithm for the automatic detection of the payload pick-up & drop-down events, in this work referred to as the A-PDD algorithm. Automatic real-time detection of the payload interaction event is essential, as it fundamentally determines the positioning accuracy of the proposed indirect tracking approach. Mistimed recognition of payload pick-up or drop-down may cause an additional, up to a meter-level error in its resulting horizontal or vertical positioning, respectively notated as  $\varepsilon_t^{x,y}$  and  $\varepsilon_t^z$  in (3).

The proposed A-PDD algorithm performs a complementary fusion of the fork elevation and distance to the payload data, respectively provided by the wire encoder and ultrasonic distance sensors. This algorithm recognizes the specific patterns in the forklift behavior to verify the occurrence of the payload pick-up or drop-down event. The graph representation of the Extended Finite State Machine (EFSM) model of the proposed A-PDD algorithm is visualized in Fig. 3. It reflects the key states (nodes) and state transitions (edges) of the algorithm, as well as their dependence on the input variables [27]–[29]. This model can also be mathematically formulated as follows:

$$\mathcal{M}^{A-PDD} = (S, S_0, I, O, X, \tau, \lambda, \eta), \quad (4)$$



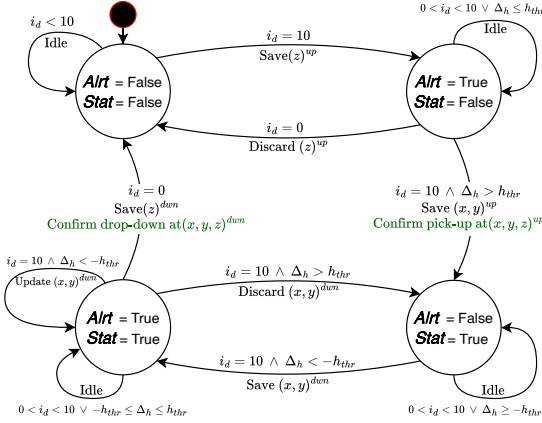


Fig. 3. Extended finite state machine model of the proposed A-PDD algorithm.

which includes set of algorithm states  $S$  with the initial state  $S_0$ , data input from the sensors  $X$ , sets of algorithm input  $I$  and output  $O$  parameters, as well as input  $\eta$ , output  $\lambda$ , and state transition  $\tau$  functions. Algorithm iteration begins by calculating the set of necessary input parameters  $I$  from the available sensors' data  $X$ . These sets are defined as follows:

$$X = \{(d_k, h_k) \mid d_k \in \mathbb{R}_{>0}, h_k \in \mathbb{R}\}, \quad (5)$$

$$I = \{(i_d, \Delta_h) \mid i_d \in \{0, \dots, 10\}, \Delta_h \in \mathbb{R}\}, \quad (6)$$

where  $d_k$  is the absolute distance to the object, measured by an ultrasonic sensor,  $h_k$  is the absolute tynes' elevation,  $\Delta_h$  is the tynes' elevation difference between measurement samples, and  $i_d$  is a counter of the latest distance measurements below the minimal threshold.

The counter variable  $i_d$  in the user-defined range ( $i_d \in \{0, \dots, 10\}$  in the case of this work) is used to mitigate the impact of possibly inconsistent distance measurements of the ultrasonic sensor in the fork occupancy detection process. Input parameters are calculated from the sensors' data by using the input function  $\eta : X \rightarrow I$ , which can be expressed as follows:

$$i_d = \eta(d_k) = \begin{cases} i_d + 1, & d_k \leq d_{thr} \wedge i_d < 10 \\ i_d - 1, & d_k > d_{thr} \wedge i_d > 0 \\ i_d & \text{otherwise} \end{cases}, \quad (7)$$

$$\Delta_h = \eta(h_k) = h_k - h_{k-1}, \quad (8)$$

where  $d_{thr}$  is the minimal distance threshold. Previous tynes' elevation measurement  $h_{k-1} = h_0$  and initial counter variable  $(i_d)_0$  at the first algorithm iteration are defined as follows:  $h_0 = h_1$  and  $(i_d)_0 = 0$ .

Available states of the algorithm are defined by boolean pick-up/drop-down status flags **Alrt** and **Stat**, and can be expressed as the following set:

$$S = s(\mathbf{Alrt}, \mathbf{Stat}) = \{s_{00}, s_{10}, s_{01}, s_{11}\}, \quad (9)$$

while the initial state  $S_0$  of the algorithm is translated from

the previous use session or defined as the default starting state  $s_{00} = (\mathbf{Alrt} = \text{False}, \mathbf{Stat} = \text{False})$ . Transitions between available algorithm states are based on the input variables  $I$  and the current state, and are described by the corresponding transition function  $\tau : S \times I \rightarrow S$ , expressed as follows:

$$\tau(s_{00}) = \begin{cases} s_{00}, & i_d < 10 \\ s_{10}, & i_d = 10 \end{cases}, \quad (10)$$

$$\tau(s_{10}) = \begin{cases} s_{00}, & i_d = 0 \\ s_{10}, & (0 < i_d < 10) \vee (\Delta_h \leq h_{thr}) \\ s_{01}, & (i_d = 10) \wedge (\Delta_h > h_{thr}) \end{cases}, \quad (11)$$

$$\tau(s_{01}) = \begin{cases} s_{01}, & (0 < i_d < 10) \vee (\Delta_h \geq -h_{thr}) \\ s_{11}, & (i_d = 10) \wedge (\Delta_h < -h_{thr}) \end{cases}, \quad (12)$$

$$\tau(s_{11}) = \begin{cases} s_{01}, & (i_d = 10) \wedge (\Delta_h > h_{thr}) \\ s_{10}, & (0 < i_d < 10) \vee (-h_{thr} \leq \Delta_h \leq h_{thr}) \\ s_{10}, & (i_d = 10) \wedge (\Delta_h < -h_{thr}) \\ s_{00}, & i_d = 0 \end{cases}, \quad (13)$$

where  $h_{thr}$  is the minimal threshold for the momentary tynes' elevation change  $\Delta_h$ .

Outputs set of the A-PDD algorithm contains the aforementioned **Alrt** and **Stat** status flags, and is expressed as follows:

$$O = \{(\mathbf{Alrt}, \mathbf{Stat}) \mid \{\mathbf{Alrt}, \mathbf{Stat}\} \in \{\text{False}, \text{True}\}\}. \quad (14)$$

The expected output of the algorithm depends on the current state and can be defined by the output function  $\lambda : S \times I \rightarrow O$  as follows:

$$\lambda(s) = \begin{cases} (\mathbf{Alrt} = \text{False}, \mathbf{Stat} = \text{False}), & s = s_{00} \\ (\mathbf{Alrt} = \text{False}, \mathbf{Stat} = \text{True}), & s = s_{01} \\ (\mathbf{Alrt} = \text{True}, \mathbf{Stat} = \text{False}), & s = s_{10} \\ (\mathbf{Alrt} = \text{True}, \mathbf{Stat} = \text{True}), & s = s_{11} \end{cases}. \quad (15)$$

The selected state transitions in the A-PDD algorithm also initiate specific actions and stages in the payload pick-up and drop-down process of the proposed indirect tracking method. Thus, the presented algorithm model may be further extended with the set of external data  $Y$  and external response function  $\mu$ . The external data  $Y$  represents the set of current payload pick-up & drop-down coordinates and can be expressed as follows:

$$Y = \{(x, y, z)^{up}, (x, y, z)^{down}\}. \quad (16)$$

These coordinates are separately saved in the proposed indirect tracking method at different state transitions of the A-PDD algorithm, which is described by the external repose function  $\mu : S \times I \times Y \rightarrow Y$ . This function is defined as follows:

$$\mu(s_{00}) = \begin{cases} (\cdot, \cdot, \cdot)^{up}, & i_d < 10 \\ (\cdot, \cdot, z_k^{fork})^{up}, & i_d = 10 \end{cases}, \quad (17)$$

$$\mu(s_{10}) = \begin{cases} (\cdot, \cdot, \emptyset)^{up}, & i_d = 0 \\ (\cdot, \cdot, z)^{up}, & 0 < i_d < 10 \vee \Delta_h \leq h_{thr} \\ (x_k^{fork}, y_k^{fork}, z)^{up}, & i_d = 10 \wedge \Delta_h > h_{thr} \end{cases}, \quad (18)$$

$$\mu(s_{01}) = \begin{cases} (\cdot, \cdot, \cdot)^{down}, & 0 < i_d < 10 \vee \Delta_h \geq -h_{thr} \\ (x_k^{fork}, y_k^{fork}, \cdot)^{down}, & i_d = 10 \wedge \Delta_h < -h_{thr} \end{cases}, \quad (19)$$

$$\mu(s_{11}) = \begin{cases} (\emptyset, \emptyset, \cdot)^{down}, & i_d = 10 \wedge \Delta_h > h_{thr} \\ (x, y, \cdot)^{down}, & 0 < i_d < 10 \vee \\ (x_k^{fork}, y_k^{fork}, \cdot)^{down}, & -h_{thr} \leq \Delta_h \leq h_{thr} \\ (x, y, z_k^{fork})^{down}, & i_d = 10 \wedge \Delta_h < -h_{thr} \\ (x, y, z_k^{fork})^{down}, & i_d = 0 \end{cases}, \quad (20)$$

where  $(x^{fork}, y^{fork}, z^{fork})_k^{up/down}$  represent the current fork location, newly assigned as payload pick-up or drop-down coordinates,  $(x, y, z)^{up/down}$  represent previously assigned coordinates, while  $\emptyset$  and  $\cdot$  respectively denote the coordinates, which were discarded or were not yet assigned.

The forklift initiates the pick-up process by approaching the payload while keeping the tynes elevated on the payload level. This step is detected by the ultrasonic distance sensor, which measures the distance  $d_k$  to the approached product. Once the forklift reaches the minimal distance threshold  $d_{thr}$ , the A-PDD algorithm triggers the pick-up alert ( $Alrt = True$ ) and reaches the  $s_{10}$  state. This further initiates the saving of the current absolute tynes' elevation  $h_k$  as a vertical pick-up coordinate  $(z)^{up}$  in the proposed indirect tracking method. At this stage, the pick-up process may be canceled by the forklift moving away from the payload without its lifting, which is detected by consistently increased distance measurements  $d_k$  beyond the threshold  $d_{thr}$ .

To confirm the pick-up event, the forklift is expected to lift the payload off the ground, which is detected by the momentary fork elevation change  $\Delta_h$  above the positive threshold  $h_{thr}$ . This confirms the payload pick-up event and enables the pick-up status flag ( $Stat = True$ ), thus reaching the  $s_{01}$  state of the algorithm. In the proposed indirect tracking method, this further initiates the saving of externally tracked fork location as 2D coordinates of the detected pick-up event  $(x, y)^{up}$ . The reliability of these 2D pick-up coordinates is explained, as to avoid a physical collision, the forklift ought to remain stationary at the moment of the payload lifting off the ground. This moment, however, is sufficient for the onboard sensors to detect the exact moment of the pick-up and define the corresponding event coordinates. Saved 2D and vertical coordinates are then immediately combined into the resulting pick-up location  $(x, y, z)^{up}$  and used further by the indirect tracking method to identify and track the picked-up product.

The payload drop-down process is performed in the opposite order and is triggered by the forklift lowering the payload to the drop-down level. Similarly, the forklift ought to remain stationary at the moment when the payload touches the ground, which corresponds to the final moment of the payload-lifting-down process. Detected payload lifting down event triggers the drop-down alert flag, resulting in the algorithm  $s_{11}$  state. This initiates the saving of the tynes' 2D coordinates  $(x, y)^{down}$ , which are then continuously updated during the entire down-lifting process. It covers a possible case, when the payload down-lifting was initiated prior to the full stop of the forklift. Moving away from the laid-down payload, on the other hand, concludes the drop-down process, returns the A-PDD algorithm to the state  $s_{00}$ , and initiates the saving of the vertical

drop-down coordinate  $(z)^{down}$  within the indirect tracking method. The resulting drop-down location  $(x, y, z)^{down}$  is then used by the indirect tracking method as a storage location for the dropped-down product. Alternatively, lifting up the payload without moving away from it will cancel the drop-down process, thus discarding the drop-down  $(x, y)^{down}$  coordinates.

---

**Algorithm 1:** Ultrasonic & wire encoder sensors-based algorithm for automatic payload pick-up & drop-down detection (A-PDD).

---

```

Initialize : Distance sensor counter:  $i_d = 0$ 
              Initial payload interaction alert flag:  $Alrt = False$ 
              Initial payload onboard state flag:  $Stat = False$ 
Parameters: Distance to payload threshold:  $d_{thr}$  [m]
              Elevation change threshold:  $h_{thr}$  [m]
Input Data: Measured tynes' elevation:  $h_k$  [m]
              Measured distance to payload in front:  $d_k$  [m]
Outputs : Payload interaction alert flag:  $Alrt$ 
            Payload onboard state flag:  $Stat$ 

1 for  $k \leftarrow 1$  to  $\inf$  do
2   if  $d_k \leq d_{thr} \wedge i_d < 10$  then
3      $i_d = i_d + 1$ 
4   else if  $d_k > d_{thr} \wedge i_d > 0$  then
5      $i_d = i_d - 1$ 
6   end
7    $\Delta_h = h_k - h_{k-1}$ 
8   if  $Stat$  is True then
9     if  $Alrt$  is True then
10      if  $i_d = 0$  then
11         $Alrt = False$ 
12         $Stat = False$  // Save  $(z)^{down} = z_k^{fork}$ 
13      else if  $i_d = 10$  then
14        if  $\Delta_h > h_{thr}$  then
15           $Alrt = False$  // Discard  $(x, y)^{down}$ 
16        else if  $\Delta_h < -h_{thr}$  then
17           $Alrt = True$  // Update  $(x, y)^{down} = (x, y)_k^{fork}$ 
18          // Drop-down alert re-initiated
19        end
20      end
21    else if  $i_d = 10 \wedge \Delta_h < -h_{thr}$  then
22       $Alrt = True$  // Save  $(x, y)^{down} = (x, y)_k^{fork}$ 
23      // Drop-down alert triggered
24    end
25  else
26    if  $Alrt$  is True then
27      if  $i_d = 0$  then
28         $Alrt = False$  // Discard  $(z)^{up}$ 
29      else if  $i_d = 10 \wedge \Delta_h > h_{thr}$  then
30         $Alrt = False$  // Pick-up process canceled
31         $Stat = True$  // Save  $(x, y)^{up} = (x, y)_k^{fork}$ 
32        // Pick-up confirmed at  $(x, y, z)^{up}$ 
33      end
34    else if  $i_d = 10$  then
35       $Alrt = True$  // Save  $(z)^{up} = z_k^{fork}$ 
36      // Pick-up alert triggered
37    end
38  end
39 end
40 return  $Alrt, Stat$ 
41 end
    
```

---

The pseudo-code of the proposed A-PDD algorithm is provided in Algorithm 1, while Table I represents a detailed state transition table of this algorithm. Arrows  $\uparrow$  &  $\downarrow$  respectively denote the flag change from False to True & from True to False. The overall complexity of this algorithm can be represented in the (Big O)  $O$ -notation as  $O(1)$  (constant) in terms of both execution time and used space [30]. The constant time complexity is explained, as the algorithm represents the defined number of conditional statements without loops or



recursions. The strictly defined number of used variables also determines the constant space complexity of this algorithm.

TABLE I

STATE TRANSITION TABLE OF PROPOSED A-PDD ALGORITHM ALONG WITH THE DESCRIBED RESPONSE OF THE PROPOSED INDIRECT TRACKING METHOD ON THE ALGORITHM OUTPUTS.

Alert flag	State flag	Action triggered
False	False	Idle mode; Await the pick-up alert
↑	False	Potential pick-up alert; Save current tynes elevation reading as $(z)^{up}$ coordinate for potential further pick-up event
True	False	Idle mode; Await the pick-up confirmation
↓	False	Pick-up aborted; Discard a recently saved tynes elevation reading
↓	↑	Pick-up event confirmation; Combine current tynes 2D coordinates $(x, y)^{up}$ with recently stored $(z)^{up}$ coordinate and save as new 3D pick-up location; Reset the Alert flag to False
False	True	Idle mode; Await the drop-down alert
↑	True	Potential drop-down alert; Save current tynes 2D coordinates $(x, y)^{down}$ of potential drop-down event
True	True	Wait for the drop-down confirmation or cancellation; Update the stored 2D coordinates $(x, y)^{down}$ at every drop-down alert reiteration
↓	True	Drop-down aborted; Discard a recently saved tynes 2D coordinates
↓	↓	Drop-down event confirmation; Combine current tynes elevation reading $(z)^{down}$ with recently stored 2D coordinates $(x, y)^{down}$ and save as new 3D drop-down location; Reset the Alert flag to False
False	↑ or ↓	<b>Unused:</b> Can be enabled to detect emergency events (e.g., payload fell off the fork)

In comparison with payload loading/unloading detection approaches, used in the available state-of-the-art indirect tracking methods, described in Section I-A, the proposed A-PDD algorithm enables an automatic and accurate two-step pick-up & drop-down detection of completely markerless products.

For instance, Franko *et al.* [13] and Zhao *et al.* [14] have used an automatic payload pick-up detection approach, based on the continuously tracked presence of payload-attached RFID tags in front of the forklift, which indicates its transportation. Compared to the proposed A-PDD algorithm, this approach yields lower detection accuracy due to delayed event recognition and possible simultaneous detections of multiple products. Additionally, the requirement for the direct product marking with RFID tags further limits the applicability of this approach in markerless product tracking.

Unlike the sole ultrasonic sensor-based payload pick-up detection approach used by Motroni *et al.* [17], the proposed sensor fusion-enabled method provides the necessary data filtering and includes a supporting sensor. This reduces possible false object detections and measurement inconsistency, preventing delayed or false payload pick-up & drop-down detection in the context of indirect tracking. The load cell-based pick-up detection approach, used by Zealabs & Sewio in their work [21], [22], is expected to offer a pick-up detection accuracy and reliability similar to the proposed sensor fusion-based method. The proposed method, however, provides significantly reduced requirements for the sensors' integration into the forklift mechanisms. It extends the applicability of the proposed method in cases when any modifications to industrial machinery are prohibited. In the indirect tracking methods proposed by Bostrell *et al.* [15] and Kovavisaruch *et al.* [19],



Fig. 4. Deployment of the sensors setup, used in the experimental testing of the proposed indirect tracking method: a) wire encoder sensor attached to the forklift mast; b) positioning unit (UWB tag) and IMU are deployed on top of the forklift; c) ultrasonic distance sensor deployed behind the fork area. d) Industrial products, tracked indirectly (using the proposed method) and directly (using the highlighted independent UWB tag) during the experimental campaign.

the payload loading/unloading detection is not automated and is performed manually.

#### IV. EXPERIMENTAL PROOF OF CONCEPT

In order to assess the working capability of the proposed indirect tracking method and demonstrate its performance, the experimental test campaign was conducted in an industrial environment. The following sensors' setup was deployed on the full-scale forklift for testing:

- As the underlying positioning unit, it was used Eliko UWB indoor positioning system with the update rate of 5 Hz (sampling delta time  $dt^{x,y} = 200$  ms) [31]. The declared accuracy of 10 - 30 cm reflects the underlying positioning system error, notated as  $\varepsilon_{pos}^{x,y}$  in (3).
- The gyroscope, available in the 9-DOF IMU model Bosch BNO055, was used at the update rate of 100 Hz (sampling delta time  $dt^{\omega} = 10$  ms) as the primary inertial heading tracking unit [32].
- Miran MPS-M series draw wire encoder was used for the absolute fork elevation tracking at the sampling rate of 12.5 Hz (sampling delta time  $dt^h = 80$  ms) [33]. The declared 1 cm accuracy of this sensor reflects the expected vertical tynes' positioning error, notated as  $\varepsilon_{fork}^z$  in (3). It was also used as a supporting sensor in the payload pickup detection.
- Ultrasonic distance sensor SEN0208 was used at the update rate of 12.5 Hz (sampling delta time  $dt^d = 80$  ms) for the tynes' occupancy status tracking as part of the automatic payload pick-up detection process [34].

The high update rates of the used sensors ensure reliable forklift monitoring and in-time detection of the occurring pick-up & drop-down events, even at high forklift operating speeds and intense maneuvering.

Physical sensors' deployment on the used forklift is shown in Fig. 4. UWB positioning unit and IMU were deployed on

top of the forklift as shown in Fig. 4b. For the accurate forklift heading estimation, these sensors were fused by the ATKF algorithm, using the default tuning parameters, provided in the appendix of the source article [26]. Figures 4a and 4c respectively demonstrate the deployment of the used wire encoder and ultrasonic distance sensors in the fork area of the forklift. These sensors were fused by the proposed A-PDD algorithm, earlier described in Section III, for automatic payload pick-up & drop-down detection. This algorithm was used with the following heuristically chosen threshold parameters, suitable for the tynes' length and average lifting speed of the used full-scale forklift: distance to the payload threshold  $d_{thr} = 275$  mm and momentary fork elevation change threshold  $h_{thr} = 5$  mm, which corresponds to the fork elevation speed of  $5 \text{ mm}/dt^h = 62.5 \text{ mm/s}$ . The implemented indirect tracking prototype setup also included a data forwarding unit, represented by a mini-PC with an attached 4G LTE modem. This unit was used for parallel sensors' data reception, synchronization, and immediate transmission to the server side by using the 4G LTE cellular connection. For a synchronized use on the server side, each data input was assigned with the corresponding UNIX timestamp by the forwarding unit before transmission.

Figure 4d shows the  $2 \text{ m} \times 1 \text{ m} \times 0.5 \text{ m}$  sized industrial payloads, used during the conducted test campaign. For later comparison of direct and indirect tracking methods, one of the products was also directly marked with a fully independent UWB tag, highlighted in Fig. 4d. The chosen deployment layout of used sensors serves conceptual testing purposes and requires further enhancement for long-term use. This includes a robust fixation of elevation and distance sensors, as well as integration with the forklift power supply. The deployment of the tynes' elevation measurement unit may be further optimized to cover extensive (multi-level) forklift masts. Even though the proposed indirect tracking setup was designed for independent use, a possible integration with the forklift CAN bus may also be beneficial.

During the test campaign, two industrial payloads were transported by the forklift between reference key spots for their temporal storage, stacking, or shelving. A total of four reference key spots (REF1-REF4) around the industrial area were manually measured with centimeter precision during the conducted test campaign by using an independent UWB tag of the same UWB positioning system. To ensure unbiased results, the UWB positioning system was also preliminarily calibrated with the laser range finder unit. The testing scenario includes a total of eight consecutive events of the forklift interactions with the test payloads. These events are:

- I Two test payloads (A and B) are stacked at the initial reference location REF1; the forklift picks up the upper payload A for transportation
- II Forklift places the transported payload A on a 1 m high shelf at the reference spot REF2
- III Forklift picks up the second payload B for transportation at the location REF1
- IV Forklift drops down the transported payload B on the ground at the reference spot REF3
- V Forklift picks up payload A at the reference spot REF2 for transportation

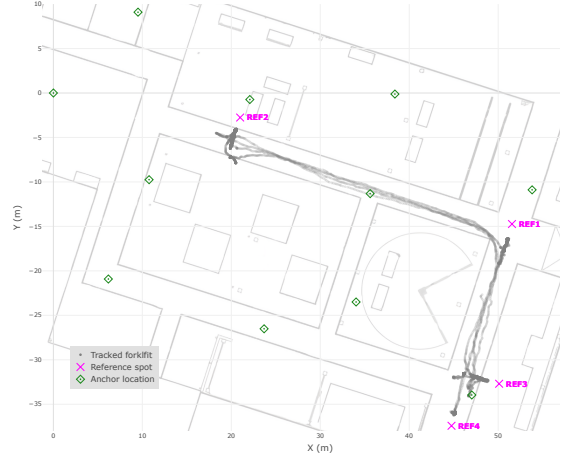


Fig. 5. Manually acquired reference spots (magenta), marked on the industrial environment map together with mapped UWB anchors' locations (green), and the forklift route (grey), tracked during the test campaign.

- VI Forklift stacks payloads by placing payload A on top of payload B at the reference spot REF3
- VII Forklift picks up the stack of payloads A & B at the reference spot REF3 for transportation
- VIII Forklift drops down the stack of both transported payloads at the reference location REF4

The exact locations of the aforementioned reference spots are shown in Fig. 5 (magenta markers) along with the enumerated payload interaction events that occurred at the respective spots. The gray-colored track reflects the forklift movement between the reference key spots during the test campaign. Mapped locations of a total of 11 UWB anchors, deployed in the test campaign area, are shown with green diamonds. The comprehensive dataset of experimentally collected multi-sensor data during the conducted test campaign is available at the database repository [35].

## V. RESULTS AND DISCUSSION

This section covers the experimental performance evaluation of the proposed indirect tracking method in terms of absolute (subsection V-A) and repeatability accuracy (subsection V-B) in product localization. These subsections also demonstrate the importance of accurate forklift heading estimation in the proposed method. Subsection V-C provides the performance comparison of the proposed indirect tracking method with the traditional direct product tracking approach.

### A. Absolute accuracy of the proposed indirect tracking method

The absolute positioning accuracy of the proposed indirect tracking method was evaluated for eight consecutive product pick-up and drop-down events, described in Section IV. The accuracy of the proposed method was evaluated in relation to the reference key spots REF1-REF4, demonstrated in Fig. 5.

TABLE II

ABSOLUTE 3D POSITIONING ACCURACY **D** OF THE PROPOSED INDIRECT TRACKING METHOD BASED ON INACCURATE (INITIAL IMU) AND ACCURATE (ATKF ESTIMATED) HEADING DATA TOGETHER WITH PRODUCT POSITIONING ERROR CAUSED BY INACCURACY IN: HEADING ESTIMATION (2D ERROR) **A**, ELEVATION MEASUREMENT (VERTICAL ERROR) **B**, AND EXTERNAL FACTORS (2D ERROR) **C**.

		Payload interaction event:							
Indirect tracking at accurate heading (ATKF estimated)	A (m)	0.01	0	0	0.06	0.04	0.14	0.04	0.01
	B (m)	0.01	0	0.02	0.02	0.03	0.01	0.04	0.02
	C (m)	0.3	0.06	0.2	0.06	0.25	0.02	0.1	0.01
	D (m)	<b>0.3</b>	<b>0.06</b>	<b>0.2</b>	<b>0.12</b>	<b>0.28</b>	<b>0.15</b>	<b>0.11</b>	<b>0.02</b>
Indirect tracking at inaccurate heading (IMU provided)	A (m)	0	0.22	0.07	0.51	1.59	1.9	1.89	2.37
	B (m)	0.01	0	0.02	0.02	0.03	0.01	0.04	0.02
	C (m)	0.3	0.06	0.2	0.06	0.25	0.02	0.1	0.01
	D (m)	<b>0.3</b>	<b>0.24</b>	<b>0.22</b>	<b>0.46</b>	<b>1.35</b>	<b>1.91</b>	<b>1.81</b>	<b>2.38</b>

The obtained absolute accuracy results of indirect product positioning are provided in the upper half of Table II. It reflects resulting, three-dimensional absolute errors of the tracked product (**D**) together with its components, including 2D positioning error caused exclusively by errors in the estimated heading (**A**), vertical error of the measured fork elevation (**B**), and 2D positioning errors caused by external factors (**C**). External errors include a human factor error (i.e., inconsistency of the human-operated forklift) and internal accuracy of the underlying UWB positioning system, respectively notated in (3) as  $\varepsilon_{pos}^{x,y}$  and  $\varepsilon_{external}^{x,y}$ . Payload positioning errors caused by errors in heading estimation were calculated according to (2). The bottom half of Table II reflects these accuracy aspects in the case when the ATKF heading estimation algorithm is replaced with initial, inaccurate IMU heading data. It is done in order to demonstrate the importance of accurate heading estimation in the proposed indirect tracking method.

The proposed indirect tracking method has demonstrated under 30 cm payload positioning accuracy in events I, III, and V, primarily caused by external factors, and under 15 cm accuracy in events II, IV, VI, VII, and VIII. These results are in the range of the expected initial accuracy of the used UWB positioning system, which indicates an overall minor positioning accuracy loss in the proposed method and positively reflects its performance. Minor, primarily under 5 cm, errors in product positioning were caused by inaccuracies in forklift heading, which indicates an outstanding performance of the used ATKF heading estimation algorithm. Below 4 cm errors in product positioning were introduced by the fork elevation sensor, which confirms its stability and robustness. The corresponding indirect tracking performance results at the reference spots are visualized in Fig. 6 with green color. The expected indirect tracking results, recreated without the use of the ATKF heading estimation algorithm, are demonstrated with red color in Fig. 6. In this case, the forklift heading was provided by the onboard IMU unit. Corresponding indirect tracking results indicate an intensive growth of product positioning error up to 2.38 m throughout the test campaign. This demonstrates

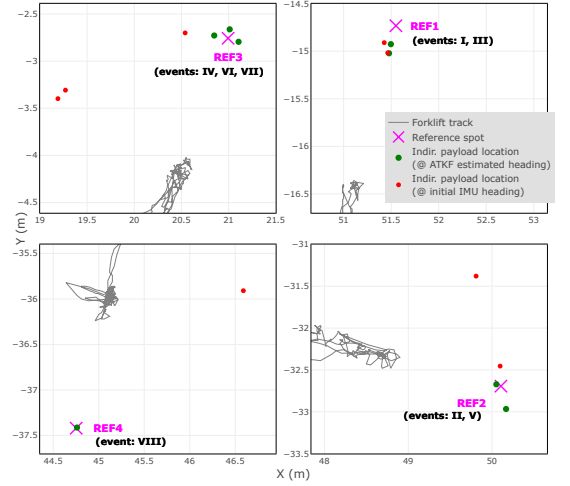


Fig. 6. Visualized 2D Indirect tracking performance at the reference key spots (magenta), based on the initial IMU provided heading (red) and on the ATKF estimated heading (green). Roman numbers indicate locations of the respective payload pick-up/drop-down events. The gray line indicates the collected forklift tracking data.

the major impact of the over-time accumulated IMU heading errors on the resulting indirect product positioning. Product positioning errors, caused by deviations in the measured fork elevation and other external factors, remain unchanged.

During the described test campaign, as well as in multiple preliminary down-scaled tests, the proposed A-PDD algorithm has demonstrated a remarkable performance, providing 100% pick-up and drop-down event recognition accuracy. The false alert cancellation mechanism of this algorithm has also demonstrated the same performance in spotting the false pick-up & drop-down events. Nevertheless, this algorithm may require separate long-term testing in order to further validate its reliability and assess its performance in a variety of different scenarios.

### B. Repeatability error evaluation of the proposed method

This subsection evaluates the repeatability performance of the proposed indirect tracking method. The repeatability results are calculated for the pair of indirectly tracked payload interaction events (i.e., pick-up or drop-down), occurred in the same physical location. For the event pairs related to payload stacking, the results are provided on a two-dimensional plane, while in the case of the pick-up of the earlier dropped-down payload, the results also include elevation error. It reflects the expected performance of the proposed method in real-life applications, where the ground truth (reference spot) of the stored product is not available.

Repeatability errors of the proposed method were evaluated in a total of 5 product pick-up/drop-down event pairs, which have physically occurred at the same reference spots during the experimental test campaign. Numerical results of the repeatability errors in the proposed indirect product localization method are demonstrated in Table III. Results are provided

separately for 2D ( $x, y$  coordinates) and vertical ( $z$  coordinate) components of the tracked product locations. Two-dimensional repeatability results are provided for both accurate (ATKF-estimated) and inaccurate (sole IMU-provided) forklift heading estimations. Results for the elevation repeatability error are not provided for the event pairs I & III, IV & VI, and VI & VII, as in these events, two products were physically stacked at the same 2D locations and different elevations.

TABLE III

REPEATABILITY ERRORS IN THE INDIRECTLY TRACKED PRODUCTS' ELEVATION AND 2D LOCATIONS, BASED ON THE ACCURATE (ATKF ESTIMATED) AND INACCURATE (SOLE IMU PROVIDED) HEADING DATA.

	Events pair	2D error ( $x, y$ coordinates)		Elevation error ( $z$ coordinate)
		ATKF heading (Accurate)	IMU heading (Inaccurate)	
Indirect tracking repeatability error (m)	I & III	0.1	0.11	NA
	II & V	0.32	1.11	0.02
	IV & VI	0.27	1.52	NA
	IV & VII	0.16	1.41	0.06
	VI & VII	0.18	0.12	NA

The proposed indirect tracking method has demonstrated two-dimensional repeatability errors in the range of 10 cm to 32 cm, similar to the observed absolute positioning performance. The obtained repeatability error results in the product elevation tracking demonstrate the presence of a minor error in the range between 2 cm and 6 cm. Similar to the obtained absolute positioning accuracy results, the provided repeatability errors are primarily caused by external factors. These include the human factor of the man-operated forklift and the initial precision of the used UWB positioning system. The proposed indirect product tracking method, based on the inaccurate initial IMU provided heading, on the other hand, has demonstrated a major repeatability error increase reaching up to 1.52 m. These results additionally confirm a determining contribution of the accurate heading estimation towards minimizing the repeatability error of the proposed indirect tracking method. These results reflect the general stability and accuracy of the proposed indirect tracking method in cases when the proposed method may only rely on the earlier self-collected product positioning data. It presumes that no additional assisting or reference data is available on the server side as predefined reference storage spots and shelves, or other dedicated areas.

### C. Comparison of indirect and direct tracking methods

This subsection covers the performance comparison of the proposed indirect tracking method with a direct product localization approach. The direct tracking method was used for this comparison as it is expected to be the default approach if real-time object localization is required. For this comparison, one of the used industrial products was equipped with an independent UWB positioning unit, highlighted in Fig. 4d, and further referred to as a benchmark tag. Positioning data from the benchmark UWB tag was collected independently during the test campaign. The benchmarked product was picked up at the reference spot REF1 (event III), transported, and dropped

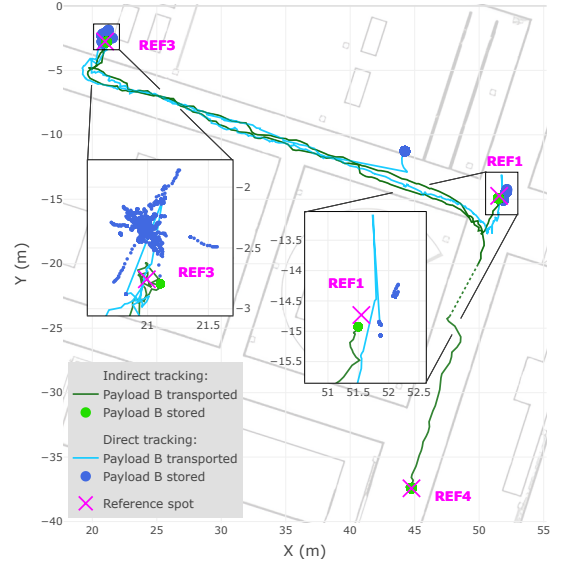


Fig. 7. Visualized 2D results of the industrial product tracking by indirect (green) and direct (blue) methods. Lines of the corresponding color indicate the path of the transported product, tracked by the aforementioned methods. Dots of the corresponding color reflect the positioning results of the stored product, tracked by the aforementioned methods. Magenta markers represent the reference (true) spots for product storage.

down at the reference spot REF3 (event IV). Later, the product was picked up at the reference spot REF3 (event VI) and dropped down at the reference spot REF4 (event VIII). Mean Absolute Error (MAE)

$$MAE_{2D} = \frac{\sum_{i=1}^N \sqrt{(x_{true} - x_i)^2 + (y_{true} - y_i)^2}}{N}, \quad (21)$$

Root Mean Squared Error (RMSE)

$$RMSE_{2D} = \sqrt{\frac{\sum_{i=1}^N \left( \sqrt{(x_{true} - x_i)^2 + (y_{true} - y_i)^2} \right)^2}{N}}, \quad (22)$$

error Standard Deviation (SD or  $\sigma$ )

$$\sigma_{2D} = \sqrt{\frac{\sum_{i=1}^N \left( \sqrt{(x_{true} - x_i)^2 + (y_{true} - y_i)^2} - MAE_{2D} \right)^2}{N}}, \quad (23)$$

and maximum error metrics were used to evaluate the accuracy and precision of both addressed payload localization methods.

Visualized performance of both direct and indirect tracking methods in a real-time industrial product localization is shown in Fig. 7, respectively, with blue and green colors. Light blue and dark green colors, respectively, show the active product transportation route, tracked by the aforementioned methods. Dark blue and light green colors indicate the stored (stationary) product, tracked by corresponding methods. Corresponding reference (true) spots are colored with magenta. Numerical accuracy and precision results of the compared indirect and

direct product tracking methods are respectively provided in the left and right halves of Table IV. Results are separately provided in 2D, vertical, and 3D dimensions for each of the three covered reference spots.

TABLE IV

VERTICAL, 2D, AND 3D ACCURACY AND PRECISION RESULTS OF THE PRODUCT POSITIONING BY DIRECT AND INDIRECT TRACKING METHODS, PROVIDED SEPARATELY FOR EACH COVERED REFERENCE SPOT

	Error metrics (m)	Indirect tracking			Direct tracking			
		2D	Vertical	3D	2D	Vertical	3D	
Payload interaction spot:	REF1	MAE	0.2	0.06	0.21	0.53	0.09	0.54
		RMSE	0.2	0.06	0.21	0.56	0.11	0.57
		SD ( $\sigma$ )	0	0	0	0.05	0.06	0.06
		Error <sub>max</sub>	0.2	0.06	0.21	0.79	0.2	0.79
	REF3	MAE	0.11	0.04	0.12	0.45	0.21	0.5
		RMSE	0.11	0.05	0.12	0.46	0.22	0.51
		SD ( $\sigma$ )	0.01	0.02	0	0.1	0.05	0.1
		Error <sub>max</sub>	0.11	0.04	0.12	0.94	0.38	0.94
	REF4	MAE	0.01	0.02	0.02	NA	NA	NA
		RMSE	0.01	0.02	0.02	NA	NA	NA
		SD ( $\sigma$ )	0	0	0	NA	NA	NA
		Error <sub>max</sub>	0.01	0.02	0.02	26.16	1.1	26.18

The proposed indirect tracking method has achieved a 3D localization accuracy of the benchmarked product between 2 cm and 21 cm. Since in the proposed method, the location of the payload pick-up or drop-down is measured only once and represents a single data point, the accuracy metrics (MAE, RMSE, and maximal error) are identical, while the precision metric (standard deviation) equals zero. For this reason, both direct and indirect methods are compared in terms of the positioning accuracy, while the precision is only evaluated for the direct tracking approach. Achieved vertical accuracy results of the proposed method do not exceed 6 cm, which is essential in covering the product stacking and shelving scenarios. During the conducted test campaign, the indirect tracking method experienced an insignificant  $\sim 1$  s gap in the positioning data, clearly observed in Fig. 7 at the coordinates (49; -22).

The direct tracking approach, on the other hand, has demonstrated the mean absolute error and RMSE of the three-dimensional positioning in the range of 50-57 cm at the reference spots REF1 and REF3, with the maximal outliers of 79 cm and 94 cm, respectively, observed at these key spots. The respective positioning error standard deviations at these key spots were 6 cm and 10 cm. The vertical accuracy of the direct tracking method at the reference spots REF1 and REF3 does not exceed 11 cm and 22 cm, respectively. The corresponding peak outliers in vertical product positioning at these reference spots were 20 cm and 38 cm, with the achieved error standard deviation in the range of 5-6 cm. These results indicate the presence of a significant systematic error, caused by numerous environmental obstacles. A relatively reliable mitigation of this error may require the use of complex techniques, such as channel impulse response (CIR) analysis or ML-based methods. During the product transportation to the reference spot REF4, however, the UWB positioning quality

for the benchmark tag has decreased to an insufficient level, entirely preventing its further tracking at the REF4 spot. At the moment of the product drop-down at the REF4 spot, its latest directly tracked location was at a distance of 26.18 m, which includes a 1.1 m vertical error. This location can be visually observed in Fig. 7 at the approximate coordinates of (44; -11).

In comparison with the direct tracking approach, the proposed indirect tracking method has demonstrated major reliability, positioning stability, and approximately four times higher overall product positioning accuracy. The achieved performance results of both direct and indirect tracking methods are explained by the physical deployment of their corresponding UWB tags. In the proposed indirect tracking method, the positioning unit is deployed on top of the  $\sim 2$  m high forklift, above the majority of signal-blocking obstacles. The benchmark tag, attached directly to the product, on the other hand, constantly remains in significantly challenging line-of-sight (LoS) conditions with the UWB positioning infrastructure. In these conditions, the directly localized product itself represents the most significant LoS-blocking obstacle. The positioning quality evaluation of the used UWB RTLS system for both methods has confirmed this conclusion. The UWB positioning system has demonstrated a 99.93% successful positioning rate of the forklift deployed tag throughout the entire test campaign and a 100% successful positioning rate at each of the covered reference spots. The benchmark tag, however, has experienced only 20.8% of a successful positioning rate throughout the entire test campaign. At the reference spots REF1 and REF3, the UWB positioning system has respectively demonstrated only 3.2% and 31.3% of successful positioning rates, and 0% at the reference spot REF4.

## VI. CONCLUSION

This paper proposed a novel method for accurate three-dimensional and real-time tracking of fully markerless industrial products, normally transported by industrial material handling equipment such as forklifts, lifters, or cranes. In this approach, the required indirect tracking setup components are deployed on the used industrial machinery, while the tracked products remain fully unmarked. As part of the proposed indirect tracking method, this work also presented the sensor fusion algorithm for automatic payload pick-up & drop-down detection (A-PDD). Based on the distance and fork elevation sensors, this algorithm monitors the forklift behavior and recognizes the occurrence of a payload pick-up or drop-down event. A capability of recognizing false event alerts additionally ensures the reliability of the A-PDD algorithm.

The experimental testing of the proposed indirect tracking method has demonstrated its capability to track an unmarked industrial product with both absolute and repeatability accuracy of below 30 cm. Experimental comparison with the direct localization method has also demonstrated a significant advantage of the proposed method in product positioning accuracy, reliability, and consistency. Since the proposed method does not require the direct product marking, it enables the localization of a theoretically unlimited number of products,



while providing a significantly increased cost- and energy efficiency. The overall energy consumption, cost, and maintenance requirements in this method are significantly reduced and are only limited by the number of operating material handling equipment units (e.g., forklifts).

With minor adjustments, the proposed method has a significant applicability potential with different types of industrial machinery, including tractors, forklifts, various loaders, and cranes. Future advancements in the proposed method also include the development of a simplified indirect tracking setup version to cover various manual transportation units, such as manual pallet jacks. Future perspectives also include the overall method optimization and further expansion of the potential applications range. The proposed A-PDD algorithm may also find its possible use in the field of robotics, automation, and industry.

## REFERENCES

- [1] F. Piccialli, N. Bessis, and J. J. Jung, "Data science challenges in industry 4.0," *IEEE Transactions on Industrial Informatics*, 2020.
- [2] A. A. Tubis and J. Rohman, "Intelligent warehouse in industry 4.0—systematic literature review," *Sensors*, vol. 23, no. 8, p. 4105, 2023.
- [3] A. K. Grover and M. H. Ashraf, "Autonomous and iot-driven intralogistics for industry 4.0 warehouses: A thematic analysis of the literature," *Transportation Journal*, vol. 63, no. 1, pp. 42–61, 2024.
- [4] S. Shyam, S. Juliet, and K. Ezra, "A UWB Based Indoor Asset Tracking Architecture for Industry 4.0," in *2022 4th International Conference on Smart Systems and Inventive Technology (ICSSIT)*. IEEE, 2022, pp. 501–506.
- [5] S. Alyahya, Q. Wang, and N. Bennett, "Application and integration of an rfid-enabled warehousing management system—a feasibility study," *Journal of Industrial Information Integration*, vol. 4, pp. 15–25, 2016.
- [6] A. Motroni, A. Buffi, and P. Nepa, "A survey on indoor vehicle localization through RFID technology," *IEEE Access*, vol. 9, pp. 17 921–17 942, 2021.
- [7] A. Volpi, L. Tebaldi, G. Matrella, R. Montanari, and E. Bottani, "Low-Cost UWB Based Real-Time Locating System: Development, Lab Test, Industrial Implementation and Economic Assessment," *Sensors*, vol. 23, no. 3, p. 1124, 2023.
- [8] V.-D. Vu, D.-D. Hoang, P. X. Tan, V.-T. Nguyen, T.-U. Nguyen, N.-A. Hoang, K.-T. Phan, D.-T. Tran, D.-Q. Vu, P.-Q. Ngo *et al.*, "Occlusion-robust pallet pose estimation for warehouse automation," *IEEE Access*, 2024.
- [9] J. Rutkowski, H. Youssef, A. Gouda, C. Reining, and M. Roidl, "The potential of deep learning based computer vision in warehousing logistics," *Logistics Journal: Proceedings*, vol. 2022, no. 18, 2022.
- [10] L. Santoro, M. Nardello, D. Eccher, M. Sittioni, D. Brunelli, and D. Fontanelli, "A tag-less ultrawide-band passive tracking system," in *2023 IEEE International Workshop on Metrology for Industry 4.0 & IoT (MetroInd4.0&IoT)*. IEEE, 2023, pp. 287–292.
- [11] M. Elsayeh, M. Haroon, B. Tawfik, and A. S. Fahmy, "Rfid-based indoors localization of tag-less objects," in *2010 5th Cairo International Biomedical Engineering Conference*. IEEE, 2010, pp. 61–65.
- [12] A. Ramezani Akhmarch, M. T. Lazarescu, O. Bin Tariq, and L. Lavagno, "A tagless indoor localization system based on capacitive sensing technology," *Sensors*, vol. 16, no. 9, p. 1448, 2016.
- [13] A. Frankó, G. Vida, and P. Varga, "Reliable identification schemes for asset and production tracking in industry 4.0," *Sensors*, vol. 20, no. 13, p. 3709, 2020.
- [14] K. Zhao, M. Zhu, B. Xiao, X. Yang, C. Gong, and J. Wu, "Joint rfid and uwb technologies in intelligent warehousing management system," *IEEE Internet of Things Journal*, vol. 7, no. 12, pp. 11 640–11 655, 2020.
- [15] H. Borstell, J. Kluth, M. Jaeschke, C. Plate, B. Gebert, and K. Richter, "Pallet monitoring system based on a heterogeneous sensor network for transparent warehouse processes," in *2014 Sensor Data Fusion: Trends, Solutions, Applications (SDF)*. IEEE, 2014, pp. 1–6.
- [16] F. Belloni, "Driving innovation: Creating a hybrid rtls positioning ecosystem," Jul 2023. [Online]. Available: <https://www.forbes.com/sites/forbestechcouncil/2023/07/18/driving-innovation-creating-a-hybrid-rtls-positioning-ecosystem/?sh=fd3636865ef6>
- [17] A. Motroni, A. Buffi, and P. Nepa, "Forklift tracking: Industry 4.0 implementation in large-scale warehouses through uwb sensor fusion," *Applied Sciences*, vol. 11, no. 22, p. 10607, 2021.
- [18] S. Konatowski, P. Kaniowski, and J. Matuszewski, "Comparison of estimation accuracy of ekf, ukf and pf filters," *Annual of Navigation*, no. 23, pp. 69–87, 2016.
- [19] L.-o. Kovavisaruch, K. Maneerat, T. Sanpechuda, K. Chinda, T. Wongsatho, S. Wisadsud, S. Lim, and K. Kaemarangsi, "UWB Tracking for Forklift in Near-Automate Warehouse," in *2024 5th Technology Innovation Management and Engineering Science International Conference (TIMES-ICON)*. IEEE, 2024, pp. 1–5.
- [20] V. Barral, P. Suárez-Casal, C. J. Escudero, and J. A. García-Naya, "Multi-sensor accurate forklift location and tracking simulation in industrial indoor environments," *Electronics*, vol. 8, no. 10, p. 1152, 2019.
- [21] "Sewio tag-less tracking project Prakab 2.0: Case Study," <https://www.sewio.net/wp-content/uploads/2023/02/Case-Study-Prakab-2.0-v4.pdf>, accessed: 2024-09-06.
- [22] R. Juráš, P. Mlýnek, and A. Čech, "A System for the Real-time Indirect Monitoring of Objects," Czech Republic patent CZ38 000U1, July 12, 2024, accessed: 2025-02-07. [Online]. Available: <https://patents.google.com/patent/CZ38000U1>
- [23] A. Fjodorov, S. Ulp, M. M. Alam, and A. Kuusik, "Inertial and Positioning Sensors Fusion for Indirect Location Tracking in Warehouse Inventory Management," in *2023 International Conference on Control, Automation and Diagnosis (ICCAD)*. IEEE, 2023, pp. 1–7.
- [24] J. H. Wall, D. M. Bevilacqua, *et al.*, "Characterization of various IMU error sources and the effect on navigation performance," in *Proceedings of the 18th international technical meeting of the satellite division of the institute of navigation (ION GNSS 2005)*, 2005, pp. 967–978.
- [25] M. L. Hoang and A. Pietrosanto, "Yaw/Heading optimization by drift elimination on MEMS gyroscope," *Sensors and Actuators A: Physical*, vol. 325, p. 112691, 2021.
- [26] A. Fjodorov, S. Ulp, T. Laadung, M. M. Alam, and A. Kuusik, "Vehicle Heading Estimation Using Positioning and Inertial Data-Based Adaptive Tandem Kalman Filter," in *TechRxiv*. IEEE, 2024, pp. 1–7.
- [27] M. Broy, B. Jonsson, J.-P. Katoen, M. Leucker, and A. Pretschner, "Model-based testing of reactive systems," in *Volume 3472 of Springer LNCS*. Springer, 2005.
- [28] P. A. Laplante, R. Cravey, L. P. Dunleavy, J. L. Antonakos, R. LeRoy, J. East, N. E. Buris, C. J. Conant, L. Fryda, R. W. Boyd *et al.*, *Comprehensive dictionary of electrical engineering*. CRC Press, 2018.
- [29] M. Foster, R. G. Taylor, A. D. Brucker, and J. Derrick, "Formalising extended finite state machine transition merging," in *International Conference on Formal Engineering Methods*. Springer, 2018, pp. 373–387.
- [30] T. H. Cormen, C. E. Leiserson, R. L. Rivest, and C. Stein, *Introduction to algorithms*. MIT press, 2022.
- [31] "Eliko UWB RTLS," <https://eliko.tech/uwb-rtls-ultra-wideband-real-time-location-system/>, accessed: 2024-02-18.
- [32] "BNO055 Intelligent 9-axis absolute orientation sensor datasheet," [https://cdn-shop.adafruit.com/datasheets/BST\\_BNO055\\_DS000.12.pdf](https://cdn-shop.adafruit.com/datasheets/BST_BNO055_DS000.12.pdf), accessed: 2024-02-18.
- [33] "Miran MPS Series Draw Wire Potentiometers," <http://www.mirantech.com/lxswycgq/488.html>, accessed: 2024-02-17.
- [34] "Weatherproof Ultrasonic Sensor SEN0208," [https://wiki.dfrobot.com/Weatherproof-Ultrasonic-Sensor-With-Separate-Probe-SKU\\_SEN0208](https://wiki.dfrobot.com/Weatherproof-Ultrasonic-Sensor-With-Separate-Probe-SKU_SEN0208), accessed: 2024-02-18.
- [35] A. Fjodorov, T. Laadung, M. Tommingas, and S. Ulp, "Dataset of Forklift-Deployed Multi-Sensor Setup for Indirect Tracking of Markerless Industrial Products," *TalTech Data Repository*, 2025. [Online]. Available: <https://doi.org/10.48726/zmv9c-p1e64>



**Aleksei Fjodorov** was born in Tallinn, Estonia, in 1995. He received his B.Sc. and M.Sc. degrees in telecommunication and electronics from the Tallinn University of Technology (TUT), Estonia, in 2017 and 2021, respectively. Currently, he is pursuing a Ph.D. degree in information and communication technology from Tallinn University of Technology. Since 2021, he has been working as a Researcher at Eliko Tehnoloogia Arenduskeskus OÜ, Tallinn. His current research covers sensor fusion methods

and algorithms, sensor fusion-enabled indoor positioning and tracking, IoT, electronics, and communication technologies.



**Sander Ulp** received the M.Sc. degree in telecommunication and the Ph.D. degree in information and communication technology from Tallinn University of Technology in 2013 and 2019, respectively. In 2018, he started working as a researcher at Eliko Tehnoloogia Arenduskeskus OÜ. Since 2019, he has been the CTO of the competence center, which develops novel indoor positioning research and technologies. His research interests are in distributed estimation, learning, and adaptation over net-

works, digital signal processing, localization technologies, and indoor positioning.



**Taavi Laadung** was born in Tallinn, Estonia, in 1990. He received his M.Sc. and Ph.D. degrees in telecommunication from the Tallinn University of Technology in 2016 and 2023, respectively. From 2015 to 2016, he served as a Practical Coursework Supervisor at the Tallinn University of Technology. From 2017 to 2019, he worked as a Communication Systems Research and Development Specialist with the Estonian Defence Forces. Since 2019, he has been a Researcher at OÜ Eliko Tehnoloogia Arenduskeskus in Tallinn, focusing on research regarding Ultra-Wideband (UWB) ranging protocols and improving the robustness of the Eliko UWB RTLS positioning system. His current research interests include the enhancement of algorithms and methodologies for wireless indoor tracking, positioning, and object-locating systems.



**Alar Kuusik** (Member, IEEE) received the Ph.D. degree in IT from the Tallinn University of Technology (TalTech), Estonia, in 2001. He is currently a Senior Research Scientist with the T. J. Seebeck Institute of Electronics, TalTech, focusing on the IoT, data acquisition, and networking technologies. He has been involved with several international research and innovation projects related to smart environments, smart cities, and wearable technologies. He has published more than 50 peer-reviewed articles and is the author

of five patent families. He is the Vice-Coordinator of the GAC of IEEE Computer Society in Region 8.



**Muhammad Mahtab Alam** (Senior Member, IEEE) received the M.Sc. degree in electrical engineering from Aalborg University, Denmark, in 2007, and the Ph.D. degree in signal processing and telecommunication from the University of Rennes1 France (INRIA Research Center), in 2013. He did his postdoctoral research (2014–2016) at the Qatar Mobility Innovation Center, Qatar. In 2016, he joined as the European Research Area Chair and as an Associate Professor with the Thomas Johann Seebeck

Department of Electronics, Tallinn University of Technology, where he was elected as a Professor in 2018 and Tenured Full Professor in 2021. Since 2019, he has been the Communication Systems Research Group Leader. His research focuses on the fields of wireless communications—connectivity, mobile positioning, 5G/6G services and applications. He has over 15 years of combined academic and industrial multinational experiences while working in Denmark, Belgium, France, Qatar, and Estonia. He has several leading roles as PI in multimillion Euros international projects funded by European Commission (Horizon Europe LATEST-5GS, 5G-TIMBER, H2020 5G-ROUTES, NATOSPS (G5482), Estonian Research Council (PRG424), Telia Industrial Grant etc. He is an author and co-author of more than 100 research publications. He is actively supervising a number of Ph.D. and Postdoc Researchers. He is also a contributor in two standardization bodies (ETSI SmartBAN, IEEE-GeeenICT-EECH), including “Rapporteur” of work item: DTR/SmartBAN-0014”.

## Appendix 5

This appendix provides the enhanced pseudocode of the developed positioning data-based algorithm for the drift error correction in the IMU provided heading information, presented in Publication I. A minor post-publication improvement for the algorithm, represented with the additional filtering (averaging) of the measured movement direction is marked in the pseudocode with the corresponding comment "// New".



---

**Algorithm 1:** Coordinates-based IMU heading drift correction algorithm

---

**Parameters:** Minimal movement speed threshold:  $v_{min}$  [m/s]

Maximal heading range threshold:  $\alpha_{max}$  [deg]

Length of the primary FIFO buffer:  $\mu$

Length of the secondary FIFO buffer:  $\eta$

Reverse movement threshold:  $\beta$  [deg]

Initial correction value:  $\delta^\psi$  [deg]

Initial heading:  $\Psi_0$  [deg]

**Input Data :** Tracked 2D coordinates:  $(x, y)_k$  [m]

IMU measured heading:  $\psi_k$  [deg]

**Outputs :** Corrected heading:  $\Psi_k$  [deg]

Heading correction value:  $\delta^\psi$  [deg]

```
1 Initialize primary FIFO buffer  $\mathbf{W}$  of size  $\mu$ 
2 Initialize secondary FIFO buffer  $\mathbf{V}$  of size  $\eta$  // New
3  $\theta_0 = \Psi_0$ 

4 for  $k = 1$  to  $\infty$  do
5    $\Psi_k = \psi_k + \delta^\psi$ 

6   if New positioning data  $(x, y)_k$  available then
7     Add new positioning data to buffer  $\mathbf{W}$ :  $\mathbf{W} = \{(x, y)_k, (x, y)_{k-1}, \dots, (x, y)_{k-\mu}\}$ 
8      $\mathbf{v}(k) = (v_1, \dots, v_n, \dots, v_\mu)$ ,  $v_n = \sqrt{(x_n - x_1)^2 + (y_n - y_1)^2}$ 
9      $\boldsymbol{\alpha}(k) = (\alpha_1, \dots, \alpha_n, \dots, \alpha_\mu)$ ,  $\alpha_n = \text{atan2}(-(x_n - x_1), -(y_n - y_1)) \cdot \frac{180}{\pi} + 180$ 

10    if  $\exists v \in \mathbf{v}(k)$  s.t.  $v \geq v_{min}$  then
11       $\mathbf{I} = \{i \mid v_i \in \mathbf{v}(k) \geq v_{min}, i \in (1, \dots, \mu)\}$ 
12      Circular mean of  $i^{th}$  elements in  $\boldsymbol{\alpha}(k)$ :  $\theta_\alpha = \overline{\boldsymbol{\alpha}(k)_i}$ ,  $i \in \mathbf{I}$ 

13      if  $|\theta_\alpha - \theta_0| \geq \beta$  &&  $|\psi_k - \psi_0| < \beta$  then
14         $\theta_\alpha = \theta_\alpha + 180$ 
15      end

16      Add movement direction  $\theta_\alpha$  to buffer  $\mathbf{V}$ :  $\mathbf{V} = \{\theta_\alpha, \theta_2, \dots, \theta_\eta\}$  // New
17      Circular range of buffer  $\mathbf{V}$ :  $R_\alpha = R^{circ}(\mathbf{V})$  // New

18      if  $R_\alpha < \alpha_{max}$  then
19        Circular mean of buffer  $\mathbf{V}$ :  $\theta = \bar{\mathbf{V}}$  // New
20         $\delta^\psi = \theta - \psi_k$ 
21      end

22       $\psi_0 = \psi_k$ 
23       $\theta_0 = \theta$ 
24    end
25  end
26 end
```

---

## Appendix 6

This Appendix provides the key matrices used by the proposed Adaptive Tandem Kalman Filter, described in Section 4.4.2:

$$\hat{\mathbf{X}}_k = \begin{bmatrix} \hat{x}_k \\ \hat{y}_k \\ v_{k-1}^x \\ v_{k-1}^y \\ v_{k-1} \\ \phi_{k-1} \\ \hat{\Psi}_k \end{bmatrix}, \quad \mathbf{X}_k^1 = \begin{bmatrix} x_k \\ y_k \\ v_k^x \\ v_k^y \\ v_k \\ \phi_{k-1} \\ \hat{\Psi}_k \end{bmatrix}, \quad \mathbf{X}_k^2 = \begin{bmatrix} x_k \\ y_k \\ v_k^x \\ v_k^y \\ v_k \\ \phi_k \\ \hat{\Psi}_k \end{bmatrix}, \quad \mathbf{X}_k = \begin{bmatrix} x_k \\ y_k \\ v_k^x \\ v_k^y \\ v_k \\ \phi_k \\ \Psi_k \end{bmatrix}, \quad (30)$$

$$\mathbf{A} = \begin{bmatrix} 1 & 0 & dt_k^{x,y} & 0 & 0 & 0 & 0 \\ 0 & 1 & 0 & dt_k^{x,y} & 0 & 0 & 0 \\ 0 & 0 & 1 & 0 & 0 & 0 & 0 \\ 0 & 0 & 0 & 1 & 0 & 0 & 0 \\ 0 & 0 & 0 & 0 & 1 & 0 & 0 \\ 0 & 0 & 0 & 0 & 0 & 1 & 0 \\ 0 & 0 & 0 & 0 & 0 & 0 & 1 \end{bmatrix}, \quad (31)$$

$$\mathbf{B} = [0 \ 0 \ 0 \ 0 \ 0 \ 0 \ dt_k^\omega]^T, \quad \mathbf{u}_k = [\omega_k], \quad (32)$$

$$\mathbf{I} = \mathbf{P}_0 = \begin{bmatrix} 1 & 0 & 0 & 0 & 0 & 0 & 0 \\ 0 & 1 & 0 & 0 & 0 & 0 & 0 \\ 0 & 0 & 1 & 0 & 0 & 0 & 0 \\ 0 & 0 & 0 & 1 & 0 & 0 & 0 \\ 0 & 0 & 0 & 0 & 1 & 0 & 0 \\ 0 & 0 & 0 & 0 & 0 & 1 & 0 \\ 0 & 0 & 0 & 0 & 0 & 0 & 1 \end{bmatrix}, \quad (33)$$

$$\mathbf{Q}_k = \begin{bmatrix} q^{pos} & 0 & 0 & 0 & 0 & 0 & 0 \\ 0 & q^{pos} & 0 & 0 & 0 & 0 & 0 \\ 0 & 0 & q^v & 0 & 0 & 0 & 0 \\ 0 & 0 & 0 & q^v & 0 & 0 & 0 \\ 0 & 0 & 0 & 0 & q^v & 0 & 0 \\ 0 & 0 & 0 & 0 & 0 & q_k^\phi & 0 \\ 0 & 0 & 0 & 0 & 0 & 0 & q_k^\Psi \end{bmatrix}, \quad (34)$$

$$\begin{aligned} {}^1\mathbf{H} &= \begin{bmatrix} 1 & 0 & 0 & 0 & 0 & 0 & 0 \\ 0 & 1 & 0 & 0 & 0 & 0 & 0 \end{bmatrix}, \\ {}^2\mathbf{H} &= \begin{bmatrix} 0 & 0 & 0 & 0 & 1 & 0 & 0 \\ 0 & 0 & 0 & 0 & 0 & 1 & 0 \end{bmatrix}, \\ {}^3\mathbf{H} &= [0 \ 0 \ 0 \ 0 \ 0 \ 0 \ 1], \end{aligned} \quad (35)$$

$${}^1\mathbf{R} = \begin{bmatrix} r^{pos} & 0 \\ 0 & r^{pos} \end{bmatrix}, \quad {}^2\mathbf{R}_k = \begin{bmatrix} r^v & 0 \\ 0 & r_k^\phi \end{bmatrix}, \quad {}^3\mathbf{R}_k = [r_k^\Psi], \quad (36)$$

$${}^1\mathbf{z}_k = \begin{bmatrix} x_k^{meas} \\ y_k^{meas} \end{bmatrix}, \quad {}^2\mathbf{z}_k = \begin{bmatrix} \hat{v}_k \\ \hat{\phi}_k \end{bmatrix} = \begin{bmatrix} \sqrt{v_k^{x2} + v_k^{y2}} \\ \text{atan2}(-v_k^x, -v_k^y) \cdot \frac{180}{\pi} + 180 \end{bmatrix}, \quad {}^3\mathbf{z}_k = [\phi_k]. \quad (37)$$



## Appendix 7

Table 16 provides the tuning parameters for both proposed IMU heading drift correction and ATKF heading estimation algorithms, used in both test simulations and in the experimental test campaign, respectively described in sections 4.4.3 and 4.4.4.

Table 16: Tuning parameters for both proposed ATKF heading estimation and IMU heading drift correction (DCA) algorithms, used in test simulations and during the experimental test campaign

	Parameter	Value		
		Simulations		Experimental tests
		Scenario I	Scenario II	
ATKF	$q^{pos}$	$1 \text{ m}^2$	$1 \text{ m}^2$	$1 \text{ m}^2$
	$q^v$	$0.1 \text{ m}^2/\text{s}^2$	$5 \text{ m}^2/\text{s}^2$	$10 \text{ m}^2/\text{s}^2$
	$q^v$	$1 \text{ m}^2/\text{s}^2$	$1 \text{ m}^2/\text{s}^2$	$1 \text{ m}^2/\text{s}^2$
	$q_{min}^\phi$	$1 \text{ deg}^2$	$1 \text{ deg}^2$	$0 \text{ deg}^2$
	$q_{min}^\Psi$	$0 \text{ deg}^2$	$0 \text{ deg}^2$	$0 \text{ deg}^2$
	$q_{max}$	$100 \text{ deg}^2$	$100 \text{ deg}^2$	$10000 \text{ deg}^2$
	$r^{pos}$	$30 \text{ m}^2$	$40 \text{ m}^2$	$3 \text{ m}^2$
	$r^v$	$0 \text{ m}^2/\text{s}^2$	$1 \text{ m}^2/\text{s}^2$	$0 \text{ m}^2/\text{s}^2$
	$r_{min}^\phi$	$100 \text{ deg}^2$	$10 \text{ deg}^2$	$0 \text{ deg}^2$
	$r_{min}^\Psi$	$0 \text{ deg}^2$	$0 \text{ deg}^2$	$0 \text{ deg}^2$
	$r_{max}$	$100 \text{ deg}^2$	$100 \text{ deg}^2$	$10000 \text{ deg}^2$
	$v_{thr}^0$	$0.07 \text{ m/s}$	$0.07 \text{ m/s}$	$0.1 \text{ m/s}$
	$v_{thr}^\phi$	$0.3 \text{ m/s}$	$0.4 \text{ m/s}$	$0.5 \text{ m/s}$
	$v_{thr}^\Psi$	$0.55 \text{ m/s}$	$0.75 \text{ m/s}$	$1.18 \text{ m/s}$
	$a^\phi$	190	230	300
	$a^\Psi$	33	445	710
DCA	$\mu$	10	5	6
	$\eta$	4	2	5
	$v_{min}$	5 m	4 m	0.3 m
	$\alpha_{max}$	10 deg	10 deg	10 deg
	$\beta$	120 deg	120 deg	120 deg



## Appendix 8

This Appendix covers the additional results of the performed simulated tests of the ATKF heading estimation algorithm and gyroscope drift mitigation algorithm. While the results on the median absolute heading error are provided and discussed in Section 4.4.3, this appendix covers the additional results, which include the accuracy metrics of mean absolute heading error (Fig. 25) and root mean squared heading error (Fig. 26), as well as precision metrics of median absolute heading error deviation (Fig. 27), mean absolute heading error deviation (Fig. 28), and heading error standard deviation (Fig. 29).

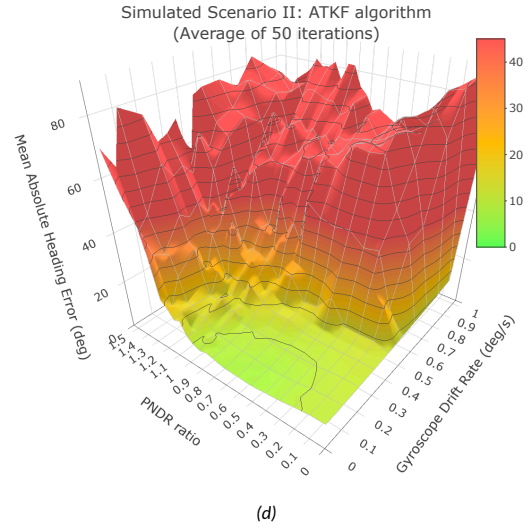
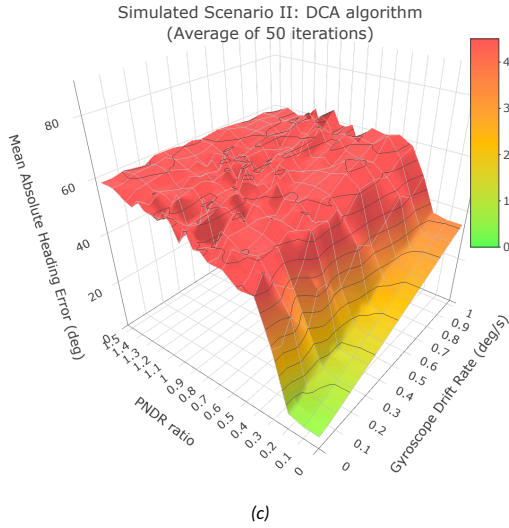
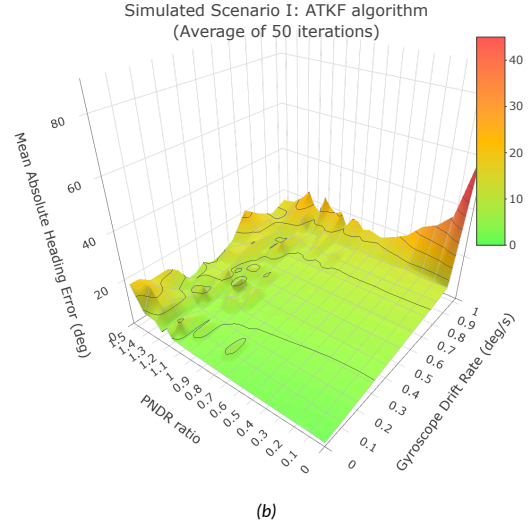
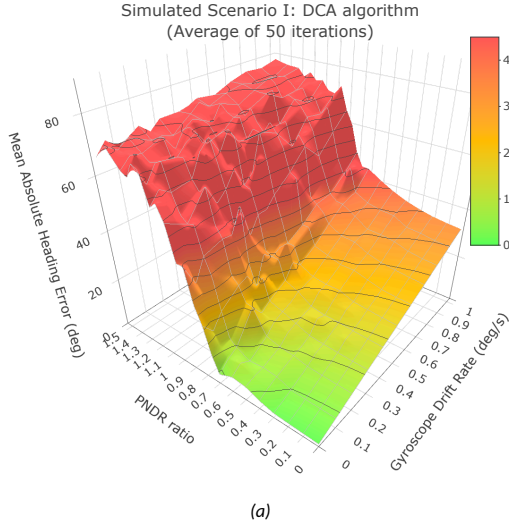


Figure 25: Averaged results on the Mean Absolute Error in the simulated vehicle heading, estimated by both DCA (left) and ATKF (right) algorithms in two different movement scenarios I (top) and II (bottom), at different combinations of PNRD and gyroscope drift ratios.

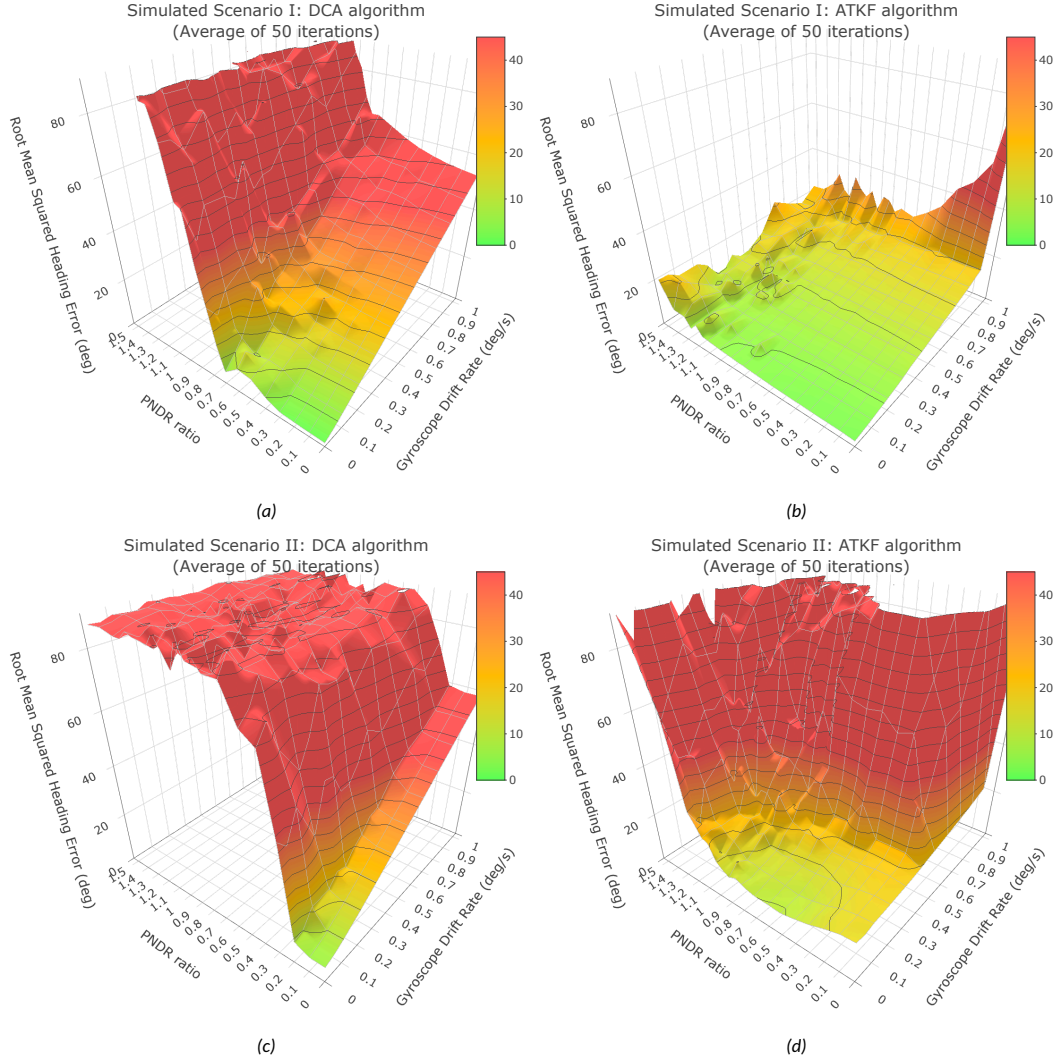


Figure 26: Averaged results on the Root Mean Squared Error in the simulated vehicle heading, estimated by both DCA (left) and ATKF (right) algorithms in two different movement scenarios I (top) and II (bottom), at different combinations of PNRD and gyroscope drift ratios.



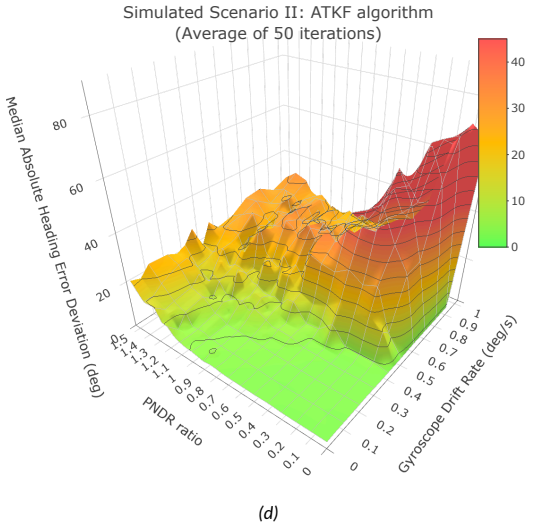
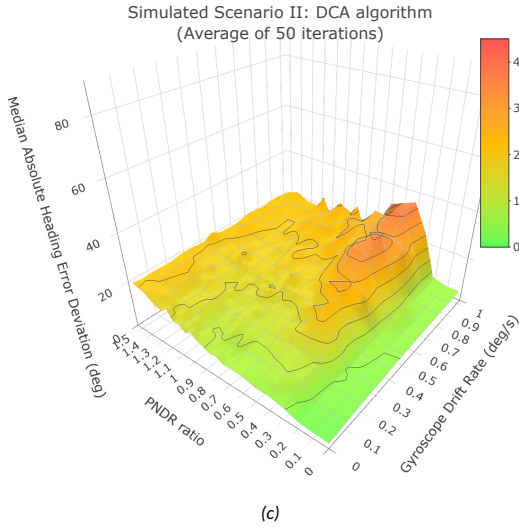
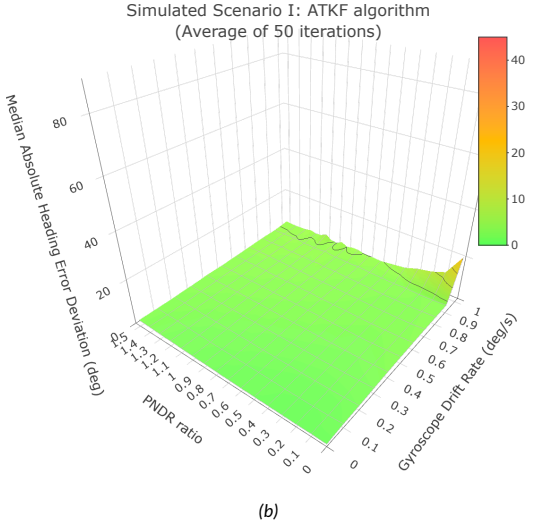
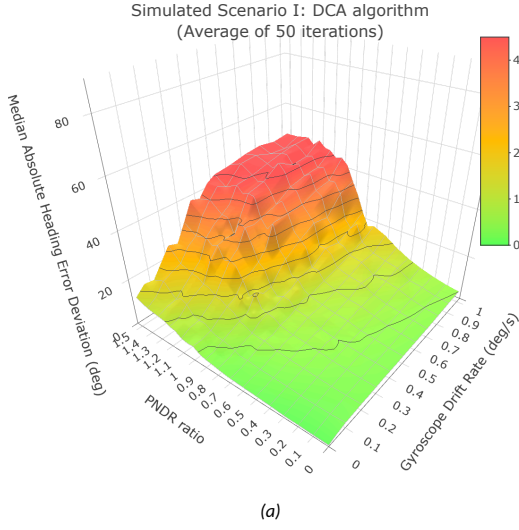


Figure 27: Averaged results on the median absolute error deviation in the simulated vehicle heading, estimated by both DCA (left) and ATKF (right) algorithms in two different movement scenarios I (top) and II (bottom), at different combinations of PNRD and gyroscope drift ratios.

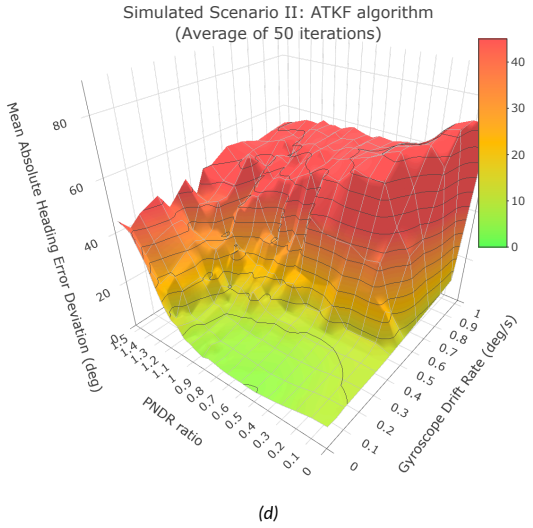
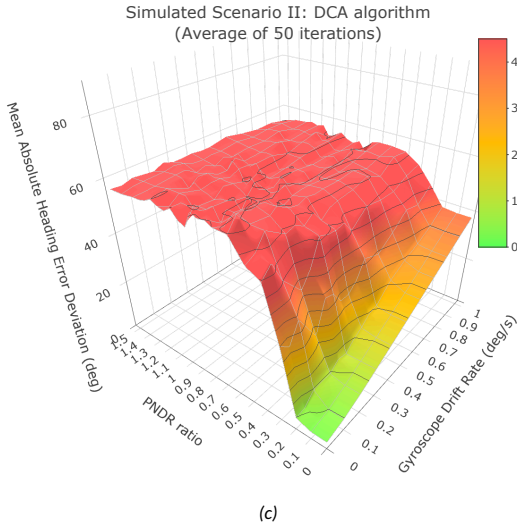
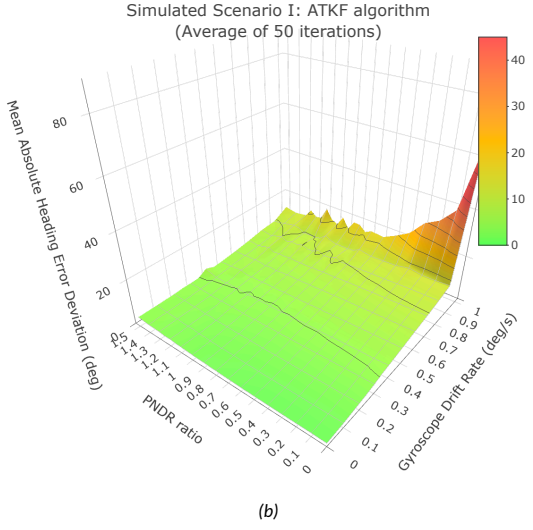
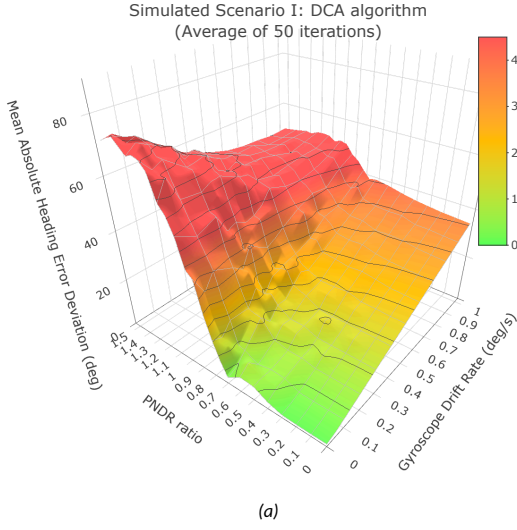


Figure 28: Averaged results on the mean absolute error deviation in the simulated vehicle heading, estimated by both DCA (left) and ATKF (right) algorithms in two different movement scenarios I (top) and II (bottom), at different combinations of PNRD and gyroscope drift ratios.

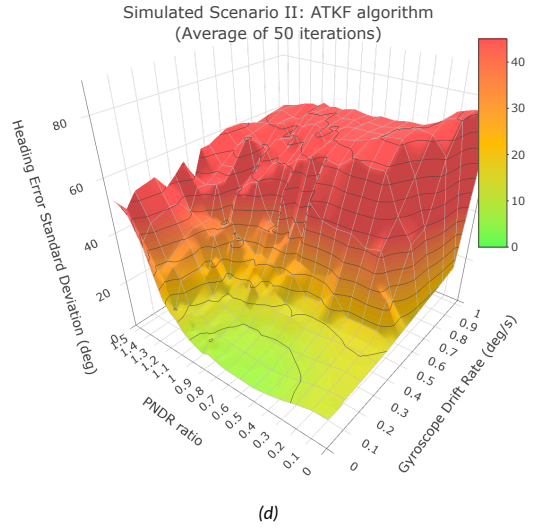
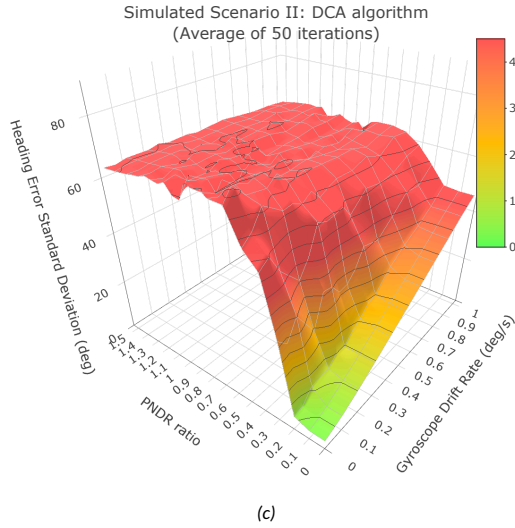
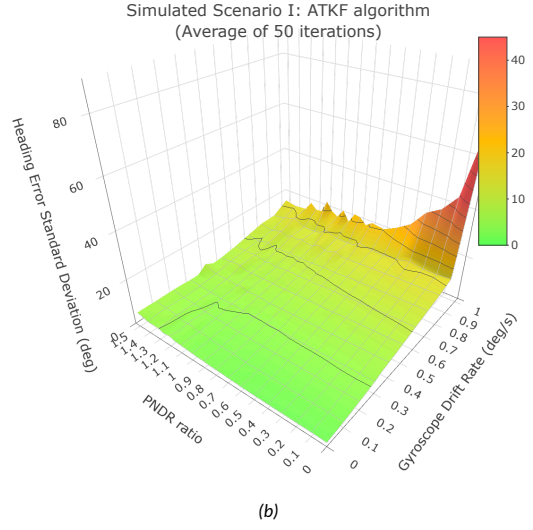
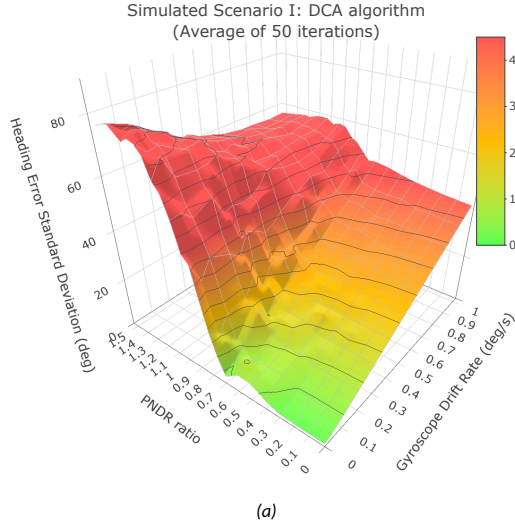


Figure 29: Averaged results on the error standard deviation in the simulated vehicle heading, estimated by both DCA (left) and ATKF (right) algorithms in two different movement scenarios I (top) and II (bottom), at different combinations of PNRD and gyroscope drift ratios.

## Appendix 9

This Appendix provides heatmaps of the UWB anchors' infrastructure ranging coverage in case of the proposed indirect tracking method (30a) and direct tracking approach (30b). Multicolored line represents the positioning data of the tracked payload (B) by the corresponding method, whereas the color reflects the number of UWB anchors used for ranging in the particular area. UWB anchors' deployment is shown with green diamonds, while the used reference points, described in Section 5.4 are shown with magenta.

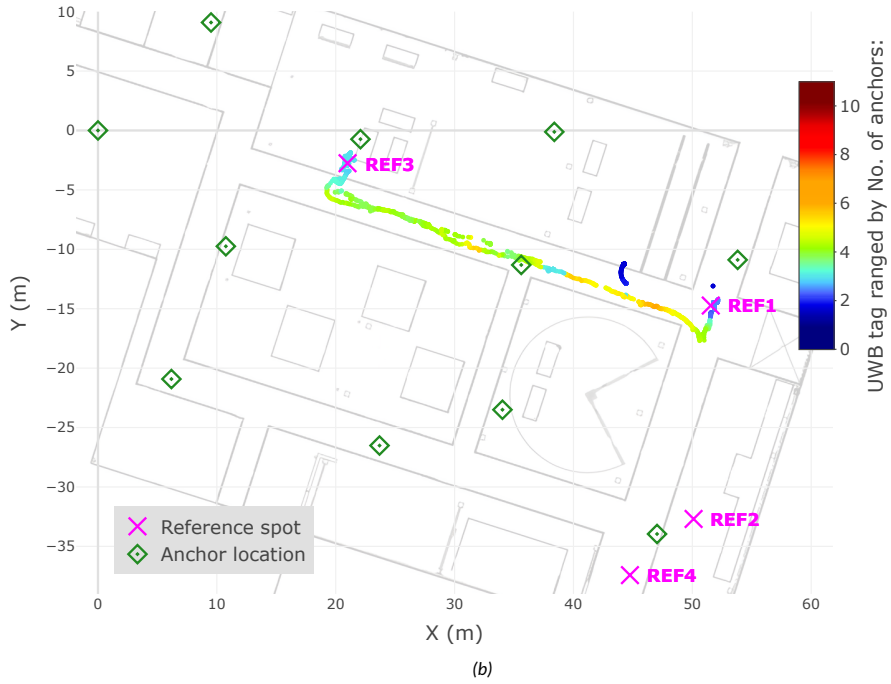


Figure 30: Heatmaps of the UWB anchors' infrastructure coverage in ranging of UWB tag in case of proposed indirect tracking method (a) and direct tracking method (b), with mapped anchors infrastructure (green diamonds) and reference points (magenta).

# Curriculum Vitae

## 1. Personal data

Name	Aleksei Fjodorov
Date and place of birth	14 March 1995 Tallinn, Estonia
Nationality	Estonian

## 2. Contact information

Address	Sõpruse pst 222-2, 13412 Tallinn, Estonia,
Phone	+372 53801358
E-mail	aleksei.fjodorov1@taltech.ee

## 3. Education

2021–...	Tallinn University of Technology, School of Information Technologies, Information and Communication Technology, PhD studies
2018–2021	Tallinn University of Technology, School of Information Technologies, Communicative Electronics, MSc
2014–2017	Tallinn University of Technology, School of Information Technologies, Electronics and Telecommunications, BSc
2002–2014	Tallinn 53 Secondary school, Primary & Secondary Education

## 4. Language competence

Estonian	fluent
English	fluent
Russian	native
German	basic

## 5. Professional employment

2024–...	Tallinn University of Technology, School of Information Technologies, Junior Researcher
2021–2024	Eliko Competence Centre in Electronics-, Info- and Communication Technologies, Junior Researcher

## 6. Computer skills

- Operating systems: Windows
- Document preparation: Microsoft Office, LibreOffice, LaTeX
- Programming languages: C, C#, Arduino, Python
- Scientific packages: MATLAB, R

## 7. Defended theses

- 2021, 5G Testbed Implementation and Measurement Campaign for Ground and Aerial Coverage at 3.5GHz Band, MSc, Supervisor Prof. Muhammad Mahtab Alam, Co-supervisor Dr. Sven Päränd, Tallinn University of Technology, School of Information Technologies, Thomas Johann Seebeck Department of Electronics.
- 2017, Software defined radio implementation of marine Automatic Identification System (AIS), BCs, Supervisor MSc. Julia Berdnikova, Tallinn University of Technology, School of Information Technologies, Thomas Johann Seebeck Department of Electronics.

## 8. Field of research

- Algorithms
- Sensor fusion
- Indoor positioning

## 9. Scientific work

### Papers

1. A. Fjodorov, A. Masood, M. M. Alam, and S. Päränd, "5G Testbed Implementation and Measurement Campaign for Ground and Aerial Coverage," *2022 18th Biennial Baltic Electronics Conference (BEC)*, pp. 1–6, 2022
2. A. Fjodorov, S. Ulp, M. M. Alam, and A. Kuusik, "Inertial and Positioning Sensors Fusion for Indirect Location Tracking in Warehouse Inventory Management," *2023 International Conference on Control, Automation and Diagnosis (ICCAD)*, pp. 1–7, 2023
3. T. Laadung, S. Ulp, A. Fjodorov, M. M. Alam, and Y. Le Moullec, "Adaptive Extended Kalman Filter Position Estimation Based on Ultra-Wideband Active-Passive Ranging Protocol," *IEEE Access*, 2023
4. I. Müürsepp, A. Fjodorov, and M. M. Alam, "Non-Line of Sight Detection Based on 5G Signal Strength-and Quality Measurements and its Impact on Mobile Positioning Accuracy," in *2024 International Wireless Communications and Mobile Computing (IWCMC)*, pp. 256–261, IEEE, 2024
5. A. Fjodorov, S. Ulp, T. Laadung, M. M. Alam, and A. Kuusik, "Vehicle Heading Estimation Using Positioning and Inertial Data-Based Adaptive Tandem Kalman Filter," *IEEE Transactions on Intelligent Vehicles*, 2025
6. A. Fjodorov, S. Ulp, T. Laadung, M. M. Alam, and A. Kuusik, "Accurate Indirect 3D Localization of Markerless Industrial Products," *IEEE Sensors Journal*, *Accepted: 18.09, 2025*

### Conference presentations

1. A. Fjodorov, A. Masood, M. M. Alam, and S. Päränd, "5G Testbed Implementation and Measurement Campaign for Ground and Aerial Coverage," *2022 18th Biennial Baltic Electronics Conference (BEC)*, pp. 1–6, 2022

2. A. Fjodorov, S. Ulp, M. M. Alam, and A. Kuusik, "Inertial and Positioning Sensors Fusion for Indirect Location Tracking in Warehouse Inventory Management," *2023 International Conference on Control, Automation and Diagnosis (ICCAD)*, pp. 1-7, 2023



# Elulookirjeldus

## 1. Isikuandmed

Nimi	Aleksei Fjodorov
Sünniaeg ja -koht	14.03.1995, Tallinn, Eesti
Kodakondsus	Eesti

## 2. Kontaktandmed

Address	Sõpruse pst 222-2, 13412 Tallinn, Estonia,
Telefon	+372 53801358
E-post	aleksei.fjodorov1@taltech.ee

## 3. Haridus

2021- ...	Tallinna Tehnikaülikool, Infotehnoloogia teaduskond, Info- ja kommunikatsioonitehnoloogia, doktoriõpe
2018–2021	Tallinna Tehnikaülikool, Infotehnoloogia teaduskond, Elektroonika ja kommunikatsioonitehnoloogiad, MSc
2014–2017	Tallinna Tehnikaülikool, Infotehnoloogia teaduskond, Elektroonika ja telekommunikatsioon, BSc
2002–2014	Tallinna 53. Keskkool, Põhi- ja Keskkharidus

## 4. Keelteoskus

eesti keel	kõrgtase
inglise keel	kõrgtase
vene keel	emakeel
saksa keel	algtase

## 5. Teenistuskäik

2024- ...	Tallinna Tehnikaülikool, Infotehnoloogia teaduskond, Thomas Johann Seebecki Elektroonikainstituut, Doktorant-nooremteadur
2021–2024	Eliko Tehnoloogia Arenduskeskus OÜ, Nooremteadur

## 6. Computer skills

- Operatsioonisüsteemid: Windows
- Kontoritarkvara: Microsoft Office, LibreOffice, LaTeX
- Programmeerimiskeeled: C, C#, Arduino, Python
- Teadustarkvara paketid: MATLAB, R

## 7. Kaitstud lõputööd

- 2021, 5G testplatvormi rakendamine ning mõõtmiskampaania 3.5GHz sagedusalas maapinnal ja õhus, MSc, juhendaja Prof. Muhammad Mahtab Alam, kaasjuhendaja Dr. Sven Pärand, Tallinna Tehnikaülikool, Infotehnoloogia teaduskond, Thomas Johann Seebecki elektroonikainstituut

- 2017, Laevade Automaatse Identifitseerimise Süsteemi (AIS) rakendus tarkvaralise raadioga, BSc, juhendaja MSc. Julia Berdnikova, Tallinna Tehnikaülikool, Infotehnoloogia teaduskond, Thomas Johann Seebecki elektroonikainstituut

## **8. Teadustöö põhisuunad**

- Algoritmid
- Andurisulandus
- Sisepositsioneerimine

## **9. Teadustegevus**

Teadusartiklite, konverentsiteeside ja konverentsiettekannete loetelu on toodud ingliskeelse elulookirjelduse juures.



ISSN 2585-6901 (PDF)  
ISBN 978-9916-80-390-5 (PDF)